Self-assembled nanostructures for photon management in optoelectronic devices

Zur Erlangung des akademischen Grades eines
DOKTORS DER INGENIEURWISSENSCHAFTEN
(Dr.-Ing.)

von der KIT-Fakultät für

Elektrotechnik und Informationstechnik
des Karlsruher Instituts für Technologie (KIT)

genehmigte
DISSERTATION

Von
M.Sc.Yidenekachew Jenberu Donie
geb. in: Yirgacheffe

Tag der mündlichen Prüfung: 18. November 2021

Hauptreferent: Prof. Dr. rer. nat. Uli Lemmer
Korreferent: Prof. Dr.-Ing. Bernhard Schmauß

Abstract

The ultimate success of solar photovoltaic (PV) and organic light-emitting diode (OLED) technologies requires significant advancements in cost reduction and efficiency improvement. Both objectives can be simultaneously achieved through the use of photon management nanostructures. The fundamental goals of photon management are reducing incident light reflection, improving absorption or enhancing outcoupling, and tailoring the optical properties of a device for use in different types of energy conversion systems. For optimal efficiency of PV cells and OLEDs, the nanostructures should provide an extended spectral and angular range of effectiveness. In this regard, photon management based on disordered nanostructures has recently garnered significant attention. Such types of photonic layers operate over a broader spectral range than their periodical counterparts and possess optical properties that can be easily predicted and tuned, unlike purely random configurations.

This thesis work presents photon management by 2D planar disordered nanostructures for optoelectronic thin film devices. Here, the nanostructures are designed to act as an antireflective or efficient scattering architecture whose primary goal is to improve the optical absorption of thin-film-based PV cells and increase their power conversion efficiency. The methodology and structures developed also have direct implications for the field of OLED devices. Thus, the engineered structures are used to ameliorate the outcoupling properties of OLEDs, which possess a comparable spectral range of operation as PV cells.

As a prerequisite for any experimental investigations, a mature fabrication route for creating nanostructures with controllable disorder properties is established using a versatile, large area, wet-chemical technique based on lateral phase separation of a polymer blend. This wet-chemical technique has often been carried out by spin-coating, which does not allow incorporating phase-separated nanostructures (PSN) into arbitrary 2D designs as is required for their deployment in commercial products. On the other hand, additive manufacturing tools like inkjet printers can create almost any geometrically complex shape across micron to macro scales. However, due to the micron-scale resolution of most conventional inkjet printers, their impact in devising nanostructured materials and devices is still absent.

For the first time, this study tackles both of these shortcomings while preserving the low-cost attractiveness and the versatility of phase-separation using homopolymer blends by exploiting the unique advantages of inkjet-printing. Upon optimized conditions, digitally printable PSN from the micrometer to sub-100 nm range are realized according to a pre-determined 2D layout. These PSN can be fabricated on various rigid and flexible substrates at a speed of 45 cm/s. The proposed approach also opens numerous new nanofabrication avenues, including dynamic variation of

PSN during inkjet printing, either by adapting printing resolution from pixel to pixel for a given ink formulation or by working with multiple polymer inks.

Moreover, PSN are commonly deposited using polymers with low glass transition temperatures, which limit their practical relevance for nanoimprint lithography (NIL) as such PSN are prone to in-plane stamp distortions in the presence of high imprinting pressure and temperature. To overcome this shortcoming, this work exploits the unique advantages of an inorganic-organic hybrid polymer (OrmoStamp) that has already gained prominence in the industry as a choice of imprinting stamps material in UV and thermal-based NIL. For the first time, this work demonstrates that nano-stamps based on PSN (made of OrmoStamp) can be directly fabricated over various rigid and flexible substrates using a phase separation process. This opens a direct route for using PSN in NIL without additional intermediate lithographic or replication steps. Thus, spin coated and printed- as well as imprinted PSN can improve photon management in manifold nanophotonic applications, demonstrated here by incorporating them in PV cells and OLEDs for power efficiency enhancement.

For PV cells, two different optical management techniques are explored. The first technique focuses on developing light scattering layers for PV cells via either a bottom-up or top-down strategy. In the bottom-up strategy, PSN are introduced into hydrogenated amorphous silicon (a-Si:H) based PV cells' backside prior to the deposition of a reflector to realize light-scattering reflectors. These light scattering reflectors yield an efficiency better than that of a device based on a commercial light-scattering substrate. Furthermore, complementary optical simulations are conducted on an accurate 3D model to analyze the developed light scattering reflectors' superior light-harvesting properties and derive general design rules. In the top-down strategy, PSN are used to pattern a resist etching mask, which is employed for transferring disordered nanoholes into a thin a-Si:H layer by dry etching. The study began by conducting three-dimensional optical simulations to investigate systematically the impact of disorder of initially periodic arrangements of nanostructures. Results of this simulation indicate that quasi-disordered structures lead to broader spectral and angular responses, which is clearly beneficial for PV application. Following the top-down approach, enhancement in integrated absorption up to 93% under normal incidence and up to 200% at large incident angles are demonstrated with respect to an unpatterned absorber. Furthermore, a similar structure can serve as nano-stamps in a top-down strategy, whereby perovskite layers are nanoimprinted by the nano-stamps using a thermal NIL system. The nanopatterned perovskite film achieves an integrated absorption and a photoluminescence emission peak increase of $7\%_{rel}$ and $121\%_{rel}$, respectively. This route paves the way for roll-to-roll processable "photonized" absorbers.

The second technique focuses on the development of antireflection layers by additionally tailoring the PSN to sub-wavelength dimensions. The design considered herein consists of a front electrode, indium tin oxide (ITO), conformally deposited onto the PSN. In the optimum case, the nanostructured ITO electrodes yield a transmittance increase of $7\%_{rel}$ with respect to planar references. Their antireflective properties are exploited to enhance the photocurrent density of 4-terminal perovskite/crystalline-silicon (perovskite/c-Si) tandem solar cells. Perovskite/c-Si tandem devices with nanostructured ITO exhibit enhanced short-circuit current density ($2.9\,\mathrm{mA/cm^2}$ ab-

solute gain) and PCE (1.7% absolute gain) in the bottom c-Si solar cell compared to the reference.

Finally, this thesis expounds the significance of the above findings for the reverse problem- light extraction in OLEDs. In the first investigated configuration, this work exploits the easily tunable light scattering properties of disordered titania nanopillars, resulting from a self-assembly and a solvent assisted lift-off process. The subsequent planarization of these nanopillars by a thin epoxy layer ensures an excellent reproducibility of the devices, an aspect that is often critical for nano-corrugated substrates, and preserves a strong spatial overlap of the trapped optical modes with the light scattering structures. As an illustration, I show that the proposed design improves the efficiency of a bottom emitting OLED ($\lambda_{\mathbf{peak}}$=520 nm) by $+22\%_{rel}$ and ameliorates the angular emission characteristics with respect to planar devices.

In the second investigated configuration, inkjet printed light outcoupling PSN with different 2D designs are tested as would be desired for their deployment into inkjet printed OLED devices. Herein, a transparent anode material is directly deposited onto PSN, resulting in the corrugation of anode/organic layers interface and subsequent scattering of the waveguide modes. An OLED ($\lambda_{\mathbf{peak}}$=520 nm) incorporating a printed PSN exhibits a 57%, device efficiency increase at a luminance of 1000 cd/m^2, relative to a planar reference device. This approach can be integrated into a high-throughput fabrication routine and be easily extended to other OLED layouts.

Kurzfassung

Für den Erfolg der Photovoltaik (PV) und der organischen Leuchtdioden (OLED) sind erhebliche Fortschritte bei der Kostensenkung und Effizienzsteigerung erforderlich. Beide Ziele können durch den Einsatz von Nanostrukturen für das Photonenmanagement gleichzeitig erreicht werden. Die grundlegenden Ziele des Photonenmanagements sind die Verringerung der Reflexion des einfallenden Lichts, die Verbesserung der Absorption oder die Verstärkung der Auskopplung sowie die Anpassung der optischen Eigenschaften eines Bauelements für den Einsatz in verschiedenen Arten von Energieumwandlungssystemen. Für eine optimale Effizienz von Solarzellen und OLEDs sollten die Nanostrukturen einen erweiterten Spektral- und Winkelbereich aufweisen. In dieser Hinsicht hat das Photonenmanagement auf der Grundlage ungeordneter Nanostrukturen in vor kurzem große Aufmerksamkeit erregt. Solche photonischen Schichten arbeiten in einem breiteren Spektralbereich als vergleichbare periodische Strukturen und besitzen optische Eigenschaften, die im Gegensatz zu rein zufälligen Strukturen leicht vorhergesag- und eingestellbar sind.

In dieser Arbeit wird das Photonenmanagement durch planare, ungeordnete 2D-Nanostrukturen für optoelektronische Dünnschichtbauelemente vorgestellt. Die Nanostrukturen sind so konzipiert, dass sie als antireflektierende oder effizient streuende Strukturen fungieren, deren primäres Ziel es ist, die optische Absorption von Dünnschicht-Solarzellen zu verbessern und ihre Energieumwandlungseffizienz zu erhöhen. Die entwickelte Methodik und die Strukturen haben direkte Auswirkungen auf den Bereich der OLED-Bauelemente. Die entwickelten Strukturen eingesetzt, um die Auskopplungseigenschaften von OLEDs zu verbessern, die einen vergleichbaren spektralen Wirkungsbereich wie Solarzellen besitzen.

Voraussetzung für alle experimentellen Untersuchungen ist eine ausgereifte Herstellungsmethode zur Erzeugung von Nanostrukturen mit kontrollierbaren Störungseigenschaften, bei der eine vielseitige, großflächige nasschemische Methode eingesetzt wird, die auf der lateralen Phasentrennung einer Polymermischung beruht. Diese nasschemische Methode wird häufig durch Schleuderbeschichtung durchgeführt, die es nicht erlaubt, phasengetrennte Nanostrukturen (PSN) in beliebige 2D-Designs einzubauen, wie es für ihren Einsatz in kommerziellen Produkten erforderlich ist. Andererseits können additive Fertigungsverfahren wie Tintenstrahldrucker nahezu jede geometrisch komplexe Form im Mikrometer- bis Makromaßstab herstellen. Da die meisten herkömmlichen Tintenstrahldrucker jedoch nur eine Auflösung im Mikromaßstab aufweisen, sind sie für die Entwicklung von nanostrukturierten Materialien und Bauelementen noch nicht geeignet.

In dieser Studie werden erstmals beide Mängel behoben und gleichzeitig die kostengünstige Attraktivität und Vielseitigkeit der Phasentrennung durch Homopolymer-

mischungen bewahrt, indem die einzigartigen Vorteile des Tintenstrahldrucks genutzt werden. Unter optimierten Bedingungen werden digital druckbare PSN vom Mikrometer- bis in den Sub-100 nm-Bereich nach einem vorgegebenen 2D-Layout realisiert. Diese PSN können auf verschiedenen starren und flexiblen Substraten mit einer Geschwindigkeit von 45 cm/s hergestellt werden. Der vorgeschlagene Ansatz eröffnet außerdem zahlreiche neue Möglichkeiten für die Nanofabrikation, einschließlich der dynamischen Variation von PSN während des Tintenstrahldrucks, entweder durch Anpassung der Druckauflösung von Pixel zu Pixel für eine bestimmte Tintenformulierung oder durch die Verwendung mehrerer Polymer-Tinten.

Darüber hinaus werden PSN in der Regel aus Polymeren mit niedrigen Glasübergangstemperaturen hergestellt, was ihre praktische Bedeutung für die Nanoimprint-Lithografie (NIL) einschränkt, da solche PSN bei hohem Druck und hoher Temperatur zu Verformungen in der Prägeebene neigen. Um dieses Manko zu überwinden, werden in dieser Arbeit die einzigartigen Vorteile eines anorganisch-organischen Hybridpolymers (OrmoStamp) genutzt, welches in der Industrie bereits als Material für Prägestempel in der UV- und thermisch basierten NIL bekannt geworden ist. In dieser Arbeit wird zum ersten Mal gezeigt, dass Nanostempel auf der Basis von PSN (aus OrmoStamp) direkt auf verschiedenen starren und flexiblen Substraten mit Hilfe eines Phasentrennungsprozesses hergestellt werden können. Dies ermöglicht den direkten Einsatz von PSN in der NIL ohne zusätzliche lithographische oder replikative Zwischenschritte. So können schleuderbeschichtete und gedruckte sowie geprägte PSN das Photonenmanagement in vielfältigen nanophotonischen Anwendungen verbessern, wie hier durch ihren Einsatz in Solarzellen und OLEDs zur Steigerung der Leistungseffizienz demonstriert wird.

Für Solarzellen werden zwei verschiedene optische Managementtechniken erforscht. Die erste Methode konzentriert sich auf die Entwicklung von lichtstreuenden Schichten für Solarzellen, entweder durch eine Bottom-up- oder eine Top-down-Strategie. Bei der Bottom-up-Strategie werden PSN in die Rückseite von Solarzellen aus hydrogeniertem amorphem Silizium (a-Si:H) eingebracht, bevor ein Reflektor abgeschieden wird, um lichtstreuende Reflektoren zu realisieren. Diese lichtstreuenden Reflektoren erzielen einen besseren Wirkungsgrad als ein Bauelement, das auf einem kommerziellen lichtstreuenden Substrat basiert. Darüber hinaus werden ergänzende optische Simulationen an einem akkuraten 3D-Modell durchgeführt, um die überlegenen Lichtsammeleigenschaften der entwickelten Streureflektoren zu analysieren und allgemeine Designregeln abzuleiten. In der Top-Down-Strategie werden PSN verwendet, um eine Resist-Ätzmaske zu strukturieren, die für die Übertragung ungeordneter Nanolöcher in eine dünne a-Si:H-Schicht durch Trockenätzung verwendet wird. Die Studie begann mit der Durchführung dreidimensionaler optischer Simulationen, um die Auswirkungen der Unordnung auf die ursprünglich periodischen Anordnungen von Nanostrukturen systematisch zu untersuchen. Die Ergebnisse dieser Simulationen zeigen, dass quasi-ungeordnete Strukturen zu breiteren Spektral- und Winkelantworten führen, was für PV-Anwendungen eindeutig von Vorteil ist. Nach dem Top-Down-Ansatz wird eine Verbesserung der integralen Absorption um bis zu 93% bei normalem Einfall und um bis zu 200% bei großen Einfallswinkeln im Vergleich zu einem ungemusterten Absorber gezeigt.Darüber hinaus kann eine ähnliche Struktur als Nanostempel in einer Top-Down-Strategie dienen, wobei die Perowskit-Schichten durch die Nanostempel unter Verwendung eines thermischen NIL-Systems nanogeprägt werden. Für den nanostrukturierten Perowskitfilm wird eine erhöhte in-

tegrierte Absorption und eine gesteigerte Photolumineszenz von $7\%_{rel}$ bzw. $121\%_{rel}$ erzielt. Dieser Weg ebnet den Weg für Rolle-zu-Rolle verarbeitbare "photonisierte" Absorber.

Die zweite Methode konzentriert sich auf die Entwicklung von Antireflexionsschichten durch zusätzliche Anpassung des PSN an die Abmessungen unterhalb der Wellenlänge. Das hier betrachtete Design besteht aus einer Frontelektrode, Indium-Zinn-Oxid (ITO), die formschlüssig auf die PSN aufgebracht wird. Im optimalen Fall führen die nanostrukturierten ITO-Elektroden zu einer Erhöhung des Transmissionsgrads um $7\%_{rel}$ im Vergleich zu planaren Referenzstrukturen. Die Antireflexionseigenschaften werden genutzt, um die Photostromdichte von 4-poligen Perowskit/Kristallsilizium (Perowskit/c-Si)-Tandemsolarzellen zu erhöhen. Perowskit/c-Si-Tandem-Zellen mit nanostrukturiertem ITO weisen eine höhere Kurzschlussstromdichte (2,9 $\mathrm{mA/cm^2}$ absolute Verstärkung) und PCE (1,7 % absolute Verstärkung) in der unteren c-Si-Solarzelle im Vergleich zur Referenz auf.

Schließlich wird in dieser Arbeit die Bedeutung der genannten Erkenntnisse für das umgekehrte Problem - die Lichtextraktion in OLEDs - aufgezeigt. In der ersten untersuchten Konfiguration nutzt diese Arbeit die leicht abstimmbaren Lichtstreueigenschaften von ungeordneten Titandioxid-Nanosäulen, die aus einer selbstorganisierenden Struktur und einem lösungsmittelbasierten Lift-off-Prozess resultieren. Die anschließende Planarisierung dieser Nanosäulen durch eine dünne Epoxidschicht gewährleistet eine hervorragende Reproduzierbarkeit der Bauelemente - ein Aspekt, der bei nanowelligen Substraten oft kritisch ist - und bewahrt eine starke räumliche Überlappung der eingefangenen optischen Moden mit den lichtstreuenden Strukturen. Zur Veranschaulichung wird gezeigt, dass das vorgeschlagene Design die Effizienz einer von unten emittierenden OLED ($\lambda_{\mathbf{peak}}$=520 nm) um $+22\%_{rel}$ und die Winkelemissionscharakteristik im Vergleich zu planaren Bauelementen verbessert.

In der zweiten untersuchten Konfiguration werden im Tintenstrahldruckverfahren hergestellte lichtauskoppelnde PSN mit verschiedenen 2D-Designs getestet, wie sie für den Einsatz in gedruckten OLED-Bauelementen vorgesehen sind. Dabei wird ein transparentes Anodenmaterial direkt auf das PSN aufgebracht, was zu einer Strukturierung der Grenzfläche zwischen Anode und organischen Schichten und einer resultierenden Streuung der Wellenleitermoden führt. Eine OLED ($\lambda_{\mathbf{peak}}$=520 nm), die ein gedrucktes PSN enthält, weist bei einer Leuchtdichte von 1000 $\mathrm{cd/m^2}$ im Vergleich zu einem planaren Referenzelement eine um 57% höhere Effizienz auf. Dieser Ansatz lässt sich in eine Hochdurchsatz-Fertigungsroutine integrieren und kann leicht auf andere OLED-Layouts erweitert werden.

List of publications and contributions to conferences

Peer-reviewed publications (first author)

[1] **Y. J. Donie**, Y. Yuan, I. Allegro, F. Schackmar, I. M.Hossain, R. Huber, U. W. Paetzold, G. Gomard, and U. Lemmer, "A Self-assembly method for tunable and scalable nano-stamps: A versatile approach for imprinting nanostructures," Advanced Materials Technologies, p. 2101008, 2021.

[2] **Y. J. Donie**, S. Schlisske, R. H. Siddique, A. Mertens, V. Narasimhan, F. Schackmar, M. Pietsch, I. M. Hossain, G. Hernandez-Sosa, U. Lemmer, et al., "Phase-separated nanophotonic structures by inkjet printing," ACS nano, vol. 15, no. 4, pp. 7305–7317, 2021.

[3] **Y. J. Donie**, D. Theobald, S. Moghadamzadeh, A. Mertens, I. M. Hossain, U. W. Paetzold, U. Lemmer, and G. Gomard, "Planarized and compact light scattering layers based on disordered titania nanopillars for light extraction in organic light emitting diodes," Advanced Optical Materials, p. 2001610, vol. 9, no. 14, 2021.

[4] **I. M. Hossain, Y. J. Donie**, R. Schmager, M. S. Abdelkhalik, M. Rienäcker, T. F. Wietler,R. Peibst, A. Karabanov, J. A. Schwenzer, S. Moghadamzadeh, et al., "Nanostructured front electrodes for perovskite/c-si tandem photovoltaics," Optics express, vol. 28, no. 6, pp. 8878–8897, 2020.

[5] **Y. J. Donie**, M. Smeets, A. Egel, F. Lentz, J. B. Preinfalk, A. Mertens, V. Smirnov, U. Lemmer, K. Bittkau, and G. Gomard, "Light trapping in thin film silicon solar cells via phase separated disordered nanopillars," Nanoscale, vol. 10, no. 14, pp. 6651–6659, 2018.

[6] **R. H. Siddique, Y. J. Donie**, G. Gomard, S. Yalamanchili, T. Merdzhanova, U. Lemmer, and H. Hölscher, "Bioinspired phase-separated disordered nanostructures for thin photovoltaic absorbers," Science advances, vol. 3, no. 10, p. e1700232, 2017.

Peer-reviewed publications (co-author)

[1] **A. Dolinko**, L. Borgmann, C. Lutz, E. R. Curticean, I. Wacker, M. S. Vidal, C. Szischik, Y. Donie, M. Inchaussandague, D. Skigin, H. Hölscher, P. Tubaro and A. Barreira, "Analysis of the optical properties of the silvery spots on

the wings of the Gulf Fritillary, Dione vanillae," Scientific reports, Vol. 11, P. 19341, 2021.

[2] **T. Abzieher**, T. Feeney, F. Schackmar, Y. J. Donie, I. M. Hossain, J. A. Schwenzer, T. Hell-mann, T. Mayer, M. Powalla, and U. W. Paetzold, "From groundwork to efficient solar cells:On the importance of the substrate material in co-evaporated perovskite solar cells,"Advanced Functional Materials, p. 2104482, 2021.

[3] **S. Perrin**, Y. J. Donie, P. Montgomery, G. Gomard, and S. Lecler, "Compensated microsphere-assisted interference microscopy," Physical Review Applied, vol. 13, no. 1, p. 014068, 2020.

[4] **A. Egel**, D. Theobald, Y. J. Donie, U. Lemmer, and G. Gomard, "Light scattering by oblate particles near planar interfaces: on the validity of the t-matrix approach," Optics express, vol. 24, no. 22, pp. 25154–25168, 2016.

Conference proceedings

[1] **Y. J. Donie**, L. G. Van Reventlow, J. B. Preinfalk, S. Moghadamzadeh, J. Van Leeuwen,T. Merdzhanova, K. Bittkau, U. W. Paetzold, A. Colsmann, U. Lemmer,et al., "Low-and high-index self-assembled nanopillars as light outcoupling elements in organic light emitting diodes," in Optical Devices and Materials for Solar Energy and Solid-state Lighting, pp. PW1C–3, Optical Society of America, 2019.

[2] **R. Schmager**, I. M. Hossain, Y. J. Donie, F. Schackmar, G. Gomard, B. S. Richards, and U. W.Paetzold, "Nanophotonic perovskite thin-film solar cells by thermal nano-imprint lithography," in Optical Devices and Materials for Solar Energy and Solid-state Lighting, pp. PM4C–3, Optical Society of America, 2019.

[3] **Y. J. Donie**, M. Smeets, V. Smirnov, J. B. Preinfalk, A. Egel, U. Lemmer, K. Bittkau, andG. Gomard, "Light management in thin film solar cells using internal scattering layers made by polymer blend lithography," in Optical Nanostructures and Advanced Materials for Photovoltaics, pp. PTh2A–6, Optical Society of America, 2016.

[4] **A. Egel**, D. Theobald, Y. J. Donie, J. B. Preinfalk, G. Gomard, and U. Lemmer, "Accurate modeling of outcoupling from OLEDs: Volumetric versus flat internal scattering layers," in Solid-State Lighting, pp. SSW2D–3, Optical Society of America, 2016.

[5] **J. B. Preinfalk**, Y. J. Donie, A. Egel, M. Hecht, J. Hüpkes, K. Bittkau, U. Lemmer, and G. Gomard, "On the fabrication of disordered nanostructures for light extraction in corrugated OLEDs," in Optical Nanostructures and Advanced Materials for Photovoltaics, pp. JW5A–20,Optical Society of America, 2017.

Contributions to conferences

[1] Y. J. Donie, L. G. Van Reventlow, J. B. Preinfalk, S. Moghadamzadeh, J. Van Leeuwen,T. Merdzhanova, K. Bittkau, U. W. Paetzold, A. Colsmann, U. Lemmer, et al., "Low-and high-index self-assembled nanopillars as light outcoupling elements in organic light emitting diodes (**Talk**)," OSA, San Francisco, 2019.

[2] Y. J. Donie, S. Schlisske, J. B. Preinfalk, J. V. Leeuwen, A. Egel, J. Hüpkes, K. Bittkau, G. Hernandez-Sosa, U. Lemmer and G. Gomard, "Towards inkjet printing of phase-separated nanostructures for light extraction in organic light emitting diodes (**Talk**)," MRS, Boston, 2018.

[3] Y. J. Donie, M. Smeets, T. Merdzhanova, V. Smirnov, J. B. Preinfalk, A. Egel, U. Lemmer, K. Bittkau, G. Gomard, "Tuning light scattering by phase-separated nanostructures for front- and rear-side light trapping in photovoltaics (**Poster**)," MRS, Boston, 2018.

[4] Y. J. Donie, A. Osypka, R. H. Siddique, T. Merdzhanova, V. R. Voggu, B. A. Korgel, J. B. Preinfalk, A. Egel, H. Hölscher, U. Lemmer, et al., "Polymer blend lithography: a versatile approach for the fabrication of disordered light harvesting nanostructures (**Talk**)," SPIE Photonics Europe, Strasbourg, 2018.

[5] Y. J. Donie, M. Smeets, A. Egel, F. Lentz, J. B. Preinfalk, A. Mertens, U. Lemmer, K. Bittaku and G. Gomard, "Phase separated scattering nanostructures for light trapping back reflectors in thin film solar cells (**Poster**)," SPIE Photonics Europe, Strasbourg, 2018.

[6] Y. J. Donie, R. H. Siddique, G. Gomard, T. Merdzhanova, U. Lemmer, and H. Hölscher, "Self-assembled nanostructures inspired by the scales of black butterflies as light-harvesting elements for photovoltaics (**Poster**)," WE-Heraeus-Seminar Bio-inspired, Nano- and Microstructured Surfaces: New Functionality by Material and Structure', BadHonnef, 2017.

[7] Y. J. Donie, M. Smeets, V. Smirnov, J. B. Preinfalk, A. Egel, U. Lemmer, K. Bittkau, and G. Gomard, "Light management in thin film solar cells using internal scattering layers made by polymer blend lithography (**Talk**)," OSA, Leipzig, 2016.

Supervised student's theses

[1] Yingxuan Yuan, "Self-assembled nanophotonic sturctures for anti-counterfeiting applications," Master thesis, Karlsruhe School of Optics and Photonics, 2021.

[2] Yidan Ma, "Display technologies based on QDs assembled in porous polymer films," Master thesis, Materialwissenschaft und Werkstofftechnologie, 2021.

[3] Yuhao Wang, "Plasma treated light extracting nanostructures for OLEDs," Master thesis, Karlsruhe School of Optics and Photonics, 2020.

[4] Siyi Gao, "Air-void optical structures via self-assembly method for light extraction in OLEDs," Internship, Karlsruhe School of Optics and Photonics, 2020.

[5] Yingxuan Yuan, "Tunable and scalable nanophotonic stamp by self-assembly method: A versatile approach for nanoimprint lithography," Internship, Karlsruhe School of Optics and Photonics, 2020.

[6] Mark Ulanov, "Light scattering dielectric nanostructures for head-up displays," Bachelor thesis, Elektrotechnik und Informationstechnik, 2019.

[7] Adrian Grande, "Light scattering of self-assembled nanostructures for optoelectronic devices," Bachelor thesis, Universitat Politècnica de Catalunya, 2018.

[8] Mohamed A. Mohamed, "Nanostructured indium tin oxide thin films Via phase-separated nanopillars for potential improved light management in perovskite solar cells," Internship, Karlsruhe School of Optics and Photonics, 2020.

[9] Dimitar Pandov, "Soft lithography of disordered light scattering nanostructures," Bachelor thesis, Elektrotechnik und Informationstechnik, 2018.

[10] Jocelyn van Leeuwen, "Phase-separated nanostructures embedded in high-index medium as planar internal scattering structures for OLEDs," Internship, University of Waterloo, 2018.

[11] Anna Osypka, "Light harvesting phase-separated quasi-random nanostructures," Bachelor thesis, Elektrotechnik und Informationstechnik, 2017.

[12] Christian Stamm, "Planarisierung von streuschichten zur verbesserten lichtauskopplung aus OLEDs," Master thesis, Elektrotechnik und Informationstechnik, 2017.

[13] Luis David Anchía Sáen, "Optical setup for measuring waveguide mode extinction through scattering geometries," Bachelor thesis, Elektrotechnik und Informationstechnik, 2016.

Contents

1. Introduction

The current energy market landscape is changing, driven by technological improvements and environmental concerns. The emerging links between environmental crisis and energy source thus open a frontier for looking into abundant, reliable, and clean energy. In this context, solar photovoltaic (PV) has become a mature technology whose global installation has increased by 1950% over the past ten years (see **Figure 1.1**).

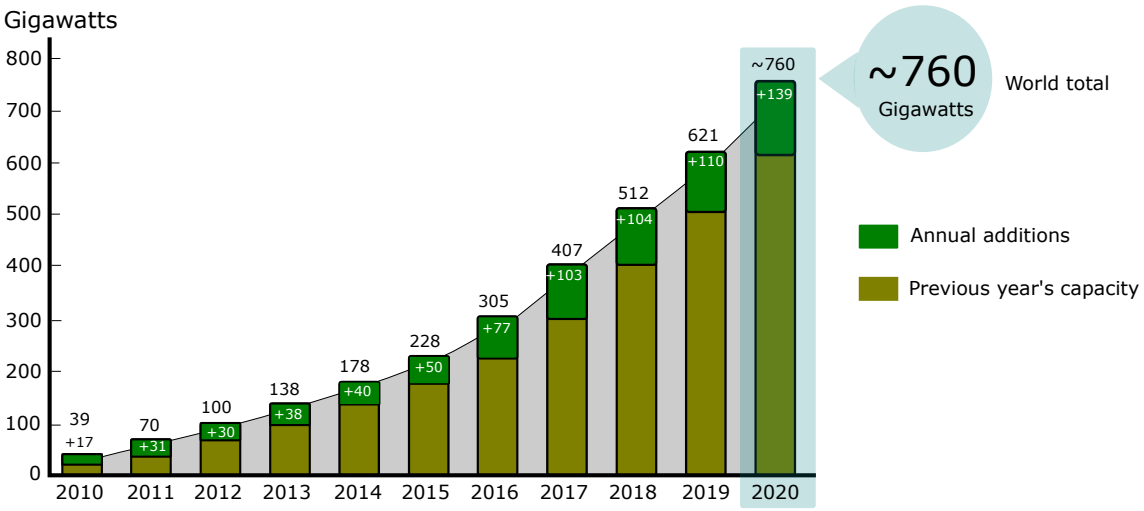

Figure 1.1. Solar PV global capacity and annual additions. Note: Totals may not add up due to rounding. (Source: www.ren21.net)

To sustain this exponential market growth, PV research is still looking for more cost-effective and efficient solutions. One way to lower the cost-per-watt ratio of solar cells is to decrease the thickness of the silicon while retaining the efficiency on a high level. This is the driving idea behind the transition from thick wafer-based solar cell devices to thin-film cells. Additionally, it can open up new design and integration possibilities (flexible substrates, building integration, compatibility with novel printing techniques, etc.). However, thin-film solar cells pose optical challenges, especially the low absorption of the photons with energy close to the

active layer's optical bandgap, which add to reflection losses. It has been discovered that nanostructures can remarkably improve the energy conversion efficiency of thin-film solar cells by eliminating losses from incomplete absorption or by reducing incident light reflection. Nanostructures rely on a core set of phenomena to attain these goals, including coupling to waveguide modes through surface structuring and gradation of the refractive index. Such structures are also relevant for the reverse process, namely for light outcoupling in organic light-emitting diodes (OLEDs). In particular, light management with nanostructures is of paramount importance for OLED in light technology. OLED light technology, as opposed to OLED display, is primarily used for general lighting and automotive applications.

Keeping in mind that about one-sixth of the total electricity is consumed for general lighting,[1] it is inevitable to use energy-saving, long-living, and environmentally friendly light sources. The US Department of Energy estimates that the transition to solid-state lighting sources will save 569 TWh of energy annually by 2035, an amount equivalent to the output of more than 92 1000-MW power plants.[2] That is a significant amount of electricity that will not be needed anymore. OLED technology is one of those types of solid-state lighting (see **Figure 1.2**). Not only is it ultra-thin, flexible, lightweight, and cool to the touch, it is glare free light surface, in contrast to the light point source LED, which are optimal for illuminating rooms. However, OLED lighting is yet to be widely adopted. In contrast, OLED displays are nowadays mass-produced for mobile phones, tablets, and TVs. The former technology is focused on niche markets: automotive and specialty lighting. Some of the critical challenges preventing the adoption of this technology for general lighting are: the cost, the efficiency, and the lifetime of the OLEDs. Typically, lighting devices require higher brightness levels than display applications, which makes practical deployment of OLED lighting much more challenging as efficiency and lifetime can degrade rather significantly when brightness level increases.

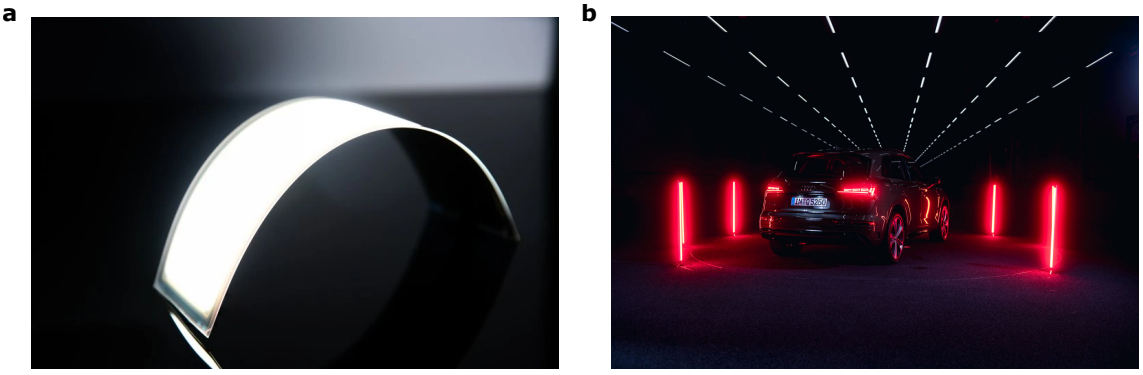

Figure 1.2. OLEDs for general lighting and automotive applications. (a) Bendable OLED panels with efficacies >60 lm/W are commercially available and exemplify the technology's flexible design possibilities. (Source: www.oledworks.com) (b) Audi Q5 with digital OLED backlight. (source: www.audi-mediacenter.com)

The lifetime of the OLED can be extended by minimizing the electric power needed to achieve high brightness. This can be achieved by, for example, eliminating optical loss channels that often put a constraint on the external quantum efficiency of OLEDs. Optical loss mechanisms responsible for that effect include light confinement in high refractive index layers (e.g., organic layers, transparent electrodes,

and glass substrate), as well as the excitation of surface plasmon polaritons at the interface between the metallic electrode and the organic layers. One possible way to improve light management in OLEDs consists of incorporating light outcoupling structures within the OLED stack.

Recent extensive studies have shown that the efficiency enhancement of both devices, solar cells and OLEDs, using light management schemes largely depends on the structural disorder of the nanostructures. In this regard, photonic materials with tailored—i.e., with deliberately introduced structural disorder continue to attract considerable attention in solar cells and OLEDs due to their extended spectral and angular range of effectiveness. These characteristics are essential for solar cells in terrestrial conditions (change in light intensity and diffused sunlight). They are also relevant for the reverse process, namely for efficient light outcoupling while maintaining stable angular and spectral emission profiles in OLEDs. Proofs-of-concept have been successfully performed by fabricating nanostructures with short-range structural correlation using a top-down method with a slow serial writing process (e-beam lithography (EBL)), limiting the demonstration to small areas (see **Table 1.1**). This shortcoming can be circumvented by tailoring the morphology of self-assemblies that inherently incorporate structural disorder and which can be more conveniently formed over large surfaces. Polymer blend lithography (PBL), relying on the lateral phase separation of a blend made of immiscible polymers, is a suitable patterning technique with that respect. Since it can be carried out rapidly, cost-effectively, and because it allows exploring a broad set of disordered configurations with tunable size distribution.

As I will show in this thesis, polymeric self-assemblies can also be obtained by inkjet-printing, provided that a proper formulation of the solution containing the two polymers is used. Moreover, this study demonstrates that disordered nanostructures can be transferred into different functional materials with high fidelity using nanoimprint lithography tools, including a roll-to-roll process. Thus, the proposed approach offers great flexibility in terms of achievable designs and materials choice to tailor light scattering and exploit it in various devices. **Table 1.1** summarizes the advantages and disadvantages of the proposed approach compared to the most well-known available disordered nanopatterning methods.

Table 1.1. Summary of lithography methods relevant for disordered nanopatterning. (++ = very high, + = high, - = low, -- = very low).

Technique	EBL	Colloidal lithography	Solid-state dewetting of thin films	PBL
Resolution	++	+	+	+
Precision	++	--	--	-
Throughput	--	+	+	++
Area	--	+	+	++
Design flexibility	++	-	-	++
Complexity	+	+	+	-
Cost	++	-	+	--
PV and OLED industrial applicability	--	+	-	++
	[3]	[4, 5]	[6, 7]	This work

The scope of this thesis is the development and evaluation of the proposed approach for light management in solar cells and OLEDs. In this regard, the thesis first highlights the suitability of the fabricated nanostructures to design light scattering back reflectors and front antireflection structures in solar cell multilayers. In addition, the intrinsic absorption properties of solar cell absorber materials are tailored by incorporating the self-assembled light scattering nanostructures inside the materials via top-down routes, including imprinting and dry etching. The optical analysis of patterned devices based on the proposed configurations above is further extended by performing simulations based on the finite element method (FEM). On the modeling side, this thesis focuses on developing a realistic 3D patterned solar cell model using a growth model that exploits disordered photonics and the implementation of the Lubachevsky-Stillinger algorithm to properly analyze structural disorder—starting from random to correlated—in different schemes. Finally, the thesis elaborates on the significance of these findings for the reverse problem, namely for light outcoupling in light-emitting diodes. In contrast to the approaches proposed for solar cell, the OLED light outcoupling layer on a substrate is planarized to obtain a physically flat substrate surface but optically corrugated in a way that allows optical scattering. As a result, the optimization of the self-assembled nanostructures with respect to light scattering as well as their integration into an OLED stack in order to achieve a functional and reproducible device is addressed. Moreover, this thesis highlights that the light outcoupling nanostructures fabricated with the proposed approach can be rapidly processed into the desired macroscopic design, as desired for their deployment into inkjet-printed OLED devices.

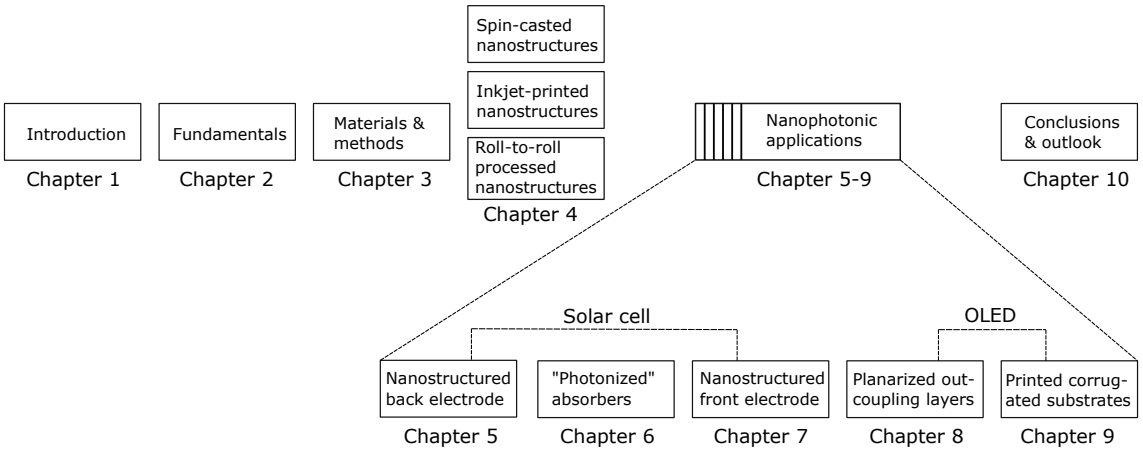

Figure 1.3. Schematic illustration of the scope of this thesis. In the top part the content of the chapters is shown. The steps made in Chapters 5–9 are in further detail at the bottom.

While the two examples above illustrate the potential of the proposed nanostructures fabrication approaches, their applications extend well beyond PV and OLED (see **Tables 4.1** and **4.2** of Chapter 4), enabling the production of nanophotonic devices of different shapes, types, and designs with precision from initial prototyping to industrial manufacturing. Accordingly, I have tried to prepare the thesis such that it is accessible for readers from the nanophotonic community without a dedicated interest in PV and OLED details (please refer to Chapter 4 only) as well as for readers from PV (please refer to Chapters 5 to 7 only) or OLED (please refer to Chapters 8 to 9 only). **Figure 1.3** highlights the chapter's flowchart.

In detail, this thesis is organized in the following way:

- Chapter 2 explains the principle of a solar cell and an OLED operation. The factors that determine the efficiency of a solar cell and an OLED will be defined. In particular, all-optical channels that influence the device's efficiency are discussed. In addition, the mechanism of nanophotonic structures fabrication based on binary blends of immiscible polymers is addressed.

- Chapter 3 presents the experimental methods, as well as the different materials and characterization techniques used in this work. In addition, this chapter introduces the optical simulation models used to investigate the light distribution within a solar cell thin-film stack and derive general rules for the design of efficient light trapping nanostructures.

- Chapter 4 is the central part of this work. This chapter addresses the interest and current state of the PBL for nanophotonic applications and structural colors. Moreover, this chapter highlights the significant stride made in the transition of PBL "from lab to fab" by developing an industry-compatible inkjet printing process and a roll-to-roll nanoimprinting process of phase-separated nanostructures. These approaches are exploited in each of the following chapters to fabricate nanostructures for light management in either solar cells or OLEDs.

- Chapters 5-7 demonstrate that the up-scalable PBL technique can be used as a versatile platform for fabricating phase-separated light scattering and antireflecting nanostructures that can be exploited in both top-down and bottom-up strategies. Chapter 5 demonstrates that the nanostructures can serve as a template in a bottom-up configuration, whereby back reflectors are deposited onto phase-separated nanostructures to enhance the light entrapment in hydrogenated amorphous silicon (a-Si:H) solar cells. In a second example, Chapter 6 elaborates that a similar structure can be used to pattern either an etching mask made of resist or nano-stamps, which are employed for direct a-Si:H and perovskite layers patterning to form light-scattering elements via a top-down approach (i.e., dry etching and imprinting). In Chapter 7, phase-separated nanostructures with dimensions smaller than the wavelength of incident light (i.e., antireflective nanostructures) are proposed to reduce reflection losses and thereby increase light absorption in perovskite and perovskite/c-Si tandem solar cells.

- Chapters 8 & 9 illustrate the application of similar structures presented in Chapters 5-7 as a light outcoupling layer for OLEDs. Chapter 8 reports on two fabrication routes: (i) on the integration of low-index nanopillars (n=1.59 at λ=520 nm) planarized by a high-index material and (ii) on high-index nanopillars (n=2.04 at λ=520 nm) planarized by a thin low-index resist layer, to further improve the reproducibility of the OLEDs performance. The light outcoupling layers are formed on top of the desired substrates (glass and flexible foil) through spin-coating starting from an optimized binary polymer mixture. In the second investigated configuration (Chapter 9), a transparent anode is directly deposited atop inkjet-printed phase-separated nanostructures resulting in the corrugation of the anode/organic layers interface and subsequently to the scattering of the waveguide modes.

- The thesis concludes with a summary of the main results and gives an outlook on promising future investigations.

2. Photonics for photovoltaic and light-emitting devices

This chapter covers the physical and technical background on which this work is based. First, an overview of the fundamental aspects of solar cell devices, including the different factors determining their power conversion efficiency, optical loss mechanisms, and the various strategies for reducing the optical losses, will be introduced. OLED devices are then reviewed. Basically, OLED and solar cell are reciprocal devices. Light incoupling and harvesting in solar cells and light-outcoupling in OLEDs can be understood as reversed processes. In particular, the importance of nanophotonic structures for light management will be illustrated by discussing all-optical loss channels which occur in solar cell and OLED devices. Finally, the mechanism of nanophotonic structures fabrication based on binary blends of immiscible polymers is reviewed.

2.1 Solar cell

Solar cells work based on the photovoltaic (PV) effect, i.e. the generation of a potential difference at the junction of two different materials in response to electromagnetic radiation. The conversion of light directly into electrical energy using the PV effect was discovered by Alexandre Edmond Becquerel in 1839.[8] The process was observed when an electrode in a conductive solution was exposed to light. From this discovery, till the current solar cells came to be, the timeline can be divided into two periods:

1. The discovery years (1839 to 1904), a period characterized mainly with an observation of the PV effect but without any fundamental understanding of the science behind the operation (see **Table 2.1**), and
2. Theoretical foundation (1905 to 1950), a phase that laid the scientific foundation for understanding PV device operation and its potential improvement.

The key events in the second period were A. Einstein's photoelectric effect theory (in 1905)[9] and fabrication of single-crystalline germanium (in 1948) and later, silicon.[8, 10] These two events mark the cornerstones of PV research.

Table 2.1. 1839-1904: Discovery years

1839—PV effect is discovered by Alexandre Edmond Becquerel[8]
1873—Selenium's photoconductivity is discovered by Willoughby Smith[11]
1877—PV effect was observed in selenium by William G. Adams and Richard Evans[12]
1883—First working selenium solar cell was created by Charles Fritz[8]
1887—Photoelectric effect is observed by Heinrich Hertz[13]

2.1.1 Electric power generation in solar cells

The generation of electric power requires the creation of free electron-hole pairs and their collection at the terminals of the solar cell junction, as illustrated in **Figure 2.1**. The basic processes involve:

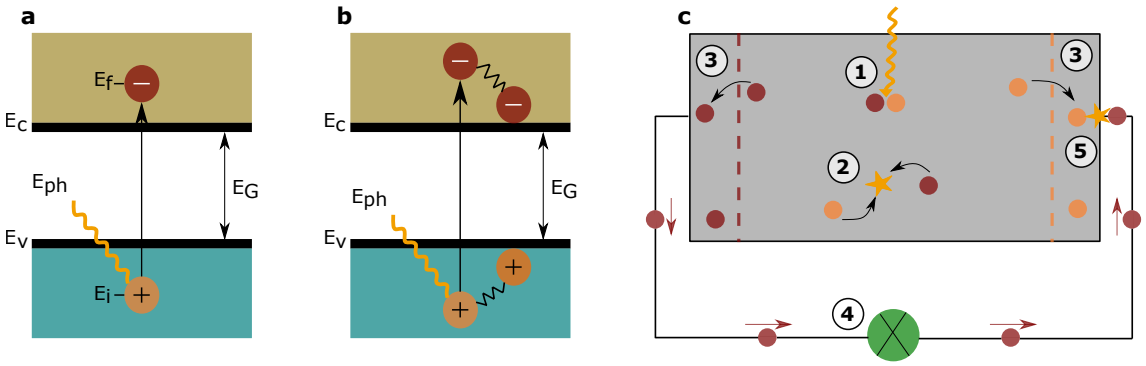

Figure 2.1. Illustration of electric power generation in solar cells. In a semiconductor with bandgap (E_g), absorption of photon ($E_{ph} = h\nu$) leads to (a) excitation of an electron from E_i to E_f when $E_{ph} = E_g$ and (b) thermalization loss for part of energy $E_{ph} > E_g$. (c) ① Absorption of a photon leads to the generation of an electron-hole pair, ② the electrons and holes recombination, ③ with semipermeable membranes the electrons and the holes can be separated, ④ the separated electrons can be used to drive an electric circuit and ⑤ after the electrons passed through the circuit, they will recombine with holes. Adapted from the Ref.[14].

Absorption

The absorption of light in a solid film involves the excitation of an electron from its initial energy level E_i to a higher energy level E_f (see **Figure 2.1a**). Only photons with energy $(h\nu) = E_f - E_i$ are absorbed,[15, 16] where h and ν are the Planck constant and the photon frequency, respectively. Photons with $h\nu < E_f - E_i$ will traverse the material without interaction or will be reflected at its interface.[15, 16] In contrast, $h\nu > E_f - E_i$ are converted to heat (see **Figure 2.1b**). In an inorganic semiconductor material, electrons are excited from the valence band (E_v) maximum to the conduction band (E_c) minimum as shown in **Figure 2.1a**. There is no allowed energy state between E_v and E_c bands that electrons can populate. Hence, this energy difference is called the bandgap, $E_g = E_c - E_v$. The electronic property of an organic semiconductor material is briefly discussed in section 2.2.1.

The change in the intensity (I, $W{\cdot}cm^{-2}$) of an ensemble of photons with incident intensity (I_0) owing to absorption is give by the Beer-Lambert law[17]:

$$I(z) = I_0\, e^{-\alpha z} \tag{2.1}$$

where z is the depth into a film, and the effectiveness of a material at absorbing photons is given by the absorption coefficient (α) as a function of photon wavelength (λ):

$$\alpha(\lambda) = \frac{4\pi\kappa(\lambda)}{\lambda} \tag{2.2}$$

where κ is the imaginary part of the material's refractive index.

Generation

The excitation of an electron from E_i to E_f, leaves behind a hole in the E_i (see **Figure 2.1a**). The absorption of photon, therefore, leads to the creation of an electron-hole pair as illustrated in **Figure 2.1c** ①. The spectral (G_λ) and total (G) generation rate of electron-hole pairs is proportional to the decay of the photon flux (ϕ)[15]:

$$G_\lambda(z,\lambda) = -\frac{\eta_q}{A} \cdot \frac{\phi_\lambda(z,\lambda)}{\partial z} = \eta_q \frac{E_\lambda(\lambda) \cdot \lambda}{hc} \alpha(\lambda) \, . \, e^{-\alpha(\lambda)z}$$
$$and \; G(z) = \int G_\lambda(z,\lambda) d\lambda, \tag{2.3}$$

where η_q is a constant describing the photon-to-electron conversion efficiency, A is the illuminated area and E_λ the spectral irradiance.

Separation

The generated electron-hole pairs exist for a time equal to the minority carrier lifetime (τ). The τ is limited by recombination, i.e. the electron will fall back to the initial energy level E_i, as illustrated in **Figure 2.1c** ②. If the carriers recombine, the resulting energy will be released either as radiative recombination or transferred to other electrons or holes or lattice vibrations (non-radiative recombination).[15, 16] For the electric power generation, a semipermeable membrane that ideally exclusively transfer one carrier type must be present on both sides of the absorber film, as illustrated in **Figure 2.1c** ③. The p-n homojunction (see **Figure 2.2a**) or p-i-n heterojunction (see **Figure 2.2b**) represents a typical implementation of this concept, where conductivities of majority and minority carriers differ by orders of magnitude in the respectively doped regions.[15] Within the p-i-n-junction, the (generated) free charge carriers are separated by a gradient in the electrochemical potential.[16] To have working solar cell, the time required for the charge carriers to reach the membranes must be shorter than their lifetime. Otherwise, the charge carriers recombine.

Collection

The charge carriers are extracted from the solar cells with electrical contacts so that they can perform work in an external circuit. Under illumination, an ideal solar cell can be described as a diode in parallel to a current source. The current output (I) for an external voltage (V) is then given by[15]:

$$I = I_0 \left[exp\left(\frac{q \cdot V}{K_B T}\right) - 1 \right] - I_{sc} \tag{2.4}$$

Here, I_0 denotes the reverse dark saturation current, I_{sc} the short-circuit current density, k_B the Boltzmann constant and T the temperature.and q the elementary charge.

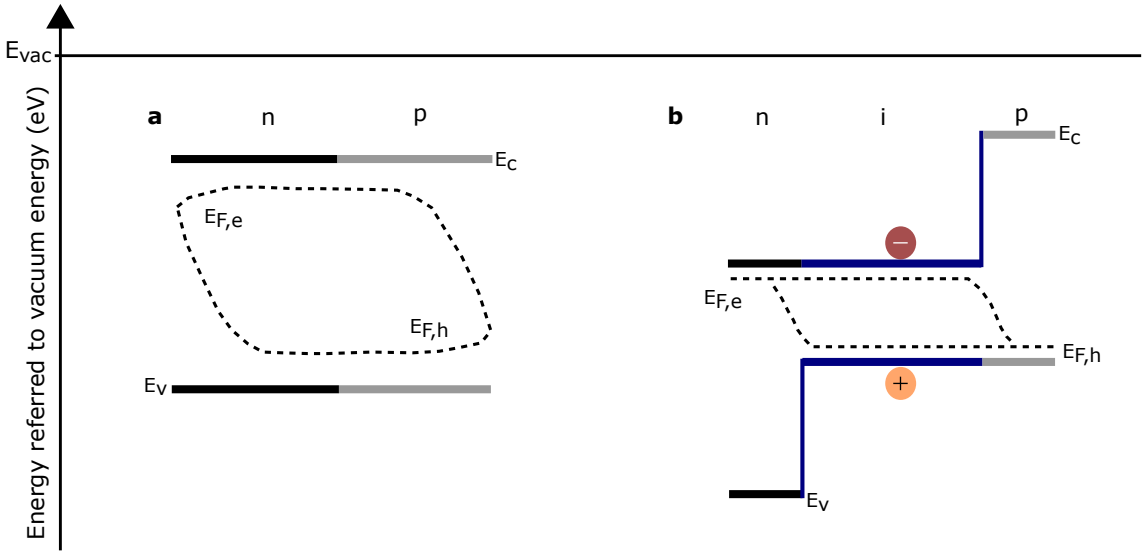

Figure 2.2. Band diagram and quasi-Fermi level splitting of (a) a p-n homojunction and (b) a double heterojunction structure under illumination. n, i and p mark n-type, intrinsic and p-type regions. E_C, E_V, $E_{F,h}$, $E_{F,e}$ denote conduction, and valence band energies, as well as quasi-Fermi energies of holes and electrons, respectively. Depiction following Ref.[15].

2.1.2 Performance parameters

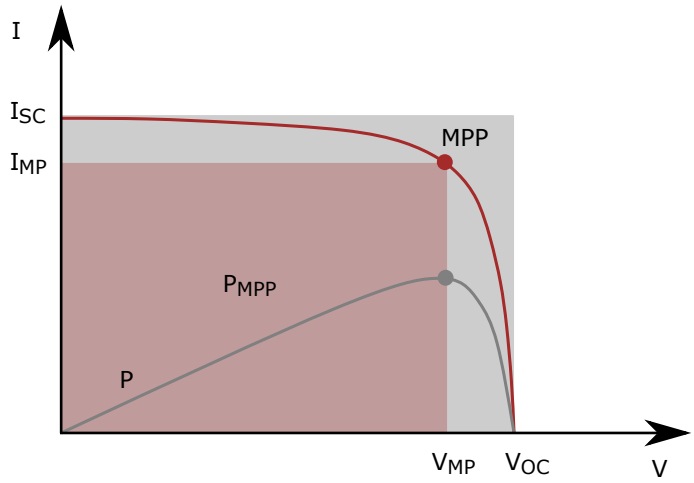

Figure 2.3. Solar Cell $I-V$ characteristic curve. The current at zero voltage (V) is defined as the short-circuit current (I_{SC}). The open-circuit voltage V_{OC} is the maximum voltage available from a solar cell, and this occurs at zero current. The working point in which $I_{MP} \cdot V_{MP}$ becomes maximal is denoted maximum power point (MPP).

The $I-V$ curve depicted in **Figure 2.3**, plotted using Equation 2.4, can be used to determine the characteristic solar cell parameters. These parameters are:

Short-circuit current

The I_{sc} is defined as the current flowing through the solar cell when the output connectors are shorted together (a short circuit condition). This value is obtained at $V = 0$, given in (Ref.[15]) as:

$$I_{sc} = q \int_0^\infty EQE_{PV}(E) \cdot \phi_{AM1.5G}(E) dE \tag{2.5}$$

where EQE_{PV} (i.e., external quantum efficiency) is the spectral photon-to-electron conversion efficiency of the solar cell, and $\phi_{AM1.5G}$ is the photon flux under AM1.5G illumination.

Open-circuit voltage

The V_{oc} is the maximum voltage when the device terminals are not connected to any load (an open circuit condition).

This value can be determined from Equation 2.4 by setting I to zero.

$$V_{oc} = \frac{K_B T}{q} ln \left(\frac{I_{sc}}{I_0} + 1 \right) \tag{2.6}$$

Fill factor

The FF is defined as the ratio of maximum obtainable power (P_{mpp}) to the product of the V_{oc} and J_{sc}.[18]

$$FF = \frac{P_{mpp}}{I_{sc} \cdot V_{oc}} \tag{2.7}$$

Where P_{mpp} is given by the product of V_{MP} and I_{MP}. This value is shown at the top right area of the brown rectangle in **Figure 2.3**.

Power conversion efficiency

The η is defined by the ratio of maximum electrical power output to an incident light intensity (P_{light})[15, 18]:

$$PCE = \frac{P_{mpp}}{P_{light}} = \frac{FF \cdot I_{sc} \cdot V_{oc}}{P_{light}} \tag{2.8}$$

2.1.3 Optical losses

The absorptance - the ratio of the total number of photons absorbed in a material to the incident flux- is a critical parameter for achieving high photo-current density and thus high-efficiency solar cells.[19, 20] However, the absorptance value of an absorber material can be limited by several channel losses:

1. Reflection losses: incident photons can be reflected at interfaces between two media with different refractive indices. For normal incident light, the reflectance at the interface of two materials with different refractive indices (n_1, n_2) is given by Fresnel equation[19]:

$$R = \left(\frac{n_1 - n_2}{n_1 + n_2} \right)^2 \tag{2.9}$$

   The derivation of Equation 2.9 can be found in Ref.[21].

2. Non absorption: incident photons can be transmitted through the absorber material with a low absorption coefficient. The absorption coefficient is best conceptualized in terms of its inverse, $\alpha(\lambda)^{-1}$.[17] The $\alpha(\lambda)^{-1}$, which defines the penetration length into an absorber material at which 67% (i.e., $1 - e^{-1}$) of photons at a given wavelength are absorbed, is an intrinsic material property.[15, 17]

2.1.4 Light management approaches

Light management approaches to overcome the optical losses discussed above while preserving the materials in a solar cell stack consist[19]: (I) optical transmittance improvement by anti-reflection effect, and (II) photon absorption rate improvement in the absorber layer by light trapping effect. Alternatively, or in addition, one can develop different absorber materials to increase the photon absorption rate and absorption bandwidth. Much of this thesis work is devoted to implementing the former two optical principles in solar cell devices to enhance their power conversion efficiency (for more details, please refer to Chapters 5-7).

2.1.4.1 Anti-reflection effect

Anti-reflective properties can be achieved by using thin films that work based on the basic principle of destructive interference, as illustrated in **Figure 2.4a**.[22] In addition, it can be obtained from micro (refer to **Figure 2.4b**) and nanostructure (refer to **Figure 2.4c**) arrays on substrates based on multiple internal reflections[16, 22] and graded changes in the refractive index (for more details, please refer to Chapter 7), respectively.

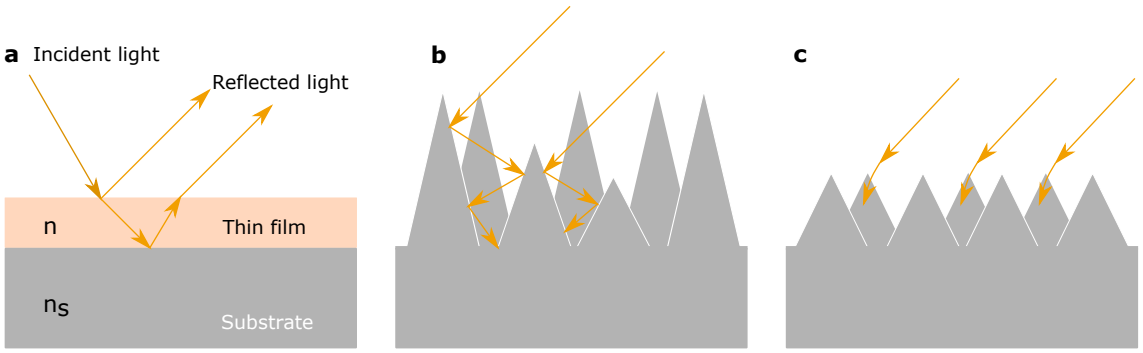

Figure 2.4. Schematic illustration of incident light propagation through (a) a single layer thin film on substrate ($n_s > n$), (b) microstructure arrayed substrate (multiple internal reflections of incident light), and (c) sub-wavelength nanostructure arrayed substrate (interaction of incident light).

2.1.4.2 Approaches to light trapping

Light trapping in solar cells is achieved when the absorption of incident light is higher than the absorption of a single light pass through the absorber material. The considerations for thick and thin film light trapping designs are quite different: for thick films light trapping can be described using ray optics, while thin-films require treatment with wave optics.

Ergodic limit for thick films

For thick films in the ergodic limit, light is not coherent over the thickness of the film and light trapping can be described with ray optics. The very basic interpretation of Equation 1 suggests that the absorptance is proportional to the travel length of photons in the absorber layer. The travel length of photons, i.e., optical distance, can be increased by changing the thickness of the absorber layer or by engineering the material. The latter can be achieved by scattering of incident light at a textured interface that allow the photon to remain in the material for much longer - to travel a much longer path length - thereby increasing the probability of absorption (see **Figure 2.5**).[17, 23] This, in short, is the goal of optical path length enhancement (light trapping[17]).

One approach to enhance the path length is to use a Lambertian surface. This surface is a perfectly randomising surface that scatters light isotropically, which means that all reflected angles have the same probability. Assuming a perfect mirror at the back side and a Lambertian scatterer at the front interface as schematized in **Figure 2.5**, the maximum path length for weakly absorbed photons is given in (Ref.[24]) as:

$$l_{eff} = 4n^2 d, \tag{2.10}$$

Where d, n represents the thickness and the refractive index of the solar cell material, respectively.

The equation is strictly valid in the geometric optics regime - where $d \gg \lambda/2n$. It represents a path length enhancement with respect to a planar semiconductor of $4n^2$, well known as the Yablonovitch limit.

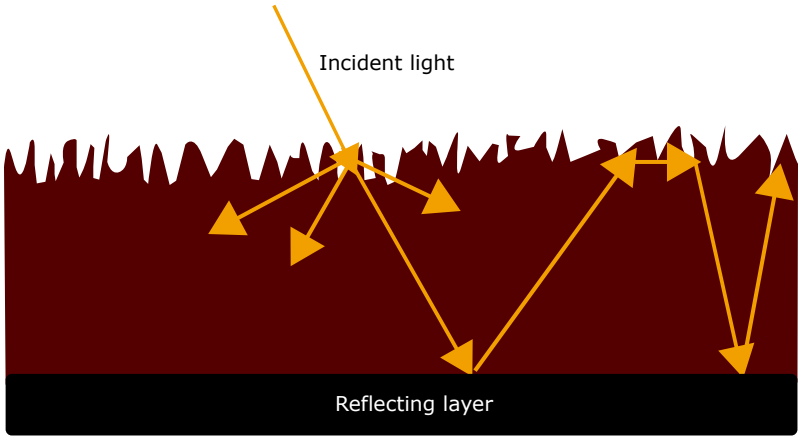

Figure 2.5. Path of light rays in the cell that is due to multiple reflections from the front and back surface.

Thin film

When nanoscale photonic structures are used to manage solar photons in a thin cell, the conventional ray optics models break down and wave optics concepts are required to establish new performance limits. In the wave-optics domain, one needs to start with an analysis of the electromagnetic modes of a solar cell. By using nanophotonic structures that enhance the density of optical modes over a broadband range of wavelengths, a light-trapping enhancement ratio significantly beyond the Yablonovitch limit can be achieved.[25]

2.2 Organic light emitting diode

Exploration of organic semiconductors as light-emitting material started about 55 years ago. The first electroluminescence of an organic compound was observed in 1965.[26] This was achieved by applying an electrical voltage to an anthracene crystal. Shortly afterward (in 1990), electroluminescence was also demonstrated in conjugated polymer based on poly(p-phenylene vinylene) film.[26] Since then, there has been intensive research into other materials such as small molecules. This class of materials is today the cornerstone technology for low-power flat panel displays and energy-efficient light sources.[26]

2.2.1 Electronic properties of organic materials

OLED active materials, i.e., luminous thin-film components, are based on organic semiconducting materials. The basic structure in these organic materials, e.g., conjugated molecules and polymers or organometallic compounds, consists of carbon compounds.[26] Their semiconducting properties arise from the delocalized π-electrons, which are formed in hydrocarbons when not only single bonds are present but also double and triple bonds. The overlap of the bonding π orbital (designated as highest occupied molecular orbital — HOMO) and the anti-bonding π^* orbital (lowest unoccupied molecular orbital — LUMO) provide a continuous system of electron density along the conjugated backbone.[21, 26] Thus, it supports mobile charge carriers. The orbitals do not form a regular uniform energy band, unlike inorganic semiconductors; it is instead a collection of states where the charges move. As a result, the hopping process is the primary charge carrier transport mechanism inside the organic semiconductor.[27] The bandgap (E_g), i.e., the energy difference between HOMO and LUMO, is analogous to the energy difference between the valence and conduction bands in the inorganic semiconductors. Generally, the E_g is in the range of 1–4 eV.[21, 26] Light emission from ultraviolet to near-infrared can be achieved by tuning the E_g. The exact value of the energy gap depends on the size of the conjugated π-system and, therefore, the molecule's size.[21]

Energy levels in organic semiconductors

If a molecule absorbs a photon, an electron is promoted from the ground state S_0 to an excited state S_n. Both energy levels have a substructure due to vibronic modes, as shown in **Figure 2.6a**. The absorption can occur from the lowest vibronic energy level $\nu = 0$ into one of the vibronic states $\nu' = n$ in the excited state. The electronic transition is subject to the Franck-Condon principle (Kasha's rule).[21] Afterward, the system relaxes thermally to the lowest level of the excited state $\nu' = 0$. From there, the vibronic relaxation from the excited states to the ground state occurs by emitting photons. Eventually, the system relaxes non-radiatively until the vibrational state $\nu = 0$ is reached. As a result, the energy difference in the emission is smaller than in the absorption, as illustrated in **Figure 2.6b**. The emission spectrum is red-shifted compared to the absorption spectrum and is called the Stokes Shift.

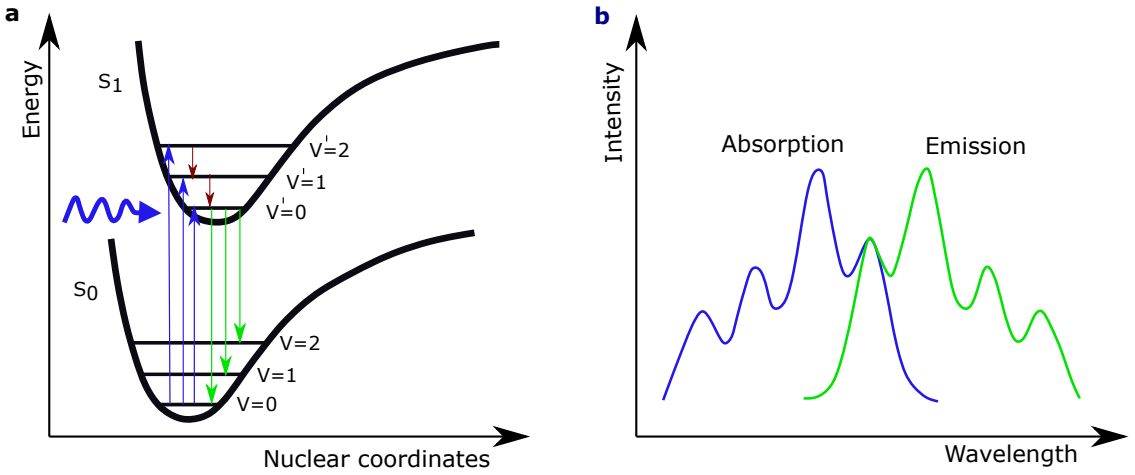

Figure 2.6. The state diagram shows the energy levels of the ground state S_0 and the first excited state S_1 in a molecule. There are different vibrational states in the same electronic state. (a) Absorption occurs between $\nu = 0$ at S_0 and several vibrational states at S_1, followed by vibrational relaxations. (b) The resulting absorption and emission intensity versus energy. The difference between the maximum absorption and emission is the Stokes shift.

The role of the spin

In organic molecules, there are well-defined spin states that play an important role in the emission mechanism. Depending on the number of spatial orientations for the spin vector, two electrons can assume single or triplet states. These states are designated by multiplicity $(2S+1)$. If the total spin $S = 0$, the multiplicity takes the value 1. This is called the singlet state and follows the Pauli exclusion principle (i.e., electrons in filled orbitals are paired with anti-parallel spins). For parallel oriented spins of two electrons, the total spin $S = 1$. Hence, the multiplicity is 3 and called the triplet state. **Figure 2.7** illustrates the vector diagram representation of the singlet and triplet states.

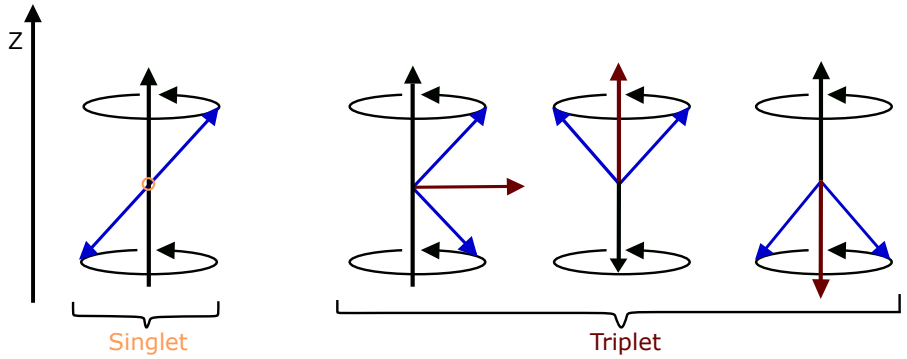

Figure 2.7. The relative spin orientations of two electrons around a local magnetic field in the z-direction. In the singlet state, the electron spins are 180° out of phase with a total spin of S = 0. There are three possible configurations for triplet states with a total spin of S = 1, where the spin directions are in phase.

Molecular luminescence

The probability of forming the triplet state is three times higher than the singlet state. Excited singlet, triplet states are referred to as S_n and T_n, respectively. All excited states S_n or T_n, except for the two lowest terms S_1 and T_1, are very short-lived.[28] The transition from S_n to S_1 takes place very rapidly (in the ns scale) and relax nonradiatively. This process is called internal conversion.[21, 28] The radiative decay mechanism of the singlet state, from the S_1 to the S_0 state, is called fluorescence (see **Figure 2.8**). The transition from the T_1 to the S_0, is not allowed due to the spin selection rules.[21, 28] As a result, organic materials display weak phosphorescence (i.e., a radiative mechanism for the triplet states). In the presence of heavy metals (e.g., in organometallic compounds), the spin selection rule is relaxed.[21, 26, 28] This allows the intersystem crossing and the radiative transition from the T_1 state to S_0 (i.e., phosphorescence), as illustrated in **Figure 2.8**. Due to the angular momentum difficulty, decay is inefficient and usually slow with a lifetime of typically milliseconds.[21, 26, 28]

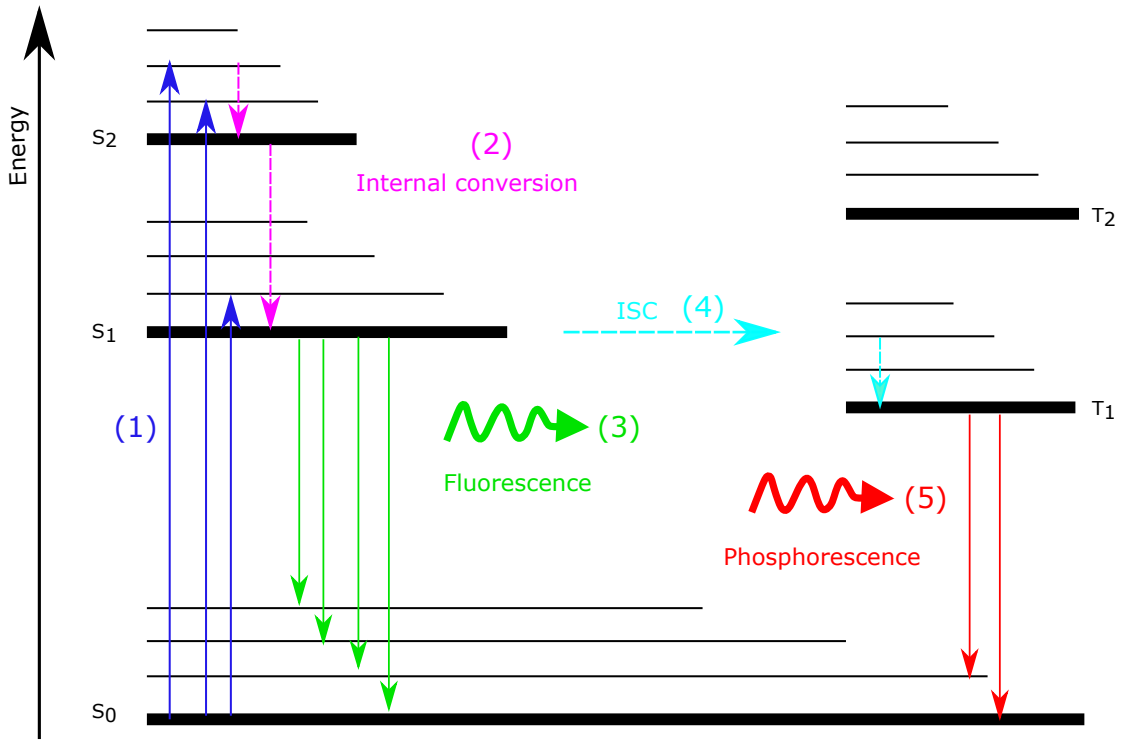

Figure 2.8. Energy level scheme of an organic molecule showing the most important transitions between various singlet levels (S_n) and triplet levels (T_n). (1) Excitation from the ground state to the excited state. (2) Non-radiative relaxation to the lowest state of S_1 (internal conversion). (3) Radiative relaxation to the ground state by emission of a photon (fluorescence) or (4) transition to the triplet state with spin conversion (intersystem crossing). (5) Radiative transition to the ground state (phosphorescence).

2.2.2 Light emission in OLEDs

The OLED working principle is reciprocal to that of a solar cell (for more details, please refer to section 2.1). An OLED emits light by conducting electricity to the

organic materials sandwiched between two electrodes, i.e., the anode and the cathode. In general, this effect is called electroluminescence. **Figure 2.9a** represents the architectural characteristics of a multilayer OLED device. An OLED device consists of a plurality of functional organic layers, including a hole transport layer (HTL), a light-emitting layer(EML), and an electron transport layer (ETL). **Figure 2.9b** depicts the operation mechanism of an OLED device. The fundamental steps involve: ① Injection of electrons and holes from cathode and anode, respectively, ② transport of charge carriers, ③ recombination of electrons and holes to form excitons, and ④ finally the radiative exciton decay and emission of light.

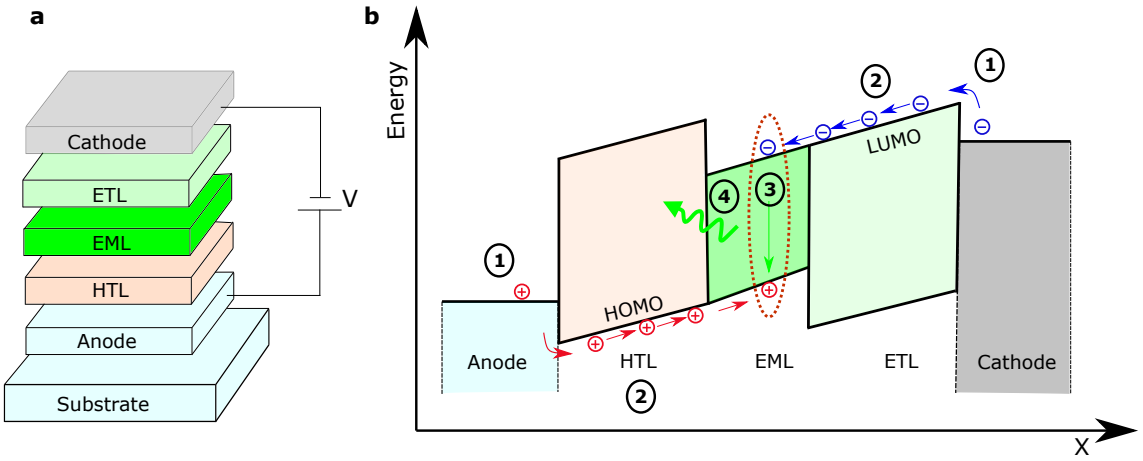

Figure 2.9. Simplified illustration of light emission in an OLED. (a) A two-layer OLED stack. ETL, EML and HTL denote the electron transport layer, the emission layer and the hole transport layer, respectively. In order to obtain light emission, a negative voltage must be applied to the cathode. (b) Schematic energy diagram and charge carrier processes in a two-layer OLED illustrating the basic processes of electroluminescence. ① Injection of electrons from the cathode into the LUMO and of holes from the anode into the HOMO, ② transport of charge carriers, ③ recombination of electrons and holes to form excitons, and ④ radiative exciton decay and emission of light.

2.2.3 Efficiency

The external quantum efficiency (η_{ext}) is the most representative performance indicator quantity when comparing different OLEDs, apart from their spectral characteristics. The η_{ext} gives the number of emitted photons (n_{ph}) to the number of injected electrons (n_e) and is described in Equation 2.11.[29] It can be separated into internal quantum efficiency (η_{int}) and optical photon extraction efficiency (η_{out}).

$$\eta_{ext} = \frac{n_{ph}}{n_e} = \eta_{int}\eta_{out} \tag{2.11}$$

The η_{int}, which is the fraction of photons generated per injected electron, can be further split into factors representing the various loss mechanisms. This efficiency is directly related to the electron-hole charge balance factor (γ), the fraction of a total number of excitons formed which result in radiative decay ($\eta_{S/T}$), and the effective

radiative quantum efficiency of the emitting material (q_{eff}). The η_{int} is related to γ, $\eta_{S/T}$ and q_{eff} by the following the relation[28]:

$$\eta_{int} = \gamma \eta_{S/T} q_{eff} \tag{2.12}$$

The γ gives the number of formed excitons divided by the number of injected charge carriers. Suppose all injected charge carriers form excitons, then $\gamma = 1$. In reality, the γ value is not unity due to injection barriers and different charge carrier mobilities.[30] Hence, it leads to reduced OLED efficiency (η_{ext}). The charge carrier balance (γ) can be improved using multilayer stacks with doped transport layers and additional blocking layers.[28, 31]

The exciton recombination efficiency ($\eta_{S/T}$) indicates the probability of an exciton formation that is allowed to decay radiatively according to the spin selection rules. It can be up to 25% for fluorescent emitters that only use singlet excitons and up to 100% for phosphorescence emitters, which harvests both singlet and triplet excitons.[28, 31]

The effective radiative quantum efficiency (q_{eff}) describes how many excitons recombine radiantly in relation to the total number of recombination events. The q_{eff} is given by the ratio of the radiative decay rate (Γ_r) to the sum of the radiating and non-radiating decay rates ($\sum \Gamma_{nr}$), according to Equation 2.13. Due to the many layers with different optical properties in an OLED, interference effects modify the radiative decay rate (Γ_r), and this is described by using the Purcell factor (F).[28, 31] The Γ_r can be modified by adjusting the microcavity effect.[28, 31]

$$q_{eff} = \frac{F\Gamma_r}{F\Gamma_r + \sum \Gamma_{nr}} \tag{2.13}$$

This thesis work is devoted to optical losses in an OLED device, and the characteristics of η_{out} and so will be explained in detail in the next section.

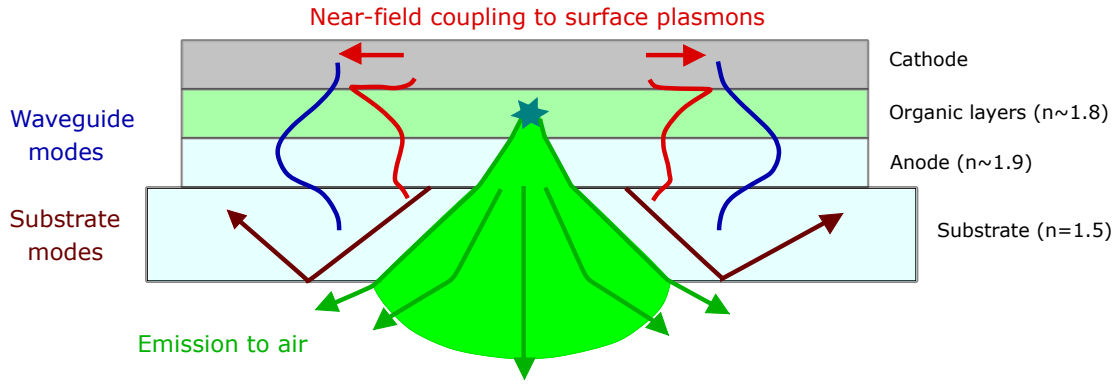

Figure 2.10. Schematic illustration of the optical loss channels in a bottom-emitting OLED. Without outcoupling enhancement, only a small fraction of light is directly emitted to air.

2.2.4 Light extraction losses

As discussed above, an η_{int} to a high level of ≈100% with the full use of both singlet and triplet states is feasible. However, most of the emitted photons are trapped

within the device because of various intrinsic light confinements by the mismatched refractive index of the multilayer structure. In a conventional bottom-emitting OLED, as shown in **Figure 2.10**, several high reflective index layers ($n_{anode}\approx2$, $n_{organic}\approx1.8$) are sandwiched between a low refractive index substrate ($n_{glass}\approx1.5$) and a reflective metal electrode. For such configuration, optical loss channels are surface plasmon polaritons (SPP),[32, 33] waveguided,[34] and substrate[35, 36] modes.

Waveguide mode

A planar waveguide formed from high index organic layers fabricated on a low index glass substrate and capped on top by a metal cathode in an OLED multilayer. Hence, an OLED can be treated as an asymmetric metal-clad waveguide (metal-dielectric-dielectric structure).[37] The scheme in **Figure 2.11a** shows the oversimplified structure and obtained by assuming the same refractive index for the anode and the organic layers. In an asymmetric metal-clad waveguide, the effect of total internal reflection (TIR) at the interface of the low refractive index medium (cladding) and the reflection from the metal electrode is used to guide light in a high refractive index medium (core). The derivation of the dispersion relation of the waveguide modes of such structures can be found in Ref.[38].

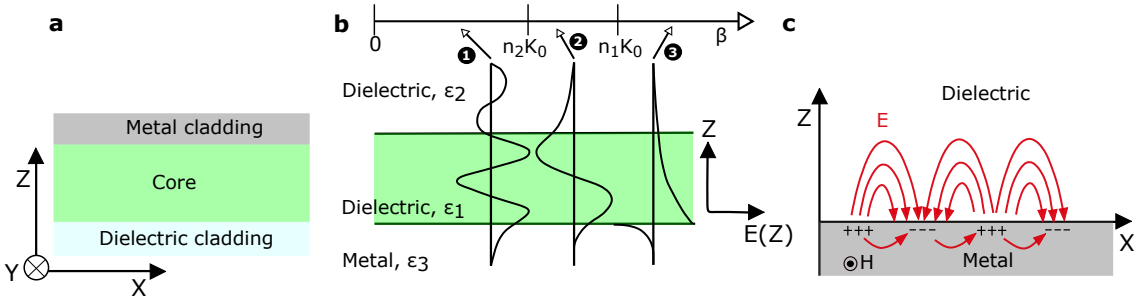

Figure 2.11. Schematic representation of the structure of a bottom emitting OLED and waves propagating inside the device. a) A bottom emitting OLED and an asymmetric metal-clad (metal-dielectric-dielectric structure). (b) Schematic of mode field profiles E(Z) of the planar slab waveguide shown in (a). The three regimes of guided modes are indicated (1) radiative, leaky or partially guided, (2) fully guided or bound, and (3) surface modes. c) Description of propagating SPP waves inside the simplified OLED structure.

The optical modes of the waveguide can be categorized based on their in-plane momentum or wavevector values, as illustrated in **Figure 2.11b**.[39] The in-plane wavevector describes the propagation of modes by the tangential component of the wave vector, kx. The three available optical modes under this consideration are:
(I) *Radiative (leaky) modes*: $0 < \beta < n_2\kappa_0$
Modes in this regime can escape as radiation since the in-plane wavevectors are below the cut-off for TIR at the substrate interface. Hence, this modes are known as 'leaky' modes.
(II) *Fully guided (bound) modes*: $n_2\kappa_0 < \beta < n_1\kappa_0$
The in-plane wavevectors of the modes in this regime are above the cut-off for the TIR at the substrate interface. As a result, the light is fully guided in the high refractive index medium (core). In the end, these guided modes are lost by edge

emission.
(III) *Surface modes*: $n_1\kappa_0 < \beta$
As highlighted in **Figure 2.11c**, these are mainly SPP modes.

SPP mode

SPP modes are related to waveguide modes in that they too are confined electromagnetic waves. SPPs are guided electromagnetic surface waves traveling along with the interface between a dielectric and a metal.[21, 28] An exemplary scheme is shown in **Figure 2.11c**. For the p-polarized wave (TM mode, the electric field component perpendicular to the surface of medium) incident on the interface, the oscillating electric field will cause surface charges at the interface between the metal and the dielectric. These are longitudinal electromagnetic waves with exponentially decaying fields perpendicular to the interface.[21] The dispersion relation of SPP strongly depends on the refractive indices of the metal and the adjacent dielectric and can be written as[37]:

$$\kappa_{spp} = \kappa_0 \sqrt{\frac{\epsilon_m \epsilon_d}{\epsilon_m + \epsilon_d}} \tag{2.14}$$

Where, ϵ_m and ϵ_d being the complex dielectric function of the metal and dielectric layer, respectively. κ_0 is the wavenumber, $\kappa_0 = \frac{2\pi}{\lambda}$.

In conventional OLEDs, the emitter molecules are located in close proximity to a metallic interface. Hence, the SPP modes can be formed via the optical near-field of the excited molecule. Notably, strong coupling of radiation can occur for organic emitter with a vertically oriented dipole moment.[37] These SPP modes travel along with the organic/metal interface and are eventually dissipated as heat.[21, 37] This leads to low-outcoupling efficiency.

Substrate mode

The thickness of a substrate ($\geq 100\,\mu m$) is much larger than the wavelength of the emitted light. Hence, the waves propagating in a substrate can be analyzed using geometrical optics. TIR can occur under a certain angle of incidence to substrate/air interface when light propagates from the high-index substrate to air. This critical angle of incidence can be described according to snell's law as follow:

$$\theta_c = \arcsin\left(\frac{n_1}{n_2}\right), n_1 < n_2 \tag{2.15}$$

Where n_1 and n_2 are the refractive indices of air and substrate, respectively. For a substrate made of glass ($n_{glass} = 1.5$), the TIR occurs at $\theta_c = 41.8°$ (see **Figure 2.12**). These substrate modes propagate along the substrate and are lost by either absorption or edge emission.

The OLED optical structure presented here is oversimplified. In reality, the interfaces between different organic layers (HTL, ETL, and EML) and the transparent anode can not be ignored since all have different values of refractive index. As a result, besides the optical losses mentioned above, there are losses due to Fresnel reflections (for more details, please refer to Equation 2.9). These arise at every transition between two materials with different refractive indices.

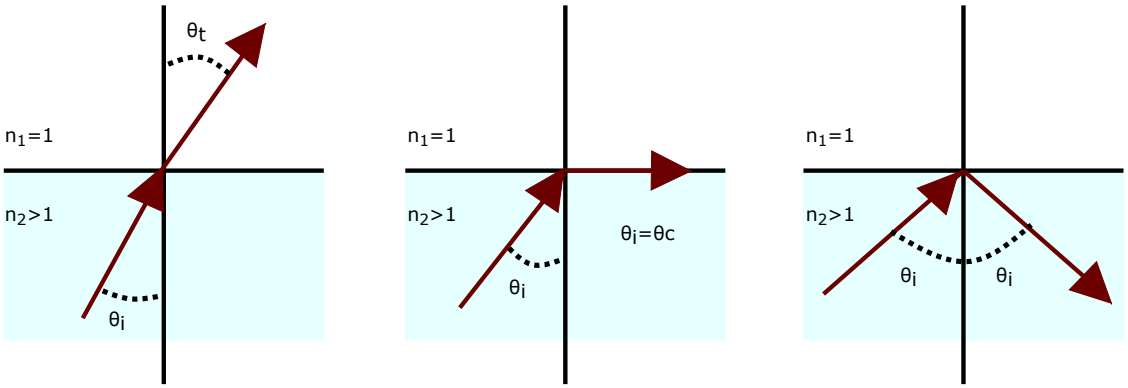

Figure 2.12. Total internal reflection at a glass/air interface: $n_{glass} > n_{air}$ ($n_{glass} = 1.5$, $n_{air} = 1$). Left: normal refraction, $\theta_i < \theta_c$ and $\theta_i < \theta_t$. Middle: $\theta_{t,max} = 90°$ for critical angle $\theta_i = \theta_c$, here $\theta_c \approx 41.8°$. Right: TIR, $\theta_i > \theta_c$.

Distribution of modes in an OLED multilayer

Considering the optical structure in **Figure 2.13a**, the optical (loss) channel of an OLED can be expressed using a dispersion relation as high-lighted in **Figure 2.13b**. The dispersion relation depends on the refractive indices of the different layers and the location where light is generated.[37] A distinction is made between four regimes: For electromagnetic radiation with an in-plane wavevector ranging between 0 and κ_0, light is out-coupled to air (air modes). At higher wave vectors (in-plane wavevector ranging between κ_0 and $n_{glass}\kappa_0$), light is trapped in the substrate (substrate mode). The dispersion relation that defines waveguide modes lies below the substrate light line $\omega = c_{glass}\kappa$, with ω being the angular frequency of the electromagnetic wave. These are propagating waves with an in-plane wavevector value ranging between $n_{glass}\kappa_0$ and $n_{organic}\kappa_0$. The waves with an in-plane wavevector larger than $n_{organic}\kappa_0$ can not radiate and are usually described as evanescent waves decaying away from the metal-dielectric interface (SPP modes).

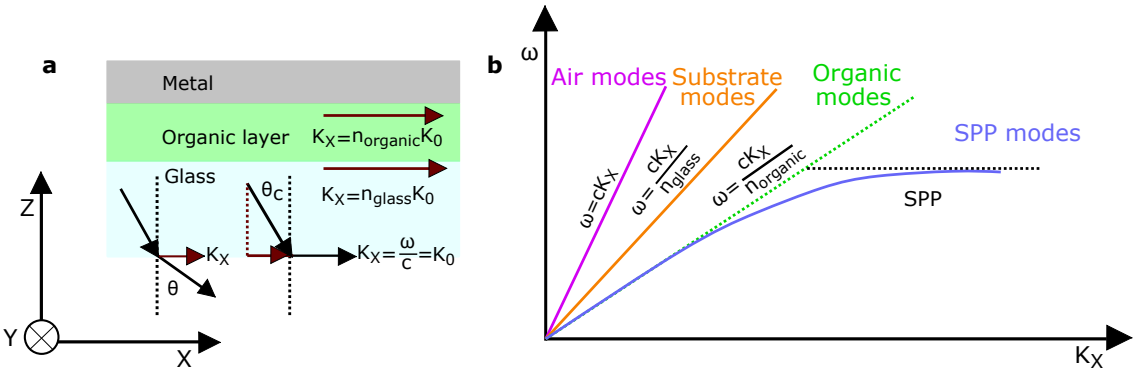

Figure 2.13. Scheme of optical modes distribution for a bottom emitting OLEDs. (a) A simplified OLED with propagating waves having a maximum in-plane wavevector in each layer. ω is the angular frequency of light and k_0 the magnitude of wavevector in free space. b) Schematic dispersion diagram for the OLED. Unlike air and substrate regions (continuum space), only waves with a certain in-plane wavevector can propagate in the organic layer and the metal surface (SPP modes).

2.2.5 Light extraction approaches

The optical losses discussed above can be minimized by optimizing the layer thickness of the organic materials (i.e., microcavity optimization) and the emitter dipole orientation. However, the dominant optical losses are not effectively minimized with the two approaches. Alternatively, or in addition, numerous light extraction structures have been investigated to outcouple the confined optical modes and further enhance the efficiency of an OLED. Broadly, these light outcoupling structures can be classified as external and internal light outcoupling layers. The external light outcoupling layer only aims to extract the confined light at the glass/air interface. The thin-film-guided modes, however, are still confined. Hence, to fully outcouple the confined light, it is also essential to incorporate an internal light outcoupling layer. The various strategies to extract the different optical modes in an OLED device are reviewed below:

Dipole moment orientation

The outcoupling efficiency of an OLED is highly influenced by the orientation of the transition dipole moment vectors of the emitting molecules with respect to the plane of the OLED substrate.[37] Among the three different optical loss channels, the orientation of emitting dipoles has a considerable effect on the coupling to SPP modes.[37, 40] For example, vertically oriented emitting dipole overlaps with the electric field of SPP and thus leading to strong coupling of the emitted light to the TM-polarized SPP modes of the metallic cathode.[40] However, a horizontally oriented dipole leads to reduced light losses from SPP modes since a dipole's radiation is the strongest in the direction vertical to the transition dipole moment.[37, 40] A horizontally orientated dipole can be achieved by either exploiting the guest-host interactions between the emitter (guest) and the host or by chemically designing an elongated rod-shaped emitter that would lay flat upon deposition.[37]

Microcavity optimization

The microcavity structure is defined by the top metal electrode layer acting as mirror and the dielectric mirror formed on a glass substrate.[41] Based on the multiple-beam interference effect between two mirrors, a light wave with the wavelength that meets constructive interference condition is strengthened while others are suppressed.[42] This effect influences the electroluminescence spectra of an OLED device. With a careful choice of the layer thicknesses and the inclusion of additional optical spacer layers, the microcavity resonance effect was shown to enhance air modes while suppressing the amount of power coupled to the waveguided and substrate modes.[41, 42]

Manipulating refractive index in OLEDs

One possible solution to reduce the optical losses in an OLED is tuning the optical material property (i.e., the refractive index) of the organic and anode layers. This can be achieved by using chemical or physical means.[37] For example, a reduced refractive index can be achieved by means of oblique angle deposition of an anode and transport layers such as HTL and ETL.[37, 40]

External light extraction layer

A large portion of the emitted light (around 40% to 60%) from the organic thin film is confined in a glass or polymer substrate as a substrate mode. This is mainly due to the TIR at the substrate/air interface, and any schemes attached to the outer surface of the substrate to reduce the propagation angle or frustrate the TIR boundary conditions are referred to as the external light outcoupling layer. Typical examples of external light outcoupling structures are index-matching lens (e.g., macro lenses and microlens array (MLA)), bulk optical scattering layers including particles or air voids, and corrugated (or wrinkle) substrates. Among the different approaches, MLAs give the highest substrate mode extraction efficiency. The substrate mode extraction efficiency of the bulk optical scattering layers highly depends on their light scattering strength and the absorption of the scattering film. The substrate mode extraction efficiency of the corrugation (or wrinkle) structures depends on the feature size (i.e., periodicity and corrugation depth). Greater feature size compared to the internal corrugation structures (for more details, please refer to Chapter 9) is required to suppress the substrate modes effectively.

Internal light extraction layer

In contrast, the internal light outcoupling structures are built inside of the OLED device. Internal schemes may be classified into two categories: compact and volumetric light scattering layer. The former includes a scattering layer (i.e., with a thickness of a few hundreds of nanometers) relying on disordered or periodic 2D/1D planar nanostructures. The latter include scattering layers, where high (or low) refractive index nanoparticles are embedded into a thick transparent matrix layer. A detailed discussion of different internal light outcoupling layers along with approaches developed in this study for improving the efficiency of OLEDs can be found in Chapters 8 and 9.

2.3 Phase separated nanophotonic structures

Polymer blends undergo a transition from a single-phase homogeneous solution into two or more distinct phases when a solvent is removed, or temperature is changed. This, in short, is referred to as a phase-separation process. The formation of distinct phases can be explained using Flory-Huggins theory,[43, 44] which deals with the equilibrium phase behavior of a mixture of two linear polymers A and B. Accordingly, the change in free energy upon mixing ΔG_m for a binary polymer blend is given by[43–45]:

$$\frac{\Delta G_m}{\kappa_B T} = \frac{\Phi_A}{N_A} \ln \phi_A + \frac{\Phi_B}{N_B} \ln \phi_B + \phi_A \phi_B \chi \tag{2.16}$$

Where κ_B denoting the Boltzmann constant, T the temperature, $N_{A/B}$ the number of monomers in the polymer chain of A and B, $\phi_{A/B}$ the volume fraction of polymer A and B in the mixture, and χ Flory-Huggins segment-segment interaction parameter.

The first two terms on the right-hand side of Equation 2.16 are related to the entropy of mixing; whereas, the last term gives the enthalpy of mixing.[43, 44] In binary polymer blends, the large chains assume fewer mixed configurational states; thus, the combinatorial entropy becomes vanishingly small. As a result, χ is a useful

parameter for explaining the phase separation of polymer blends. The phase separation occurs when a single-phase system enters either the metastable or the spinodal (i.e., $\frac{\partial^2 \Delta G_m}{\partial^2 \phi} = 0$) region (for more details, please refer to Chapter 4). The critical thermodynamic condition for phase separations is given by[43, 46]:

$$\frac{\partial^2 \Delta G_m}{\partial^2 \phi} = \frac{\partial^3 \Delta G_m}{\partial^3 \phi} = 0 \tag{2.17}$$

The χ parameter at the critical point χ_{cr} can be obtained from the definition of the critical point (Equation 2.17) and Equation 2.16. Thus, χ_{cr} given by the expression[43, 46]:

$$\chi_{cr} = \frac{1}{2}\left(\frac{1}{\sqrt{N_A}} + \frac{1}{\sqrt{N_B}}\right)^2 \tag{2.18}$$

Where χ is treated as composition independent.

The final morphology of the phase-separated polymers is influenced by the polymer blend recipe and the deposition conditions.[44] Chapter 4 demonstrates how the morphology depends on the blend properties and how processing conditions can control phase size and shape.

3. Materials, methods and characterization

This chapter covers the different materials, methods and characterization techniques used in this work. Section 3.1 gives an overview of the materials used for solar cell and OLED devices fabrication, as well as for polymer blend lithography. Section 3.2 presents the methods used for processing the materials. At the end of the chapter, the optical and electrical characterization techniques used for the devices are briefly discussed. In addition, the techniques used for the topographical characterization of the devices and the phase-separated nanostructures are highlighted.

3.1 Materials

Hydrogenated amorphous silicon

a-Si:H layers were prepared using plasma-enhanced chemical vapor deposition (for more details, refer to the Methods section) at a plasma excitation frequency of 13.56 MHz and a substrate temperature of 180 °C. A high discharge power of 0.3 W/cm^2 and a SiH_4/H_2 flow of 41/339 SCCM (standard cubic centimeter per minute) was used for the deposition of the a-Si:H films. More details regarding the deposition parameters are provided in Ref.[47, 48].

Silver

a-Si:H based solar cells have front- and back-side metalized portions (front and back electrodes). As a back electrode, a 250 nm thick silver (Ag) layer fabricated using a thermal evaporator is used. As a front contact, Ag grids with a finger width of around 100 μm, periods in the mm-range and a finger thickness of 700 nm are used.

Aluminum doped zinc oxide

ZnO:Al layers were prepared using a magnetron-sputtering method. The target consists of 98 wt.% Zinc oxide (ZnO) and 2 wt.% Al_2O_3. In particular, the latter increases the conductivity of the material. More details regarding the role of the dopant aluminum is provided in Ref.[49]. ZnO:Al layers were used as a buffer and capping layer in n-i-p a-Si:H solar cells (for more details, refer to Chapter 5).

Hydrogen-doped indium oxide

IOH (In_2O_3:H) thin films were deposited using a sputter deposition system constructed by Kurt J. Lesker Company Ltd. The sputter coater was equipped with a 6″ In_2O_3 target with 99.99% purity. The process gasses used were argon, a 10% hydrogen mixture in argon, and a 10% oxygen mixture in argon. More details regarding the stability and the deposition parameters of IOH are provided in Ref.[50]. IOH layers were used as transparent conductive oxides in n-i-p a-Si:H solar cells (for more details, refer to Chapter 5).

Indium tin oxide

ITO was applied by Kurt J Lesker PVD-75 thin film deposition system. The deposition was carried out at room temperature (25 °C) with a deposition time of 2000 sec, 0.8 mtorr, and 2.5% O_2. Then, the samples were further annealed for 15 min on a hot plate at 200 °C to improve the transmission and the conductivity. The layers exhibit a sheet resistance of 22.9 Ohms/sq for a film thickness of 135 nm.

Emitter: Ir(ppy)$_3$

Tris[2-phenylpyridinato-C2, N]iridium (III) ($Ir(ppy)_3$) exhibits a very bright phosphorescence with an internal quantum yield of almost 100% [51], with an emission maximum at λ_{peak}= 520 nm. This green light-emitting utilize all of its singlet and triplet excitons for the emission. The emitter material was doped in a double-layer consisting of the hole and the electron transport materials, both at a concentration of 7 vol.% (for more details, refer to Chapters 8 & 9). The material was purchased from Lumtec Corp.

Injection and transport materials

Molybdenum oxide (MoO_3) was used as a hole injection material, 4,4′,4″-Tris[phenyl(m-tolyl)amino]triphenylamine (m-MTDATA) as a hole transport material, 4,7-Diphenyl-1,10-phenanthroline (BPhen) as the electron transport material. Lithium fluoride (LiF) was used as the electron injection layer, followed by the cathode material (Aluminum). The materials were deposited using a high vacuum thermal evaporator (Lesker Spectros) at a pressure of 10^{-6} mbar. The transport materials were purchased from Lumtec Corp.

Polymer blend

The polymer blend solutions were prepared by dissolving each mixture of methacrylate) (PMMA) and polystyrene (PS) precursor in a common solvent such as methyl ethyl ketone (MEK, Sigma-Aldrich). PMMA and PS with different molecular weights were purchased from PSS Polymer Standards Service GmbH (PSS) and used without further modification.

3.2 Methods

Spin coating

Spin-coating is a method used for the deposition of a liquid phase (i.e., a solution) onto a substrate that is subsequently rotated at high speed to form a thin layer. Film thinning occurs due to rotational forces (hydrodynamic thinning) and through evaporation (evaporative thinning). A number of parameters affect the interplay between hydrodynamic and evaporative thinning including viscosity, vapor pressure, molecular weight, acceleration rate, and rotational rate.[52]

Inkjet printing

Inkjet printing is a non-contact, digital printing process. Based on operation modes, inkjet printing is classified into two, continuous inkjet (CIJ) and drop-on-demand (DOD) inkjet.[53] In a CIJ printer, ink droplets are produced and ejected continuously. An inkjet printer based on a piezoelectric DOD inkjet head (Pixdro LP 50) is used in this research work. In a piezoelectric DOD inkjet head, a waveform is applied to a piezoelectric pressure transducer to control the ejection of individual ink droplets in a DOD manner onto a printing substrate to produce a computer-defined layout (for more details, refer to Chapter 4).[54]

Wet etching

Wet etching involves stripping off material from a substrate using liquid chemicals or etchants. Such a process can be carried out by protecting an area of the material not to be etched using a mask, for example, isotropic patterning of sputtered ITO in hydrochloric acid (Merck KGaA, 37 vol.%) bath to form anode contacts. In contrast, wet etching without a mask is carried out to develop a material from a substrate selectively. In this work, the latter process is used to selectively develop either a PS using cyclohexane (Merck KGaA) or a PMMA using acetic acid (ThermoFisher GmbH) after the deposition of a PS/PMMA polymer blend on a substrate.

Dry etching

Dry etching is used as an alternative to wet etching. In this work, reactive ion etching (Oxford 80 Plasmalab Etcher, United Kingdom)) is used to transfer pattern into the a-Si:H layer by using a nanostructured PMMA matrix layer as an etching mask (for more details, refer to Chapter 6). The a-Si:H is etched using a SF_6/Ar-based plasma at operational pressure and power of 25 mT and 50 W, respectively. The SF_6/Ar flow rate was fixed at 5/20 sccm.

Sputtering

Sputtering is a vacuum technology for applying coatings of pure materials to the surface of various substrates. The material to be deposited is called the "target". Ions generated by an electrical or magnetic field accelerate and knock atoms out of this target, which is then coated onto a substrate. With this method, thin-film conductive oxides such as indium tin oxide, aluminum-doped Zinc oxide, and hydrogen-doped indium oxide were deposited onto various substrates.

Thermal evaporation

Thermal evaporation is used to produce organic, metal, and dielectric coatings. A high-vacuum vapor deposition system (Kurt J. Lesker) was used to achieve these coatings. The system is equipped with a three-stage pump system to reach working pressure of less than 10^{-6} mbar. Organic materials are placed inside a quartz glass tube and heated using a surrounding heating coil until the materials evaporate. The metal and dielectrics are placed inside resistance evaporators (so-called crucibles) and heated up to 400 amp. The samples to be coated are positioned above the crucible and rotated to have a homogeneous coating.

Plasma enhanced chemical vapor deposition

Chemical vapor deposition (CVD) is a process by which thin films of various materials can be deposited on substrates, using precursors in the gas phase at elevated temperatures. CVD process requires a temperature in the range of 600 °C-800 °C and thereby restricts its use to substrates that can withstand these deposition temperatures. As an alternative for low-temperature substrate (typically heated to 250 °C to 350 °C), plasma is used to provide energy during the material deposition process (so-called plasma-enhanced chemical vapor deposition).[55]

Optical simulation

The optical properties of thin-film solar cells based on a-Si:H were simulated by the finite element method (FEM) available in COMSOL Multiphysics version 5.2a. Here, rather than reviewing the well-known FEM algorithm itself (which is thoroughly covered elsewhere[56]), the focus is on the particular design decisions that went into developing the physical and mathematical model of the simulation domains discussed in Chapters 5 & 6. The modeling capabilities in COMSOL are accessed via predefined physics interfaces, referred to as wave optics/RF interfaces, which allow to set up and solve electromagnetic models. The simulation domains are sampled using mesh elements. A straightforward example of a vital simulation parameter to choose is the domain sampling distance or mesh elements distance. In optical problems, wave propagation is characterized by the wavelength of light, λ. Thus, it is found that spacing between mesh elements not larger than a fraction of the wavelength is adequate to avoid numerical artifacts and obtain accurate results. An optimum choice that minimizes the computational load and gives results with reasonable accuracy is $\frac{\lambda}{10}$. The effect of an infinite structure is achieved by the use of a floquet boundary condition. This condition mimics the bulk structures required to model a device's optical properties, thereby saving memory and computational time. Hence, it is used to flank simulation models from the sides. In contrast, perfectly matched layers were introduced on the top and bottom of the simulation window to avoid the reflection of the backward propagating light back to the simulated domain.

For a normally incident plane wave with transverse-electric (TE) and transverse-magnetic (TM) orthogonal states, the integrated absorption was obtained using[57, 58]

$$\mathrm{IA} = \frac{\int_{\lambda_m in}^{\lambda_g} A(\lambda)\frac{\mathrm{d}I}{\mathrm{d}\lambda}\mathrm{d}\lambda}{\int_{\lambda_{min}}^{\lambda_g}\frac{\mathrm{d}I}{\mathrm{d}\lambda}\mathrm{d}\lambda}, \tag{3.1}$$

where $\frac{\mathrm{d}I}{\mathrm{d}\lambda}$ is the incident solar radiation intensity per unit wavelength, and $A(\lambda)$ is the absorption

$$A(\lambda) = \frac{\iiint_V P_{abs}^{a-Si:H} dv}{P_{incident}(\lambda)}. \tag{3.2}$$

$P_{incident}(\lambda)$ is the incident power in watt, $P_{abs}^{a-Si:H} = \frac{1}{2}\omega\epsilon^{||}|E(\lambda)|^2$ is the power absorbed per unit volume calculated from the divergence of the Poynting vector. $|E(\lambda)|^2$ is the magnitude of the electric field intensity, $\omega = \frac{2\pi c}{\lambda}$ is the angular frequency of the light, where c is the speed of light in vacuum and $\epsilon^{||}$ is the imaginary part of the dielectric permittivity.

3.3 Characterization

Atomic force microscopy

AFM uses a cantilever with a very sharp tip to probe surfaces. Forces between the tip and a sample surface deflect the cantilever. A laser beam is used to detect cantilever deflections towards or away from the surface. The detected beam is converted into an electronic signal and thereby utilized to reconstruct an image of the surface. It offers qualitative and quantitative information on many physical properties including size, morphology, surface texture, and roughness. In this work, AFM investigations were performed by using a JPK nanoWizard II atomic force microscope in intermittent contact mode (so-called "Tapping Mode"[59]) under ambient conditions. Herein, the measuring tip is set into oscillations close to its resonance frequency and positioned above the surface so that it touches the surface for a very small fraction of its oscillation period.

Focused Ion Beam

FIB is used to make a cross-section on the surface of a sample to be examined. This process is often achieved by applying gallium ions to the surface of the sample. This process removes material from the surface and creates a hole with a smooth cut edge. A scanning electron microscope (SEM) is then used to observe the cross-section by tilting the sample. In SEM, a glow (so-called "hot cathode") or a field emission cathode first emits primary electrons. These electrons are focused on the sample, where they are scattered back or re-emitted as secondary electrons. A detector is used to detect this electron beam, and the beam's position is combined with the intensity of the detected signal to produce an image. The FIB-SEM investigations were performed by using Zeiss Crossbeam 1540 ESB.

UV-vis-NIR spectrometer

The total transmittance (T) and reflectance (R) of samples were measured using a UV-VIS spectrometer (Lambda 1050, PerkinElmer Inc.) equipped with a 150 mm integrating sphere. For this, a light source (i.e., halogen lamp) spectrally selected using an optical grating and split into two beams. The sample to be examined is positioned in one of the two beams, while the other beam is used as a reference. The R or T is determined by the ratio of the measured intensities of the reference and sample beam. The absorptance (A) of the samples was then derived by applying $A = 1 - T - R$ for every wavelength. The diffused T and R were performed by letting the direct T and R escape out from the integrating sphere, respectively. A haze was measured by making the ratio of the sole diffused reflected or transmitted light to the overall reflected or transmitted light. Angle-resolved measurements were performed by fixing the samples in the middle of the integrating sphere using a vise-type center-mount, and the sample holder was rotated around its vertical axis.

Solar cell EQE setup

External quantum efficiency (EQE) of solar cells based on a-Si:H was measured using a differential spectral response setup with a lens in order to display the exit slit of the monochromator again with its smaller size to avoid partial shading by the front grid. Data were acquired using 10 nm intervals.

Solar cell simulator

The current–voltage characteristics of solar cells based on a-Si:H were obtained under simulated AM1.5G illumination conditions at room temperature following standard calibration and measurement procedures using a WACOM-WXS-140s-super (Class A) AM1.5 sun simulator. The solar cells are defined by a mask during the sun simulator measurements in order to avoid current collection at the solar cell boundaries.

Integrated sphere

The luminous flux of an OLED device was measured using an integrated sphere with a 20 cm diameter. The inside of the integrated sphere is coated with barium sulfate ($BaSO_4$) that has effective diffused reflectance in the spectral range of 350-2400 nm. The OLED device is positioned at an entrance opening and operated electrically. The emitted luminous flux introduced into the integrating sphere strikes the reflective walls and undergoes multiple diffuse reflections. The sphere exit is provided with shading (baffle), reflecting diffusely and blocking direct emission. The sphere exit is connected with glass fiber, which is connected to an external spectrometer (CAS140CT, Instrument Systems GmbH). The scheme that represents the system is shown in **Figure 3.1**. The absolute value of the luminous flux can be determined by calibrating the integrated sphere with a luminous flux standard. A halogen lamp with 17.1 lm from TechnoTeam GmbH was used as a luminous flux standard for calibration. An aiding lamp is also integrated into the system to consider the effect of different substrate holders on the measured spectra. The OLED devices' electrical

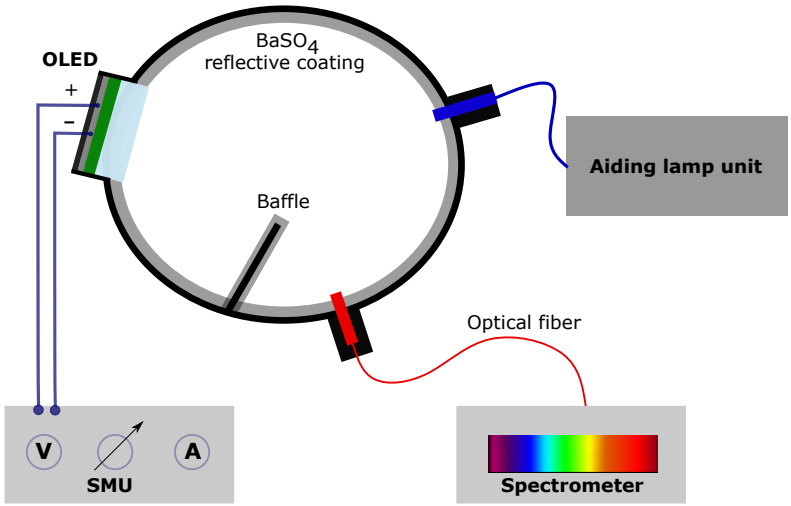

Figure 3.1. Measurement setup for determining the luminous flux of an OLED. The SMU controls the OLED placed inside of the integrated sphere. The emitted light is collected by the detector, which is connected to a spectrometer. The detector is screened from direct light by the baffle.

characteristics (current and voltage) were monitored using a source measurement unit (SMU, Keithley 2400).

Goniometer

A goniometer is used to measure the angle-dependent radiation characteristics of an OLED device. A scheme of the setup is shown in **Figure 3.2**. Herein, the OLED

device is operated at a fixed current or voltage. An SMU (Keithley 238) serves as the current or voltage source. A multi-mode glass fiber connected to a spectrometer (Ocean Optics USB2000) is used to collect the emitted light. The fiber cable was located at a distance of ≈15 cm from the OLED device. The distance is chosen so that the numerical aperture of the glass fiber corresponds to the angular interval of the rotation. This distance is big enough to avoid near-field effects of the emission. The angle-dependent radiation intensity is calculated by integrating the spectrum in the visible range.

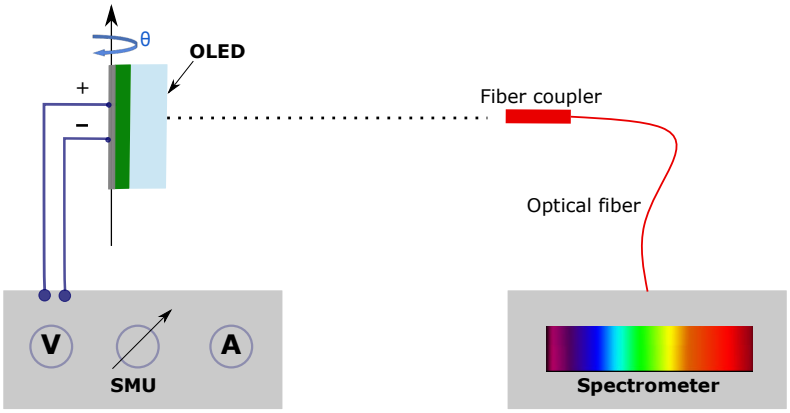

Figure 3.2. Goniometer setup for measuring the angle dependent radiation characteristics of an OLED. The OLED is rotated around the vertical axis. The emitted light is detected and guided to a spectrometer via an optical fiber.

4. Self-assembled nanostructures: From spin-casting to printing to imprinting

Quasi-periodic or disordered assemblies of light scatterers are playing an unprecedentedly important role in optics and photonics. Recently, particular attention is focused on the formation of such nanostructures in an inexpensive and facile way. In this direction, a maskless lithographic approach (polymer blend lithography) based on the spontaneous phase-separation of two or more polymers has shown great potential to fabricate such structures at high throughput and low cost. In this chapter, the interest and current state of the polymer blend lithography for nanophotonic applications and structural colors are first addressed. Moreover, this study identifies key challenges and opportunities within the field. In section 4.1, a spin-coating method is investigated as a deposition method to fabricate polymer blend lithography-based tailored disordered nanophotonic layers. Herein, the tailored disorder is achieved by adjusting the deposition condition and polymer blend parameters. The following sections address the significant stride made in the transition of polymer blend lithography "from lab to fab" by developing an industry compatible inkjet printing process (section 4.2) and a roll-to-roll nanoimprinting process (section 4.3) of phase-separated nanostructures. Finally, the chapter concludes with some perspectives and outlook on the future developments in the field. Parts of the results presented in this chapter have previously been published in the journal of ACS Nano and Advanced Materials Technologies.[60, 61]

Bottom-up nanostructures fabrication methods such as the self-assembly of amphiphilic lipids,[62] block-copolymers,[63] polymer blends,[64] or colloidal particles[65] have stimulated numerous studies due to their importance in basic scientific research and potential technological applications. The top-down approaches offer the advantages of high fidelity and high controllability.[66, 67] Among many available top-down approaches, optical lithography[66] and electron-beam lithography (EBL)[67] have been well developed and widely used by the conventional semiconductor industry. Optical lithography, however, lacks the resolution to pattern thin films into small features due to the optical diffraction limit. In contrast, EBL allows fabricating finer

structures but has limited throughput. In an alternative strategy, bottom-up approaches based on the phase-separation of homopolymer blends or block copolymers can provide a route to the fabrication of finer patterns (e.g., feature size<50 nm) with higher throughput. In this approach, a single-phase homogeneous solution demixes into two or more distinct phases.[68, 69] Our everyday experience with water and oil droplets illustrates such a spontaneous liquid-liquid phase separation. Because most polymer blends are incompatible, films undergo phase separation in the presence of a hard wall and free surface.[68, 69] Afterward, one of the constituents can be selectively removed, whereas the remained phase provides a template for additive or subtractive pattern transfer operations. The attractiveness of phase-separation processes for optics and electronics is highlighted in **Table 4.1**.

Table 4.1. Examples of phase-separated nanostructures processed by spin-coating and ordered by increasing feature size. Adapted with permission from Ref.[60]. © 2021 American Chemical Society.

Application / optical material	Feature size [nm]
Magnetic recording device	<10,[70] <50[71]
Field effect transistor	<15,[72] <30[73]
Phase change memory	<20[74]
Nanocrystal memory device	20[75]
Laser diodes	20[76]
MOS capacitor	20[77]
Metasurfaces	<40,[78] 80-200[79]
Anti-reflective coating	<50,[80] 100[81]
Photonic band-gap material	50,[82] 500[83]
Optical filter	<160[84]
Sensor (pressure,[83, 85] protein, DNA,[86] RNA[87])	500,[83] <500,[85] 200-800[86, 87]
Solar cells	200-600,[88] 140-560,[89] 40-300[90]
OLEDs	200-1000[91]
Photodiodes	10000-15000[92]

The successful transfer of phase-separated nanostructures (PSN) from lab-scale demonstrators into real-world products; however, is limited by three factors:

1. The PSN are randomly oriented with poor long-range order.
2. The deposition of the polymer blends using spin-casting (used for the applications gathered in **Table 4.1**), restricts the incorporation of PSN into uniform films and only offers limited control over the patterned areas location, size or geometry.
3. The polymer blend recipe (e.g., molecular weight, mass-ratio and concentration) fixes the structural parameters such as size, periodicity and shape of the nanoscale domains across the film.

Techniques for directed self-assembly based on chemically[70, 93, 94] and topographically [95, 96] patterned substrates address the first two limitations. Several approaches such as sequential solvent annealing,[97, 98] chemically patterned substrates,[99, 100] and external fields (stimuli)[101–103] were investigated to address the third limitation. The materials and insights gleaned from these works are impressive; however,

their industrial relevance is limited by the reliance on multiple steps and the use of lengthy thermal annealing processes that are not suited for high–production industrial applications. Eliminating such constraints could be valuable in many different application contexts (see **Table 4.1**).

In this study, first the well-established spin-coating method will be used to generate tailored disordered self-assembled nanostructures. Interest is driven by the need for tunable nanophotonics structures to improve light management in optoelectronics devices (which is also the topic of discussion in the following chapters of this thesis work). The following section highlights the development of inkjet printable polymer blend inks to fabricate 2D planar PSN using inkjet-printing (IJP). This approach is exploited to overcome the second and third limitation of PBL that are discussed above. In what follows, the homopolymer blend ink formulation is further tailored to meet the growing interest for photonic materials and devices fabrication by roll-to-roll (R2R) nanoimprinting lithography.

4.1 Spin-casted nanophotonic structures

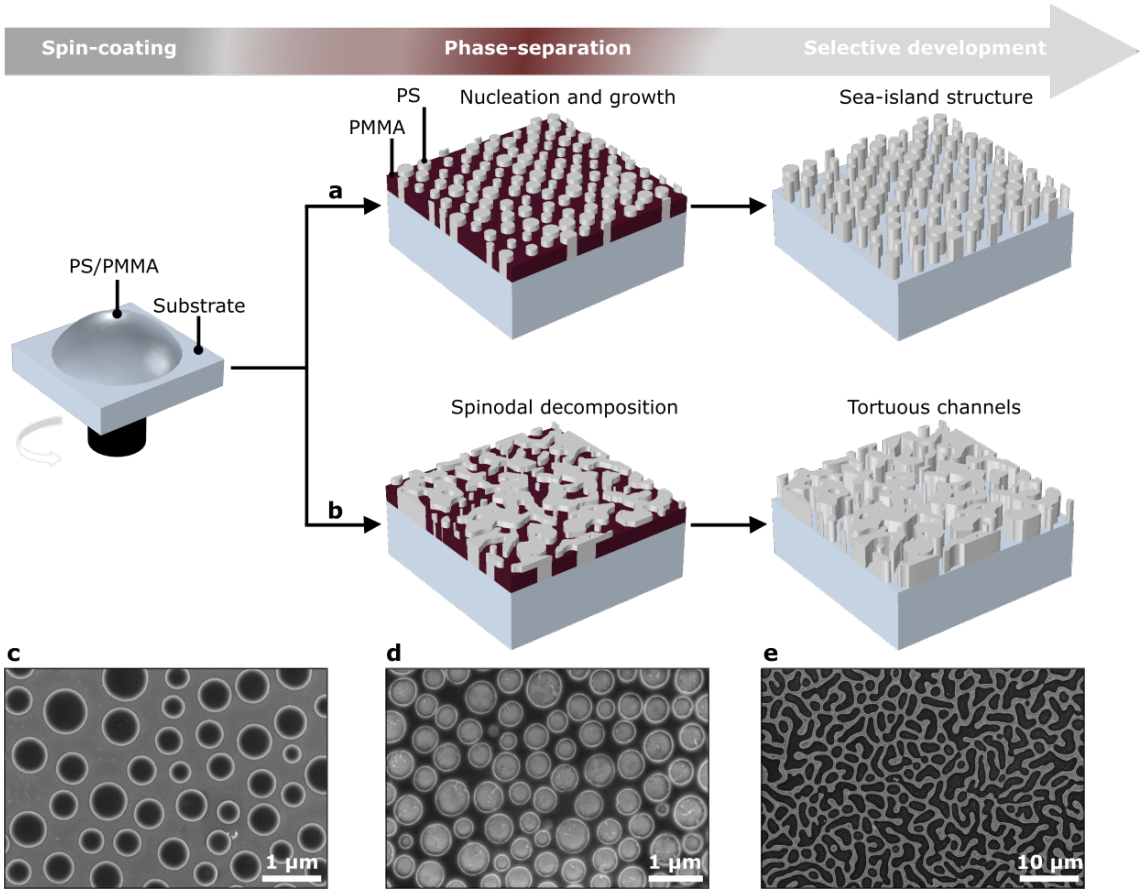

Figure 4.1. Phase-separated nanostructures via the self-assembly of PS/PMMA. A schematic illustration of the formation of spin-casted PSN via (a) nucleation and growth, and (b) a spinodal decomposition mechanism at room temperature. SEM images of the PSN formed via nucleation and growth (c,d), and spinodal decomposition mechanism (e), after the selective development of the PMMA (c) or of the PS (d,e) phase.

This section establishes a stable and reproducible fabrication route for the PSN with tunable characteristics using a spin-coating approach. To fabricate the PSN, a polymer blend consisting of two immiscible phases (polystyrene (PS) and poly(methyl methacrylate) (PMMA)) dissolved in methyl ethyl ketone (MEK) is used. As schematized in **Figure 4.1**, initiation of phase separation in the spin-casted thin film occurs through solvent evaporation. There are many routes to the formation of solid phases from a homogeneous PS/PMMA solution, but they all involve one of the two fundamental mechanisms of phase separation, nucleation and growth (N & G) or spinodal decomposition (SD).[104, 105] When the starting condition from which the new phase is formed is metastable, the phase transition occurs initially by N & G. Such phase transition mechanism leads to the formation of PSN with island-sea morphology as highlighted in **Figure 4.1a**. Outside of the N & G region, i.e., when the homogeneous phase becomes thermodynamically unstable, phase separation occurs via SD. The PSN formed via SD exhibit a disordered bicontinuous network (tortuous channels) morphology as shown in **Figure 4.1b**. Either of the formed phases via N & G or SD can be selectively dissolved afterwards. Herein, cyclohexane (acetic acid) enabled the development of the PS islands (PMMA matrix) selectively, leaving random nanoholes in a thin PMMA layer (random PS nanopillars) on the substrate, respectively. As an example, **Figure 4.1** presents scanning electron microscopy (SEM) images of PSN formed via N & G and rinsed in acetic acid (**Figure 4.1c**) and cyclohexane (**Figure 4.1d,e**) afterwards. The SEM image in **Figure 4.1e** show a representative morphology of PSN formed via SD.

For the spin-coating of polymer blend films, there are many parameters and conditions, such as the concentration of the polymer solution, the spin rate, and the surface property of the substrate, among others, that affect the final morphology of the polymer blend film. The following sections present a brief discussion on the influence of each parameter on the resulting morphology of PSN.

4.1.1 Rate of solvent evaporation

The morphology of the PSN can be controlled by adjusting the common solvent evaporation rate. This is attributed to the time-dependent domain coarsening behavior of PSN.[106, 107] The spin-coating approach allows controlling the solvent evaporation rate and hence domain coarsening behavior of PSN by simply adapting the rotational speed. Primarily, an increase in spin-casting speed shortens the time available for the PS domains to coalesce into larger ones by accelerating the MEK evaporation rate. Thus, it leads to the formation of finer PS nanopillars domains at higher speed. **Figure 4.2a** atomic force microscopy (AFM) images highlight the spin-casting speed's significant role in manipulating the PSN surface morphology. When PS/PMMA solution is spun at 500 rpm, the average diameter of the islands is about 606 nm, and a very wide diameter distribution from about 200 to 1000 nm is obtained. In contrast, the same solution spun at 3000 rpm exhibits an average diameter of about 411 nm and a narrower diameter distribution from about 200 to 700 nm is found (see **Figure 4.2b**). Tuning the rotational speed during PS/PMMA deposition also leads to variation in the layer thickness of the final PS nanopillar domains on a substrate as highlighted **Figure 4.2a,c**.

In an alternative strategy, the solvent evaporation rate during spin-coating can be controlled by adjusting the external environment conditions such as humidity and

temperature.[64, 108] Since the preparation of samples in this study carried out in a cleanroom with a controlled environment (with relative humidity between 40%-50%, and temperature in the range of 21-23 °C), the role of humidity and temperature is addressed only briefly. This will be an interesting aspect to analyze in a follow-up study. Herein, modest solvent evaporation rate control during deposition has been achieved by opening and closing the spin-coater chamber. **Figure 4.3** highlights that a closed spin-coater chamber during spin-coating slows (down) the evaporation rate thereby leading to larger PS domains (i.e., both in thickness and diameter) compared with with open chamber deposition (see **Figure 4.2**).

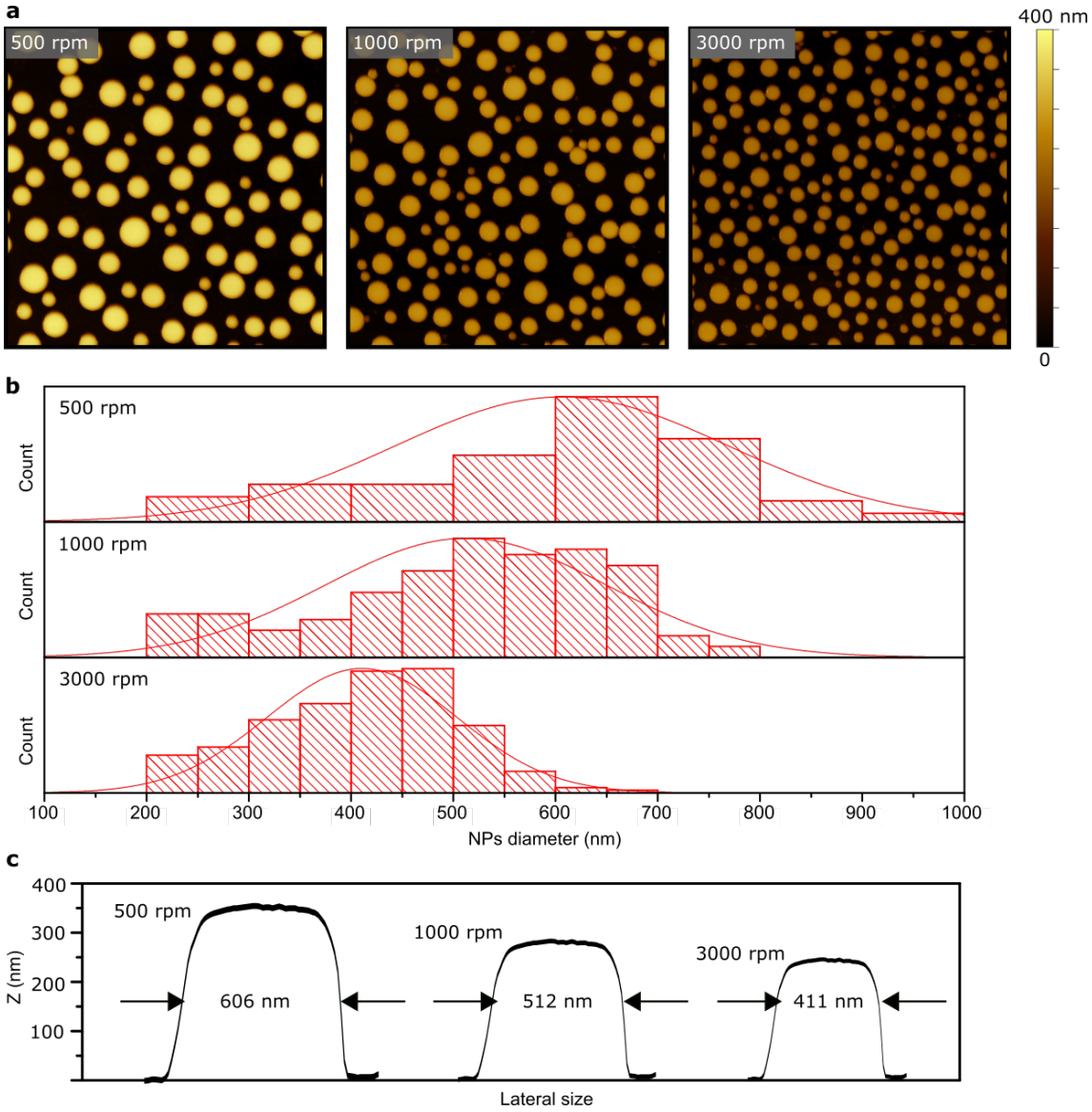

Figure 4.2. Influence of spin-casting speed on the PS nanopillars diameter and height. AFM images of the PS nanopillars fabricated using spin-casting speed of (a) 500 rpm, 1000 rpm and 3000 rpm with a open spin-coater chamber. (b) Distribution of the diameters of PS nanopillars of various spin-coating speed. (c) Height profiles of selected PS nanopillars of the average size. The scan areas of all AFM images are 10 μm × 10 μm. Samples prepared using PS(34K)/PMMA(15K) with a 4:6 weight ratio in MEK, with a concentration of 20 mg·ml^{-1}.

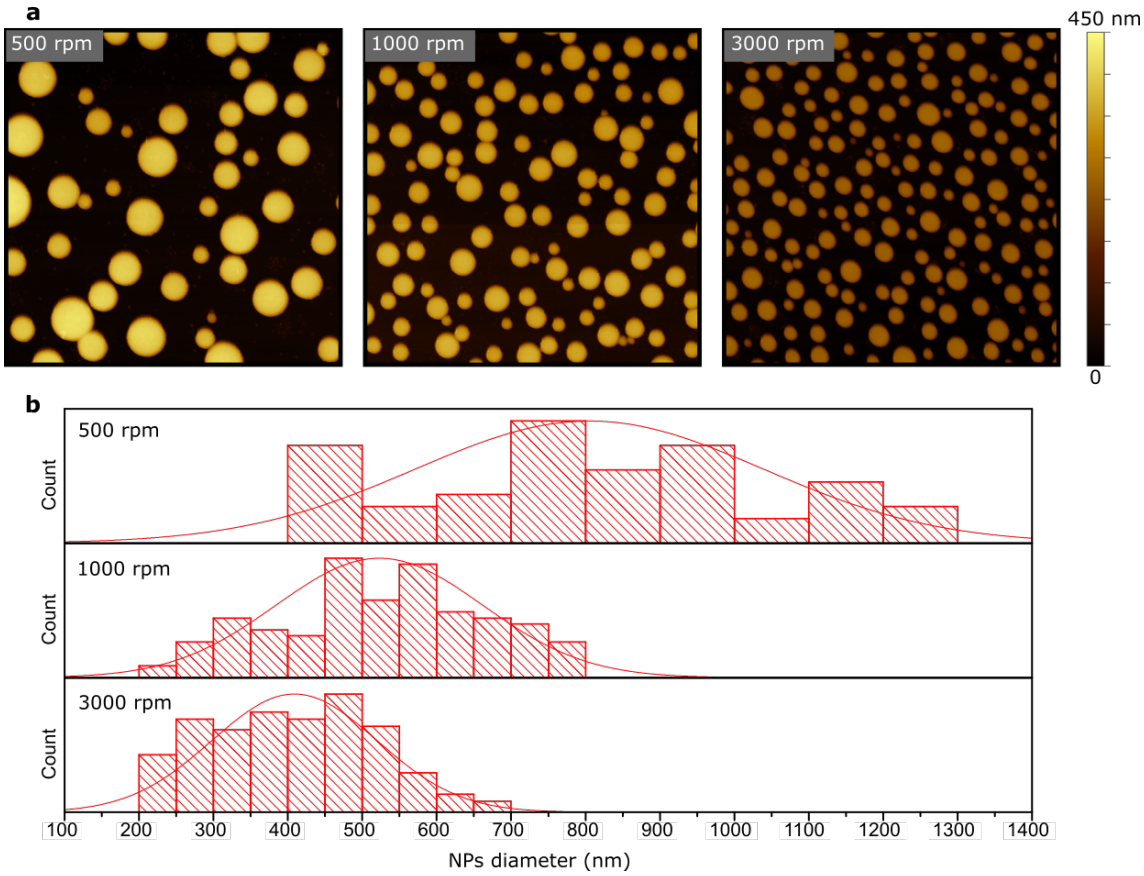

Figure 4.3. Dependence of the PS nanopillars diameter and height on the solvent evaporation rate with open and closed spin-coater lid. AFM images of the PS nanopillars fabricated using spin-casting speed of (a) 500 rpm, 1000 rpm and 3000 rpm with a closed spin-coater chamber. (b) Distribution of the diameters of PS nanopillars of various spin-coating speed. The scan areas of all AFM images are 10 μm × 10 μm. Samples prepared using PS(34K)/PMMA(15K) with a 4:6 weight ratio in MEK, with a concentration of 20 mg·ml^{-1}.

4.1.2 Composition of the blend

A change in PSN surface morphology similar to that shown in **Figure 4.2** and **4.3** (achieved by adjusting the depositions conditions) can also be achieved by varying the PS/PMMA blend compositions. **Figure 4.4** shows representative AFM images of the morphology for the sample prepared using PS/PMMA with different blending ratios. When the weight ratio of the PS in the blend is increased, PS nanopillars with larger diameter and increased thickness exist in polymer films. The driving force for these behaviors during spin-coating on a substrate is based on the difference in solubility of the PS and PMMA polymers in MEK.[109] Previous experimental studies showed that MEK is a better solvent for PMMA than for PS.[88, 109, 110] This leads to more MEK solvent in the PMMA-rich phase compared to the PS-rich phase. One way to lower the MEK in the PMMA-rich phase is to increase the weight ratio of the PS in the blend. Doing so, provides a longer period of time for the solvent in the PS-rich phase to evaporate and hence sufficient time for the domains to coalesce into larger ones (see **Figure 4.4a,b**). In contrast, when PS phase exceeds 40% in the solution, a PS matrix with nanoholes is formed on the substrate as shown in **Figure 4.4c**. The change of the dispersed phase from PS-rich to PMMA-rich, with change

in blend composition, is known as phase-inversion.[111] The resulting phase-inversion phenomenon is commonly associated with the change in the viscosity ratio of the polymer blends.[111, 112] It is predicted that the respective blend viscosity reaches a maximum at the point of phase inversion.[112]

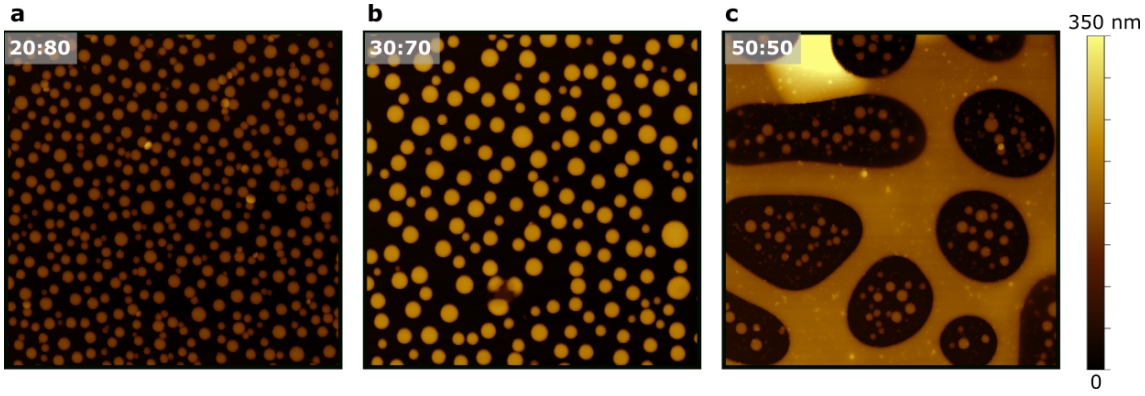

Figure 4.4. Influence of the polymer blend weight ratio on the resulting morphology of the PSN. AFM images of the PS morphology fabricated using different PS/PMMA weight ratios= (a) 20:80, (b) 30:70 and (c) 50:50. The scan areas of all AFM images are 10 μm × 10 μm. Samples prepared using PS(34K)/PMMA(15K) in MEK, with a concentration of 20 mg·ml^{-1}.

4.1.3 Concentration

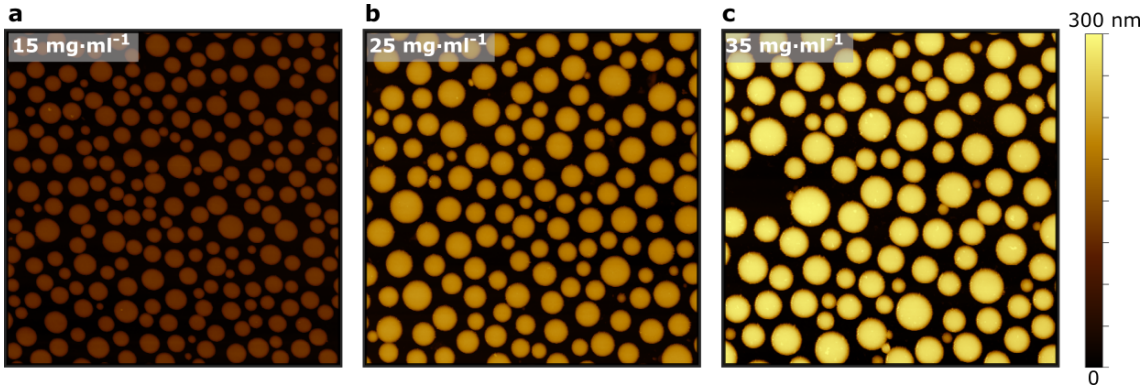

Figure 4.5. Influence of the polymer blend concentration on the resulting morphology of the PSN. AFM images of the PS nanopillars fabricated using three different polymer blend concentrations: (a) 15 mg·ml^{-1}, (b) 25 mg·ml^{-1} and (c) 35 mg·ml^{-1}. The scan areas of all AFM images are 10 μm × 10 μm. Samples prepared using PS(34K)/PMMA(15K) with a 4:6 weight ratio in MEK.

In a spin-casted polymer solution, film thinning occurs through centrifugal and viscous forces.[113] The latter highly depends on the concentration of the polymer in the solution. A more diluted solution exhibits lower viscosity and higher diffusivity, leading to a thinner polymer film on the substrate. In contrast, undiluted solutions lead to a thicker layer, and such films are known to retain solvents for a more extended period. Thus, it provides sufficient time for the PS nanopillar domains to coalesce into larger ones. As shown in **Figure 4.5**, the average diameter of the PSN spun with a more dilute solution is significantly smaller (average diameter=464 nm) as compared

to that spun with the more concentrated solution (average diameter=738 nm). The PS nanopillar domain height also increased linearly as the polymer concentration was increased from 15 mg·ml^{-1} to 35 mg·ml^{-1}.

4.1.4 Molecular weight

The polymerization degree of PS, expressed with molecular weight, is the main parameter for varying the thickness of the polymer film. An increase in PS molecular weight, increase the viscosity of the solution and consequently increases the film thickness.[64] This leads to increased diameter of the PS domains by increasing the polymer film drying time. **Figure 4.6** shows the dependence of the PS domains height and diameter on the molecular weight of the PS polymer. The PS nanopillar domains diameter increased from 383 to 748 nm as the PS molecular weight was increased from 19 kg·mol^{-1} to 96 kg·ml^{-1}.

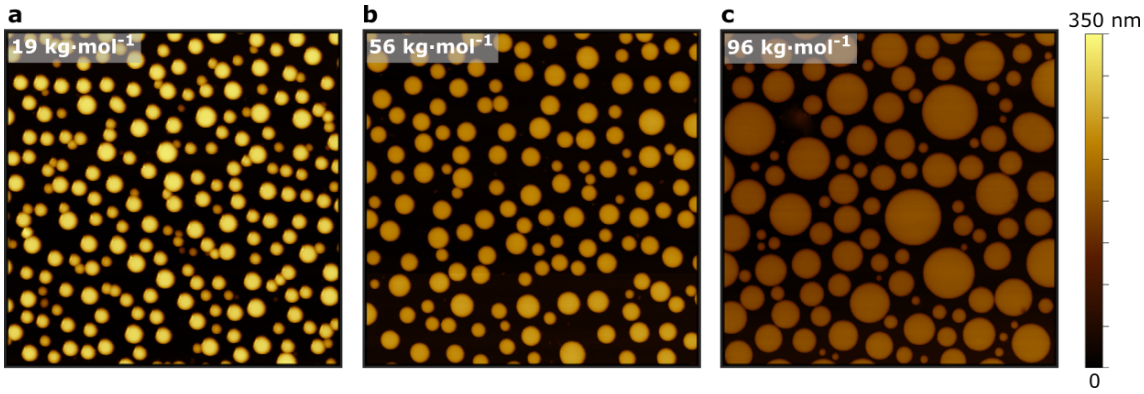

Figure 4.6. Influence of the PS molecular weight on the resulting morphology of the PSN. AFM images of the PS nanopillars fabricated using three different molecular weight of PS: (a) 19 kg·mol^{-1}, (b) 56 kg·mol^{-1} and (c) 96 kg·mol^{-1}. The scan areas of all AFM images are 10 μm × 10 μm. Samples prepared using PS/PMMA(15K) with a 4:6 weight ratio in MEK, with a concentration of 20 mg·ml^{-1}.

4.1.5 Solvent

The common solvent of a PS/PMMA blend determines the phase that solidifies first on a substrate. Typically, less soluble component depletes into solid earlier. However, the solvent effect is substrate-dependent, too. Different indicative morphologies, fabricated by solely switching the common solvent from MEK to chloroform, toluene and tetrahydrofuran (THF) can be seen in the AFM images shown in **Figure 4.7**. In contrast to MEK, the other solvents considered above are better solvents for PS.[110] As result, the PMMA phase is expected to collapse earlier into solidification and form islands-like structures while PS forms the surface-covering layer. With chloroform, as expected the PS polymer forms a matrix layer while the PMMA forms the nanopillars structures (see **Figure 4.7a**). In contrast for toluene and THF, the PS and PMMA formed tortuous channels via SD (**Figure 4.7b,c**).

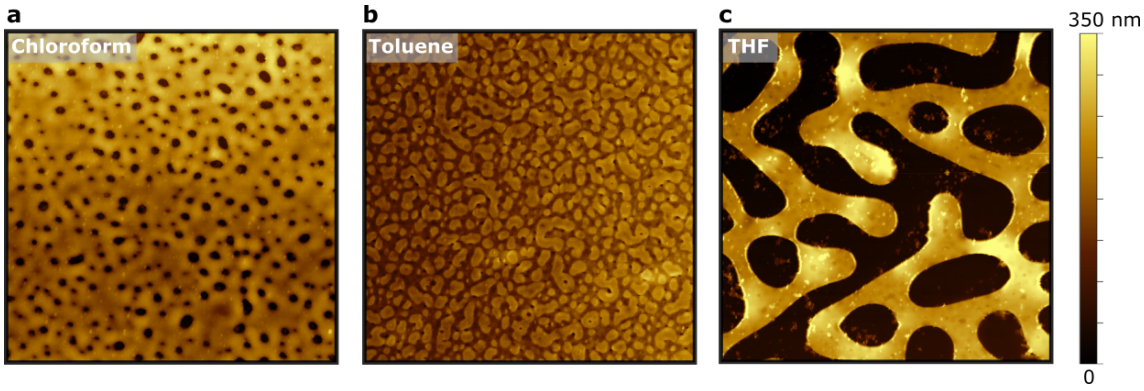

Figure 4.7. Influence of the common solvent on the resulting morphology of the PSN. AFM images of the PS morphology fabricated using three different solvents: (a) chloroform, (b) toluene and THF. The scan areas of all AFM images are 10 μm × 10 μm. Samples prepared using PS(34K)/PMMA(15K) with a 4:6 weight ratio, with a concentration of 20 mg·ml^{-1}.

4.1.6 Substrate

The type of substrate used for the deposition of the PS/PMMA blend determines the wetting behavior of the polymers at the substrate interface.[114] For hydrophilic substrates (here achieved by oxygen (O_2) plasma treatment for 5 min), the more polar PMMA is strongly attracted to the substrate interface (for more details, refer to section 4.2). Hence, the PMMA might form a wetting layer. The difference on the substrate between O_2 plasma treated and untreated could change the kinetics (mobility) of PS in these films. This might explain the PS nanopillars size distribution difference between PSN prepared on O_2 plasma treated and untreated substrate (see **Figure 4.8**).

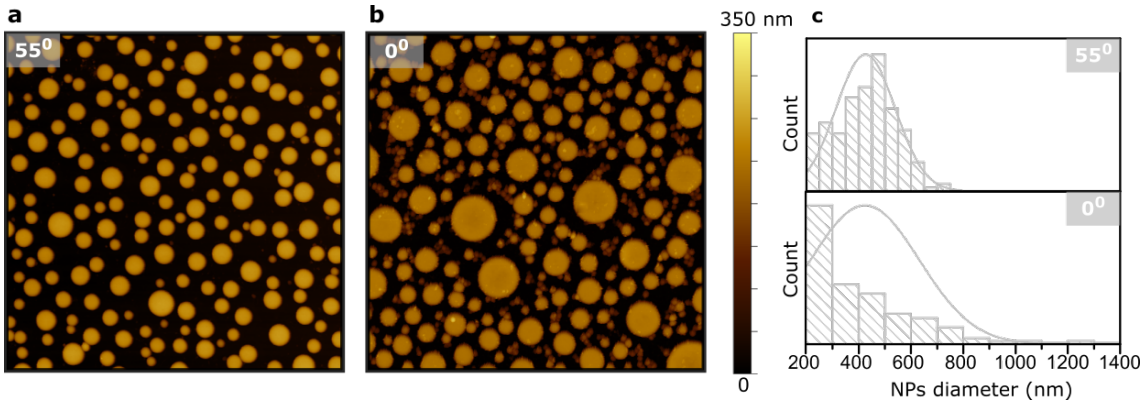

Figure 4.8. Influence of substrate wetting on the resulting morphology of the PSN. AFM images of the PS nanopillars fabricated on subtrate that has a water contact angle of (a) 55° and (b) 0°. (c) The corresponding distribution of the diameters of PS nanopillars. The scan areas of all AFM images are 10 μm × 10 μm. Samples prepared using PS(34K)/PMMA(15K) with a 4:6 weight ratio in MEK, with a concentration of 20 mg·ml^{-1}.

In summary, the findings reported here illustrate a PSN based on the phase separation of PS and PMMA polymer blends through spin coating process. The process of fabricating a cylinder like nanoholes and pillars, and bicontinuous network

(tortuous channels) nanostructures based on this phase separation approach were demonstrated. The required feature size of the nanostructures could be obtained conveniently by tuning the parameters of the polymer blend recipe and the deposition conditions. The successful use of these easily tunable PSN for light management in optoelectronics devices is highlighted in the following chapters. However, the spin-coating method used to fabricate PSN limits their design possibilities, which in turn hinders the deployment of PSN in commercialized products. To tackle this shortcoming, in the next section a versatile and industrially scalable deposition method based on inkjet-printing (IJP) of a polymer blend is introduced. Thus, the presented approach offers a great flexibility in terms of achievable designs and materials choice in order to tailor light scattering and to exploit it in various devices.

4.2 Inkjet printed nanophotonic structures

IJP is a system for depositing a material onto a specific place (for more details, refer to Chapter 3). This system has gained significant interest in industry for depositing materials with specific electrical, optical, chemical, biological, or structural functionalities. This is owing to its high scalability and cost-effectiveness.[115] Its benefits are therefore well aligned with those provided by a phase-separation process. The following sections demonstrate a versatile deposition method to fabricate arbitrary patterns of 2D planar PSN via the IJP of PS/PMMA blend inks over different substrates including glass, and polymer foils without physical contact. Here, tunable PSN are demonstrated by adjusting the deposition conditions such as resolution or post-annealing temperature. In addition, tunable PSN are achieved by tailoring the initial mixture recipe such as PS/PMMA weight-ratio.

4.2.1 IJP ink formulation

In spin-coated PS/PMMA inks (refer to section 4.1), homogeneously distributed PSN are achieved due to the dominating centrifugal force that leads to uniform but dispersive distribution of inks. In contrast, the IJP process depends highly on the PS/PMMA ink dynamics such as its viscosity (η) and surface tension (γ). For IJP inks, the desired processing windows are $1 < \eta < 25\,\mathrm{mPa.s}$ and $20 < \gamma < 90\,\mathrm{mN.m^{-1}}$. In addition, IJP inks are commonly prepared with solvents possessing a boiling point over 150 °C. This helps to keep the nozzles wet, and therefore avoiding detrimental clogging effects.

Herein, small molecular weight (MW) PS (MW=19 $\mathrm{kg{\cdot}mol^{-1}}$) and PMMA (MW=15 $\mathrm{kg{\cdot}mol^{-1}}$) polymers are employed with a concentration of 50 $\mathrm{mg{\cdot}ml^{-1}}$ to maintain a stable jetting process. The polymer blends were dissolved homogeneously in cyclohexanone with a boiling point of 155.6 °C.

4.2.2 Direct writing of PSN enabled by IJP

The working principle of IJP for writing customizable 2D designs incorporating PSN is schematized in **Figure 4.9a**. Here, an applied waveform to a piezoelectric transducer ejects droplets of PS/PMMA blend ink from each nozzle in drop-on-demand manner onto the printing substrate to produce the computer defined layout incorporating the PSN. For this ink formulation, phase-separation was assisted by a rapid thermal annealing process after printing.

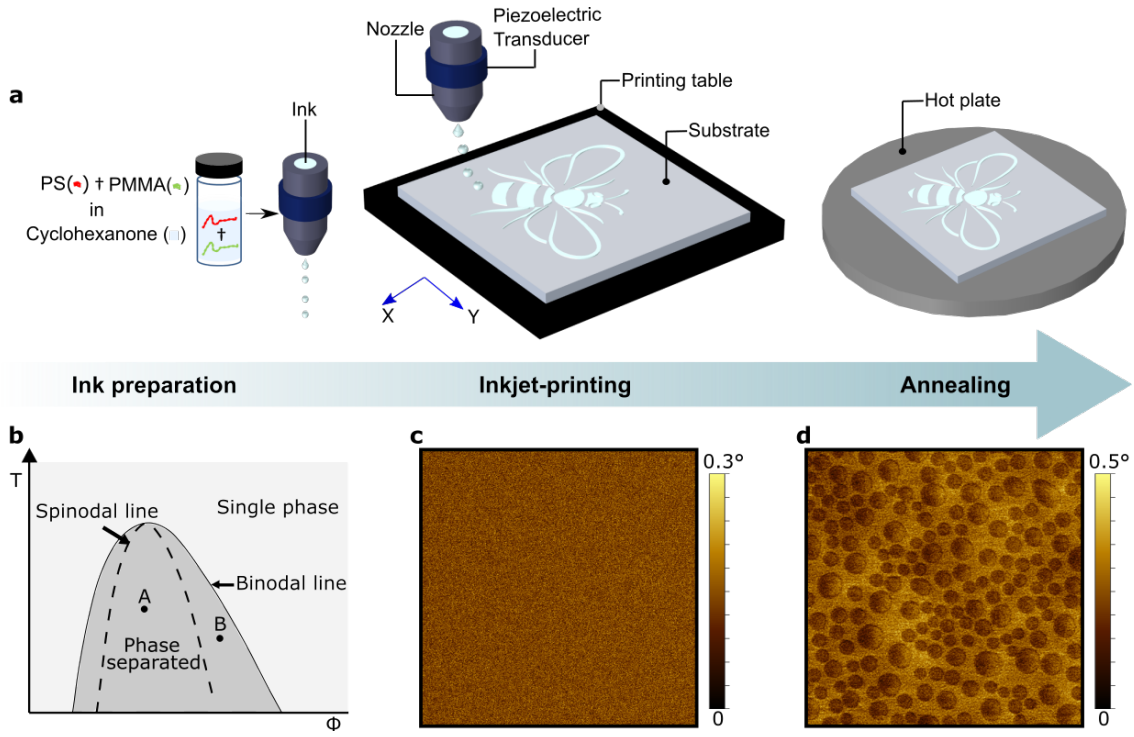

Figure 4.9. IJP enables the direct writing of PSN in complex designs. a) Schematic illustration of the key steps involved in IJP of the PS/PMMA=30:70 ink. (b) Schematic phase diagram of a polymer blend of PS and PMMA as a function of weight ratio of PMMA, ϕ and temperature, T. Above the binodal line, the system is a one-phase mixture. Below the binodal line, the mixture separates into PS and PMMA phases. Between the binodal and spinodal (dashed) line at B, the phase separation happens via nucleation and growth. Outside of the nucleation and growth region (A) phase separation occurs via spinodal decomposition and leads to disordered bicontinuous network (tortuous channels). AFM phase images ($8\,\mu m \times 8\,\mu m$) of the film (c) pre-annealing and (d) post-annealing. Adapted with permission from Ref.[60]. © 2021 American Chemical Society.

Samples are annealed at higher temperature than the glass transition temperature of both polymers (105 °C for PS and 115 °C for PMMA) under normal atmosphere. Then, the phase separation takes place during the annealing process and is either based on N & G or SD mechanism as schematized in **Figure 4.9b**. **Figure 4.9c,d** highlights the AFM phase images of printed PS/PMMA film pre-annealing (no PSN) and post-annealing (with PSN). Printed lines (post-annealing) forming the bee logo layout on a glass substrate (**Figure 4.10a**) and on a flexible plastic foil (**Figure 4.10b**), present examples that demonstrate the versatility of these processes in terms of printed film uniformity, geometry and PSN distribution. The SEM image (see **Figure 4.10c**) of the printed bee logo (after selectively developing the PS phase) shows that the PSN do not feature local clustering of the phase-separated nanodomains. Furthermore, the resulting morphology of the printed PSN are independent of the printed pixel size. **Figure 4.10d** highlights the dependence of the surface morphology on the printed pixels area that include a microscopic (smallest possible side dimension of 100 μm) and macroscopic scale. In particular, the average NH depth and diameter for the printed pixels with different scales shown in **Figure 4.10d** are 80 nm, 79 nm and 96.2 nm, 97.4 nm, respectively.

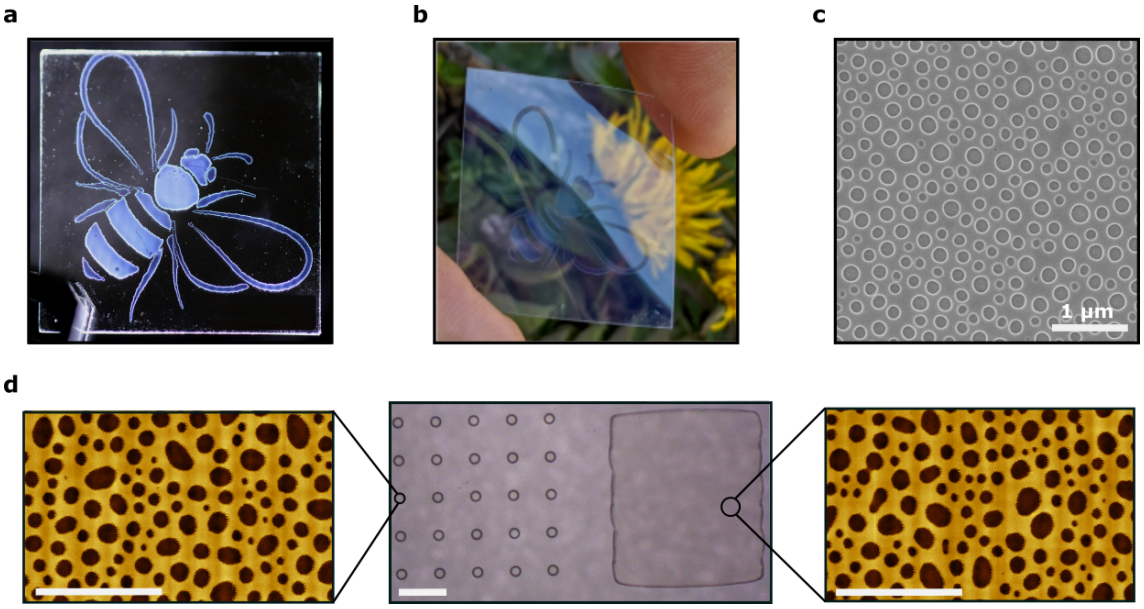

Figure 4.10. IJP enables the direct writing of PSN over diverse substrates. a) Photograph of an IJP 25 mm × 25 mm glass substrate illuminated by a white LED from the edge. The PSN efficiently scatter out the in-coupled light, revealing the bee logo. b) Photograph of the same IJP bee logo on a flexible plastic foil made of polyethylene terephthalate. c) Representative SEM top-view image of the disordered and uniformly distributed nanoholes (NHs) in a PMMA matrix, fabricated on a glass substrate after selective development of the phase-separated PS domains. (d) Center: Light microscopic image of printed pixels with the same thickness but with different lateral scales. The enlarged AFM images (left and right) show the corresponding surface morphology. The scale bar in the light microscopic image and the AFM image represents 0.5 mm and 1 μm, respectively. Adapted with permission from Ref.[60]. © 2021 American Chemical Society.

4.2.3 Dynamic variation of the PSN's morphology during IJP

In similar manner as that of the spin-casted PS/PMMA film, the orientation of the inkjet printed phase-separated domains depend on the printed film thickness. This is attributed to the change in the kinetics of phase-separation[116] and time required for the rearrangement for stable chain conformation depending on the considered film thickness.[117, 118] The IJP approach allows controlling the film thickness by simply adapting the printing resolution. This offers the possibility of adjusting the surface morphology of PSN, defined at the printing step, without changing the ink formulation. From an application viewpoint, this approach opens the possibility to digitally control the in-plane shape, the effective period and the diameter size distribution of the PSN at pre-determined locations over the same substrate, which would not be possible with ordinary spin-casting approach discussed above.

In order to explore the influence of the printed PS/PMMA thickness on the PSN surface morphology, squares with an area of 25 mm^2 were printed on a substrate with varying printing resolution from 400-1200 dpi as highlighted in **Figure 4.11a**. For a low resolution (here at 400 dpi), discontinuous films are formed due to the small number of ink droplets over the printed area. In contrast, printing resolutions above 500 dpi provide continuous films with a uniform thickness.

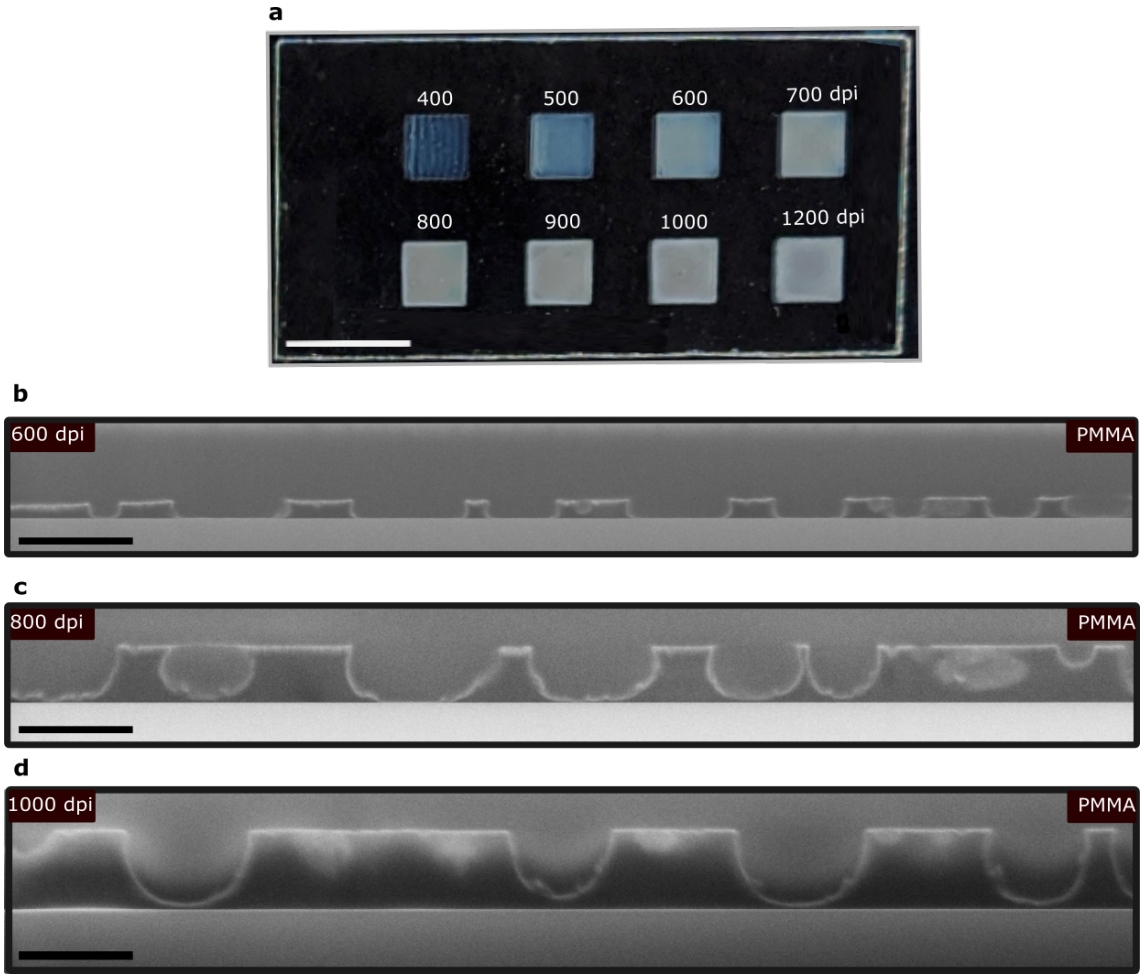

Figure 4.11. Influence of the printed pixel thickness on the nanoscale morphology of the phase-separated polymer films. a) Photograph of pixels printed at an increasing resolution and including NHs in a PMMA matrix after selective development of the PS phase (ink based on PS/PMMA (30:70)). The scale bar represents 1 cm. Cross-sectional SEM of pixels printed with a resolution of (b) 600 dpi, (c) 800 dpi and (d) 1000 dpi. The scale bar represents 0.5 μm. Adapted with permission from Ref.[60]. © 2021 American Chemical Society.

Figure 4.11b-d shows cross-sectional SEM images of FIB cut pixels printed with different resolutions. Depending on the printing resolution used, a different wetting layer formation is observed. Both polymers wet the substrate for a printing resolution of <700 dpi, as shown in **Figure 4.11b**. For films printed with higher resolutions, mainly the PMMA layer wets the substrate (see **Figure 4.11c,d**). In polymer blends, the air-polymer interfacial region is normally enriched in the polymer of lowest surface energy in order to minimize the interfacial free energy.[118, 119] Here, despite similar surface energies of PS and PMMA,[118, 119] cross-sectional SEM images of focused-ion-beam (FIB) cut PS/PMMA films have demonstrated the tendency of PMMA to form the wetting layer (see **Figure 4.11c,d**). The only possible reason for the preferential surface enrichment is the influence of the substrate used. Herein, the substrates were exposed to Argon plasma for 5 min. Hence, the more polar PMMA is strongly attracted to the hydrophilic substrate and forms a wetting layer.

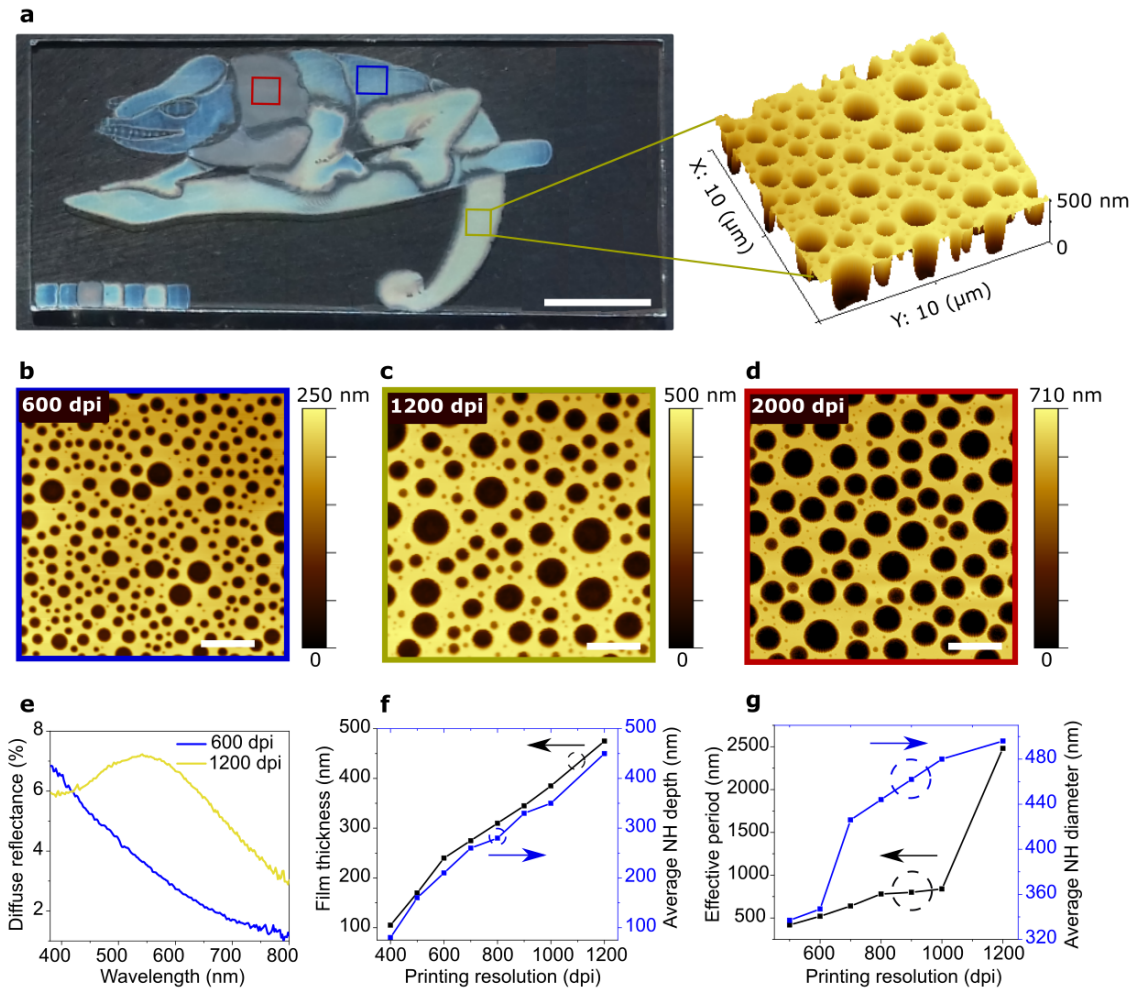

Figure 4.12. Defining the PSN's morphology at the inkjet-printing step. a) Photograph of chameleon logo layout printed with different resolutions and including NHs in a PMMA matrix after selective development of the PS phase (ink based on PS/PMMA (30:70)). The scale bar represents 1 cm. The inset 3D AFM image shows the NHs fabricated with 1200 dpi. (b)-(d) Corresponding AFM images from selected areas showing an increase of the mean NH diameter together with the printing resolution. The scale bar represents 2 μm. e) Measured diffuse reflectance from pixels printed with different resolution over the visible spectrum (under close to normal incidence). f) Thickness of printed square films (area of 4 mm^2) measured using contact profilometer before annealing as a function of the printing resolution and average depth of NHs in the PMMA matrix from AFM measurements. Dependence of the PSN structural parameters as a function of the printing resolution: (g) Effective period of the NH array calculated using a pair correlation function and average diameter of the NHs in the PMMA matrix. Adapted with permission from Ref.[60]. © 2021 American Chemical Society.

In one application example, the developed approach is used for printing customized structural colors. **Figure 4.12a** display a photograph of a chameleon logo pixels obtained upon a gradual change of the printing resolution. **Figure 4.12b-d** shows the corresponding AFM topography images of the PSN. The resulting pixels display different haze and colors arising from spectrally dependent light scattering at the PSN with different feature sizes (see **Figure 4.12e**). The thickness of the printed films

(before annealing) reported in **Figure 4.12f** increases with the printing resolution. After annealing the films, it is observed that the average depth and diameter of NHs in the PMMA matrix increases with the printing resolution, as shown in **Figure 4.12f,g**. The pair correlation function (denoted "PCF"[120]), was used to derive the effective period from the AFM images. It can be concluded from **Figure 4.12g** that the calculated effective period also increases with the printing resolution.

4.2.4 Ink composition dependence of the PSN's morphology

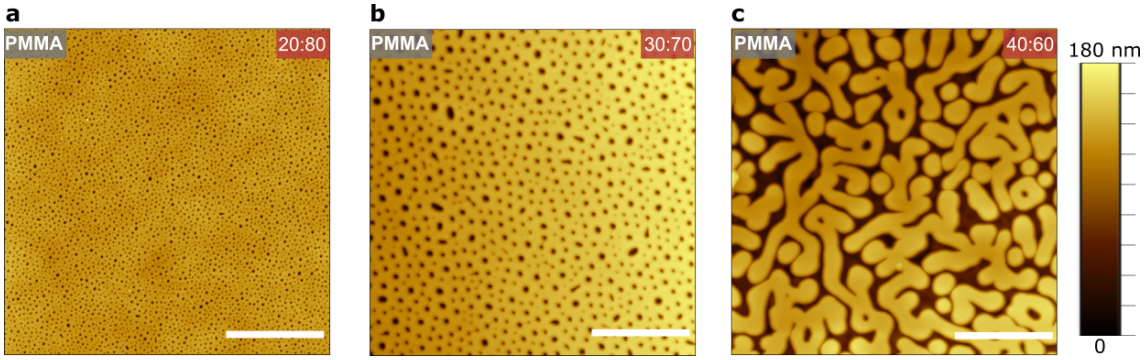

Figure 4.13. Influence of the polymer blend weight ratio on the resulting morphology of the phase-separated nano-/micro-domains. AFM images of the PMMA matrix fabricated using three different PS/PMMA weight ratios (PS/PMMA)= (a) 20:80, (b) 30:70, (c) 40:60, and obtained after 5 min of annealing at 150 °C, and after the selective development of the PS phase. The scale bar represents 3 μm in all AFM images. Adapted with permission from Ref.[60]. © 2021 American Chemical Society.

The processes of printed PS/PMMA film formation and phase separation depends strongly on blend composition. Effects related to blend composition emerge from a change in concentration of either PS or PMMA for a fixed PS/PMMA solution concentration. A series of printed films printed using PS/PMMA inks with a weight ratio of 20:80, 30:70 and 40:60 served as the basis of investigations (see **Figure 4.13**). PSN with a diameter size distribution centered at 113 nm obtained by increasing the weight-ratio of PS in the PS/PMMA blend to 30:70 from an original composition of 20:80, for which this distribution is peaking at 40 nm only (see **Figure 4.14**). Since the high PMMA weight ratio (for a fixed PS/PMMA solution concentration) also decreases the PS concentration, it is expected that the PSN made of PS resulting from a high PMMA weight ratio have smaller diameter (for more details, refer to section 4.1). When the PS weight ratio exceeds a given value, 30% in the present case, one observes a transition of the PSN morphology from a "sea-island" configuration (see **Figure 4.13a,b**) to a disordered bicontinuous network, involving domains with a width of a few hundreds of nanometers. A representative AFM image is given in **Figure 4.13c** for a blend composition of 40:60.

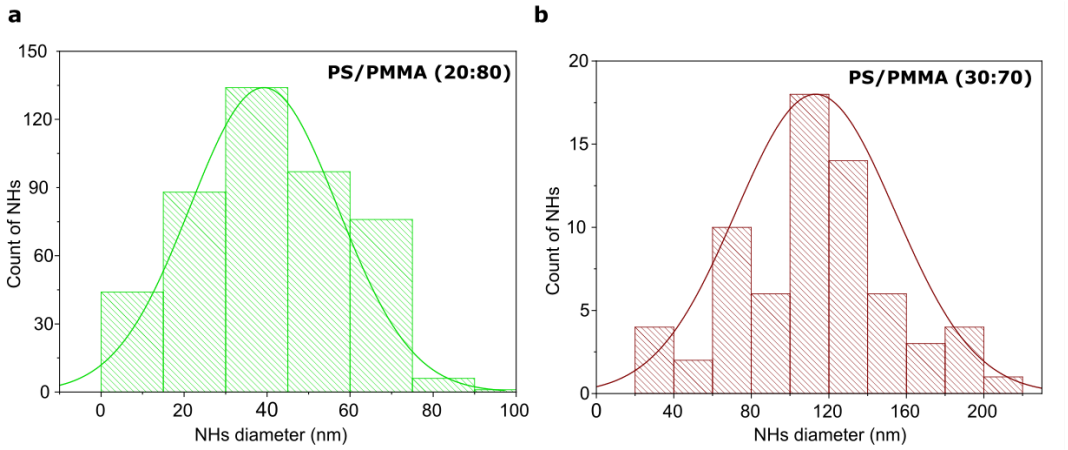

Figure 4.14. Size analysis of the disordered NH array for different weight ratios of PS/PMMA. A Gaussian distribution with a mean hole diameter of (a) 40 nm, and (b) 113 nm is obtained for inks with a PS/PMMA weight ratio of 20:80 and 30:70, respectively, and after annealing at 150 °C for 5 min and after the selective development of the PS phase. The solid lines in (a) and (b) represent the Gaussian fit. Adapted with permission from Ref.[60]. © 2021 American Chemical Society.

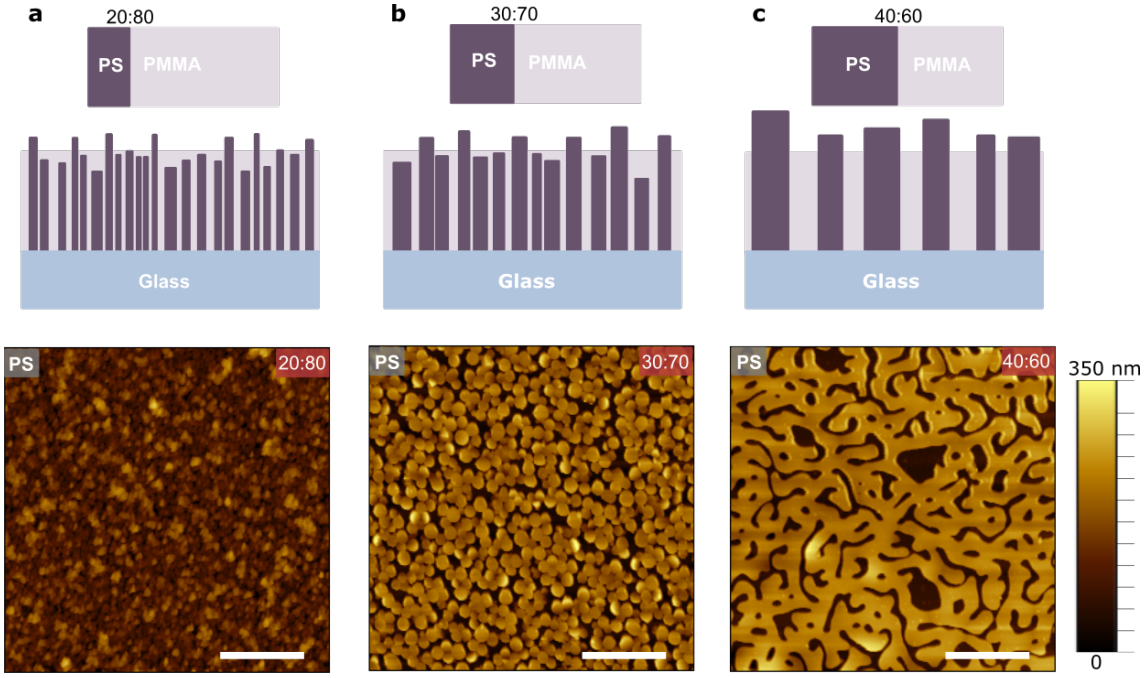

Figure 4.15. The dependence of the phase-separated nano-/micro-domains on the polymer blend weight ratio. Schematics depicting the phase-separation mechanism for different weight ratios. AFM images of the PS domains fabricated using three different PS/PMMA weight ratios (PS/PMMA)= (a) 20:80, (b) 30:70, (c) 40:60, and obtained after 5 min of annealing at 150 °C, and after the selective development of the PMMA phase. The scale bar represents 3 μm in all AFM images. Adapted with permission from Ref.[60]. © 2021 American Chemical Society.

4.2.5 Annealing temperature dependence of the PSN's morphology

The growth of the PS domains' lateral size in PS/PMMA film is largely determined by the diffusion rate of the PS in the system, which is known to increase with a rise of

the annealing temperature.[121] This PS phase coarsening phenomenon in the PMMA matrix follows the Ostwald ripening mechanism.[122] For an annealing temperature of 150 °C, the PS domains for thinner films printed with a resolution of 550 dpi after selective development of the PMMA phase are shown in **Figure 4.15**. Similar density of PS domains and NHs in the PMMA matrix is expected when only switching the developer solvent. Herein, the density of PS domains is significantly higher than the NHs in the PMMA matrix (see **Figure 4.13a,b**) when the PS/PMMA weight ratio is 20:80 and 30:70. The reduction in the NHs density in the PMMA matrix indicate that most PS domains fail to come into a direct contact with the polymer-air interface and are buried in the PMMA layer as illustrated using the schematics in **Figure 4.15**.

Typically, PS/PMMA films that are in non-equilibrium evolve towards the minimization of the surface energy once the polymers become mobile upon increasing the annealing temperature.[123, 124] **Figure 4.16** highlights the morphology of printed PSN obtained by varying the annealing temperature for PS/PMMA with a weigh ratio of 30:70. As the lateral size and thickness of the PS domains increase with the annealing temperature, the adjacent PMMA layer becomes thinner with an increase in surface coverage. By increasing annealing temperature from 150 to 300 °C, the average lateral size and thickness of the PS domains was tuned from 113 to 1500 nm and 350 to 1300 nm, respectively.

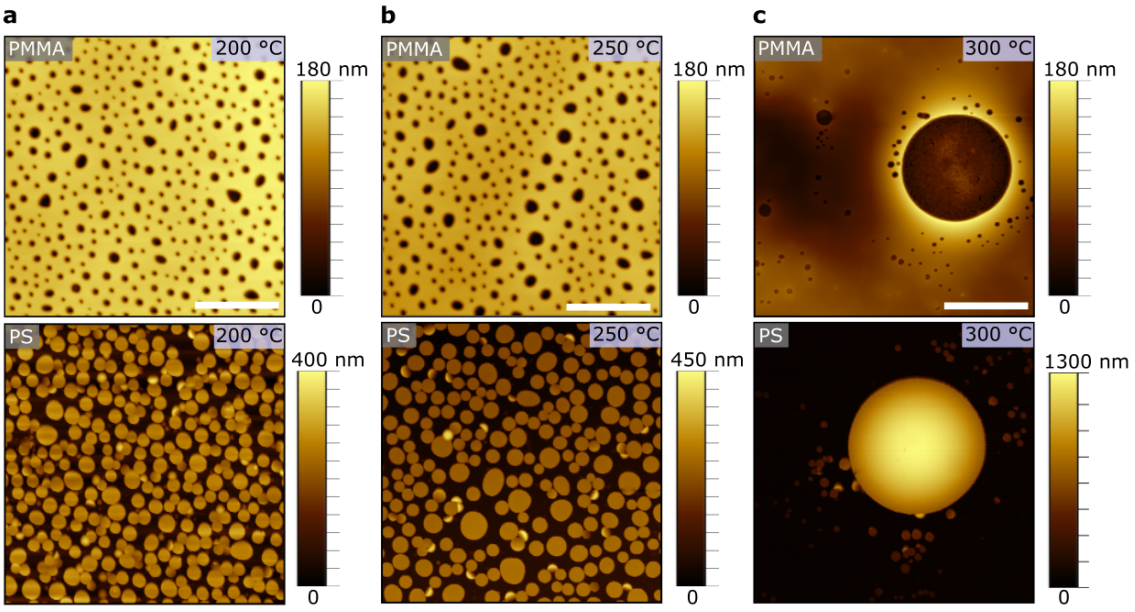

Figure 4.16. Influence of the annealing temperature on the resulting morphology of the phase-separated nano-/micro-domains. The AFM images of samples obtained after annealing PS:PMMA (30:70) blend thin films fabricated using 550 dpi at a temperature of 200 °C, 250 °C and 300 °C for 5 min are shown in (a), (b), (c), respectively, after selective development of PS (top row) or of PMMA (bottom row). The scale bar in (a) and (b) represents 3 μm, and 9 μm in (c). Adapted with permission from Ref.[60]. © 2021 American Chemical Society.

For a printing resolution >700 dpi, the resulting phase morphology at lower temperature (150 °C) is different from the situation shown in **Figure 4.15**. As can be seen in **Figure 4.11c,d**, the PS domains extend over most of the film thickness, but do not reach the interface with the substrate (here the PMMA forms a wetting layer) for high printing resolutions. As a result the selective development of the PMMA layer leads to the collapse of the PS domains. A higher annealing temperature of printed PS/PMMA film decreases the thickness of the PMMA layer wetting the substrate and consequently the PS domains grow towards the substrate, as highlighted in **Figure 4.17a,b**. Herein, standing hemispherical PS domains were achieved by selectively developing the PMMA matrix as shown in the cross-sectional SEM images of FIB cut pixel (**Figure 4.17b**). A few PS domains that are not vertically standing on the substrate were also observed as shown in the SEM image of the pixel (see **Figure 4.17b**). This is due to the difference in the thickness of the wetting PMMA layer below the PS domains.

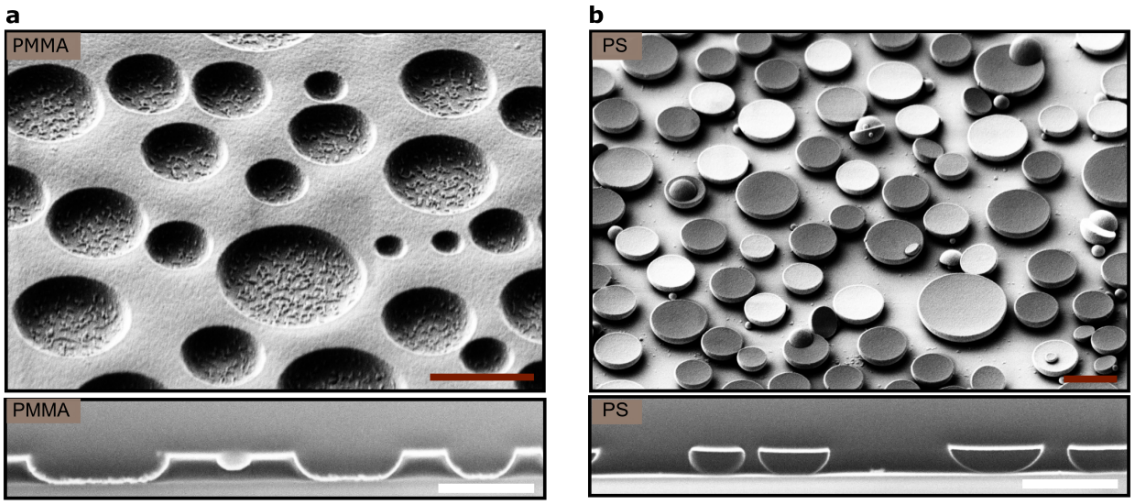

Figure 4.17. Morphology of the PS domains fabricated with 1000 dpi under a high annealing temperature of 250 °C. SEM top-view images (top row) of 45° tilted samples obtained after annealing PS/PMMA (30:70) blend films and selective development of (a) PS or of (b) PMMA. The bottom row shows the corresponding cross-sectional SEM images of the pixels. The scale bar represents 1 μm. Adapted with permission from Ref.[60]. © 2021 American Chemical Society.

Lastly, the effect of annealing duration on the morphology of PSN is investigated. Indeed, the lateral size of the PS domains increased with an increase in annealing duration for a given temperature (see **Figure 4.18**). For example, as the annealing duration of a printed film of PS/PMMA (30:70) increases from 15 min (**Figure 4.18a**) to 60 min (**Figure 4.18b**), the average lateral size increases by 59 nm. This finding highlights that a similar change in the surface morphology of printed PS/PMMA films can be obtained by varying the annealing duration instead of the annealing temperature. To quantitatively analyze the photonic properties of the films annealed for different duration, the normally incident diffuse reflection spectra is measured (see **Figure 4.18c**). It is readily apparent that as annealing duration increases, there is a red-shift in the peak reflected wavelength (which corresponds to the increase in average lateral size).

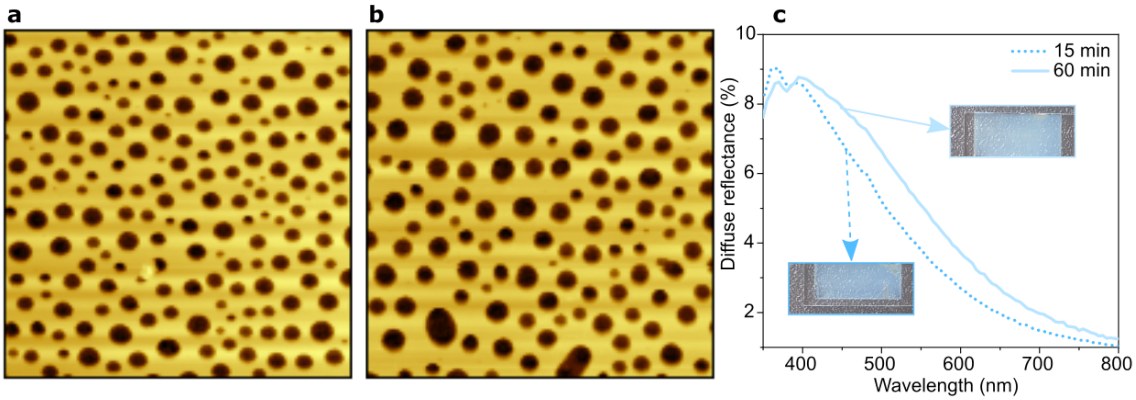

Figure 4.18. Influence of the annealing duration on the morphology of the printed PSN for a film printed with 550 dpi. AFM images (5 μm $\times$ 5 μm) of the surface morphology obtained after annealing PS:PMMA (30:70) films at 150 °C for different durations (a) 15 min, (b) 60 min. (c) Corresponding diffuse reflectance spectra measured in samples annealed for 15 min and 60 min (cropped photographs of the samples shown as insets). Adapted with permission from Ref.[60]. © 2021 American Chemical Society.

In summary, the findings reported here illustrate that direct, additive inkjet printing and self-assembly of PS/PMMA can be used together to form deterministically defined structures in wide-ranging, hierarchical patterns with feature sizes in PSN ranging from a few μm down to 100 nm. A critical feature of this scheme is that it enables to easily adapt the morphology of the PSN at the micro-/nanoscale in pixels shaped according to any pre-determined 2D design and printed over the same substrate by varying the printing resolution. It is expected that, with modest adjustments, these printing approaches solve the second and third limitations of PBL discussed above that restricted its advance from "lab to fab". In addition, in this approach the PSN morphology can be tailored by adjusting the ink formulation (weight ratio of the binary blends) or the annealing post-treatment. These manifold possibilities facilitate the development of printed photonic layers for various applications, two examples of which are given in our work.[60] One of the example is briefly discussed in Chapter 9.

Until now, PSN have been fabricated using polymers with low glass transition temperatures, which limit their practical relevance for nanoimprint lithography (NIL), as the PSN are prone to in-plane stamp distortions in the presence of high imprinting pressure and temperature. On the other hand, inorganic-organic hybrid polymers have already gained significance in industry and are successfully used for imprinting stamp material in UV and thermal-based NIL. For NIL, inorganic-organic hybrid polymer copies of the PSN can often be employed, but direct micro-/nanostructuring of this polymer using phase separation process for NIL is still absent. In the following section, these shortcomings are tackled by exploiting the unique advantages of a homopolymer/inorganic-organic hybrid polymer (PS/OrmoStamp) blend and phase separation processes. Upon optimized conditions, imprinting stamps based on PSN (made of inorganic-organic hybrid polymer) are directly fabricated over various rigid and flexible substrates. As demonstrations of the envisioned applications, the developed imprinting stamps are integrated into a roll-to-roll (R2R) NIL system for patterning a PS thin-film.

4.3 Roll-to-roll imprinted nanophotonic structures

Since the early Mesopotamian civilizations, direct printing techniques (e.g., hot embossing) have been used to impart relief patterns.[125] The technique evolved to replicate nanometer length scale relief patterns in 1995.[126] This route to patterning, known as NIL, offer many advantages such as high throughput and resolution, applicability to curved and large-area substrates, and a low fabrication cost due to its simple manufacturing process. Hence, it is important to industries invested in photonic and optoelectronic devices,[127, 128] high-density integrated circuits,[129] nanofluidics,[130] and many biological applications.[131, 132]

In the NIL process, a patterned stamp containing an inverse of the desired patterns is pressed onto a resist-coated substrate or a polymer foil. When heat and pressure (also known as thermal NIL[133, 134]) or pressure and ultraviolet exposure (also known as ultraviolet NIL[135]) are applied, the pattern is transferred with excellent fidelity via mechanical deformation. In terms of imprint contact types, NIL processes can be categorized into three types: plate-to-plate (P2P) NIL,[133] roll-to-plate (R2P) NIL,[136] and R2R NIL.[134] The successful implementation of the different nanoimprinting techniques require a durable and long lasting nanophotonic stamp, which will allow to replicate nanofeatures with high fidelity over hundreds of imprinting cycles. Beside these properties, a semi-flexible nanophotonic stamps are required for R2R NIL process. The conventional semi-flexible nanophotonic stamp fabrication method; however, involves a series of steps:

1. Fabrication of a master stamp made of soft material using different lithography approaches including, but not limited to, EBL,[134] laser interference,[137] and colloidal lithography.[138, 139]

2. Replication of the master stamp to polydimethysiloxane (PDMS).[140]

3. A daughter stamp fabrication made of semi-flexible material such as UV-curable OrmoStamp[141] via another soft NIL using the patterned PDMS.

To this end, the resulting stamps have been successfully used for patterning different functional materials (see **Table 4.2**). Their fabrication, however, involves a complicated process and is usually time-consuming. In some cases, these processes are expensive to carry out and pose a challenge to further development of NIL-based devices (see **Table 4.2**) in terms of commercialization. Bottom-up lithography approaches based on the phase-separation of homopolymer blends, which is briefly discussed in section 4.1 and 4.2, can provides a route to the fabrication of imprinting stamps with higher throughput and low-cost. The attractiveness of PBL for NIL-based devices (see **Table 4.2**) results from its capacity to generate easily tunable quasi-periodic patterns to aperiodic, disordered ones with unique properties at high throughput and low-cost.[60, 88, 142] Its benefits are therefore well aligned with those provided by NIL. In general, NIL utilizes a high temperature ($\geq$100 °C) for pattern transfer to the underlying film by mechanical deformation.[143, 144] However, the polymers used in section 4.1 and 4.2 to fabricate the PSN exhibit low glass transition temperatures.[64, 145] The direct use of the PSN based on these materials as an imprinting stamp causes in-plane stamp distortions or stress build-up during the cooling cycle.[143, 144] Hence, it affects the pattern fidelity and registration accuracy.

These issues have to be addressed to translate the PBL benefits into a commercially viable NIL manufacturing process.

This section reports the realization of scalable and tunable imprinting stamps for NIL tools through a phase-separation of inorganic–organic hybrid polymer/homopolymer blend. Herein, a UV-cross-linkable inorganic–organic hybrid polymer (OrmoStamp) is used as one of the two components of the polymer blend. Compared with the the polymers used in section 4.1 and 4.2 to fabricate the PSN, OrmoStamp exhibits high thermal stability (up to 270 °C).[146] Furthermore, the values of OrmoStamp modulus of elasticity (650 MPa) and hardness (36 MPa) are sufficient for imprinting of micro-/nano-structures without in-plane stamp distortions.[146] These properties of OrmoStamp are attributed to its chemical composition, which contains Si-oxygen-Si networks connected covalently to the organic backbone.[146] In what follows, this study address the original points listed below:

1. The influence of the deposition conditions and of the PS/OrmoStamp polymer blend formulation (weight ratio of the two polymers in the blend, their concentration and common solvents) on the shape and size of the phase-separated domains, which can be tailored from the micrometer down to the sub-100 nm range at room temperature.

2. The successful implementation of PSN-based imprinting stamps for the R2R NIL system, whereby PSN (made of OrmoStamp) are used as imprinting stamps to nanopattern PS thin films.

Table 4.2. Imprinted functional materials using either hard or soft nano-stamps.

Imprinting stamp	Functional materials	Application/optical materials
Hard material		
—silicon	quantum dots,[147] perovskite [148]	photodetectors
—quartz	transparent polymer[149]	security and authentication
—AAO[a]	UV-curable resin[150]	SERS[b] substrate
—nickel	polystyrene,[134] fluoropolymer film[151]	microfluidic SERS, solar cells
Soft material		
—PDMS	nanocrystal,[152] organometallic assemblies[153]	sensor, memory devices
—perfluoropolyether	nanoparticles, conductive polymer [154]	OLEDs and organic solar cells
—ETFE[c]	conjugated polymer[155]	organic solar cells
—polyurethane acrylate	UV-curable resin[156] and metal oxide[157, 158]	ARC, optical filters
—polycarbonate	ferroelectric polymer[159]	organic electronics
—polyvinylsilazane	polyurethane acrylate resin[160]	optoelectronic devices
—ormostamp	perovskite[133]	solar cells

[a]Anodic aluminum oxide, [b]Surface-enhanced Raman scattering, [c]Ethylene tetrafluoroethylene

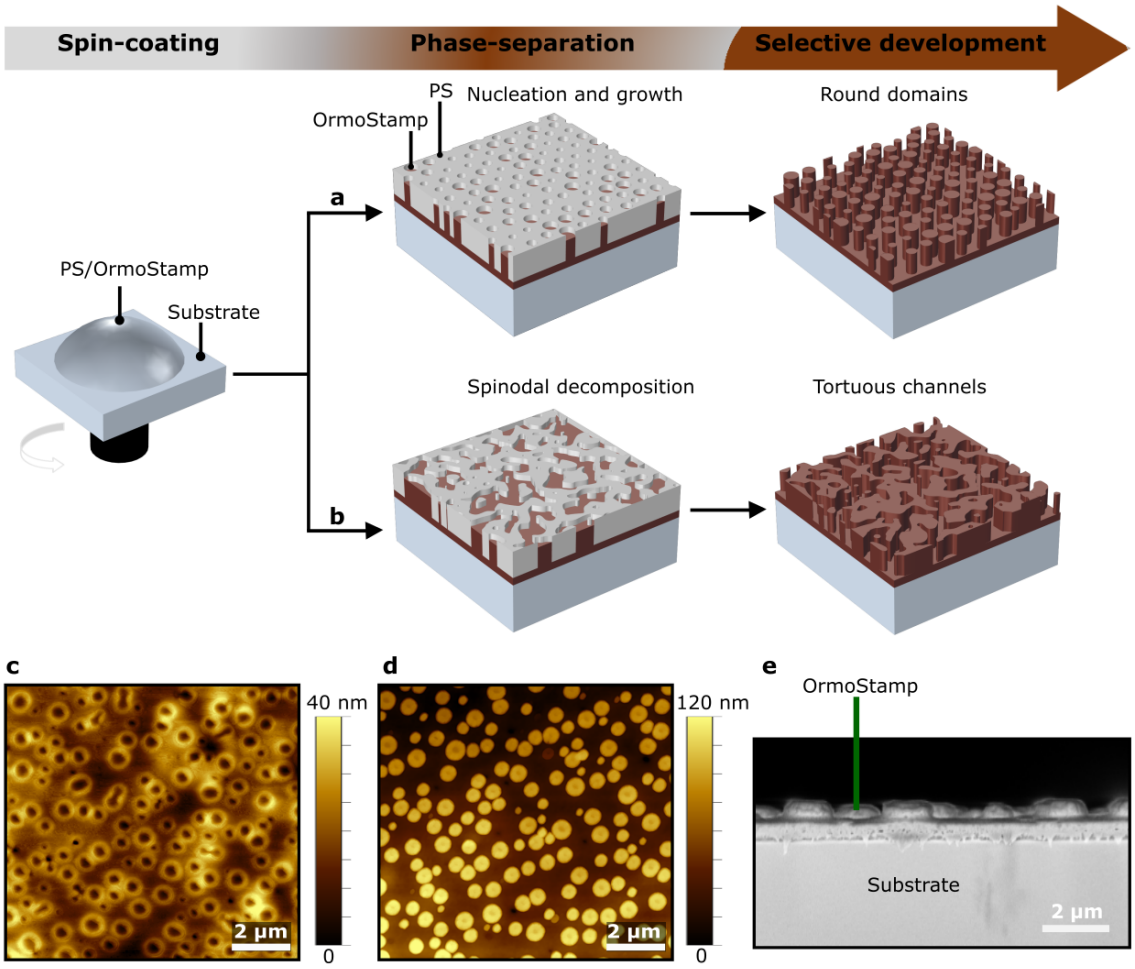

Figure 4.19. PS/OrmoStamp blend enables the direct patterning of OrmoStamp material via PBL. A schematic illustration of the formation of spin-casted PSN via (a) nucleation and growth, and (b) spinodal decomposition mechanism. Afterward, the PS matrix is selectively etched using O_2 plasma treatment. AFM images of the PSN before (c) and after (d) O_2 plasma treatment of a sample prepared using PS/OrmoStamp with a 3:1 ratio in toluene, with a concentration of 35 mg·ml^{-1}. A spin-casting speed of 1500 rpm is used for producing the PSN. The Ormostamp nanopillar top surface is represented by a black color in (c) and with a bright color in (d). (e) Cross-sectional SEM image of the Ormostamp nanopillars in (d). Adapted with permission from Ref.[61], © John Wiley & Sons.

4.3.1 Formation of nano-stamp via PBL

The imprinting stamps based on PSN were fabricated by PBL following the sequence illustrated in **Figure 4.19a,b**. A blend of two immiscible polymers, namely PS (MW=100 kg·mol^{-1}) and OrmoStamp, was spin-coated over substrates in order to achieve phase separation initiated by solvent extraction. After the formation of PSN, the OrmoStamp phase is solidified by UV-initiated crosslinking. This process leads to the formation of a three-dimensional polymer network in OrmoStamp.[141, 146] Thus, it makes the material resistant to O_2 plasma.[141, 146] As a result, the PS/OrmoStamp film was treated using O_2 plasma at an operational power of 100 W, and the O_2 flow rate was fixed at 45 cm^{-3} min (qn). This process allows to selectively remove the PS at etching rate of 50 nm·min^{-1} and thereby obtain PSN made of Or-

moStamp. For inks with a weight ratio of PS/OrmoStamp (3:1) in toluene, PSN are directly formed via N & G and visible after spin-casting, upon solvent evaporation at room temperature (see **Figure 4.19a**). The AFM images of the PSN before (see **Figure 4.19c**) and after (see **Figure 4.19d**) the O_2 plasma treatment, reveal different surface morphology. Before the selective etching of PS (see **Figure 4.19c**), the top surface morphology of the resulting PSN is composed of a continuous matrix with shallow nanoholes. The scale bar in the AFM image reveals an average nanohole depth of 40 nm. After O_2 plasma treatment, nanopillars instead of the nanoholes were observed in the AFM image, as highlighted in **Figure 4.19d**. Thus, it can be concluded that the polymer matrix is made of PS and the nanopillar domains of OrmoStamp. A SEM image of a cut substrate, after O_2 plasma etching of the PS matrix, has demonstrated the tendency of OrmoStamp to form a wetting layer, as highlighted in **Figure 4.19e**. As discussed in the section 4.2, the wetting layer formation is largely related to surface energy difference between the two polymers in a blend, whereby the polymer with the lowest surface energy is enriching the air-polymer interfacial region.[118, 119] Here, the OrmoStamp exhibit lower surface energy ($23\,\mathrm{mN{\cdot}m^{-1}}$[161]) compared to the PS ($40.2\,\mathrm{mN{\cdot}m^{-1}}$[162]). However, the OrmoStamp forms the wetting layer. The result indicate that the difference in surface energy of the two polymers is not the main factor here for the preferential surface enrichment. It might be attributed to the difference in density between OrmoStamp ($\rho = 1.14 \pm 0.01\,\mathrm{g{\cdot}cm^{-3}}$ [163]) and PS ($\rho = 0.97\,\mathrm{g{\cdot}cm^{-3}}$ [164]).

The ability to easily tune the structural parameters of the imprinting stamps is high priority in NIL. The following section demonstrates the versatility of the developed imprinting stamps by tuning the PS/OrmoStamp deposition conditions and the initial mixture recipe.

4.3.2 Tuning the morphology of PBL based nano-stamps

For PS/Ormostamp in toluene, structural parameter (i.e., domain size, height and average inter-distance) control of the resulting OrmoStamp domains can be achieved by tuning the deposition conditions and the polymer blend recipe as discussed in section 4.1 and 4.2 for the PS/PMMA blend. **Figure 4.20** highlights the AFM images of OrmoStamp nanopillars fabricated using different spin-casting speed, concentration and weight-ratio of PS/OrmoStamp in the solution. With an increase in spin-casting speed, finer OrmoStamp nanopillar domains have been observed (see **Figure 4.20a**). Conversely, the increase of the PS weight ratio in PS/OrmoStamp blend (see **Figure 4.20b**) and concentration of the PS/OrmoStamp in the solution (**Figure 4.20c**) lead to an increase in the average diameter of the OrmoStamp nanopillars. The phase separation mechanism and domain coarsening behaviors of polymer blend during spin coating are briefly discussed in section 4.1 including for different spin-casting speed, concentration and weight-ratio of polymers in the solution. The influence of an external environment (e.g., humidity), substrate surface treatment, and molecular weight of the PS on the resulting morphology of PSN based on PS/OrmoStamp are briefly discussed in our work.[165]

Beside tuning in-plane parameters (i.e., domain size, height and average inter-distance) of the OrmoStamp domains by adjusting with the polymer blend recipe and disposition conditions, their shape can be changed. Herein, the shape of the PSN were tuned either by adjusting the weight-ratio of the polymers in the solution or by

changing the common solvent. **Figure 4.21a** shows AFM image of sample fabricated using solution based on higher content of OrmoStamp phase in PS/Ormostamp blend. When the Ormostamp phase exceeds 75% in weight-ratio, an OrmoStamp matrix with nanoholes (see **Figure 4.21a**) is observed instead of OrmoStamp nanopillars (see **Figure 4.20c**). In contrast, changing the common solvent for the polymer blend leads to a drastic change in the surface morphology as highlighted in **Figure 4.21b,c**. The OrmoStamp domains shown in **Figure 4.19d** are modified from round domains to a disordered bicontinuous network (tortuous channels) morphology by switching the blending solvent from toluene to either anisole (see **Figure 4.21b**) or to cyclohexanone (**Figure 4.21c**).

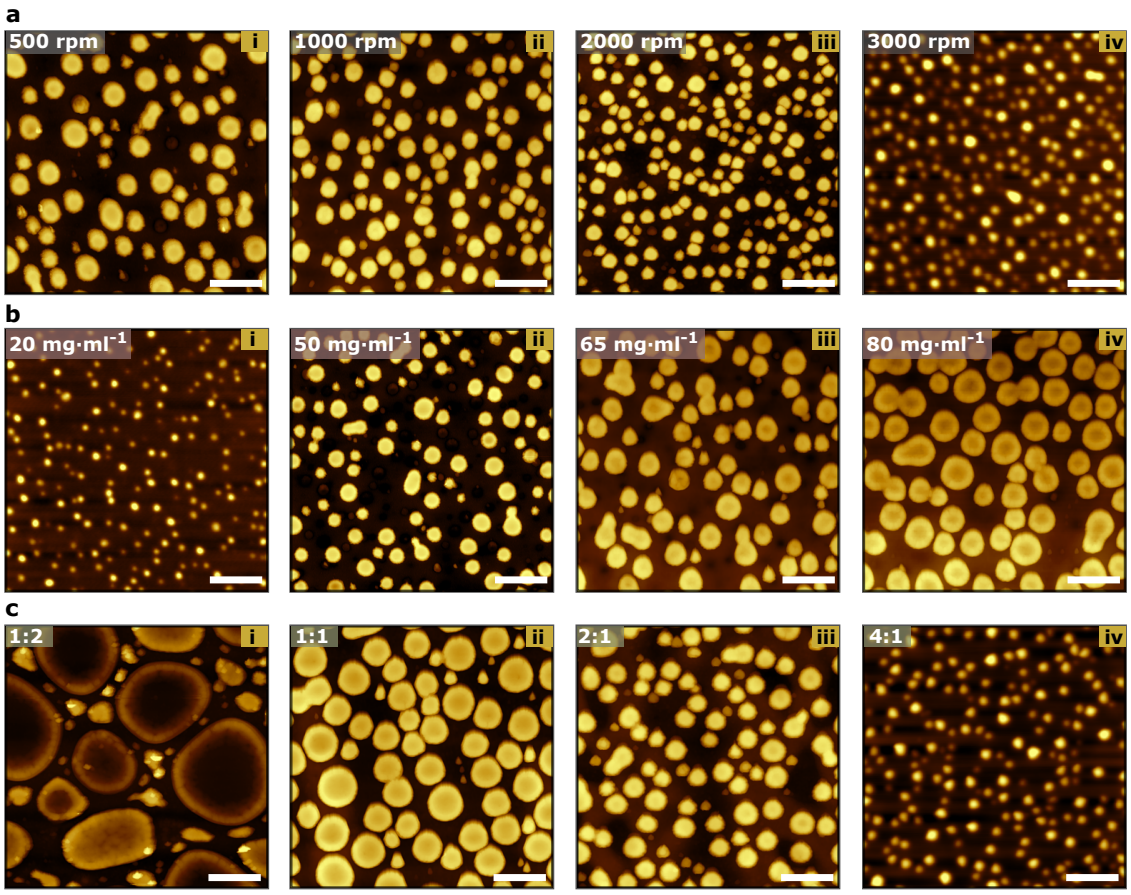

Figure 4.20. Influence of the ink composition and the deposition parameters on the resulting morphology of the PSN. (a) AFM images of Ormostamp nanopillars fabricated using four different spin-casting speeds: (i) 500 rpm, (ii) 1000 rpm (iii) 2000 rpm, and (IV) 3000 rpm. A PS/OrmoStamp=3:1 blend in toluene solvent with a concentration of 35 mg·ml^{-1} was used. (b) AFM images of Ormostamp nanopillars prepared with different concentrations of PS/Ormostamp with a 3:1 weight ratio in toluene: (i) 20 mg·ml^{-1}, (ii) 50 mg·ml^{-1}, (iii) 65 mg·ml^{-1} and (iv) 80 mg·ml^{-1}. A spin-casting speed of 1500 rpm is used to produce the PSN. (c) AFM images of Ormostamp nanopillars prepared with different weight-ratios of PS and OrmoStamp in the blend, PS/OrmoStamp weight ratio: (i) 1:2, (ii) 1:1 (iii) 2:1 and (iv) 4:1. The blends were dissolved in toluene with a concentration of 35 mg·ml^{-1} and spin-casted at 1500 rpm. All AFM images were acquired after the selective etching of the PS matrix using O_2 plasma. The scale bar represents 2 μm in all AFM images. Adapted with permission from Ref.[61], © John Wiley & Sons.

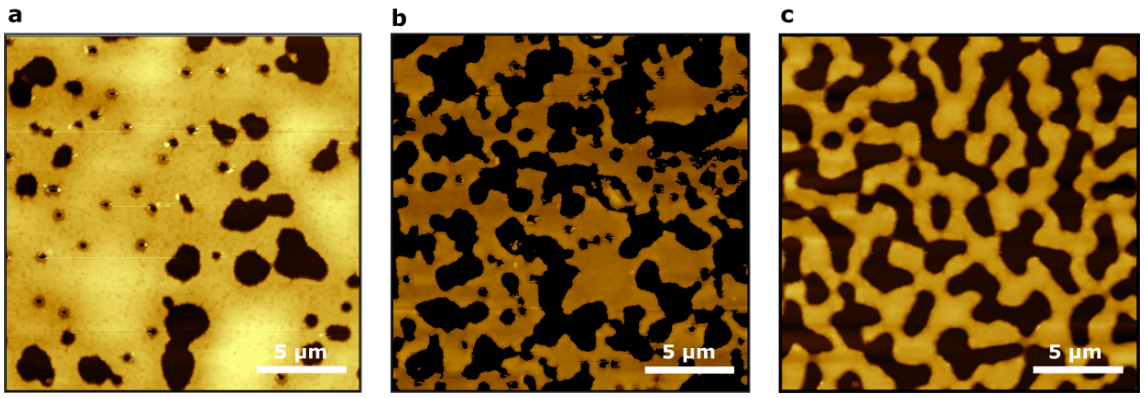

Figure 4.21. PS/OrmoStamp blend enables the formation of PSN with tunable shape. Tuning the shape of the PSN shown in 4.20c by solely switching PS/OrmoStamp weight ratio to 1:3 (a) or by switching the common solvent from toluene to anisole (b) and cyclohexanone (c). Adapted with permission from Ref.[61], © John Wiley & Sons.

The developed PSN, benefit from the properties of Ormostamp, which is a material of choice for an imprinting stamp.[141, 146, 161] Practically, these imprinting stamps can be directly integrated into the respective NIL systems regardless of the imprint contact types (i.e., P2P NIL,[133] R2P NIL,[136] and R2R NIL[134]). This is owing to the implemented fabrication approach, which allows the production of large-area imprinting stamps over a wide variety of substrates, including silicon wafers as large as 4 inches in diameter (**Figure 4.22a**), a semi-flexible polymer (**Figure 4.22b**), and a metal foil (**Figure 4.22c**). Similar PSN morphologies as highlighted in **Figure 4.22d-f** were obtained for samples prepared on various substrates (for a given PS/OrmoStamp blend and for the same spin-casting parameters). These manifold possibilities facilitate the development of imprinted photonic layers for various applications using different NIL systems, one example of which is given in the next section.

4.3.3 PSN enabled roll-to-roll processed nanophotonic polymer films

R2R systems can today produce imprinted thin film layers in the range of 0.2-30 m per min, depending on the structures.[166, 167] Nonetheless, R2R NIL holds much promise in enabling various new applications; their imprinting stamp fabrication is challenging. The challenge is the need for a cylindrical-shaped imprinting stamp. Herein, patterned metal foil mounted onto an imprint roller is used to imprint nanostructures under load onto a flexible substrate placed onto a supporting roller as highlighted in **Figure 4.23a**. **Figure 4.23b-d** displays the photographs of the imprinting stamps along with their corresponding AFM images obtained over metal foils upon a gradual change of the spin-coating speed, and after selectively etching of the PS phase using O_2 plasma. These stamps display different haze and colors arising from spectrally dependent light scattering at the nanopatterend ormostamp with different feature sizes. In an example process, the nanophotonic stamps were integrated into R2R NIL tool to pattern a 120 μm thick PS foil as shown in **Figure 4.23a**. **Figure 4.23e** highlights the AFM image of the imprinted PS film using a stamp shown in **Figure 4.23d**. Full height transfer from the stamp to the PS foil is achieved by using an imprinting temperature close to the glass-transition of the foil

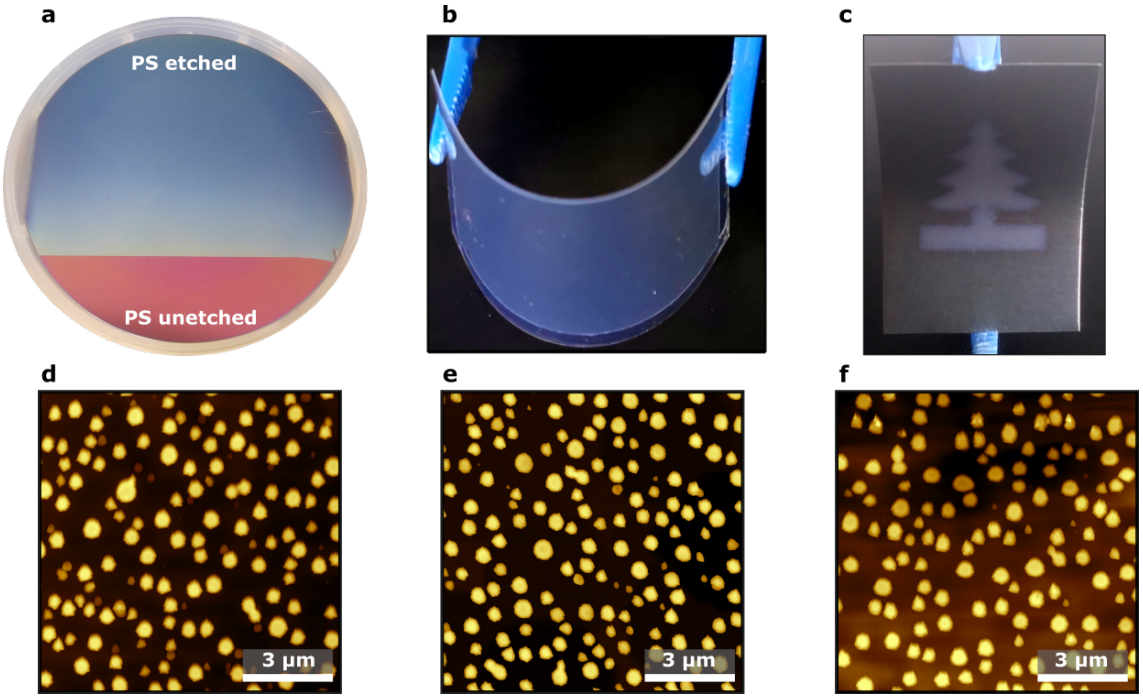

Figure 4.22. Fabrication of PSN using PS/OrmoStamp blend on various substrates. (a) Photograph of 4 inch silicon wafer coated with PS/OrmoStamp blend before and after selectively etching of the PS matrix. The reddish area corresponds to the unetched part. (b) Photograph of a flexible plastic foil (25 mm × 50 mm) made of polyethylene terephthalate and covered with OrmoStamp nanopillars after selective etching of the PS matrix. The blueish appearance is due to the optical scattering. (c) Photograph of a Christmas tree logo on a flexible (stainless steel) metal foil (25 mm × 50 mm) formed by selectively etching the PS matrix in the foil's unmasked area. The samples in (a)-(c) were prepared using the same recipe as in Figure 4.19. AFM images of the PSN on (d) silicon wafer, (e) flexible plastic foil made of polyethylene terephthalate, and (f) flexible metal foil. The AFM images were acquired after the selective etching of the PS matrix. Adapted with permission from Ref.[61], © John Wiley & Sons.

(≈80 °C). Homogeneous imprinting of PS was achieved for a pneumatic cylinders pressure higher than 5 bar. The patterned PS foil can be employed in many-fold optical applications. A typical application area will be in surface-enhanced Raman spectroscopy measurements.[134]

Summing up the results above, the introduced PBL based on OrmoStamp/PS blend enables to easily adapt the morphology of the NIL stamps surface texture. This can be achieved by varying the spin-coating speed, the polymer blend recipe such as weight ratio, concentration or solvent. These manifold possibilities facilitate the development of tunable and scalable nanophotonic stamps over different substrates for patterning photonic materials using NIL. As demonstrations of the envisioned applications, the developed imprinting stamps were integrated into a roll-to-roll NIL system for patterning a PS thin-film. An additional example is given in Chapter 6, whereby PSN (made of OrmoStamp) are used as imprinting stamps to nanopattern a perovskite layer and improve its light absorption capability for photovoltaic applications and light emission properties for light-emitting devices. The PSN made of

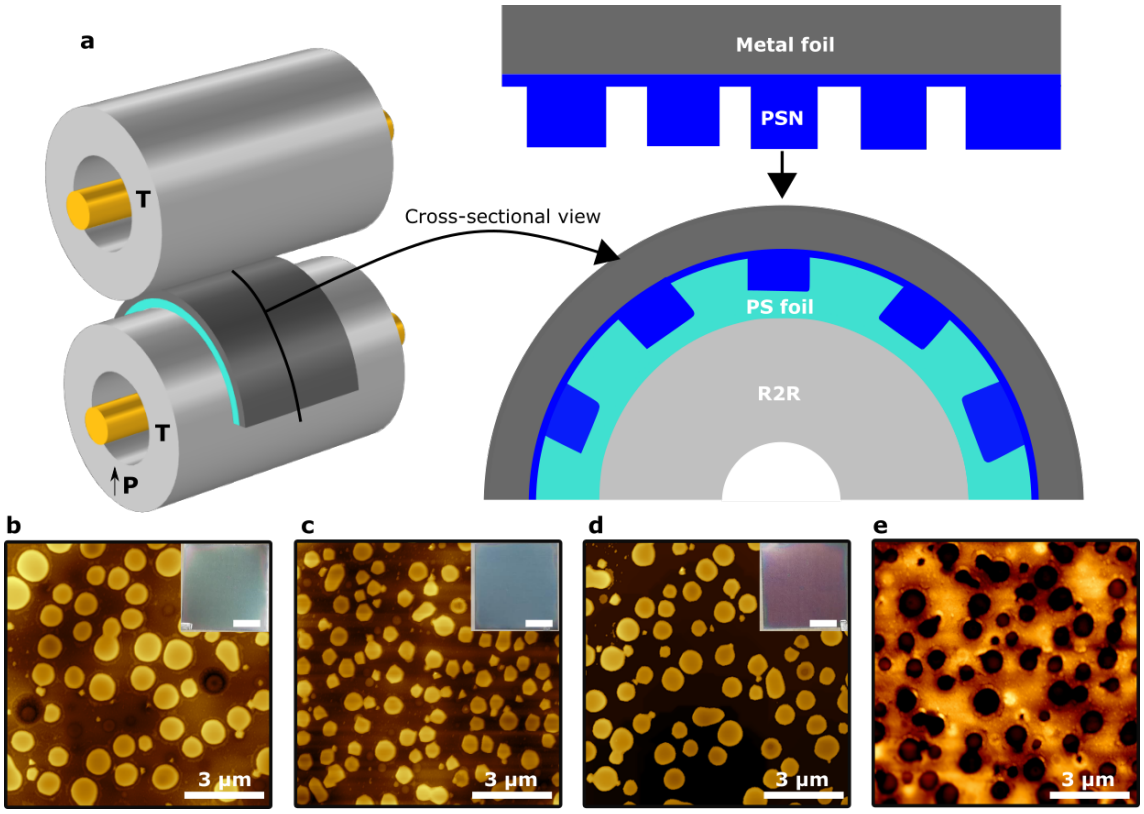

Figure 4.23. Roll-to-roll hot embossing of PS foils using PSN based imprinting stamp. a) Schematic of the R2R hot embossing setup. The lower embossing cylinder carries the imprinting stamp and PS foil, both cylinders are heated, and pressure is applied to the lower cylinder. Controlled motors drive the upper and the lower embossing cylinder to realize a stable imprinting velocity. (b,d) AFM images of imprinting stamps prepared by varying the spin-coating speed. The insets in (b,d) show the photographs of the imprinting stamps, fabricated on a stainless steel foil using PS/OrmoStamp=3:1 with a concentration of 50 mg·ml^{-1}. (e) AFM image of the nano-imprinted PS foil using an imprinting stamp shown in (d). Adapted with permission from Ref.[61], © John Wiley & Sons.

OrmoStamp material can also be applied to many other technologies such as nano-transfer printing (i.e., transferring patterns between substrates by manipulating the adhesion forces between the nanophotonic stamp/functional material and the functional material/substrate) as illustrated in the Ref.[168]. Moreover, the PSN based on Ormostamp materials can be used as biomedical substrate (e.g., to prevent bacterial adhesion as highlighted in Ref.[169] and as light management nanostructures for optoelectronic devices.[89, 91]

4.4 Summary and discussion

Phase-separated nanostructures (PSN) are nowadays used in a myriad of applications as they can spontaneously form functional nanostructures over large areas and be tuned to achieve various morphologies, from completely periodic patterns to structurally disordered ensembles.

Herein, first a stable and reproducible fabrication route is established using spin-coating method for phase-separated disordered nanostructures with tunable char-

acteristics for light management in optoelectronic devices. In this work, tailored disorder is achieved by adjusting the deposition conditions or by tuning the initial polymer blend recipe. In the following chapters, the interest of spin-casted disordered phase-separated nanostructures for improving the light management in light-emitting diodes and thin-film solar cells is addressed. However, the polymer blend deposition methods restricted the incorporation of the phase-separated nanostructures into uniform films and hence only offered a limited control over the location, size or geometry of the patterned areas. The successful transfer of phase separated nanostructures from lab-scale demonstrators into real-world products will depend on the possibility to easily form these micro-/nanostructures over a pre-defined macroscopic design without the need for additional masks and patterning steps.

Next, a digitally printable nanophotonic structures are demonstrated using IJP to overcome the limitations mentioned above. The step from spin-coating towards inkjet printing is a major achievement both from a basic scientific and an application point of view. IJP opens a new world of science and applications as it is a method that allows laterally defined deposition and thus a lateral patterning. Basically all commercially relevant applications rely on a lateral control of device structures and can not be realized by spin-coating. Here, a completely new ink-formulation is established to meet the requirements of this demanding process. The developed IJP based approach has two key advances:

1. phase-separated domains with a scaling from a few μm down to sub-100 nm range, processed on arbitrary substrates and obtained within any pre-determined 2D design without template or mask; and

2. two ways of varying the morphology of the phase-separated micro-/nanostructures during printing, either by adapting the printing resolution from pixel to pixel for a given ink formulation, or by working with multiple inks (using, for example, different PS/PMMA weight ratios).

While this approach was introduced with a homopolymer blend ink, it is also applicable to block co-polymers and biopolymers. Moreover, as this cost-effective method can be readily scaled up to large areas, it will foster the widespread implementation of PSN in nanophotonic applications. The successful implementation of printed PSN for two of the most relevant promising applications: light emitting devices (refer to Chapter 9) and pixelated point-of-care biosensors are highlighted in our work.[60]

Lastly, a completely new ink-formulation consisting of the homopolymer—PS and the inorganic-organic hybrid polymer—OrmoStamp is established to improve PSN practical relevance for nanoimprint lithography. The resulting PSN based on OrmoStamp, owing to the material's nature, exhibit excellent bulk flexibility with mechanical stability. The phase-separated OrmoStamp domains tuned from a few μm down to 100 nm range. The PSN structural parameters were tuned over various substrates through an interplay of the initial polymer blend recipe and process parameter. Upon optimized conditions, the resulting PSN made of Ormostamp were integrated into roll-to-roll nanoimprint lithography system to pattern PS film. Such approach opens the way for large-area roll-to-roll based processing of photonic materials. Thus, it helps to meet the growing interest for photonic materials obtained by

additive manufacturing. As an additional example, light management by nanopatterning of a perovskite semiconductor in plate-to-plate process is demonstrated in Chapter 6.

5. Nanophotonic back reflector for light trapping in thin-film solar cells

In this chapter, a back reflector deposited onto phase-separated nanostructures is proposed as a solution for enhancing the light entrapment in hydrogenated amorphous silicon (a-Si:H) solar cells. In section 5.1, the concept and design of nanophotonic reflectors with tunable optical properties used in this work are explained. In the following section, experimental results of a-Si:H solar cells with nanophotonic reflectors along with benchmark devices are discussed. By coupling optical characterizations with computer modeling in section 5.3, general guidelines for nanophotonic reflector designs are discussed briefly. Finally, the results of this chapter are summarized. Parts of the results presented in this chapter have previously been published in the journal of Nanoscale.[89]

In a thin film absorber with a back reflector, incompletely absorbed light can reflect off each interface several times, making multiple passes through the semiconductor as in a Fabry-Perot cavity.[170] When nanostructures are introduced, however, the absorption in the film will depend on many effects such as scattering, localized modes, and guided modes, which significantly modify both the magnitude and the location of absorption within the thickness of the device.[57, 171] In this study, nanostructured reflective electrodes are introduced into thin film hydrogenated amorphous silicon (a-Si:H) solar cells (see **Figure 5.1**) to couple light into in plane waveguide modes of the thin a-Si:H layer, thereby increasing photon absorption at energies just above the a-Si:H band-gap.[172] This optical absorption enhancement, in turn, allows for decreasing the a-Si:H layer thickness, and hence lowering material costs. Besides, it can lead to higher conversion efficiencies as a thinner a-Si:H layer offers improved conditions for carrier collection, potentially a higher open-circuit voltage.[173, 174]

To date, nanostructured back reflectors with widely varying morphologies have been developed by using e-beam lithography,[175] colloidal lithography,[173] and spontaneous self-assembly approaches.[7, 176–178] Owing to its large area patterning compatibility and tunable geometries, the spontaneous self-assembly approach was widely employed as a method for the fabrication of scattering nanostructures. For example, the efficiency of n-i-p a-Si:H solar cells was significantly enhanced compared to

state-of-the-art random textures by incorporating self-assembled silver nanoparticles in a plasmonic back reflector configuration.[7] However, it is not easy to tune the structural parameters (i.e., size, inter-distance, shape, and thickness) of the nanostructures obtained with this approach. As a result, it is challenging to obtain an optimal optical scattering at the spectral regions of interest. Also, the light scatterers suffer from significant parasitic absorption losses due to their irregular contour profiles,[7, 176–178] hampering the ultimate efficiency gain they can provide. Furthermore, the high temperature (400–500 °C) required for the annealing step negatively impacts such solar cells' fabrication costs and limits their application.[173] This issue calls for alternative patterning approaches that can be implemented at room temperature, without requiring an e-beam lithography or a dry etching step, and that can provide proper control over the morphology of the scattering nanostructure.

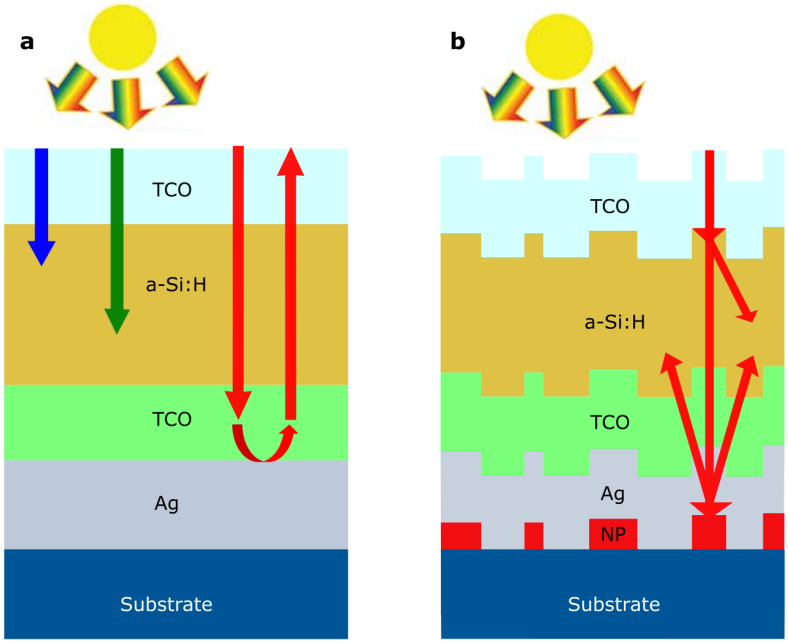

Figure 5.1. Schematic view of light scattering by planar and nanostructured reflective electrode layer of a-Si:H solar cells. The a-Si:H solar cell stack, deposited on the (a) planar and (b) nanopillar (NP) array, consists of an Ag back reflector, a rear transparent and conductive oxide (TCO) layer, an a-Si:H n-i-p type active layer, and a front TCO layer. Light trapping in (b), where the cell's surface is structured to guide incident light, as an electromagnetic wave, inside the solar cell.

In this study, a fabrication route that can satisfy all the requirements mentioned earlier is introduced. The proposed approach exploits the up-scalable polymer blend lithography technique. To this end, the study make use of phase-separated nanostructures (PSNs) discussed in Chapter 4. Onto these patterns, silver (Ag) is evaporated thereby leading to scattering back reflective electrodes. This work show that the phase-separation process enables to tune the morphology of the scattering nanostructures easily and to obtain regular and smooth surface profiles. These characteristics result in excellent light-scattering properties and limit parasitic absorption in the devices, which is a significant advantage compared to commercial randomly textured substrates. Moreover, absorption losses are analyzed in-depth using optical simulations performed on a realistic 3D model built from the measured

scattering reflectors profile. I also numerically investigate the influence of the main scattering layer geometrical parameters on the solar cells' overall absorption and derive general rules to design efficient light scattering back reflectors. It should be noted that Hubert *et al.* (2020) extended the approach developed here for silicon-based tandem solar cells to enhance their infrared response.[179] Thus, highlighting the potential of the developed approach for other photovoltaic technologies.

5.1 Design of nanophotonic back reflector

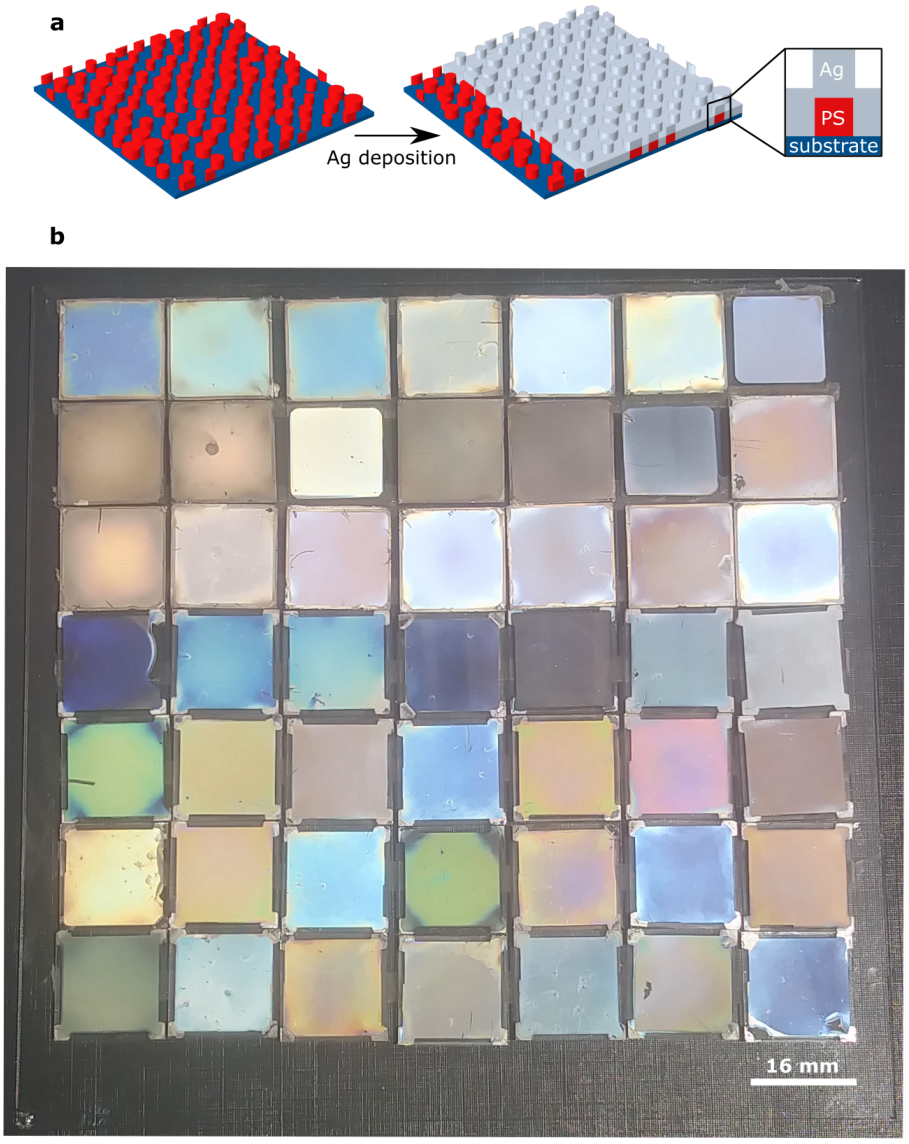

Figure 5.2. Light scattering back electrode fabrication via polymer blend lithography. (a) Phase-separated polystyrene (PS) NPs on a substrate after the selective development of the PMMA matrix. Followed by the deposition of Ag onto the PS NPs. (b) Photographs of Ag coated samples with different PS NPs densities and lateral size, fabricated following the route (a).

The light scattering back reflectors (SBR) were obtained by conformal deposition of a 200 nm thick Ag film onto the PSNs, as illustrated in **Figure 5.2a**. **Figure 5.2b** displays the photographs such SBR prepared using PSNs with different morphology.

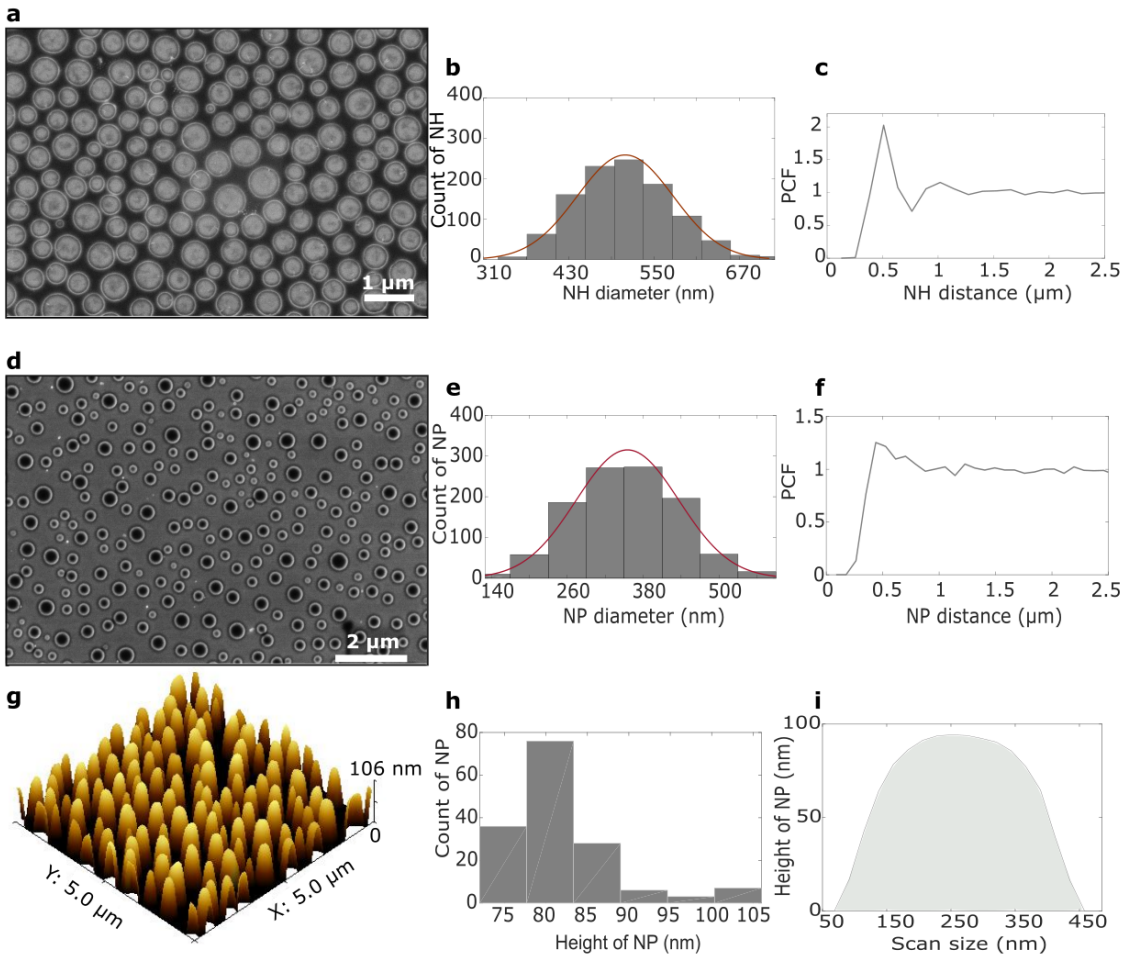

Figure 5.3. Topographical characterization of the disordered NH and NP array. (a) SEM top-view image of the disordered and uniformly distributed NHs. The diameter size distribution and pair correlation function (PCF) of this array are reported in (b) and (c), respectively. (d) SEM top-view image of the PS NP array. The diameter size distribution and PCF of this array are reported in (e) and (f), respectively. The solid red line in (c) and (f) represents Gaussian fit. The height distribution within the NP array can be appreciated in the $5\,\mu$m $\times$ $5\,\mu$m AFM image in (g) and analyzed in more detail (h). A single NP vertical profile is measured in (i) and emphasizes a smooth transition from base to apex. Both SEM and AFM images are representative of the whole patterned surface (5 cm $\times$ 5 cm). Adapted from Ref.[89] with permission from the Royal Society of Chemistry.

By changing the polymer blend recipe (for details, please refer to Chapter 4) and keeping the Ag layer thickness at 200 nm, the SBR reflection peak wavelength can be modulated, as highlighted in **Figure 5.2b**. The morphology of the nanohole (NH) and nanopillar (NP) array leading to the best light-trapping properties in a-Si:H solar cell (refer to section 5.2) were experimentally analyzed (see **Figure 5.3a-f**). The scanning electron microscopy (SEM) images displayed in **Figure 5.3a**,**d** gives a qualitative impression of the NHs and NPs self-organization. The SEM topographies have also been analyzed to assess the nanostructures' size distribution and periodicity by extracting the area-weighted base radius and the pair correlation function (radial distribution[120]). The NPs and NHs diameter size distribution are reported

in **Figure 5.3b**,**e** for the selected configuration, respectively. It can be concluded that they follow a Gaussian distribution, with a mean diameter of 357 nm (NP configuration) and 510 nm (NH configuration). The calculated mean surface coverage (SC) is 30% for NP and 50% for NH configuration. The nearest neighbor peak (average periodicity) for both configurations is around 0.5 μm on the deduced pair correlation function shown in **Figure 5.3c**,**f**, indicative of short-range order. From an AFM image of the NP array (see **Figure 5.3g**), an average NP height of 80 nm (**Figure 5.3h**) is calculated. Thus, it leads to a mean aspect ratio (height/diameter) of around 0.22, and such a moderate value promotes high-quality layers on top of the patterned substrate (refer to section 5.2). The NP also exhibits a smooth transition from the base to its apex, as highlighted in **Figure 5.3i**, and as will be discussed in the following, it is free from sharp edges responsible for high parasitic absorption losses.[180, 181]

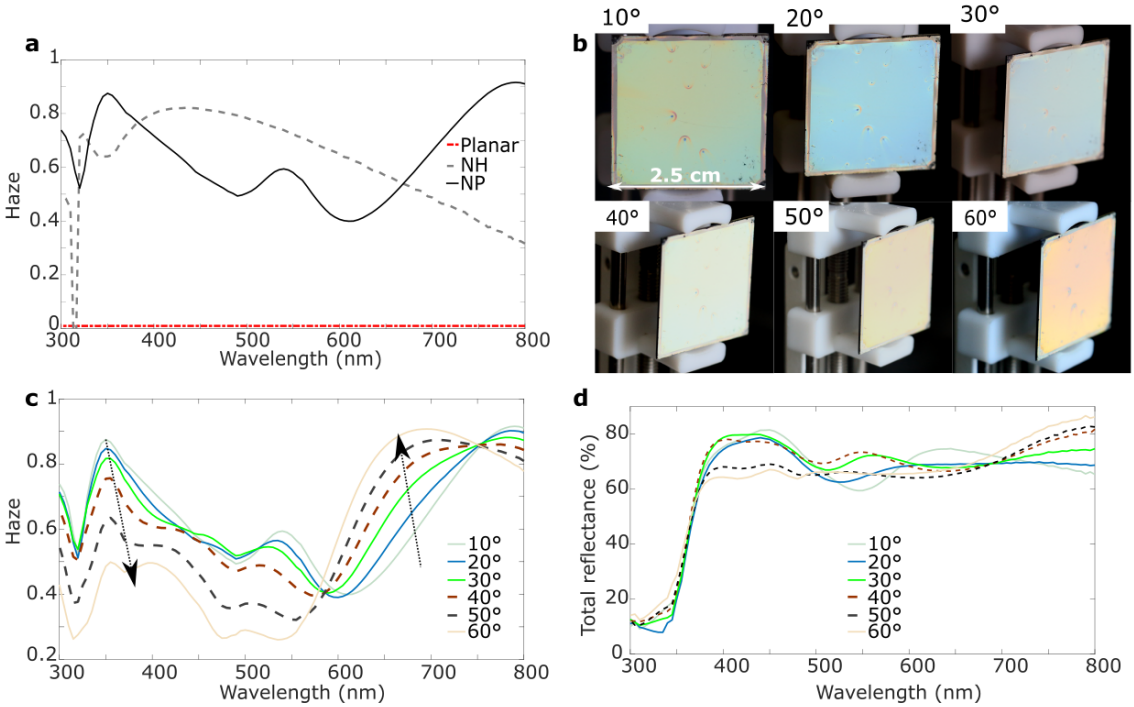

Figure 5.4. Light scattering properties of the patterned back reflectors. (a) Measured haze spectra from a planar Ag/Zno:Al layer, and Ag/Zno:Al layer processed ontop of NH and NP array over the visible spectrum (under close to normal incidence). (b) Photographs of the patterned reflectors taken under varying incidence angles after the Ag and ZnO:Al deposition layers on top of the NP array. (c) Corresponding haze spectra showing a high scattering coefficient above 600 nm. The arrows follow the increase of the angle of incidence. (d) Total reflectance of the scattering back reflectors. Adapted from Ref.[89] with permission from the Royal Society of Chemistry.

The haze (defined as the diffused fraction of the overall reflected light) usually characterizes the light-scattering properties of the SBRs and is correlated with the light trapping capacity of solar cells. The samples' haze was measured as function of the wavelength from 300 nm to 800 nm using a PerkinElmer Lambda 1050 spectrophotometer with an integrating sphere. Experimental details of the measurements can be found in Chapter 3. As shown in **Figure 5.4a**, the flat back reflector's haze pa-

rameter is zero, as expected. The scattering layer based on NPs has the highest haze values in the weak absorption regime of an a-Si:H active layer, which implies that the scattering layer's shape is an essential factor in reaching the appropriate light scattering regime.[182–185] A promising approach for increasing the light-trapping efficiency in a-Si:H solar cell devices is to design a nanopatterned back reflector that allows a proper scattering of the incoming light, regardless of the incidence angle. Consequently, the reflection spectra of the scattering layer based on NPs have been experimentally studied under various incidence angles. **Figure 5.4b** gathers photographs of the patterned reflectors for viewing angles ranging from 10° to 60°, and the corresponding reflectance spectra are shown in **Figure 5.4c,d**. Irrespective of the illumination condition, high reflectance is measured for the NP-based scattering reflectors (65% on average between 400 nm and 800 nm, see **Figure 5.4d**). Combined with the broadband peak measured above 600 nm (maximum value exceeding 85%) as shown in (see **Figure 5.4c**), the NP-based scattering layer can provide efficient light trapping over a broad spectral range.

To directly assess the NP and NH-based backscattering layer's light-trapping potential under realistic conditions, devices were subsequently fabricated according to the layout introduced in **Figure 5.1**.

5.2 Nanophotonic back reflector-based a-Si:H solar cells

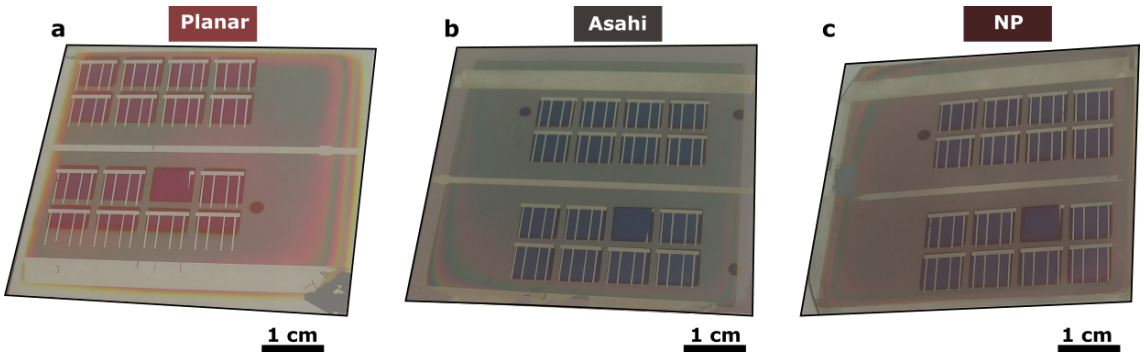

Figure 5.5. Photographs of a-Si:H solar cells prepared over various substrates. Images of the a-Si:H solar cells processed atop the planar glass (a), the state-of-the-art randomly textured Asahi substrates (b), and the disordered phase-separated NP array. The solar cells in (b) and (c) demonstrate the high absorption properties with respect to the planar device.

The light-trapping capability of solar cells based on disordered NP and NH array is evaluated by comparison with devices processed on the top of planar reflectors, and state-of-the-art randomly textured Asahi substrates.[186, 187] More precisely, the Ag layer and ZnO:Al buffer layer were sputtered onto a planar substrate, onto the disordered NP and NH array, and onto glass substrates covered with an as-grown textured, SnO_2:F layer, provided by the Asahi Glass Company. On top of this a-Si:H layers were prepared in an n-i-p deposition sequence by plasma-enhanced chemical vapor deposition (for details, refer to Ref.[47]). A hydrogenated indium oxide (IOH) layer with 5 mm × 5 mm pads was then deposited through a contact mask to define the solar cell active areas. Lastly, a ZnO:Al layer was used as a capping layer. The fabrication of the solar cells was finalized by evaporating Ag grids with a finger

width of around 100 μm, periods in the mm range, and a finger thickness of 700 nm. All the devices were annealed at 160 °C for 30 minutes to improve their electrical performance. One sample consisted of 16 solar cells, each with an active area of 5 mm × 5 mm, as shown in **Figure 5.5** photographs. The optical images in **Figure 5.5** highlight the solar cells' darkish appearance processed on patterned substrates due to enhanced light trapping compared to the unpatterned solar cell.

5.2.1 a-Si:H solar cells atop of nanohole array

In **Figure 5.6a,b**, the cross-sectional SEM images made using focused ion beam (FIB) milling of the solar PV stack grown on the NH array and Asahi substrate are shown. All devices' light-harvesting properties were evaluated by measuring the overall PV stacks' absorption spectra (see Figure **Figure 5.6c**). For wavelengths (λ) above 620 nm, the absorption of the solar cell deposited on NH based back reflector is significantly enhanced with respect to a solar cell equipped with a planar reflector. **Figure 5.6c** also shows the absorption within the "Asahi" solar cell stack, which overcomes the "NH" configuration over almost the whole spectral range considered.

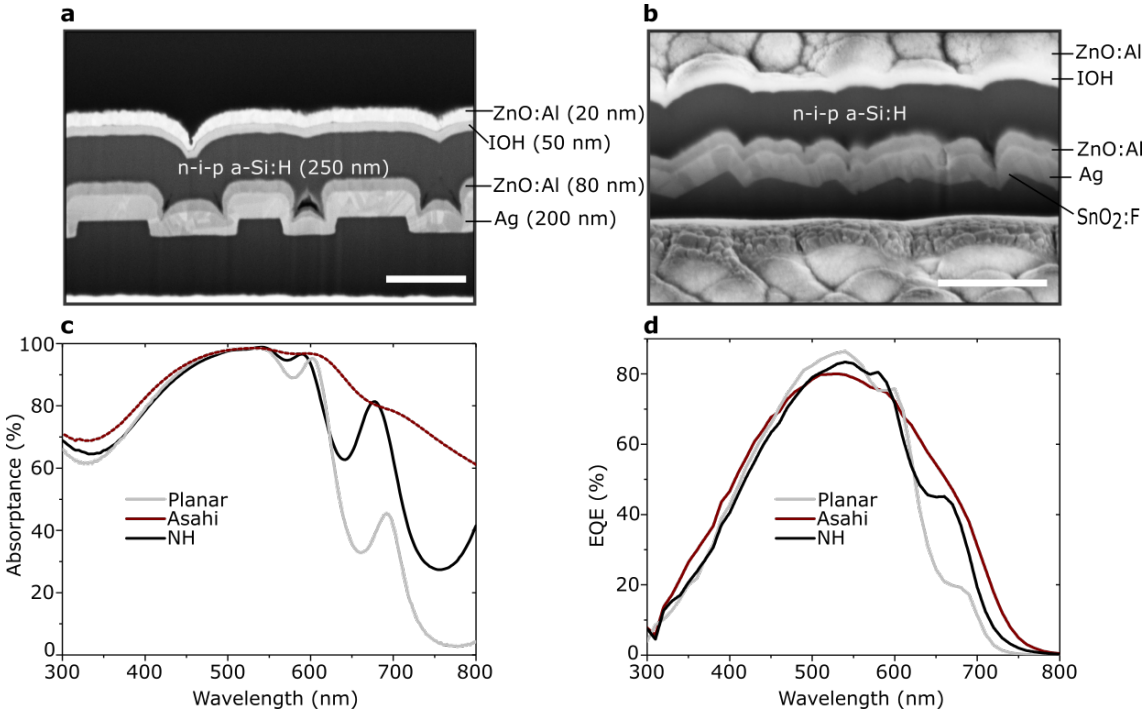

Figure 5.6. Improved light-harvesting properties of thin-film solar cells integrating the scattering NH array. SEM cross-sections of (a) the a-Si:H solar cell deposited on the substrate with NH array ("NH") and of (b) a similar thin-film stack processed atop the Asahi substrates ("Asahi"). The scale bar represents 500 nm. (c) Absorptance spectrum of the solar cell based on the "NH" design, benchmarked against "Asahi" type devices and equivalent but planar solar cells ("Planar"). The improved light trapping properties of the "NH" configuration translates into a substantial increase of its external quantum efficiency (EQE) above 600 nm, as shown in (d). All spectra were acquired under close to normal incidence. Adapted from Ref.[89] with permission from the Royal Society of Chemistry.

The external quantum efficiency (EQE) spectra were acquired (see **Figure 5.6d**) to

separate the parasitic and useful absorption, i.e., the optical absorption that translates for the generation and collection of charge carriers. The NH-based reflector enables the increase of EQE over a wavelength of larger than 620 nm thanks to its light scattering properties and to its topography that allows capitalizing on most of the absorption gains. Additionally, it can be observed that the "Asahi" design yields the best EQE in this spectral range. Compared to the planar design, the scattering NHs, and "Asahi" design improve the short-circuit current density (J_{SC}) by ≈21.8% and ≈24.5% (relative values), respectively. Even though solar cell deposited on the "NH" design exhibits improved light trapping, the light trapping is not competitive with the state-of-the-art texture-based devices. This is due to the NH-based light scattering layer's low haze values over a $\lambda \geq$670 nm (refer to **Figure 5.4a**). Thus, the NP array-based light scattering layer (which exhibits strong light scattering properties over $\lambda \geq$670 nm) has been utilized in the following section to enhance the performance of PSNs based solar cells performance.

5.2.2 a-Si:H solar cells atop of nanopillar array

Figure 5.7a shows a cross-sectional SEM image of a solar cell fabricated on top of the NP-based back reflector. The characteristics absorption spectra and EQE spectra curves of all three types of devices (i.e., "Planar", "Asahi", and "NP") are shown in **Figure 5.7b** and **c**, respectively. With the "NP" design, a significant absorption increase is achieved over almost the whole spectral range relative to the "planar" design. Below 450 nm, the "NP" design's significant absorptance gain originates from the strong parasitic absorption in the corrugated front layers (IOH and ZnO:Al, see inset image in **Figure 5.7a**). As a result, the planar device EQE configuration dominates or equals those obtained with the patterned devices at these wavelengths, as highlighted in **Figure 5.7c**. At wavelengths longer than 600 nm, there is a dramatic increase in the EQE of the "NP" solar cell assisted by the light scattering NPs with respect to the "Planar" one. Unlike periodic diffraction gratings, which introduce a limited set of new EQE peaks,[183] the disordered NPs efficiently scatter light over an extended spectral range. **Figure 5.7c** also shows the superior light utilization of the "NP" based devices compared to solar cells fabricated on top of the commercial Asahi substrates. The optical improvement is achieved by limiting the amount of parasitic absorption compared to the "Asahi" counterpart. More precisely, the regularly shaped NP scatterers exhibit negligible parasitic absorption losses (for details, refer to section 5.3) and are therefore desired for solar PV applications. Furthermore, the Asahi texture incorporates sharp-edged nano-features, which create undesired local thickness inhomogeneities (see **Figure 5.6b**) and, in turn, potential electrical shorts. However, the NPs smooth and low aspect ratio profile leads to functional and reproducible devices with improved efficiency compared to the "Asahi" configuration.

Table 5.1. Influence of the reflector design on the J_{SC}, V_{OC}, FF, and the power conversion efficiency (η) of the a-Si:H solar cells.

Reflector design	J_{SC} [mA/cm^2]	V_{OC} [mV]	FF [%]	η [%]
Planar	10.2	873	51.9	4.6
Asahi	12.7	900	64.4	7.3
NP	13.6	901	62.3	7.6

The performance data of the three types of solar cells are summarized in **Table 5.1**. They were derived by averaging the values of the 16 devices shown in **Figure 5.5**.

The standard deviation of the efficiency measured on a single substrate is 0.5% for the "Asahi" based devices and 0.1% for the "NP" and "Planar" based solar cells. The "NP" based solar cell lead to a +34% and +7% photocurrent improvement compared to "Planar" and "Asahi" based devices, respectively. The photocurrent improvement in the "NP" based solar cell is achieved without degrading the filling factor (FF) and open-circuit voltage (V_{OC}) of the device. Compared to the planar devices, the scattering NPs improves the V_{OC} and FF of the "NP" cells, whereby the higher FF could be the consequence of an increased conductivity of the nanostructured ZnO:Al layers.[7] This property ultimately results in a power-conversion efficiency enhancement of +4% and +65%, compared to devices deposited atop an Asahi substrate and a flat substrate, respectively. This gain is analyzed by simulating the complete solar cell in the next section using the so-called "growth model", accounting for the exact nano-corrugation at all interfaces. These complementary numerical results allow us to investigate the light distribution within the solar cell stacks (i.e., the different optical loss channels are quantified). Hence, to derive general rules for the design of efficient light scattering disordered NP array for a-Si:H solar cell.

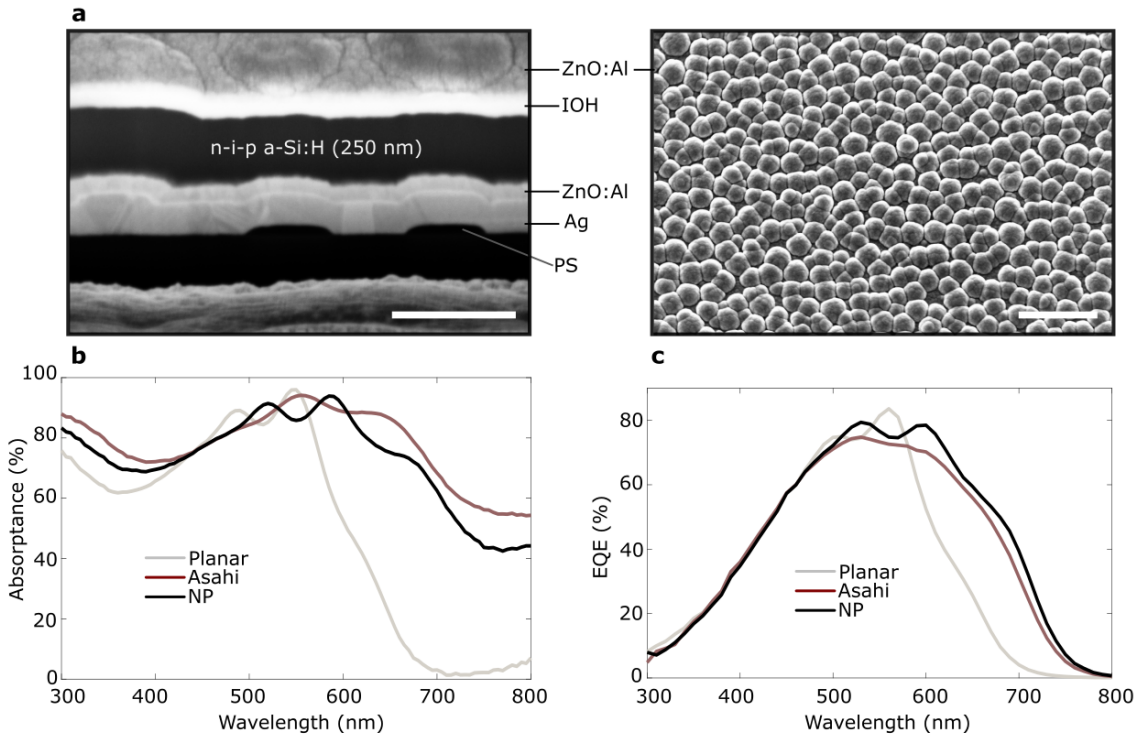

Figure 5.7. Improved light-harvesting properties of thin-film solar cells integrating the scattering NP array. (a) SEM cross-sections of the a-Si:H solar cell deposited on the substrates with NP array ("NP"). The scale bar represents 500 nm. The SEM top-view image of the front side (ZnO:Al layer) of the solar cells are shown as an inset. The scale bar in the inset represents 2 μm. (b) Absorptance spectrum of the solar cell based on the "NP" design, benchmarked against "Asahi" type devices and equivalent but planar solar cells ("Planar"). The improved light trapping properties of the "NP" configuration translates into a substantial increase of its external quantum efficiency (EQE) above 600 nm, as shown in (d). All spectra were acquired under close to normal incidence. Adapted from Ref.[89] with permission from the Royal Society of Chemistry.

5.3 Optical modelling of nanophotonic a-Si:H solar cells

The thin-film solar cells' optical properties were simulated by the finite element method (FEM) available in COMSOL Multiphysics version 5.2a,[188] with a rendered a-Si:H/ZnO:Al/Ag interface that is an approximation to the experimental back reflector geometry as found in **Figure 5.7a**. The developed 3D model illustrated in **Figure 5.8a** consists of a supercell integrating 124 disordered NPs to compute statistically relevant optical properties. It was obtained by first extracting, using AFM, the topology of 124 phase-separated NPs (**Figure 5.3g**). I slightly modified this topology to impose continuity at the simulation window's boundaries (periodic boundary conditions in the horizontal plane). The exact morphology of the different interfaces in the solar cell stacks was reproduced in the 3D FEM model using the growth model described in Ref.[189], which exploits the surface morphology of the NPs and the layer thickness as input data. The FEM computation performed using a lateral simulation window of 5 μm by 5 μm with a spatial grid of $\lambda/10$. The selected simulation window size is sufficiently large to ensure the convergence of the results.[190] Moreover, a perfectly matched layer was introduced on the top of the simulation window to avoid reflecting the backward propagating light to the simulated stack.

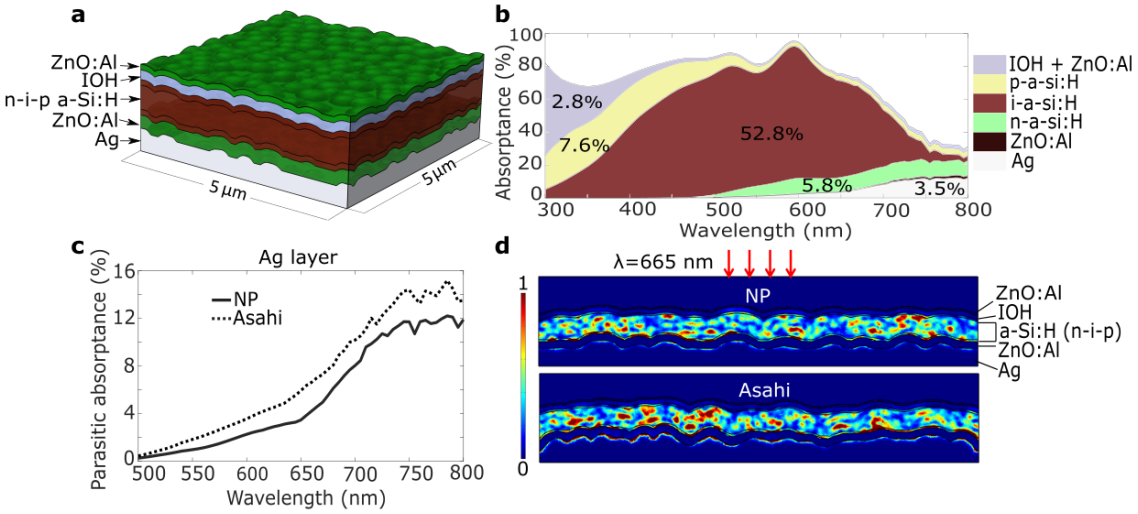

Figure 5.8. Numerical analysis of the parasitic absorption effects in the patterned solar cells (a) 3D model developed to accurately compute the optical properties of the a-Si:H solar cells integrating the disordered NP array with a mean diameter of 357 nm, SC of 30% and average height of 80 nm. These parameters corresponds to the fabricated structure shown in Figure 5.3. (b) Distribution of the absorptance in the different layers of the PV stack shown in (a). The reported values correspond to the integrated absorptance for each layer. (c) Comparison of the Ag reflector's parasitic absorption between solar cells based on the NP and the Asahi designs (in the 500-800 nm range). (d) Normalized electromagnetic power loss density simulated in the NP- and Asahi-based solar cells at λ=665 nm (cross-section views). All the simulations are performed under normal incident light. Adapted from Ref.[89] with permission from the Royal Society of Chemistry.

Figure 5.8b gives an overview of the absorptance in the different layers of the 3D model considered. The overall spectral shape corresponds well to the measured spectral response data (see **Figure 5.7b**), reproducing the predominant spectral peaks

and shoulders, indicating that the optical absorption model is reasonable for comparison to the experimental data. It is evident from **Figure 5.8b** that high parasitic absorption losses take place in the front layers (ZnO:Al, IOH, and p-a-Si:H) at short wavelengths. These optical losses account for 24% of the overall spectrally weighted absorptance between 300 nm and 500 nm. In this wavelength range, the optical losses can be overcome by tuning the disordered NPs average period, as discussed in Chapter 7. Above 500 nm, the primary optical losses are in the rear layers (mainly n-a-Si:H and Ag). In particular, the Ag reflector's parasitic absorption becomes increasingly detrimental towards the a-Si:H optical bandgap. To gain further insights into the impact of these optical losses, I also computed the parasitic absorption stemming from the reflector integrated into the "Asahi" type solar cells (see **Figure 5.8c**). A comparison of the optical losses in the "NP" and "Asahi" back contact shows that the losses are higher for the "Asahi" back contact. The low parasitics absorption in the "NP" device is due to the NP improved regularity (in-plane) contour profile. As highlighted in **Figure 5.3i**, the NP profile is free from sharp edges responsible for high parasitic absorption losses. Besides, Asahi substrates exhibit a higher average peak-to-peak height of the nano-features (up to 200 nm) compared to the mean NP height of 80 nm. This effect can also be visualized in **Figure 5.8d**, which illustrates the cross-sectional view of the normalized electromagnetic power density inside each layer of the a-Si:H solar cells for a normally incident plane wave at λ=665 nm. Herein, λ=665 nm corresponds to a wavelength for which Asahi-based solar cells possess a much higher absorptance but a lower EQE value than NP-based devices (see **Figure 5.7b-c**). In **Figure 5.8d**, the Ag layer has a higher power density for the Asahi texture than the NP case, and this implies a more significant parasitic absorption for the former, which again advocates using the scattering NPs possessing a low surface roughness and a smooth profile.

Finally, I investigated the NP design's robustness following a variation of the NP mean height or SC. The NP design was realized numerically in order to modify only one parameter at once. To generate the different designs, I modified the measured AFM data (i.e., the height and diameter sizes of the NPs) shown in **Figure 5.3g** using the Gwyddion software package,[191] while maintaining the same correlation length (scattering centers) for each configuration. As a merit figure, I calculated the solar cell stacks' EQE by multiplying the polarization-averaged absorption efficiency of the sole i-a-Si:H layer by internal quantum efficiency (IQE). Herein, I assumed a 100% IQE. This approach is a widely adopted standard method for determining the EQE from a simulated thin-film solar cell.[172, 192]

5.3.1 Influence of the NP height

The generated configurations with different heights of NPs are displayed in **Figure 5.9**, along with the corresponding front side textures of the solar cell stack grown on top (i.e., the capping ZnO:Al layer). The measured mean NP height (value of 80 nm) was varied from (50 nm) to (130 nm), see **Figure 5.9a-c**. The NP's increased mean height increased the front side nanotextured ZnO:Al surface coverage, as highlighted in **Figure 5.9d-f**. **Figure 5.10a** depicts the NP array with the different mean heights in the simulated solar cells' cross-section view. **Figure 5.10b** highlights that the overall absorbed light decreases as the NP's mean height increases to 130 nm, or decreases to 50 nm from the experimentally optimized value of 80 nm.

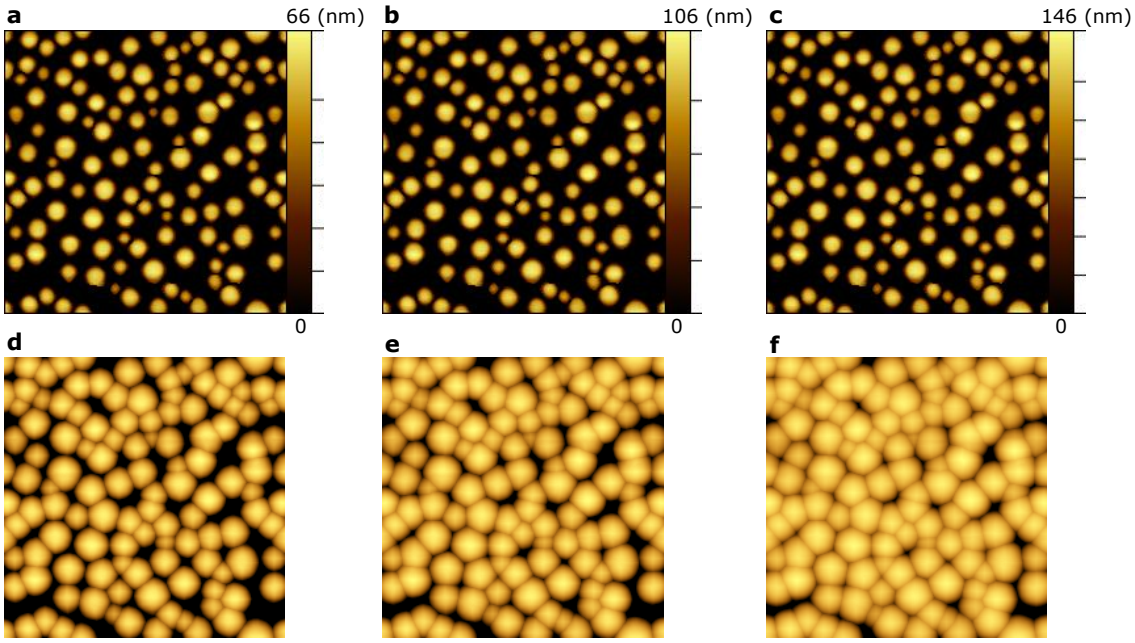

Figure 5.9. Surface morphology of the front side texture of the a-Si:H solar cell simulated by growth model for different NP heights. (a)-(c) Texture of the PS NPs derived from AFM measurements. The profiles shown in (a) and (c) are generated by down- or up-scaling the measured profile displayed in (b). The corresponding front side textures (ZnO:Al layer exposed) are subsequently modeled and shown in (d)-(f). Adapted from Ref.[89] with permission from the Royal Society of Chemistry.

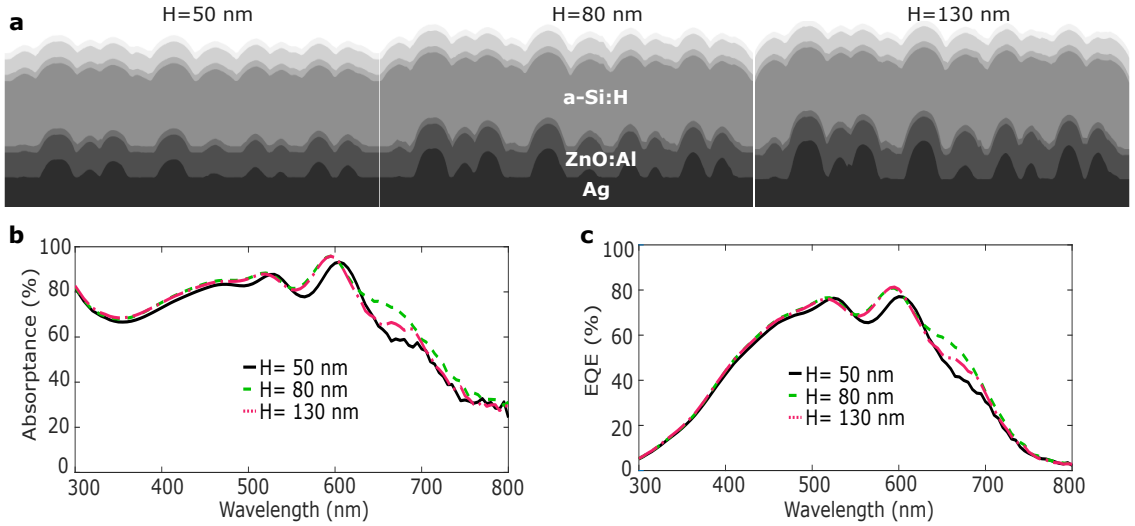

Figure 5.10. Simulated optical properties of the a-Si:H solar cells with increasing NP heights. (a) Cross-sectional view of the simulated solar cells deposited on the NPs with a mean height (H) of 50 nm, 80 nm, and 130 nm. The overall absorptance spectra (b) and EQE (c) of the complete solar cell stack depicted in Figure 5.8a are simulated as a function of the NP mean height *H*. A normal incidence of the light was considered in all the simulations. Adapted from Ref.[89] with permission from the Royal Society of Chemistry.

For the smallest mean NP height, both the overall absorptance (**Figure 5.10b**) and the EQE spectra (see **Figure 5.10c**) of the solar cells are negatively impacted. The

integrated absorption (IA) value, calculated in the sole intrinsic a-Si:H layer, drops from 52.8% to 49.9%. Inversely, for a mean NP height of 130 nm, the front side texture is not dramatically affected, and hence the overall absorptance and EQE spectra are nearly untouched. The weaker response between 600-700 nm leads to a reduced IA of 51.6% in the i-a-Si:H layer, which is less severe than for the lowest NP mean height. The results indicate that the nanopillars' profile does influence the absorption efficiency, and the mean nanopillar's height should be carefully adjusted to retrieve the most benefits from the light-trapping reflector.

5.3.2 Influence of the NP surface coverage

Tuning the SC of the NP array is achieved by adjusting the NPs diameter in the measured AFM data, as illustrated in **Figure 5.11a-c**. The SC was varied from 13% to 49%. The smallest SC (value of 13%), is the limiting value for keeping all the NPs and 49%, above which the NPs would otherwise overlap (not observed in actual samples, see **Figure 5.3d**). An increase in the surface coverage of the NPs leads to a similar change in the a-Si:H solar cell front side texture (ZnO:Al layer) as illustrated in **Figure 5.11d-f**, in comparison with NP height change (see **Figure 5.9d-f**). **Figure 5.12a-b** shows a weak influence of the SC for $\lambda < 500$ nm on the corresponding simulated solar cell spectra. An increase in SC impacts both the overall absorptance and the EQE spectra of the solar cells above λ=500 nm. For example, a maximum EQE decrease of 3.5% for SC=49%, against only 1.4% for SC=13% is reported.

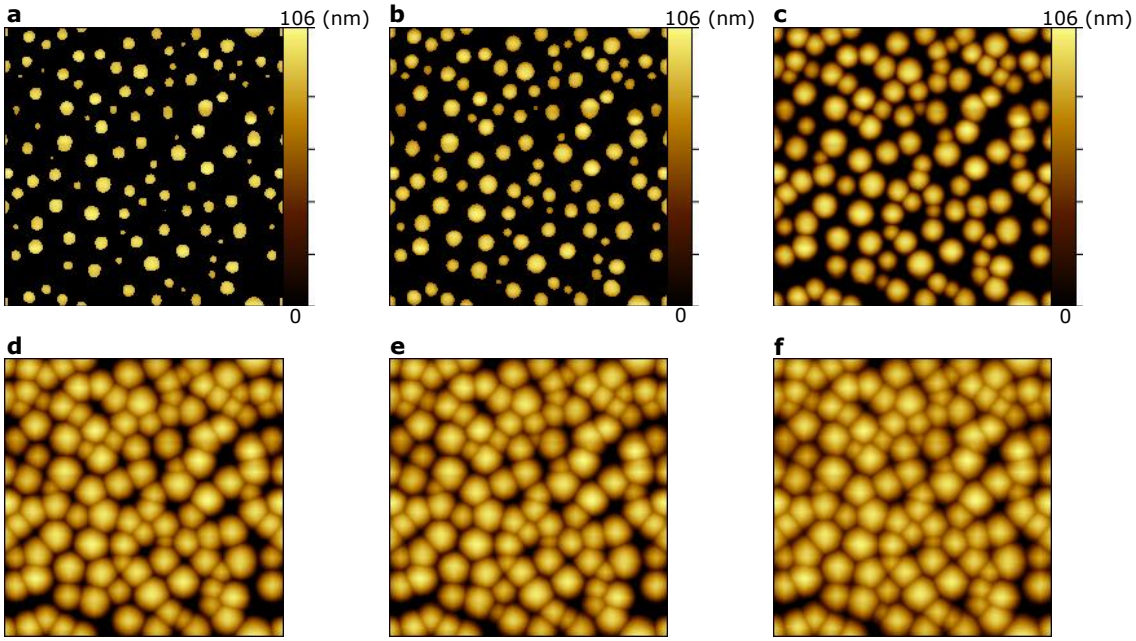

Figure 5.11. Surface morphology of the front side texture of the a-Si:H solar cell simulated by growth model for different NPs SC. (a)-(c) Texture of the PS NPs derived from AFM measurements. The profiles shown in (a)-(c) are generated by increasing or decreasing the PS domains' lateral size measured by AFM (shown in Figure 5.10b). Thus, the base surface has a SC of (a) 13%, (b) 24%, and (c) 49%. The corresponding front side textures (ZnO:Al layer exposed) are subsequently modeled and shown in (d)-(f). Adapted from Ref.[89] with permission from the Royal Society of Chemistry.

Therefore, it can be inferred that the fabricated NPs geometrical parameters introduced in **Figure 5.3d** lie in an optimized range and that the light-harvesting properties of such scattering reflectors can be globally preserved even for a significant variation of the mean NP height and SC.

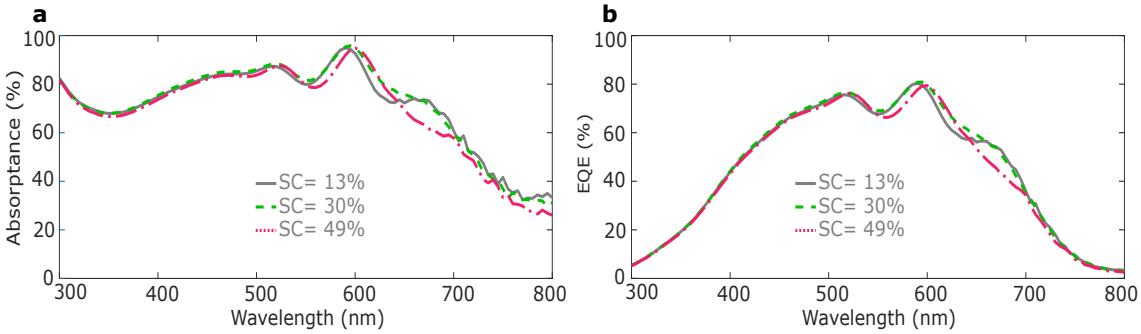

Figure 5.12. Simulated optical properties of the a-Si:H solar cells with increasing NPs SC. The overall absorptance spectra (a) and EQE (b) of the complete solar cell stack depicted in Figure 5.8a are simulated as a function of the NPs SC. A normal incidence of the light was considered in all the simulations. Adapted from Ref.[89] with permission from the Royal Society of Chemistry.

5.4 Summary and discussion

In this study, nanophotonic back reflectors with broadband light scattering properties were developed using polymer blend lithography for thin-film solar cells. The scattering layer fabrication method's advantages are: (i) its versatility, enabling it to quickly adapt and control the scattering layer morphology to obtain the desired scattering properties over an extended wavelength range, (ii) its up-scalability, demonstrated by processing substrates over several tens of cm, and (iii) its solution-processability, which helped to avoids using an annealing step at a high temperature. Among the investigated configurations, disordered NPs with a smooth profile can achieve broadband scattering while limiting parasitic absorption compared to the state-of-the-art randomly textured Asahi substrates. As a proof-of-concept, the light-trapping capability of those structures was tested in a-Si:H devices.

To this end, I have shown that including disordered NPs on the back contact of an n-i-p a-Si:H solar cell enhances the red-response of the device, predominantly through a $33\%_{\mathrm{rel}}$ increase in J_{SC} compared to devices based on planar reflectors, and even outperform randomly textured Asahi solar cells ($+7\%_{\mathrm{rel}}$ in J_{SC}). A power conversion efficiency enhancement of $+4\%_{\mathrm{rel}}$ and $+65\%_{\mathrm{rel}}$ was measured, compared to devices deposited atop an Asahi substrate and a flat substrate, respectively. It was observed that the photocurrent enhancements are most prominent at wavelengths longer than 600 nm; no decrease in performance is found at shorter wavelengths.

Optical simulations carried out on an accurate 3D model revealed that the disordered NPs superior light-harvesting properties notably stem from reduced absorption losses in the reflector above 500 nm, compared to Asahi devices that feature sharp-edged textures. Furthermore, the smooth profile of the NPs allows fabricating functional and reproducible devices with improved efficiency. I have also numerically shown

that the proposed design is tolerant to NPs height and diameter variations. The nanostructures introduced herein are particularly attractive for organic photovoltaics exploiting polymer substrates.

6. Tailored disorder: nanophotonic solar cell absorber layers

In this chapter, as an alternative to the bottom-up approach (please refer to Chapter 5), direct photovoltaic absorber layer patterning to form light-scattering elements via a top-down approach is proposed. First, the concept of patterned absorber layers as a solution for assisting light trapping of low energy photons in hydrogenated amorphous silicon (a-Si:H) and perovskite-based photovoltais is explained. Secondly, the role of ordered versus disordered nanostructures in light trapping is elaborated using optical simulation of directly patterned a-Si:H absorber layers. On the basis of these results, nanostructured a-Si:H absorber layers that offer efficient light-trapping properties together with a high angular robustness are designed. Furthermore, the numerically optimized a-Si:H absorber layers are fabricated using a scalable, self-assembly patterning technique based on the phase separation of binary polymer mixture. Thirdly, the concept discussed in the second part of this study for a-Si:H absorber layer is extended for the perovskite absorber layer. Finally, the results of this chapter are summarized. Parts of the results presented in this chapter have previously been published in the journal of Science Advances and Advanced Materials Technologies.[61, 88]

In the previous study, Chapter 5, light-trapping is addressed by patterning the back electrode. Herein, the PV absorber layer's direct patterning is explored as an alternative to the approach developed in Chapter 5. Methods for direct patterning of an absorber layer include dry[193–195] or wet[196, 197] etching, nanoimprinting,[198] light-induced (Focused-Ion-Beam/Laser) patterning,[199, 200] and template-assisted patterning (lift-off).[200] The resulting layers form light-scattering elements that benefit from the high refractive index contrast between the absorber (refractive index around 3.9[88] and 2.5[201] in the hydrogenated amorphous silicon (a-Si:H) and perovskite material at a wavelength of 750 nm, respectively) and the ambient (only 1 and 1.5 for air and glass, respectively). Higher conversion efficiencies are possible in this approach by increasing photons lifetime in the active layer and thereby enhancing absorptance near the PV active material's band edge.[23, 133] To this end, a nanophotonic absorber layer with periodic (ordered) and random patterns has been investigated extensively for light trapping in solar cells.[23, 133, 202, 203] Ordered

pattern provides strong resonant absorption enhancement via excitation of quasi-guided modes in the absorber layer,[23, 202] but the restricted number of resonant wavelengths they excite suggests that they are operating in a sub-optimal regime for PV applications. The main advantage of ordered structures is the tunability of diffraction,[23, 202] which allows a dramatic increase in absorption in a targeted, though restricted, spectral range. On the other hand, many resonances are required to cover a large bandwidth and hence produce a significant absorption enhancement in PV devices.[23] In this direction, randomly textured absorbers excite many resonances because of their large number of diffraction orders, but the coupling with each of these resonances is weak.[23] This situation leads to numerous but low-intensity new absorption peaks.[23, 190, 204] The ideal photonic structure should target the highest integrated absorptance possible and therefore combine a sufficiently high density of resonant wavelengths over the low absorption spectral range and an efficient coupling for each of the resonances involved.[23, 190] More recently, photonic structures featuring a tailored degree of disorder—i.e., lying halfway between ordered and random configurations—have attracted considerable interest in PV due to their extended spectral and angular range of effectiveness.[204] Notably, quasi-random nanostructures realized by e-beam lithography (EBL) have been integrated into solar cells as broadband light trapping elements and have been shown to approach the theoretical (Lambertian) limit.[204] Despite recent research efforts aiming at increasing the EBL writing speed,[205] alternative routes based on self-assemblies have the highest potential in reaching industrial implementation as they allow to rapidly process disordered structures over large areas (tens of cm^2).[64, 206]

In this study, inspired by the cellular phase separation mechanism of the black butterfly wing scales, lateral phase-separation of binary polymer mixture is proposed to introduce tailored disorder patterns into absorber layers. To this end, two ways to integrate the bioinspired scattering nanostructures into absorber layers of solar PV stacks are considered. First, the proposed approach is used to pattern an etching mask made of resist, which is employed for transferring disordered nanoholes (NHs) into a thin a-Si:H layer by dry etching (top-down route). A second example demonstrates that similar structures can serve as an imprinting stamp to pattern perovskite absorber layer via thermal nanoimprinting lithography (NIL). The latter route is expected to pave the way for roll-to-roll processed "photonized" absorbers film for PV devices. Finally, the significance of these findings for other PV materials, namely organic and quantum dot-based solar cell devices is elaborated.

6.1 Photonics of black butterfly: Nanostructures and physics behind

The scales of black butterflies' wings, particularly *Pachliopta aristolochiae* (**Figure 6.1a**), that exhibit a wide variety of hierarchical micro- and nanostructures (**Figure 6.1b**) with specific functionalities such as visual appearance and thermoregulation were the source of inspiration for this study.[88, 207] Herein, the focus is mainly on the role of micro- and nanostructures on visual appearance of these butterfly wings. More details regarding the morphology of the butterfly wing scales and computational models are given in our study.[88] The blackness of these butterfly wings is attributed to the light-harvesting micro- and nanostructures in addition to the pigmentation. The scales consist of periodic micro-ridges connected with a disordered

NH network (**Figure 6.1b**). These scales' mean thickness is about 1 μm (15 times thinner than a human hair) with a material filling fraction (*ff*) of only 31%. However, such thin scales absorb almost 98% of the incoming light in the visible range (**Figure 6.1c**). Therefore, understanding the light-harvesting properties of black butterflies result in a lightweight, cost-effective yet efficient absorber for thin-film PV, for which efficiencies are limited by severe optical losses (reflection losses and incomplete absorption of the collected sunlight).

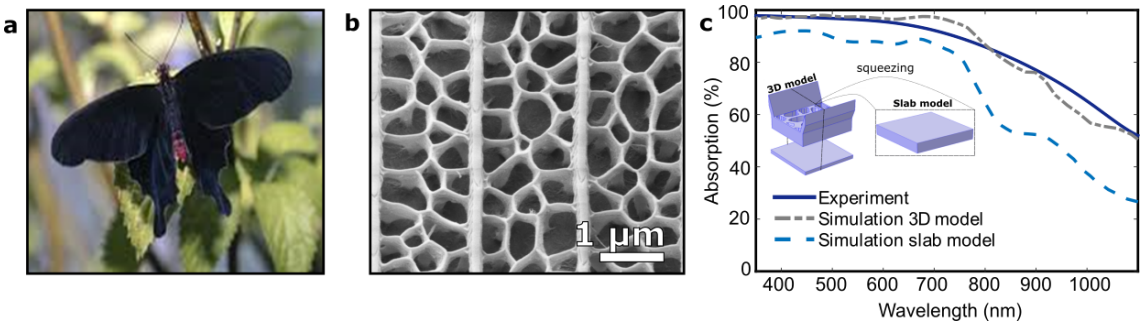

Figure 6.1. (a) Photograph of the *Pachliopta aristolochiae* black butterfly, (b) Scanning electron microscope (SEM) topview image of the micro- and nanostructures of the black butterfly scales consisting of periodic micro-ridges with 2D disordered cross-rib (NH) structures, (c) Influence of the micro- and nanostructures on the light harvesting properties of the black butterfly (under normal incidence). The absorption spectrum of a 3D model exactly reproducing the hierarchical structures shown in b) and Ref.[88] is simulated and compared to that of an unpatterned slab with similar absorbing volume, and to the measured absorption spectrum of a scale. Adapted from Ref.[88] with permission from American Association for the Advancement of Science.

To gain insight into the influence of the micro- and nanostructures of *P. aristolochiae* on its overall absorption properties, 3D finite-element-based optical simulations were performed. The "3D model" parameters for these simulations were taken from surface and cross-sectional SEM images (for more details, please refer to Ref.[88]). To evaluate the influence of these structures, an unpatterned slab with an equivalent absorbing material volume was used as a reference ("slab model"). The overall agreement between the simulated and experimental data (see **Figure 6.1c**) confirms the validity of the developed model. **Figure 6.1c** shows that, for an equivalent volume of material, structuring the absorbing medium as found in the scales of the black butterfly leads to a marked increase in the light absorption over the whole spectral range considered (covering the operational wavelength range of most PV technologies). Quantitatively, this translates into overall spectrally weighted absorptance, an integrated absorption (IA) increase of +18% with respect to the unpatterned slab.

To understand how these micro- and nanostructures assist the light absorption process, light propagation through the black butterfly scales was investigated using field mapping at four different wavelengths (see **Figure 6.2**). At 350 nm, simulated field maps show that the light is channeled inside the NHs and partially absorbed at their surface. The "channeled modes", primarily concentrated in the low–refractive index region (air), lead to a lower mean refractive index. Consequently, reflection losses are decreased because of an improved impedance matching between the incident medium (air) and the wing. The situation differs as the wavelength increases

(see, for instance, at 850 nm), and the light is then efficiently scattered over the NH array. Both effects—"vertical channeling" and "in-plane scattering"—act together at 550 nm (where the peak of the solar radiation spectrum lies). The micro-ridges start playing a noticeable role on the light propagation mechanism only in the near infra-red (1050 nm).

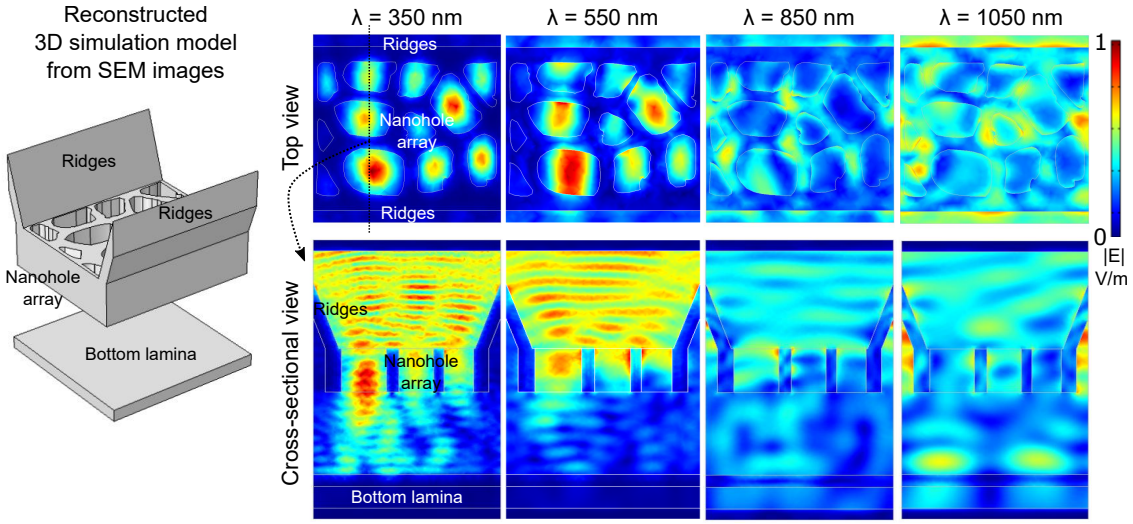

Figure 6.2. Wavelength-dependent light propagation regimes within the micro- and nanostructures of the *P. aristolochiae* black butterfly. The normalized electric field intensity distribution is simulated over the hierarchical structures of the black butterfly for normal incidence via 3D finite element optical simulations. Adapted from Ref.[88] with permission from American Association for the Advancement of Science.

Thus, the outstanding light-harvesting properties of the black butterfly originate from a multilevel system where the 2D disordered NH network primarily assists light absorption through efficient light in-coupling and light scattering (trapping) mechanisms.[88] As mentioned earlier, the NH array is found to be the main contributing element for the absorption in the ultraviolet-visible (UV-vis)–NIR region. Therefore, further analysis is needed to understand the influence of the NH size and position disorder on the absorption to design improved thin-film absorbers inspired by black butterfly scales.

6.2 Nanophotonic a-Si:H absorber layers

Inspired by the black butterfly study, the ability of disordered NHs to harvest sunlight for a-Si:H layers is numerically analyzed in section 6.2.1. The impact of disorder on the optical properties of patterned a-Si:H films is systematically investigated by starting from an optimized periodic arrangements of NHs. Eventually, with a top-down approach, the optimized NHs are transferred into the a-Si:H absorber layer by combining self-assembly and a dry etching process (see section 6.2.2).

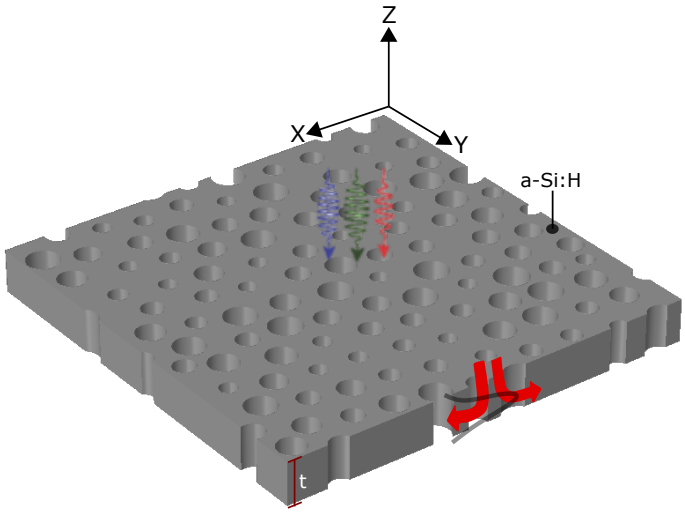

Figure 6.3. 3D simulation model developed to compute the optical properties of an a-Si:H layer (t=100 nm) consisting of bio-inspired disordered NH array.

6.2.1 Design of nanophotonic a-Si:H absorber layers

Numerical simulation based on a finite element method (FEM) is used to retrieve design rules to fabricate bio-inspired and highly absorbing a-Si:H absorber layers. The developed 3D model is illustrated in **Figure 6.3**. For analysis, an "ordered" periodic arrangement of holes with a single diameter, a "perturbed" periodic arrangement of holes with varying diameters, and finally a "correlated" combination of position and diameter size disorder inspired by the black butterfly scales (see **Figure 6.4a)** were introduced. An unpatterned slab with a thickness of 100 nm served as a reference. All layers were simulated with air as a surrounding medium. For periodic configuration, the period of the structure (300 nm) and the hole diameter (240 nm) were adopted from Ref.[202], where the 2D patterned a-Si:H absorber layer was already optimized with respect to its IA. Compared to the periodic configuration, the NHs decorating the wings of the black butterfly *P. aristolochiae* features disorder in position as well as diameter size distribution. To discriminate the contribution of the position and the diameter size distribution on the absorption properties, a controlled amount of disorder in the diameter size distribution (see **Figure 6.4b**) was introduced into the periodic configuration. The resulting configurations are called "perturbed" structures and have a Gaussian distribution of hole diameters (average of 240 nm, variance of 20 nm), as shown in **Figure 6.4b**. A Gaussian distribution is chosen as it reflects what is obtained experimentally, as discussed in the following sections. The bio-inspired disordered NH array, obtained by shifting the position of the "perturbed" periodical arrangement (see **Figure 6.4a**) by the application of the Lubachevsky-Stillinger (LS) algorithm.[208] The generated configurations using the LS algorithm are called "correlated" disordered structures and exhibit only short-range order (see the ring-shaped feature on the 2D Fourier spectrum in **Figure 6.4a**). A fixed volume of absorbing materials is considered for the three configurations discussed above. The total absorbing volume, however, is lower than that of the planar reference due to patterning. The simulated absorption spectra for a plane wave with a normal angle of incidence (AOI) of the four configurations are shown in **Figure 6.4c**. The periodic structure's absorption peaks in **Figure 6.4c** can be attributed to the coupling of the incident plane wave with pseudo-guided modes, which is en-

abled by periodic patterning.[202] The non-uniform radius (perturbed configuration) only slightly broadens the ordered array's absorption spectra, while the absorption spectra of correlated configuration is almost completely broadened.

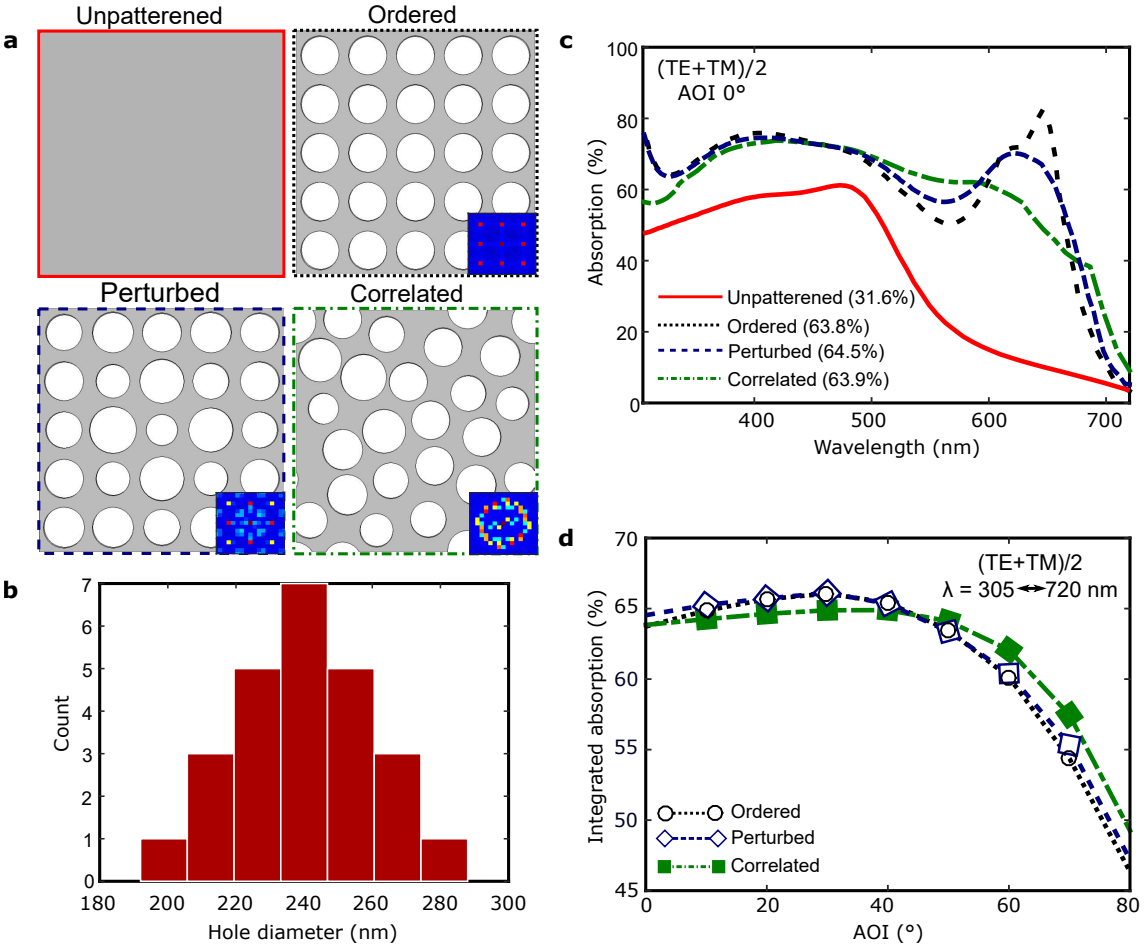

Figure 6.4. Simulated optical properties of thin and patterned absorbers made of a-Si:H with increasing disorder magnitudes. (a) Schematic view of the four considered geometries: 'unpatterned' bare slab, 'ordered' periodically arranged holes with single diameter, 'perturbed' structure of holes with periodic arrangement but varying diameters, 'correlated' structure with disordered hole positions and varying diameters. The ordered structure has a hole diameter of 240 nm and a period of 300 nm. The *ff* of all patterned configurations is set to 50.26%. The insets in the lower right corners show the 2D Fourier power spectra of the corresponding structures. (b) A Gaussian distribution with a mean hole diameter of 240 nm and a variance of 20 nm is introduced into the ordered configuration to investigate the effect of size dispersion. (c) Absorption spectra of the four simulated geometries under normal incidence for unpolarized light ((TE+TM)/2). The integrated absorption of each geometry is reported in the legend. (d) Integrated absorption of the three patterned geometries vs. the angle of incidence (AOI). The resulting integrated absorption varies between 67% to 45% for angles up to 80°. Adapted from Ref.[88] with permission from American Association for the Advancement of Science.

To quantify each configuration's light-trapping efficiency, the simulated absorption was weighted by the solar spectral irradiance. Then, the resulting IA was used as a figure of merit. Details of the IA calculation are given in Chapter 3. In the

case of the unpatterned reference slab, the IA is only 31.6% (in accordance with Ref.[202]). On the other hand, the photonic slab with ordered hole array exhibits 63.8% of the average optical absorptivity weighted by solar spectral irradiance in the wavelength range between 305 nm to 720 nm. This outcome is already two times larger than the bare slab. The perturbed structure, however, has an increased IA of 64.5%. Introducing correlation to the holes' position together with size dispersion, similar to the black butterfly, leads to an IA of 63.9%. All three photonic structures double the IA by a factor of more than 2 compared to the unpatterned layer. For normal AOI, the three photonic structures exhibit comparable IA. The significant absorption reduction at short wavelengths (below 450 nm) and around 650 nm limits the IA gain of the "correlated" design. However, if oblique AOI is considered, the IA of the correlated disorder is better than that of the ordered array, as shown in **Figure 6.4d**. The IA drop in the correlated structure is limited to 22.8% between 0° and 80°, whereas the ordered (perturbed) structure exhibits a drop in IA as high as 27.3% (respectively 26.8%). The result indicates that the bio-inspired "correlated" structures lead to broader spectral and angular responses, clearly beneficial for PV application. This property is attributed to many accessible diffraction orders (see also the Fourier spectrum in **Figure 6.4a**) in their design, which is crucial for the absorption enhancement. In contrast, the IA in the periodical or slightly perturbed structures relies on a limited number of sharp absorption peaks. Based on the numerical analysis, the bio-inspired NHs distribution may provide a better route towards realizing thin-film PV with high performance over a wide range of operating criteria over the purely periodic one.

6.2.2 Fabrication of nanophotonic a-Si:H absorber layers

Motivated by the optical simulations' positive outcome (see section 6.2.1), black butterfly-inspired thin PV absorbers incorporating disordered NH were designed, which combine efficient light in-coupling and light-scattering properties with high angular robustness. Inspired also by the butterfly scales' cellular phase-separation mechanism,[209, 210] a self-assembly patterning technique based on the phase-separation of a binary polymer mixture was used to fabricate the disordered nanostructures (for details, please refer to Chapter 4). **Figure 6.5a** illustrates the fabrication process flow. An a-Si:H layer of thickness 130 nm was deposited on glass substrates using plasma-enhanced chemical vapor deposition. More details regarding the deposition parameters are given in methods section (Chapter 3). The a-Si:H layer on glass is used as a substrate for spin coating the polymer blend. For this study, a polymer blend of Poly (methyl methacrylate) (PMMA, Mw=9.59 kg·mol^{-1}) and polystyrene (PS, Mw=19.1 kg·mol^{-1}) dissolved in methyl ethyl ketone with a mass ratio of 60% and 40% were used. The concentration of the solutions was fixed to 20 mg·ml^{-1}. The solution was spin-coated atop the a-Si:H layer with a spin-casting speed of 1500 rpm and an acceleration of 2000 rpm/s for 30 seconds. After phase-separation of the polymer blends, PS was selectively developed using cyclohexane. The nanostructured polymer matrix made of PMMA was then used as an etching mask for a reactive ion etching process that resulted in the formation of NHs in the a-Si:H layer, as shown in **Figure 6.5a**. The a-Si:H was etched using a SF6/Ar-based plasma at operational pressure and power of 25 mT and 50 W, respectively. The SF6/Ar flow rate was fixed at 5/20 sccm. Afterward, the etching mask (i.e., PMMA matrix) was removed using oxygen plasma.

Figure 6.5b show the optical photographs of the unpatterned a-Si:H absorber (left) in comparison to a-Si:H absorber that has been patterned and completely etched sample (right). The photograph shows an apparent visual effect: the improved absorption's darkish appearance due to the absorber layer's patterning with bio-inspired light scatterers.

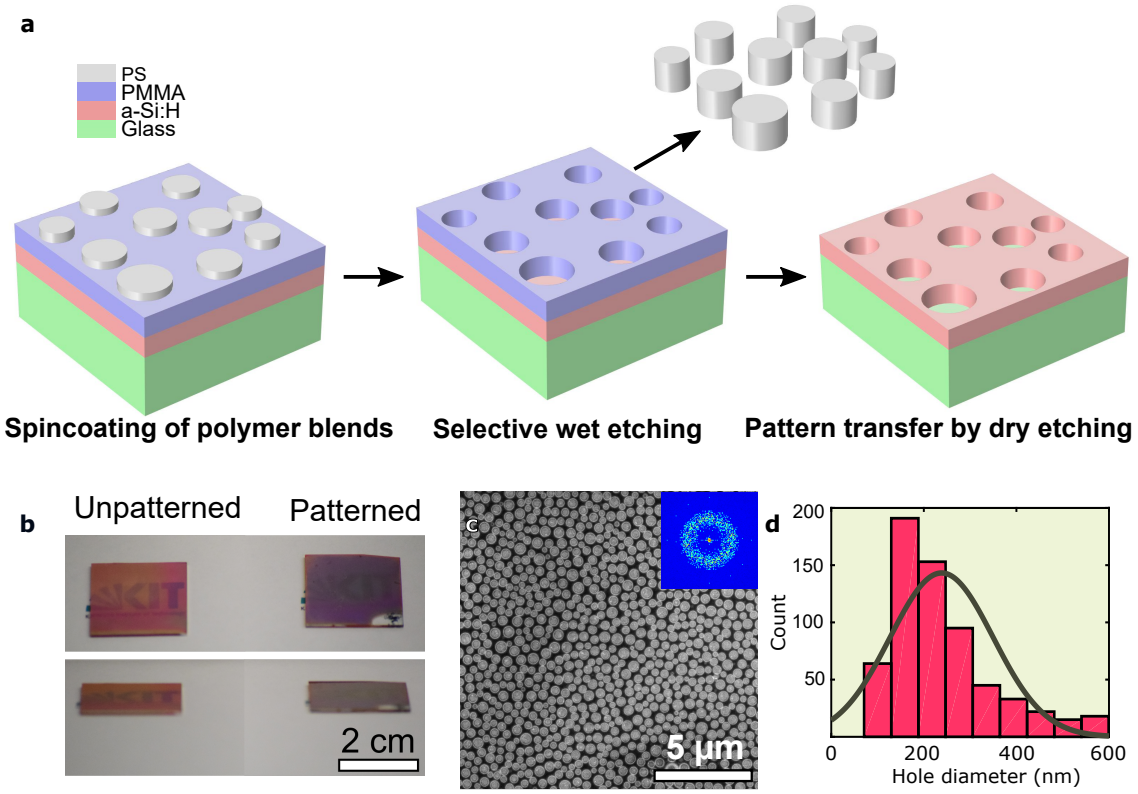

Figure 6.5. Fabrication of the bio-inspired patterned thin PV absorbers. (a) Schematic view of the three main fabrication steps including the spin-coating of a blend solution of Poly (methyl methacrylate) (PMMA) and Polystyrene (PS) in MEK on thin a-Si:H layer deposited on a glass substrate, followed by a selective development of the PS and finally the transfer of the pattern into a-Si:H by dry etching (RIE). (b) Photo of a patterned 130 nm thin a-Si:H layer on a glass substrate with completely etched disordered nanoholes (right) demonstrates the high omnidirectional absorption properties with respect to the unpatterned sample (left). All photos were taken under diffusive white light with observation angles of 30° (top) and 80° (bottom). (c) SEM top view image of the nanostructured a-Si:H thin film shows the distribution of nanholes with both size and position disorder. The ring-shaped pattern in the 2D Fourier power spectrum corresponding to this SEM image (inset) confirms the correlated disorder nature of the nanoholes introduced in the thin absorber. (d) Statistical analysis of the nanohole diameters of this sample. The histogram depicting the distribution of nanohole diameters can be approximated by a Gaussian profile with a mean diameter of 238 ± 105 nm. Adapted from Ref.[88] with permission from American Association for the Advancement of Science.

The scanning electron microscopy (SEM) image of the resulting correlated disordered NHs in the PV absorber is shown in **Figure 6.5c**. A corresponding 2D Fourier power spectrum in the overview SEM image's inset demonstrates the correlated disorder nature of the NHs. The NH diameters follow a Gaussian distribution and

range between 100 nm and 600 nm with a mean diameter of 238 nm, exhibit a *ff* of 41%. The NHs size distribution is shown in **Figure 6.5d**. The etching profile, a 1D line profile extracted from an atomic force microscopy (AFM) image of the patterned a-Si:H is shown in **Figure 6.6a**.

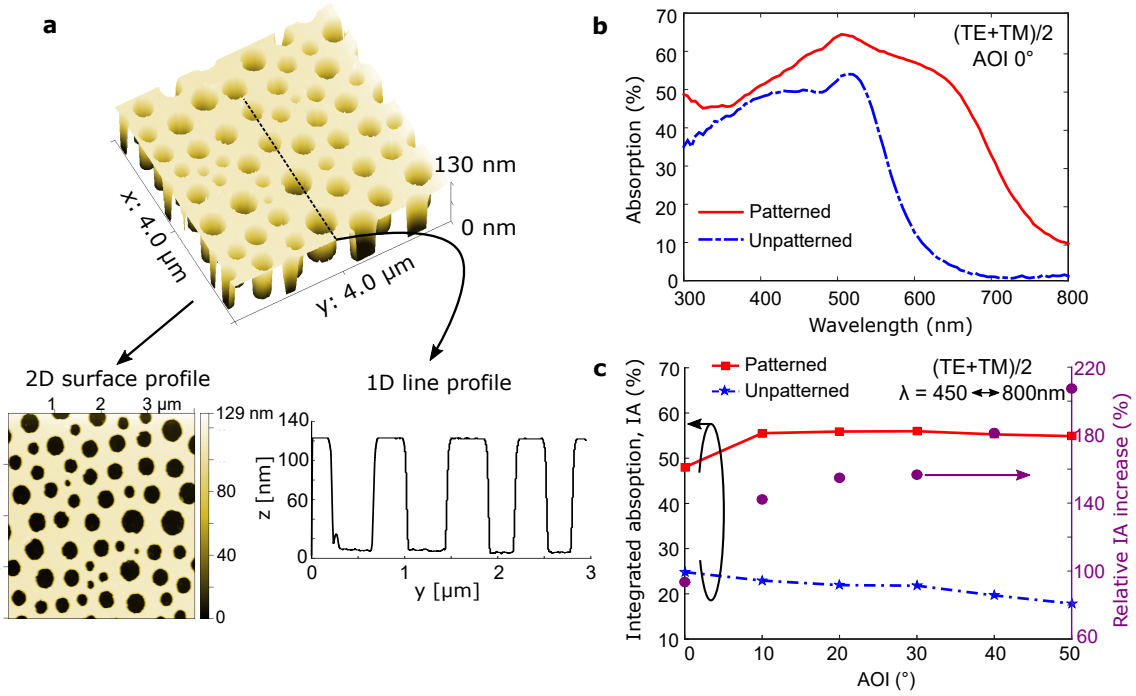

Figure 6.6. Characterization of the bio-inspired patterned thin PV absorbers. (a) AFM image of the bio-inspired a-Si:H thin film show uniform surface patterning with height (etching) profile. (b) Impact of the etched disordered nanoholes on the absorption spectrum measured at normal angle of incidence with unpolarized light. (c) Angular dependence of the integrated absorption of the patterned and unpatterned samples. The relative increase of IA raises up to +200% for an angle of incidence (AOI) of 50°. Adapted from Ref.[88] with permission from American Association for the Advancement of Science.

The line profile shows that the etching is achieved throughout the whole absorber thickness. The benefit of patterning the a-Si:H layer with bio-inspired nanostructures is apparent in **Figure 6.6b**. At normal AOI, the patterned a-Si:H layer enhances the absorption over the whole spectral range compared to a planar one (blue dash-dotted line in **Figure 6.6b**). The latter features a low absorption for wavelengths above 500 nm, where the absorption coefficient of a-Si:H is low,[88] and exhibits an IA of just 24.8%. The bio-inspired disordered NHs based a-Si:H layer, in contrast, has an IA of 48%. This is attributed to the light-trapping (coupling to pseudo-guided modes) effect of the patterned design. Thus, a relative IA increase of 93% was measured under normal incidence and between 450 nm and 800 nm. As demonstrated experimentally (**Figure 6.6c**), the disordered NH array enables to maintain a high absorption even at oblique angles, which is an asset for PV systems that should collect both direct and diffuse sunlight. Besides, it is important to note that the relative IA enhancement is even higher at larger AOI and reaches $+207\%_{rel}$ at an incident angle of 50°.

However, keeping the planar PV device's electrical performance is very challenging, as the nanotexturing damages the absorber, and the sensitivity to the surface recombination is dramatically increased.[211] By taking care, in particular, of the etched sidewalls' surface passivation as discussed in Ref.[211], a subsequent increase in the conversion efficiency is expected for a solar cell based on the bioinspired, patterned a-Si:H thin-film layer.

6.3 Nanophotonic perovskite absorber layers

For the last few years, metal halide perovskite semiconductors have attracted a lot of attention in optoelectronic device research as they offer strong optical absorption and emission, as well as high charge carrier mobilities.[133, 148, 198, 212, 213] Furthermore, these are solution processable, low-cost materials and can be processed with a wide range of cost-effective fabrication approaches, including roll-to-roll processing.[214] Compared with the planar, the nanostructured perovskite thin films exhibit enhanced optical performance in various photonic devices and materials such as solar cells,[133] light-emitting diodes (LEDs),[198] lasers,[213] metamaterials,[212] and photodetectors.[148] For example, nanostructured perovskite thin films can be used in solar cells to enhance current generation by coupling the incident light to quasi-guided modes.[133] They can also be exploited in LEDs, lasers, photodetectors, and metamaterials to gain multifold photon emission enhancements.[148, 198, 212, 213]

In this section, the concept of light management using bio-inspired nanostructures (discussed in section 6.1) is extended for perovskite-based PV. The etching technique developed in section 6.2.2, however, is not suitable for patterning perovskite material. The wet or dry etching approaches discussed in section 6.2.2 require the employment of the patterned resist as an etching mask for patterning the perovskite material, followed by the removal of the residual resist mask from the perovskite film after etching. Since perovskite are soluble materials (sensitive to various solvents and gases) accomplishing all of the above steps without damaging the film is highly challenging.[199] Herein, nanophotonic perovskite layers are demonstrated with improved optical properties using a thermal NIL method. Compared to the etching technique (refer to section 6.2.2), there is no loss of absorbing material with the thermal NIL approach. The total absorbing volume before and after the NIL process remains the same.

6.3.1 Fabrication of nanophotonic perovskite absorber layers

The patterning of perovskite films via thermal NIL using a conventional imprinting stamps (made of OrmoStamp material) involves a series of fabrication steps: (1) fabrication of master using different lithography approaches, (2) replication to polydimethylsiloxane (PDMS) from master via soft NIL, and (3) another soft NIL based replication to OrmoStamp material (working stamp) from PDMS.[133] In this study, the imprinting stamps are prepared using a self-assembly method based on the phase-separation of PS/OrmoStamp blend (for details, refer to Chapter 4). Compared to the conventional fabrication approach, the self-assembly method involves only a single spin-coating step to prepare the stamps.

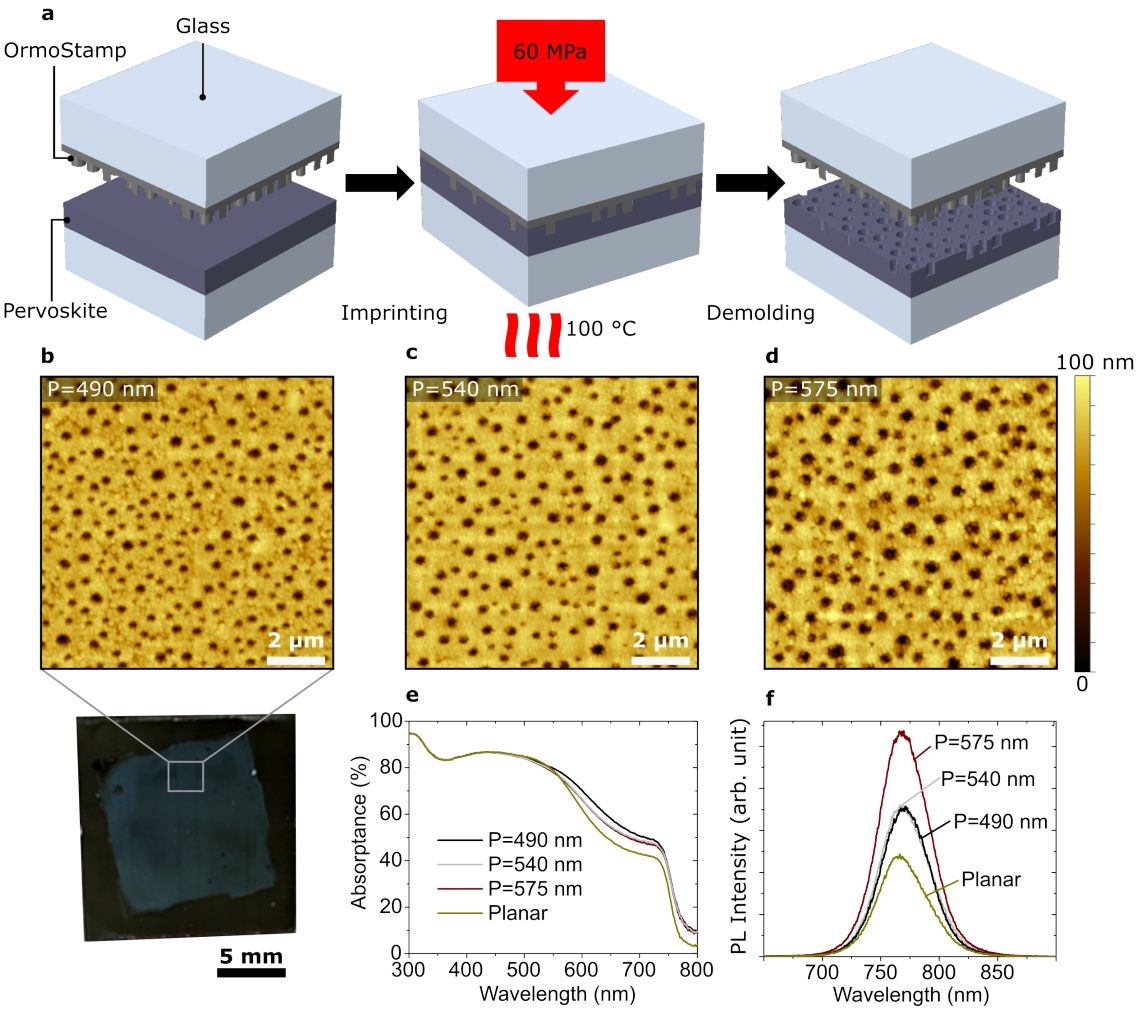

Figure 6.7. Improved light management in nano-imprinted perovskite films using PSN based imprinting stamp. (a) Schematic illustration of the imprinting process of the perovskite films on glass using P2P NIL tool. Imprinting stamps with surface relief shown in Figure 4.20a(iii,iv) and 4.19d are used for the thermal NIL process. (b-d) AFM images of the corresponding nano-imprinted perovskite films with effective period of (b) P=490 nm, (c) P=540 nm, and (d) P=575 nm. The photograph of the imprinted perovskite film using P=490 nm is shown in (b). (e) Optical absorption of the planar and the patterned perovskite films with a thickness of 250 nm. (f) PL spectrum of the planar perovskite film compared to the PL spectrum of three different nano-imprinted films. Adapted with permission from Ref.[61], © John Wiley & Sons.

For example, to highlight the potential of the phase-separated nanostructures (PSN) to achieve optically tunable and efficient nanophotonic perovskite films via thermal NIL, the nano-stamps shown in **Figure 4.19d** and **4.20a(iii,iv)** are used as imprinting stamps. Before their integration into the thermal NIL tool, the imprinting stamps were treated with 1H,1H,2H,2H-Perfluorooctyltrichlorosilane to improve their anti-sticking property and reduces the demolding forces substantially.[161] Afterward, the thermal NIL of the triple cation perovskite ($Cs_{0.1}(MA_{0.17}FA_{0.83})_{0.9}Pb(I_{0.83}Br_{0.17})_3$) films is done with a temperature of ≈100 °C, and a pressure of ≈60 MPa in a nitrogen environment, as illustrated schematically in **Figure 6.7a**. Details of the perovskite

layers preparation are given in Ref.[133, 215]. For thermal NIL, an in-house developed hot embossing machine is used.[216] The different imprinting parameters' effect using this machine on the perovskite film is discussed briefly in Ref.[16, 133], using imprinting stamps based on periodic nanostructures. The surface morphology of the nano-imprinted perovskite films can be seen in the AFM images in **Figure 6.7b-d**. **Figure 6.7b** also includes the photograph of the nano-imprinted perovskite film. The nanoholes of the nano-imprinted perovskite films show an average depth of 80 nm.

Figure 6.7e highlights the substantial absorption increase following the imprinting of the disordered PSN into the perovskite layers and their superior utilization of the collected low-energy photons with respect to the unpatterned perovskite layer. As revealed by AFM images, this is notably attributed to the regular nanoholes pattern imprinted into the perovskite material. Thus, the pattern leading to an enhanced light-scattering and an efficient light in-coupling. The IA was calculated to assess the perovskite films' light-harvesting capabilities under consideration. In the case of the unpatterned ("planar") perovskite film, the IA is 62.3%. On the other hand, the patterned perovskite films based on the PSN with effective period (P)=490, 540, and 575 nm improve the IA by 7, 4.6, and $4\%_{rel}$ relative to the planar counterpart, respectively. Herein, the highest optical absorption gain is observed for the pattern with the smallest P. The finding highlights that one can mitigate the toxic lead content in perovskite-based devices by reducing the thickness of the perovskite material and enhancing the optical property of thinner films.[133] As such, optical solutions are promising avenues for improving not only the power conversion efficiency by allowing physically thinner but optically thicker devices, but also their market applicability by enabling higher mechanical flexibility due to the reduced thickness (in the same way as targeted for a-Si:H technology). The developed PSN can also serve as an imprinting stamp for nanopatterning organic solar cells and thereby improve their optical properties, as highlighted in Ref.[155, 217].

The nanostructured perovskite thin films can also be exploited in LEDs to gain photon emission enhancements due to favored nanostructure morphology, contributing to better light out-coupling compared to pristine ones. **Figure 6.7f** shows enhanced photoluminescence (PL) spectra from nanoimprinted perovskite films compared to a planar counterpart. Quantitatively, the PL emission peak (located near the bandgap of the perovskite material) is enhanced by $47\%_{rel}$ (for P=490 nm), $48\%_{rel}$ (for P=540 nm), and $121\%_{rel}$ (for P=575 nm), respectively. A continuation of this work could be dedicated to the fabrication of patterned perovskite layer-based LED devices. Moreover, this work opens up a new and simple way to fabricate nanoimprinted high-refractive-index active photonic nanostructures based on quantum dots for visible light.[218]

6.4 Summary and discussion

In this chapter, "photonized" thin-film absorber layers are investigated to enhance solar cells' efficiency. Disordered structure of nanoholes (NHs) inspired by the black butterfly were implemented to realize efficient "photonized" absorber layers. As a proof-of-concept, this pattern were tested in thin-film absorber layers based on hydrogenated amorphous silicon (a-Si:H) and perovskite materials.

In the case of a-Si:H, a top-down approach based on the phase-separation of PS/PMMA polymer blend combined with dry etching was developed to pattern the ab-

sorbing layer. Herein, a polymer matrix (made of PMMA) with NHs was utilized as a dry etching mask after the selective development of PS domains to transfer the disordered NHs into a-Si:H layer. The patterned a-Si:H layer exhibited an integrated absorption (IA) increase of $93\%_{rel}$ compared to their planar counterpart under normal angle of incidence. As demonstrated experimentally, the NH array enables to maintain a high absorption even at oblique angles. Using optical simulations, the present study also show that the disordered NH array leads to improved angular robustness compared to the periodic NH array. This is a direct consequence of the higher number of resonances involved in disordered NH array. Therefore, the latter enables highly absorbing active layers over a broad spectral and angular range, as desired for solar PV applications.

In a second example, it was demonstrated that similar structures could be used to pattern a perovskite absorber layer using thermal NIL. To imprint the absorber layer using thermal NIL, the OrmoStamp nanopattern fabricated via phase-separation of PS/OrmoStamp polymer blend is directly used as a nano-stamp. The patterned perovskite films demonstrated enhanced optical absorption and photoluminescence compared to the pristine ones. The introduction of nanophotonics into the perovskite layer also sets the path for scaling down the absorber layer's thickness and hence reducing the harmful lead. Overall, this study uniquely ventures into the territory of combining bio-inspired disordered NH array with thin-film PV absorber layer. It also provides a pathway for a further systematic study of nature-inspired nanostructures for PV devices' optimal design and function.

7. Antireflective coatings for efficient perovskite/c-Si tandem solar cells

The successful development of multi-junction photovoltaic devices with two or more subcells (e.g., perovskite/c-Si tandem solar cells) has placed additional importance on the design of high-quality broadband antireflection coatings. In this chapter, phase-separated nanostructures with dimensions smaller than the wavelength of incident light (i.e., antireflective nanostructures (ARN)) are proposed to reduce reflection losses and thereby increase light absorption in perovskite and perovskite/c-Si tandem solar cells. First, the working principles of antireflection coatings are discussed, with an emphasis on ARN. The different approaches to fabricate ARN are reviewed. The fabrication of tunable ARN using polymer blend lithography (PBL) is demonstrated (section 7.1). Finally, the PBL based ARNs are integrated into perovskite /c-Si tandem solar cells to enhance their optical performance. Parts of the results presented in this chapter have previously been published in the journal of Optics Express.[90] In this study, Ihteaz M. Hossain carried out the solar cell devices fabrication and characterization.

In Chapters 5 & 6, phase-separated nanostructures (PSNs) were implemented as light-trapping layers. They thus increased the optical absorption of thin-film solar cells, close to the device's active materials band edge. In this chapter, we extend the application of the PSNs and implement them as an antireflection layer to enhance the performance of perovskite/c-Si tandem solar cells. The reflection losses in planar solar cells originate from the thin-film interference in the layers stack.[219] An antireflective coating (ARC) based on either a single/multi-layer[220, 221] or subwavelength structures[219, 222] can reduce the reflection losses in the planar solar cells (for details, refer to Chapter 2). Among the two ARC approaches, ARC based on subwavelength structures is gaining more attention as an ideal candidate for ARC in thin-film solar cells. This is due to their excellent performance as broadband, omnidirectional, and polarization-insensitive ARC layer.[223, 224] These characteristics are essential for solar panels in terrestrial conditions (cloudy weather, change in light intensity, and diffused sunlight).[225]

The antireflective effect of subwavelength structures can be explained by a homogeneous medium whose optical properties are a weighted spatial average of the profiles' optical properties,[226] as illustrated in **Figure 7.1**. This is attributed to their dimensions being less than the wavelength range of incident light and effectively acting as an impedance matching layer, smoothing the transition between one layer and another. These properties are the basis for an effective medium theory (EMT).[223, 226, 227] Hence, the subwavelength structured interface region can be modeled by replacing them with a stack of many layers, each with an effective refractive index (n_{eff}), as shown in **Figure 7.1**. Modeling and designing of subwavelength structures using EMT are briefly discussed in Ref.[16, 223, 226, 227]. Modeling with EMT is effective when the dimension of the subwavelength structures (d) is much smaller than the incident light wavelength (λ) and breaks when d approaches λ.[226] In this direction, excellent work has been done using numerical simulation to design and understand the effect of varying d with respect to λ on the ARC optical properties.[228, 229]

In nature, biological systems also use subwavelength structures to produce unique functionality.[230] Moth's eye, for example, has evolved nipple arrays of sub-300 nm size to reduce reflectivity from their compound eye and thus protect themselves from predators.[231] In physical science, ARC's breakthrough based on subwavelength structures technology came in the late 1800s by Lord Rayleigh.[232] He discovered that a slightly tarnished glass allowed more light through than a planar glass.[22, 232] Afterward, a range of nanoscale fabrication techniques has been employed to create subwavelength structures in various materials. In general, this involves using electron-beam,[233] laser interference,[228, 234] nanoimprint,[235] colloidal lithography,[236, 237] as well as spontaneous and self-assembled approach.[238–240] The latter approach, e.g., based on self-assembled nanoparticles obtained using a thermal dewetted metal thin film, was analyzed and evaluated by many researchers for its relatively fast, simple, and inexpensive large area application.[238–240] Nevertheless, such metal-based subwavelength structures can not be directly used for solar cell devices due to their significant parasitic absorption and have to be transferred to lossless material using a dry or wet etching process.[238–240] Furthermore, the dewetting process's annealing step necessitates a high temperature between 400-500 °C, limiting practical ARC's mass production using this approach. These limitations call for alternative patterning approaches that can be implemented at room temperature without requiring an e-beam lithography or etching/nanoimprint to transfer the structures to another material. Thus, they provide proper control over the morphology of the nanostructures. In this context, the realization of subwavelength structures by the phase separation of immiscible polymer blends is a relevant alternative, as it can be carried out at room temperature (for details, refer to Chapter 4).

This study presents a low-cost method for fabricating antireflective polymer surfaces based on lateral phase separation of spin-coated binary polymer blends. The approach enables wafer-scale production of disordered nanostructures with subwavelength dimensions (for details, refer to Chapter 4). Meanwhile, we systematically investigate the antireflective and electrical properties of nanostructured indium tin oxide (ITO), which is one of the common transparent conducting oxide materials used as a transparent electrode layer in solar cells. Herein, the nanostructured ITO is fabricated by conformal deposition onto the phase-separated subwavelength struc-

tures. This ultimately allows us to realize their optical benefit in pervoksite/c-Si tandem solar cells.

7.1 Fabrication of nanophotonic electrodes

In this study, PBL based on a polymer blend of two immiscible phases is used to generate subwavelength structures. More specifically, a blend of polystyrene (PS) and poly(methyl methacrylate) (PMMA) is implemented to generate subwavelength PS nanopillars (NPs) with a mean height of 130 nm. More details regarding the fabrication approach are given in Chapter 4. Herein, small molecular weight (MW) PS (MW=3.25 or 8.21 kg·mol^{-1}) and PMMA (MW=5.50 kg·mol^{-1}) polymers with a concentration of 15 mg·ml^{-1} were employed to achieve the subwavelength PS NPs. The nanophotonic electrode was obtained by conformally depositing a 135 nm thick ITO film on the phase-separated PS NP array following the sequence illustrated in **Figure 7.1**.

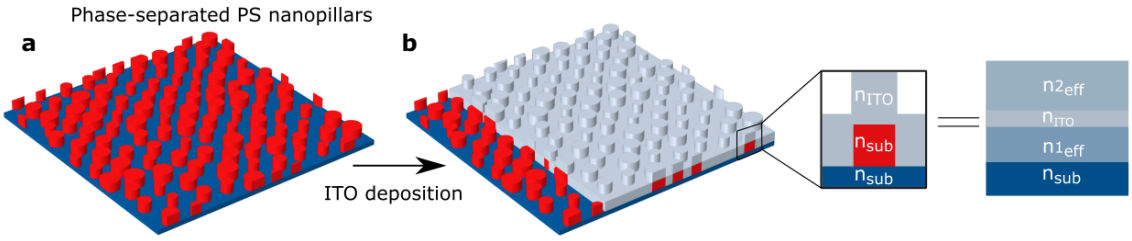

Figure 7.1. Subwavelength structures fabrication using polymer blend lithography (PBL) and their analogous refractive index profiles. (a) The phase-separated polystyrene (PS) nanopillars (NPs) on the substrate after the selective development of the poly(methyl methacrylate) (PMMA) matrix. (b) Sputtering of indium tin oxide (ITO) onto the PS NPs. The inset schematics show the ridge profile after the ITO deposition and its analogous refractive index profile, as experienced by incident light.

The nanophotonic electrode's surface morphology, specifically the effective period (P), was tailored by adjusting the polymer blend composition and the deposition conditions used to fabricate PS NPs. The AFM images displayed in **Figure 7.2a-c** give a qualitative impression of the ITO deposited onto the PS NP. The P of the ITO-coated NPs is deduced from the pair correlation function (PCF); see the details in Chapter 4. The PCF was used to derive the P from the AFM images. A P of 550 nm (see **Figure 7.2a**) was obtained using PS with a higher MW. Reducing the MW of PS in the blend mixture (PS/PMMA) to MW=5.50 kg·mol^{-1} from an original MW=8.21 kg·mol^{-1} leads to a decrease in the P-value of the ITO coated NPs from 550 to 310 nm (see **Figure 7.2b**). A small value of P is desirable to achieve efficient antireflective properties in broadband wavelength spectra.[228, 229] Nanostructured (NS) ITO with a P of 210 nm was obtained (see **Figure 7.2c**) by increasing the weight-ratio of PS in the PS/PMMA blend to 40:60 from an original composition of 30:70. The NS ITO size distribution with a P of 210 nm was experimentally analyzed, as shown in **Figure 7.2d**.

To assess the NS ITO's antireflective properties, we measured their transmittance and reflectance spectra (see **Figure 7.2e**). The optimized NS ITO electrode with a

P of 210 nm exhibited significantly reduced reflection and improved transmission for a broad range of wavelengths compared to the other configurations, see **Figure 7.2e**. Compared to the planar ITO electrode, the integrated transmittance weighted by the air mass 1.5 global (AM1.5G) spectrum between 300-1200 nm is $7\%_{rel}$ higher for the NS ITO electrode. This increased optical gain is due to the smaller period of the NS ITO in contrast to the incident wavelength, which allowed to suppress light scattering in the broadband wavelength regime and provided a gradual change in refractive index from the glass substrate (n_{sub}=1.51 at λ=600 nm) to ITO electrode (n_{ITO}=1.81 at λ=600 nm). This property ensures that the incident light does not encounter a sudden change in refractive index, which would cause a proportion of it to be reflected.

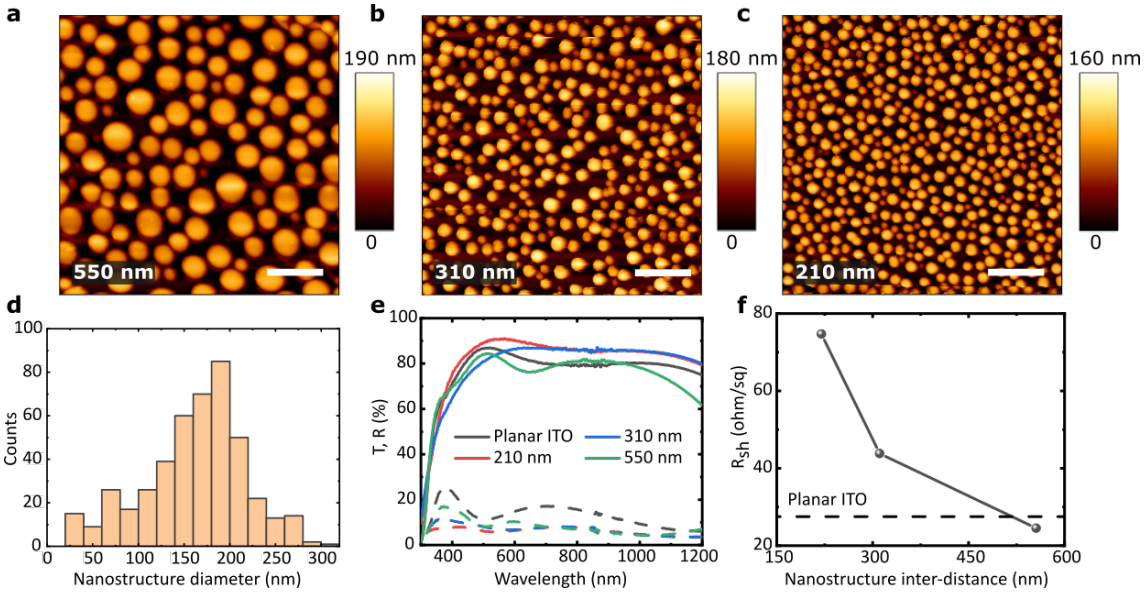

Figure 7.2. Influence of the PS NP array morphology on the opto-electrical properties of the NS ITO electrode. (a-c) AFM images of the nanostructured ITO electrode for an effective period (i.e., nanostructures inter-distance) of (a) 550 nm, (b) 310 nm, and (c) 210 nm. (d) Statistical analysis of the diameter of the nanostructures in the optimized nanostructured ITO electrode derived from AFM measurement. (e) Transmittance T and reflectance R, and (f) sheet resistance (Rsh) of the planar ITO electrode and the NS ITO electrode for effective period of 210 nm, 310 nm, and 550 nm. The scale bar represents 1 μm. Adapted with permission from Ref.[90]. © 2020 Optical Society of America.

Herein, it is essential to keep the electrical performance of the NS ITO at the same level as that of the planar one to translate the optical gain into solar cell device power. **Figure 7.2f** shows the sheet resistance (R_{sh}) values of the different investigated configurations. The R_{sh} of the champion NS ITO electrode was higher by 46 ohm/sq when compared to a planar ITO. This might be attributed to minor cracks in the NS ITO (for details, please refer to section 7.2) or the possible increased number of grain boundaries reducing charge carriers' mobility. To explore the NS ITO's impact on functional solar cells' performance, devices were subsequently fabricated according to the layout introduced in **Figure 7.3** using the champion NS ITO electrode.

7.2 Solar cell devices based on nanophotonic electrodes

The light in-coupling capability of solution-processed semi-transparent perovskite solar cell (PSC) devices based on NS ITO (P=210 nm) electrode ("NS ITO-PSC") was assessed by characterizing reference devices processed on an identical stack but without PS NPs ("Planar ITO-PSC"). The semi-transparent perovskite stack consists of an ITO front electrode, SnO_2-np, $Cs_{0.1}(MA_{0.17}FA_{0.83})_{0.9}Pb(I_{0.83}Br_{0.17})_3$, spiro-MeOTAD, MoO_x, and an ITO rear electrode. More details regarding the stack layers fabrication and their functionality are reported in Hossain *et al.*. study.[90] The device configuration and the associated layers' thicknesses are shown in **Figure 7.3**. In this study, the active illuminated area is 10.5 mm^2. **Figure 7.4a** and **b** show the cross-sectional scanning electron microscopy (SEM) images of the focused ion beam (FIB)-cut "Planar ITO-PSC" and "NS ITO-PSC" devices, respectively. For the latter, the conformal deposition of the SnO_2-np and perovskite layers on the top of NS ITO electrode leads to nanostructured film interfaces in the device stack. These nanostructured interfaces potentially can reduce PSC devices' reflection compared to their counterparts (see **Figure 7.4a**).

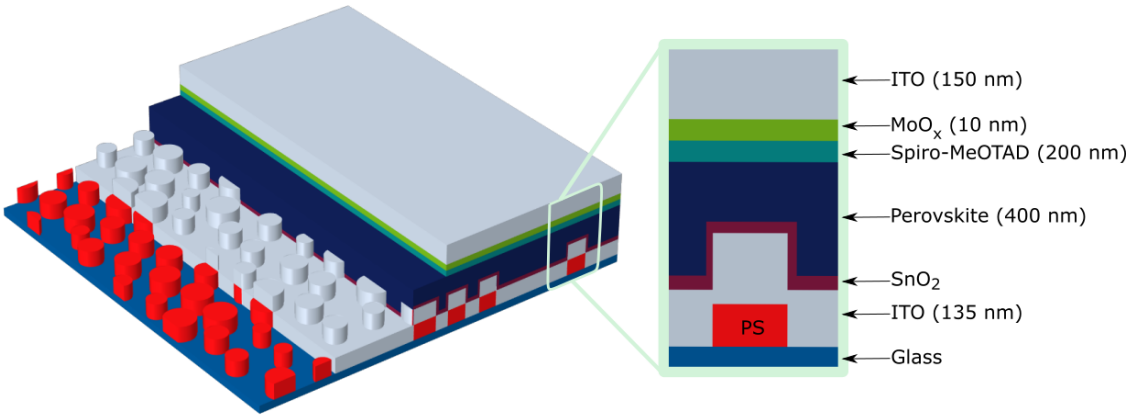

Figure 7.3. Schematic view of the semi-transparent perovskite solar cell (PSC) integrating the subwavelength disordered PS NP array in their front electrode. The fabricated stack, deposited on the PS NP array, consists of an ITO front electrode, electron transport layer made of SnO_2-np, perovskite active layer, hole transport layer (spiro-MeOTAD), and rear ITO electrode on the top of MoO_x buffer layer.

The light in-coupling properties of all devices were evaluated by measuring the overall solar cell device reflection spectra. Consistent with the reflectance values reported in **Figure 7.2e** for the NS ITO, the PSC devices processed on the top of NS ITO electrode exhibit significantly reduced reflection compared to "Planar ITO-PSC" devices (see **Figure 7.4c**). Moreover, a significant interferences reduction is achieved with respect to the planar design. **Figure 7.4d** shows the transmission through the "NS ITO-PSC" device, which overcomes the "Planar ITO-PSC" configuration below the perovskite material's bandgap. External quantum efficiency (EQE) spectra were acquired (see **Figure 7.5a**) to analyze how the reduced reflection losses below the perovskite material's bandgap translate for the charge carriers' generation and collection. Below λ=450 nm, the EQE of the "Planar ITO-PSC" configuration dominates that obtained with the "NS ITO-PSC" devices. This indicates a higher amount of parasitic absorption in the front NS ITO electrode.

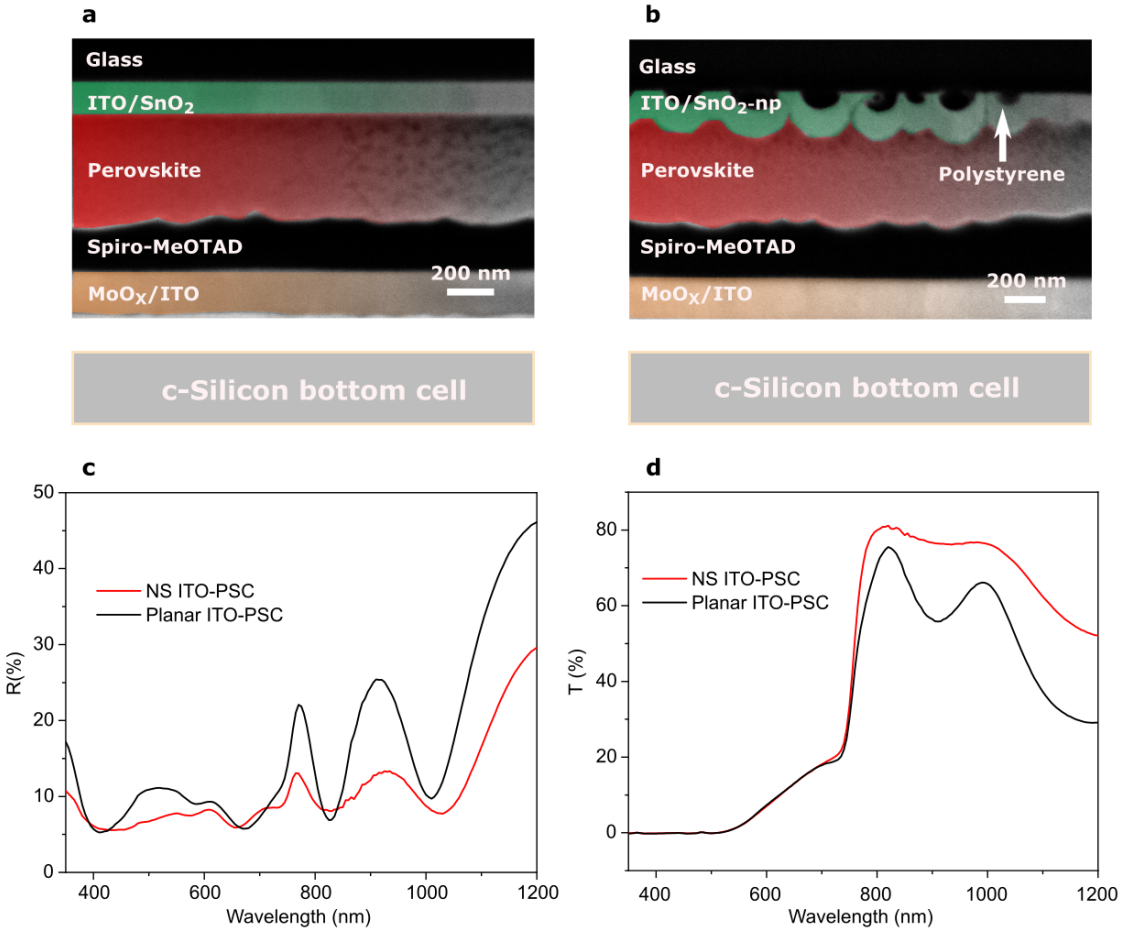

Figure 7.4. Improved light in-coupling properties of semi-transparent perovskite solar cell integrating the subwavelength NP array. FIB-cut SEM cross-section of (a) the perovskite solar cell deposited on the planar ITO coated substrates ("Planar ITO-PSC") and of (b) a similar thin-film stack processed atop the nanostructured ITO ("NS ITO-PSC"). (c) Reflectance (R), and (d) transmittance (T) spectrum of the solar cell based on the NS ITO design, benchmarked against planar ITO type. All spectra were acquired under close to normal incidence. Adapted with permission from Ref.[90]. © 2020 Optical Society of America.

However, "NS ITO-PSC" devices exhibit improved EQE above 450 nm compared to the "Planar ITO-PSC" reference. Overall, an improvement of $2\%_{rel}$ in the short current density (J_{SC}) is achieved for "NS ITO-PSC" devices (see **Figure 7.5b**). In contrast, the electrical performances (i.e., open-circuit voltage (V_{OC}) and fill factor (FF)) of the "NS ITO-PSC" devices reduced compared to "Planar ITO-PSC" devices, as highlighted in **Table 7.1**. The electrical losses might be due to the substantial surface area increase and the highly defective regions in the NS ITO layer (see **Figure 7.4b**). Consequently, this led to a decrease in the charge carrier's lifetime (measured using time-resolved photoluminescence (PL) spectroscopy) as compared to the planar reference devices (for details, refer to the PL measurements in Ref.[90]). In general, a reduction in carrier lifetime leads to high non-radiative recombination. Hence, the power conversion efficiency (PCE) of the semi-transparent "NS ITO-PSC" devices is reduced compared to the "Planar ITO-PSC" reference devices (see **Table 7.1**).

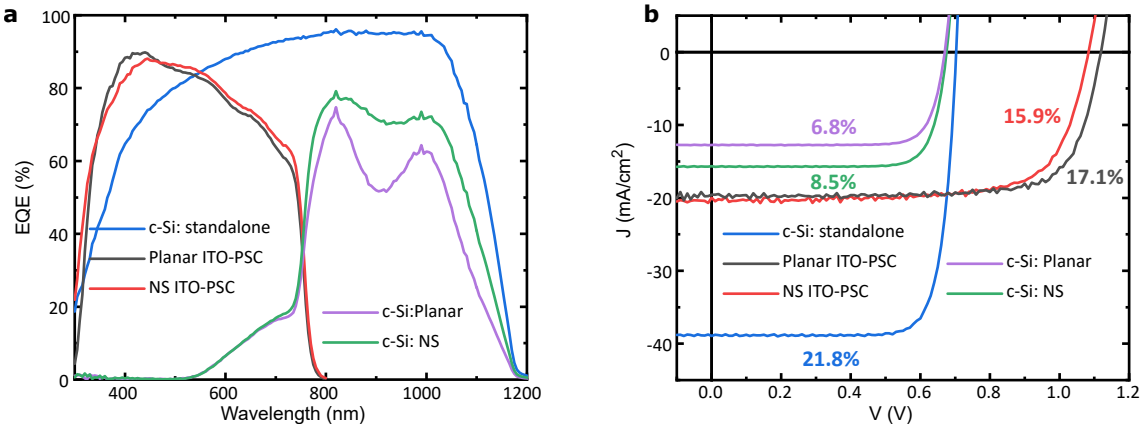

Figure 7.5. (a) External quantum efficiency (EQE) and (b) current density - voltage (J-V) characteristic of the perovskite solar cells with nanostructured ITO ("NS ITO-PSC") and planar ITO ("Planar ITO-PSC"), and stand-alone c-Si solar cell. Also, the measured EQE and J-V of c-Si solar cell using "NS ITO-PSC" and "Planar ITO-PSC" as a filter on the top. Adapted with permission from Ref.[90]. © 2020 Optical Society of America.

As mentioned above, the front NS ITO in the semi-transparent "NS ITO-PSC" configuration asides from their antireflective photonic effects above the perovskite material's band-gap leads to reduced reflection below its band-gap, as highlighted in **Figure 7.4c**. This reduction of the reflection loss, which leads to an improvement in the transmission (see **Figure 7.4d**), is favorable for efficient light management in tandem configuration. To utilize this transmission gain, mechanically-stacked 4 T perovskite/c-Si tandem solar cells (with an air gap between the perovskite and c-Si solar cell) were studied (see **Figure 7.4a** and **b**). More details regarding the preparation of the bottom c-Si solar cells are given in Hossain *et al.*. study.[90] **Figure 7.5a** gives the c-Si devices' EQE with the NS and planar front ITO electrode in PSC/c-Si tandem configuration. The EQE of the bottom c-Si solar cell in NS ITO-PSC/c-Si tandem configuration is enhanced for the entire range of wavelengths (780–1200 nm), leading to an enhancement in J_{SC} up to 2.9 mA/cm^2 (23%$_{rel}$) compared to the planar reference device (see **Figure 7.5b**). The improvement in the sum of J_{SC} generated by the top and the bottom cell is 10%$_{rel}$ higher for the NS ITO-based PSC/c-Si tandem cells compared to the planar ITO-PSC/c-Si configurations (see **Figure 7.5b**). Nevertheless, the PCE gain in PSC/c-Si tandem solar cells with NS ITO is only 0.5% absolute (see **Table 7.1**).

Table 7.1. Electrical parameters of the planar and NS ITO based PSC, stand-alone c-Si and their tandem (PSC/c-Si) solar cell configurations.

Parameters	Planar ITO-PSC	NS ITO -PSC	c-Si: stand-alone	c-Si: Planar	c-Si: NS	ITO-PSC/ c-Si tandem	NS ITO-PSC/c-Si
V_{OC} (V)	1.12	1.08	0.70	0.67	0.67	-	-
J_{SC} (mA·cm^{-2})	19.6	20.0	38.9	12.8	15.7	-	-
FF	0.78	0.73	0.80	0.80	0.80	-	-
PCE (%)	17.1	15.9	21.8	6.8	8.5	23.9	24.4
SPCE (%)	16.0	15.0	-	-	-	22.8[a]	23.5[a]

[a]The stabilized PCE (SPCE) for tandem devices is calculated from the PCE of the top semitransparent PSC (after 5 min) and of the bottom c-Si cell at the maximum power point.

The limited gain in the PSC/c-Si with NS ITO compared to reference planar solar cells is attributed to the electrical loss (V_{OC} and FF) in the top NS ITO-based PSCs. Therefore, it is essential to evaluate the trade-off between the electrical (V_{OC} and FF) and optical properties (J_{SC}) in NS ITO-based PSC devices to enhance further the PCE gain of NS ITO-based PSC/c-Si devices. In this regards, one strategy is to mitigate the crack that is visible in NS ITO (see **Figure 7.4b**) by

1. optimizing the deposition condition of the ITO,
2. changing the phase-separated NPs material from PS to temperature stable one, or
3. transferring the phase-separated NPs to glass substrate via dry or wet etching using the phase-separated NPs made of PS as an etching mask.

7.3 Summary and discussion

This study presented antireflective nanostructures fabricated using the phase separation process for efficient light management in perovskite/c-Si tandem solar cells. The phase-separated nanopillars (NPs) enabled the conformal deposition of the sputtered front ITO electrode. The characterization of the front nanostructured (NS) ITO electrode's optical performance over λ=300-1200 nm reveals, a $7\%_{rel}$ transmission gain compared to the planar reference. The transmission gain can be largely attributed to the reduced reflection losses (through the beneficial optical effects of the subwavelength NPs). The optical gain in the NS ITO electrode comes with an increase in the sheet resistance when compared to a planar ITO reference.

Semi-transparent perovskite solar cells (PSCs) fabricated on top of the champion NS ITO show an increase in the J_{SC} of $2\%_{rel}$. In contrast, the NS ITO PSC's electrical performance (V_{OC} and FF) was reduced. The electrical loss might be due to the substantial surface area increase caused by nanopatterning the thin film layers of the PSC device and the highly defective regions introduced in the NS ITO layer. Compared to the top PSC solar cells in NS ITO PSC/c-Si tandem configurations, the J_{SC} improvement in the bottom solar cell (c-Si) due to the enhanced transmittance in low energy photons regime is more prominent ($23\%_{rel}$ vs. $2\%_{rel}$). Thus, it enhanced the PCE of the bottom c-Si solar cell by 1.7% absolute. For PSC/c-Si tandem configuration, however, the PCE gain is only 0.5%. The limited PCE gain in the tandem configuration is caused by the loss in V_{OC} and FF of the top solar cells. The electrical loss can be overcome by optimizing the front ITO deposition condition and the antireflective nanostructures material property.

Overall, our results demonstrate that phase-separated nanostructures can be applied to solution-processed perovskite solar cells and pave the way to increased power conversion efficiencies through light management not only in single perovskite junction but also in perovskite-silicon tandem solar cells. The developed nanostructured ITO application is not limited to solar cells; its application can be extended to organic light-emitting diodes to fabricate very efficient and transparent devices.

8. Planarized low- and high-index light outcoupling structures for OLEDs

This chapter illustrates the application of phase-separated nanostructures presented in Chapters 5-7 as a light outcoupling layer for organic light-emitting diodes (OLEDs). In contrast to the approaches shown in the previous chapters for solar cells, OLED light outcoupling layer on a substrate is planarized to obtain a physically flat substrate surface but optically undulated in a manner that enables optical scattering. First, a review of OLEDs' well-known light outcoupling layers is given, focusing on internal light outcoupling layers. Then, fabrication of low- and high-index light scattering nanostructures using polymer blend lithography is discussed, followed by optically favorable planarization layers and the morphology and optical characteristics of final light outcoupling layers. As a proof-of-concept, the light outcoupling capability of planarized layers is tested by depositing an OLED stack on top. Parts of the results presented in this chapter have previously been published in the journal of Advanced Optical Materials.[142] In this study, Dominik Theobald simulated mode profiles of normalized electric field intensities in OLED devices.

The technical challenge of the OLED devices discussed briefly in Chapter 2 is that their external quantum efficiency is limited by the light outcoupling efficiency of the device, which is indeed unresolved because of the optical loss reduction in three main light modes: surface plasmon polaritons (SPP), waveguided and substrate. This underlines the need for simultaneously tackling the losses occurring within the thin films stack (to ameliorate the so-called "internal outcoupling") and in the substrate (improvement of the "external outcoupling"). This chapter focuses on internal light outcoupling layers. These layers can be achieved by integrating volumetric[241–243] or compact[91, 154, 244–247] based system, and of periodic[154, 244] or stochastic[91, 245–247] nanostructures configuration. Volumetric scattering layers can be realized by embedding nanoparticles in polymer layers.[241–243] However, the position of the nanoparticles within the polymer matrix is random, and agglomeration of nanoparticles tends to introduce additional and unwanted randomness into the system (affecting the size and shape of the scattering objects), which may also trigger surface roughness. Besides, achieving an appropriate mean refractive index and ensuring a sufficiently high refractive index contrast between the nanoparticles and the matrix material as

required for efficient scattering is challenging. Moreover, these films exhibit strong haze (i.e., diffused fraction of the overall transmitted light) with significantly reduced overall transmission[248, 249] and possess a thickness ranging from a few μm up to several tens of μm.[242, 249, 250] Alternatively, more compact (i.e., with a thickness of a few hundreds of nanometers) periodic[154, 244] or disordered[91, 245–247] scatterers can be engineered to achieve a strong overlap of the trapped modes with the light outcoupling elements, which fosters light outcoupling.

The diffraction properties of compact periodic structures such as 1D or 2D planar gratings are easily controlled, albeit optimized for a limited spectral and angular range.[251, 252] As a result, they lead to color-distortion effects when applied to white OLEDs.[253] Alternatively, disordered systems have been employed to allow efficient light outcoupling while maintaining stable angular and spectral emission profiles.[91, 245–247] For example, 2D corrugated substrates have been investigated by forming buckling patterns (originating from compressive stress).[254, 255] These patterns form a network without any preferred orientation (directional randomness), nevertheless possess a characteristic wavelength and a tunable depth that can be adjusted for broadband devices such as white OLEDs. On the other hand, scattering layers made of isolated nano-objects lying on a plane (referred to as 2D structures) have been obtained by dewetting a thin metallic layer at high temperatures, leading to non-ordered metallic islands. The latter were either directly employed[256] or used as etching masks to create depressions around them in the underlying layer.[257] It was shown that the mean base radius of the islands was correlated to the initial metallic layer thickness and as such, could be tuned to improve the efficiency of OLEDs.[256] However, the shape of the islands is hardly controllable, and a high temperature of up to 400-500 °C is required for the annealing step to initiate the dewetting process. Due to the factors above, the metal dewetting approach's practical relevance for fabricating light outcoupling layers is limited. This issue calls for alternative patterning approaches that offer tunable optical scattering layers with low cost for practical light management in OLED applications.

In this study, polymer blend lithography (PBL) is used to fabricate compact 2D disordered light scattering layers at room temperature. The following sections illustrate that PBL enables engineering morphologies of light scattering layers over different large-area substrates such as glass and plastic foils. Herein, prior to the OLED fabrication, the scattering nanostructures are planarized with high (see **Figure 8.1a**) or low (see **Figure 8.1b**) index material. These layers are primarily needed to achieve efficient OLED devices with stable electrical characteristics. In what follows, PBL is introduced first for fabricating low- and high-optical index light scattering layers that comply with the mass production of large-scale lighting panel requirements. Then, key parameters to tune the surface morphologies of the resulting scattering layers and their optical properties are briefly discussed. In particular, this work addresses the challenge of achieving suitable planarization materials for the scattering layers and their optical shortcomings in OLED devices. Finally, the light outcoupling capability of the resulting devices following one of the routes is evaluated by comparing them with OLED devices processed on the top of planar glass substrates. The developed approach is demonstrated using bottom-emitting monochromatic (emission peak at λ=520 nm) OLED devices and can also be applied to white OLEDs.

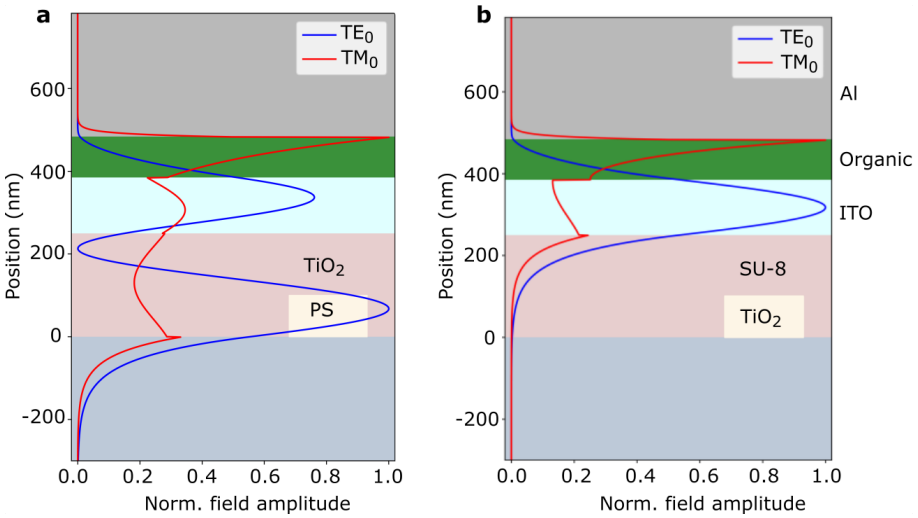

Figure 8.1. Schematic illustration of the mode profiles of the normalized electric field intensities in the light outcoupling layer, indium tin oxide (ITO), and OLED thin-film stack with change in the planarization layer and scattering nanopillars (NPs) refractive index (n). Scattering NPs and planarization layer made of (a) polystyrene (PS, n=1.59 at λ = 520 nm) and titania (TiO_2, n=2.04 at λ=520 nm), and (b) TiO_2 (n=2.04 at λ=520 nm) and SU-8 (n=1.56 at λ=520 nm), respectively. The computation of the mode profiles was carried out using scattering NPs and a planarization layer with a thickness of 100 nm and 250 nm, respectively. The blue and red lines represent the field distribution of the TE and TM modes.

8.1 Design of planarized light outcoupling layers

For the fabrication of light outcoupling layers, PBL based on the demixing of two incompatible polymers, here poly(methyl methacrylate) (PMMA) and polystyrene (PS), is investigated (for more details, refer to Chapter 4). The light outcoupling layers are formed on top of the desired substrates (glass and flexible foil) through spin-coating starting from an optimized binary polymer mixture. The fabrication of low-and high-index light extraction layers is briefly discussed in sections 8.1.1 and 8.1.2, along with the optically favorable planarization layer for their integration in OLED devices.

8.1.1 Low-index light scattering nanopillars

Phase-separated PS NPs (after the selective development of the PMMA matrix) shown in **Figure 8.2a** were investigated as a low-index scattering layer. To facilitate their integration in an OLED stack, high-index materials ($n \approx n_{ITO}$) are investigated as a planarization layer (see **Figure 8.2b,c**). A key advantage herein is the refractive index matching between the planarization layer and the anode material of an OLED (i.e, ITO) that minimizes internal reflections and fosters the leakage of trapped waveguided modes into the light outcoupling layer, as highlighted in **Figure 8.1a**.

To form the planarization layer, either a titania solution based on titanium diisopropoxide bis(acetylacetonate) precursor or zirconium dioxide (ZrO_2) nanoparticles dispersed in 1-methoxy-2-propanolacetate was dropped onto the PS nanostructures and then spin-coated, as illustrated in **Figure 8.2**. The wavelength-dependent optical refractive indices of the spin-coated ZrO_2 layer are shown in **Figure 8.3a**.

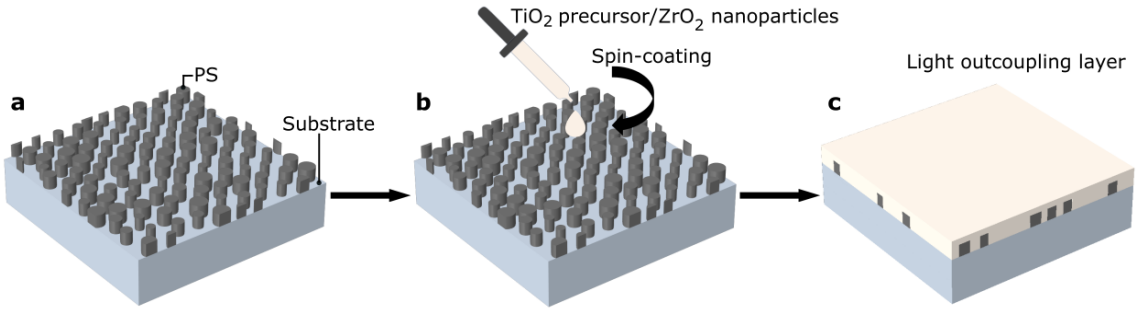

Figure 8.2. Schematic illustration of the fabrication process for low-index scattering nanopillars (PS NPs) based light outcoupling layer. (a) Phase-separated PS NPs. (b) Spin-coating of high-index TiO_2 precursor/ZrO_2 planarization layer onto the PS NPs. (c) Formation of a light outcoupling layer composed of low-index scattering elements (PS NPs) and a high-index planarization layer (TiO_2 or ZrO_2).

Titania layers formed by spin-coating were baked on a hot plate at a temperature (T) of 190 °C and 500 °C for 10 and 60 min, respectively, to get high index planarization layers. The wavelength-dependent optical refractive indices of the resulting titania layers as a function of baking temperature are shown in **Figure 8.3b**. An increase of the refractive index of the titania layer from n=1.77 (T=25 °C) to n=2.1 (T=500 °C) at $\lambda = 520$ nm was achieved through baking. The optical index of the titania layer baked at high-T and the room-T processed ZrO_2 nanoparticles is comparable to that of ITO. Such layers promote the overlap of the waveguide modes with the light outcoupling PS NPs (see **Figure 8.1a**). However, the resulting light outcoupling layers based on these planarization materials coated onto the light scattering PS NPs (**Figure 8.4a**) exhibit small cracks on the surface (see **Figure 8.4b,c**). Such layers induce an internal short circuit in OLED devices (for more details, please refer to our work[258]). To mitigate the limitations of this approach, the inverse material's architecture (i.e., a low-index polymer planarization layer applied onto high-index light scattering NPs) has been investigated in the next section.

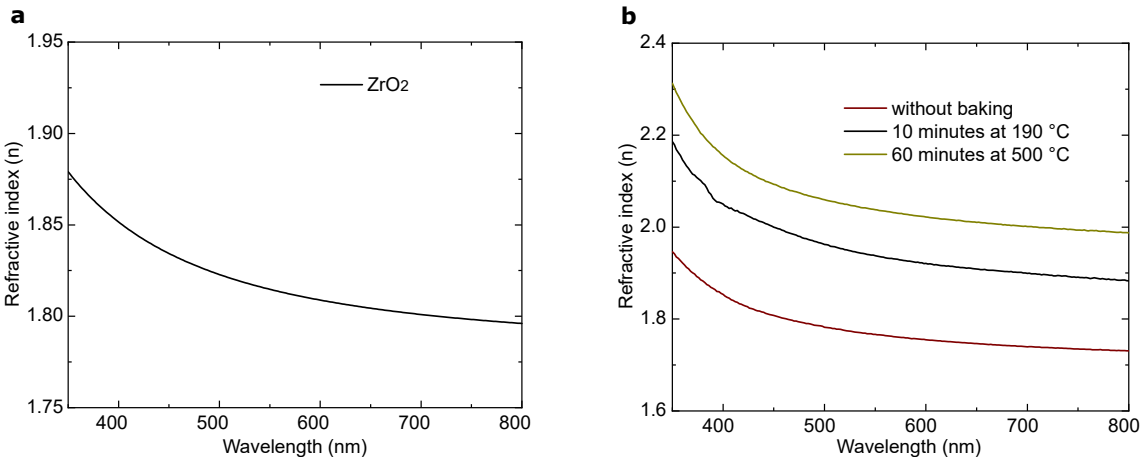

Figure 8.3. Investigated planarization materials with optical index comparable to the ITO electrode. Refractive indices of spin-coated (a) ZrO_2 nanoparticles and (b) TiO_2 precursor before and after baking at different temperatures.

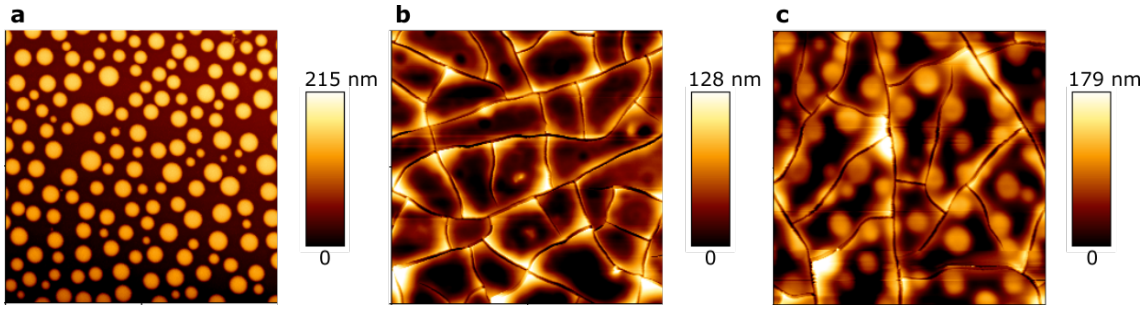

Figure 8.4. Topographical characterization of the internal light outcoupling layers based on a low-index scattering elements and high-index planarization layers. Atomic force microscopy (AFM) images of (a) the disordered PS NPs, and after spin-coating (b) TiO_2 and (c) ZrO_2 on the top of PS NPs (a). The scale bar represents 2 μm in all AFM images.

8.1.2 High-index light scattering nanopillars

As high-index light scattering NPs, titania material-based nanostructures were investigated. The titania nanostructures were fabricated using two different techniques: (i) a soft imprint nanopatterning method (section 8.1.2.1), which exploits flexible patterned stamps replicated from phase-separated PS NPs, and (ii) the lift-off method (section 8.1.2.2) that involves electron beam (e-beam) deposition of titania in the phase-separated PMMA matrix with nanoholes and subsequent lift-off.

8.1.2.1 Nanoimprinted titania scattering layers

Figure 8.5 shows the schematic illustration of the fabrication sequence for high-index titania nanostructures based on soft imprint lithography. Soft stamps made of poly-(dimethylsiloxane) (PDMS) replicated from the phase-separated PS NPs (see **Figure 8.5a**) were used to nanopattern sol-gel-derived titania precursor as shown in **Figure 8.5b**. The sol-gel-derived titania precursor was prepared by dissolving titanium diisopropoxide bis (acetylacetonate) precursor in ethanol. Then, it was spin-coated on glass substrates and imprinted using the PDMS stamps before its solvent evaporate. Before the imprinting, the top surface of the PDMS stamps was spin-coated with hexamethyldisilazane. This coating allows detaching the stamps easily from the titania layers after the imprinting process. The nanoimprinting pressure was applied on the PDMS stamps using manually placed weights (see **Figure 8.5b**). As a final step, the titania layers were baked to remove the remaining solvent while still in contact with the PDMS stamps. After baking, the PDMS stamps were carefully separated from the titania layer. **Figure 8.6** display the photographs of the resulting samples with their corresponding scanning electron microscopy (SEM) images. Pattern transfer from the PDMS to the titania layer was achieved successfully. However, the replication process was not reproducible, as highlighted in **Figure 8.6a,b** due to the lack of accurate control of the PDMS placement onto the titania layer and the applied pressure. Details of this study are reported in our work.[259] A standard solution to overcome the issue above involves the use of special (automated) nanoimprint equipment.[260]

In the next section, as an alternative material to the solution-processed titania layer, evaporated titania is investigated to fabricate high-index light scattering NPs.

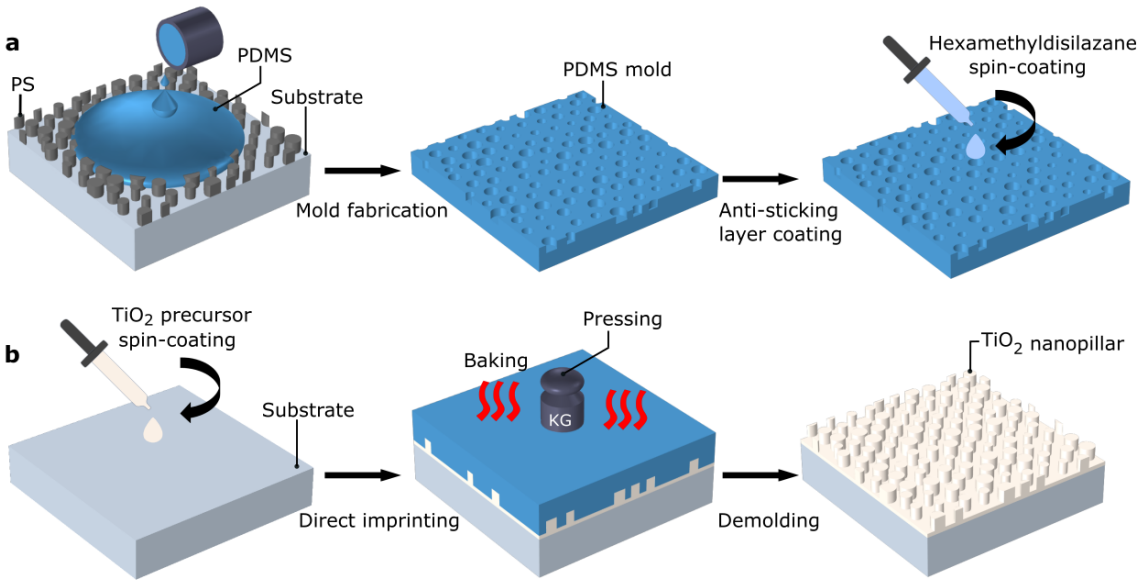

Figure 8.5. Schematic illustration of the fabrication process for high-index light scattering TiO_2 NPs using nanoimprint lithography. (a) PDMS stamp fabrication by pouring a 1:10 mixture of Sylgard 184A and Sylgard 184B (Dow Corning) onto the phase-separated PS NPs master mold. (b) Then, the replicated PDMS stamp was placed over the spin-coated TiO_2 precursor, and pressure was applied at 80 °C for 5 min. The PDMS stamp was then removed, and the resulting TiO_2 NPs on the glass substrate was baked at 190 or 500 °C to increase its refractive index.

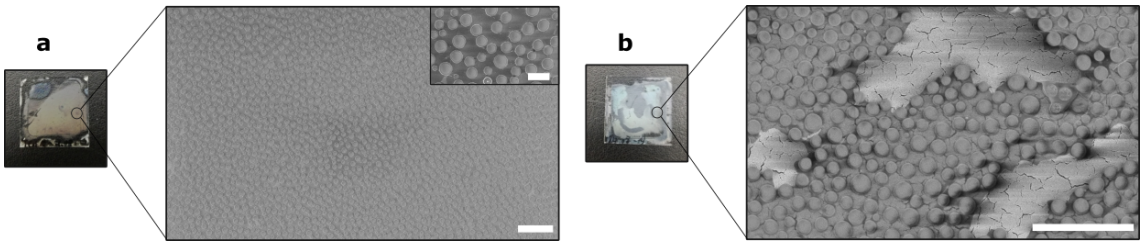

Figure 8.6. Nanoimprinted TiO_2 precursor with manually controlled imprinting pressure. Photographs of imprinted samples (16 mm × 16 mm) with (a) homogeneous and (b) inhomogeneous distribution of TiO_2 NPs. The main scale bar in the SEM images represents 5 μm and 1 μm for the inset SEM image (a).

8.1.2.2 Evaporated titania based scattering layers

Herein, polydisperse TiO_2 NPs are prepared by combining a polymeric self-assembly matrix and a subsequent e-beam evaporation and lift-off process following the sequence illustrated in **Figure 8.7**. Polymer blend solutions of PS (MW=34 kg·mol^{-1}) and PMMA (MW=15 kg·mol^{-1}) with different PS/PMMA weight-ratios (PS/PMMA=2:8, 3:7 and 4:6) were used to produce the light scattering layers. Upon selective development of the PS domains after phase separation (see **Figure 8.7a**), a polymer matrix (made of PMMA) with nanoholes is obtained (see **Figure 8.7b**). The nanostructured polymer matrix was then coated by an e-beam evaporated titania layer (measured refractive index (n)=2.1 at λ= 520 nm), as illustrated in **Figure 8.7c**. The sacrificial layer (polymer matrix) was lifted off through an ultrasonic agitated acetone bath (see **Figure 8.7d**) to obtain the light scattering TiO_2 NPs. Prior to

OLED deposition, a planarization layer was coated onto the TiO_2 NPs using a low index transparent UV-curable film (n=1.56 at λ=520 nm[261]) fabricated from the epoxy resin (SU-8). The epoxy resin has a refractive index comparable to the glass substrate and negligible absorption at wavelengths greater than 380 nm, making it a good candidate for planarizing the TiO_2 NPs. Meanwhile, the large refractive index contrast between the epoxy resin and TiO_2 NPs ensures efficient light scattering, needed for outcoupling the (wave)guided modes.

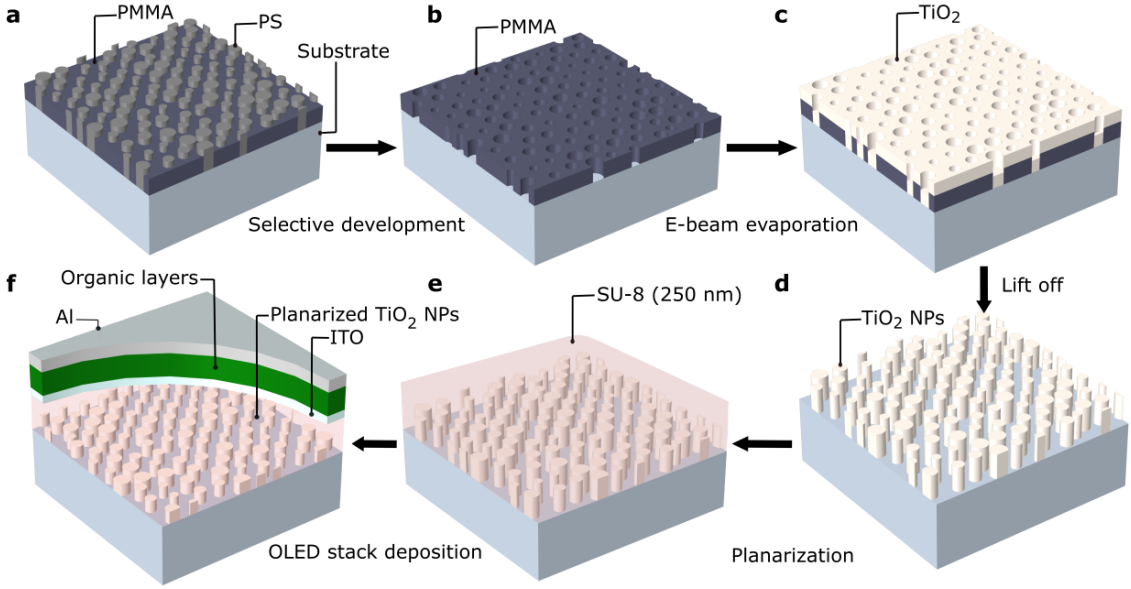

Figure 8.7. Schematic illustration of the fabrication process for bottom-emitting OLEDs integrating planarized TiO_2 NPs. (a) phase separation of the polymer blend, (b) selective development of the PS NPs, (c) e-beam evaporation of TiO_2 onto the nanopatterned PMMA matrix, (d) subsequent lift-off process, and (e) planarization of the TiO_2 NPs with SU-8 polymer prior to the (f) deposition of a transparent and conductive oxide layer made of ITO and an OLED stack atop. The final OLED stack consists of 5 nm MoO_3, 15 nm m-MTDATA, 20 nm m-MTDATA:$Ir(ppy)_3$, 20 nm BPhen:$Ir(ppy)_3$, 40 nm BPhen, 1 nm LiF, 100 nm Al.

Figure 8.8a-c highlights the SEM images of the fabricated PMMA matrix with different filling fractions of nanoholes. The diameter size distribution of the nanoholes in the polymer matrix covers a range of 250-780 nm to enable an efficient scattering over the whole visible spectrum. The nanopatterned polymeric matrices forming the lift-off mask on a flexible plastic foil (**Figure 8.8d**) and on a glass substrate (**Figure 8.8e**), present examples that demonstrate the versatility of these processes in terms of film uniformity and phase-separated nanostructures distribution. A TiO_2 layer with a thickness of 100 nm is deposited onto these polymeric matrices to form the TiO_2 NPs. The selected TiO_2 thickness value is within the polymeric matrix film thickness range, thereby facilitating the lift-off process. AFM images of the resulting TiO_2 NPs after washing the lift-off mask are shown in **Figure 8.9a-c**. These AFM images were used to determine the surface coverage (SC) of the resulting NPs prior to planarization. The calculated SC of the TiO_2 NPs is 19%, 33%, and 50% for the different polymer blend weight ratios. The planarization of the 100 nm thick TiO_2 NPs using a transparent UV-curable film can be seen in the focused ion beam

(FIB)-cut SEM cross-section in the inset of **Figure 8.10a**. It is evident that the nanostructures are completely covered by the epoxy resin, which results in a planar interface that facilitates the processing of the OLED stack atop. The thickness of the planarization layer is only 250 nm, which ensures a high overlap of the waveguided modes with the TiO_2 NPs. The thin line-like features at the rim of the TiO_2 NPs (see inset image of **Figure 8.10a**) most likely stem from evaporated material on the sidewalls. It does not significantly impact the optical properties of the scattering layer.

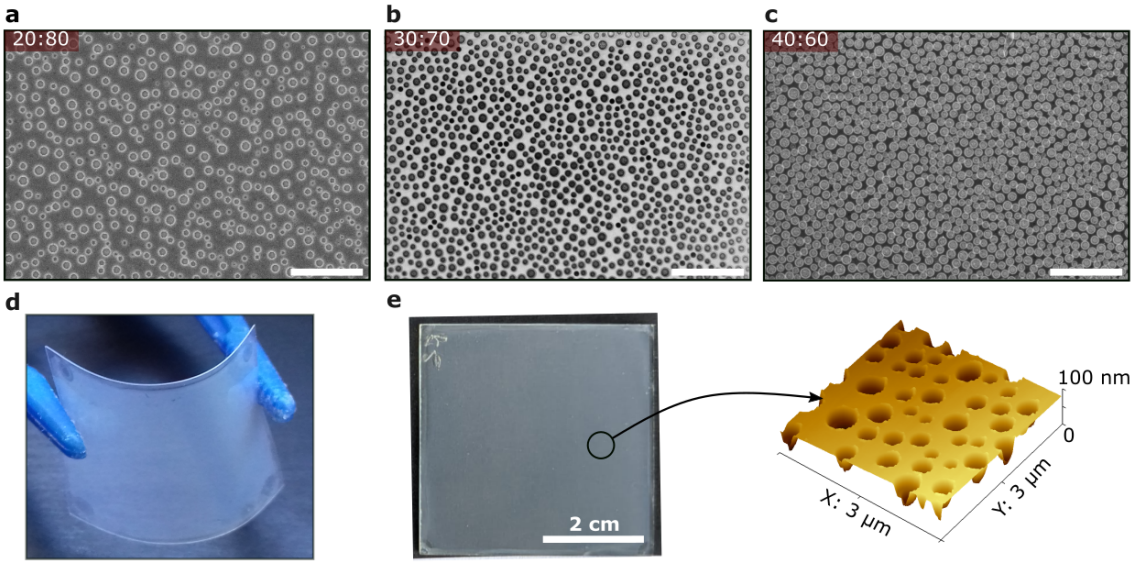

Figure 8.8. Nanostructured polymeric matrix on a glass substrate and flexible plastic substrate. SEM images of the polymeric matrix prepared using different weight-ratios of PS/PMMA= (a) 20:80, (b) 30:70 and (c) 40:60. The scale bar represents 3 μm in all SEM images. Photograph of the sample fabricated using PS/PMMA=40:60 on (d) plastic foil and (e) glass after the selective development of the PS phase. The inset 3D AFM image shows the nanoholes with an average depth of 100 nm in the polymeric matrix.

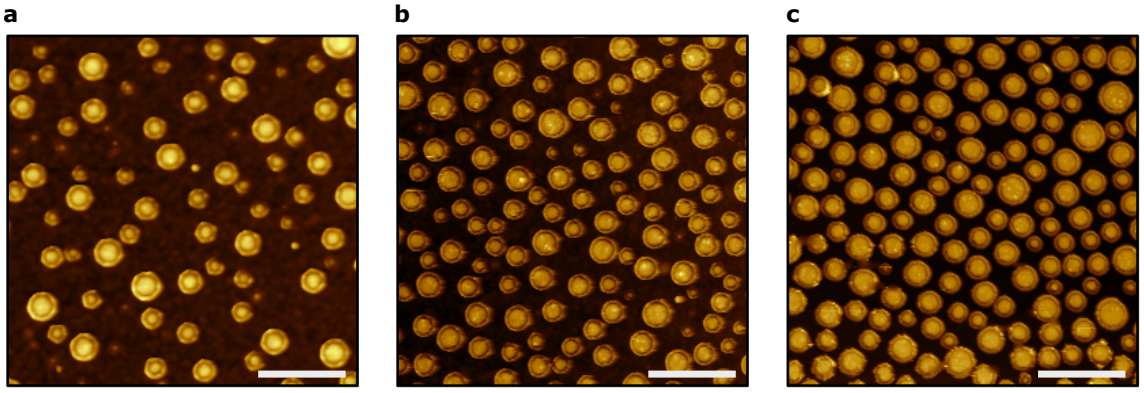

Figure 8.9. Topographical characterization of the internal light outcoupling layer. AFM images of uniformly distributed TiO_2 NPs with a mean height of 100 nm and SC of (a) 19%, (b) 33% and (c) 50%. The scale bar represents 2 μm in all AFM images. Adapted with permission from Ref.[142], © John Wiley & Sons.

To assess the light scattering properties of the planarized TiO_2 NPs, their overall and solely diffused transmittance spectra are measured for light emerging out of the glass substrate (see **Figure 8.10**). The average transmittance ranged between 90.6% and 91.1% at (λ= 520 nm), compared to the 91.2% for the reference glass substrate (see **Figure 8.10a**). In contrast, the optical transmittance of light outcoupling layers based on dewetted metallic (Ag) nanostructures[256] and volumetric scattering layer [250] decreased by more than 10% over the visible range when compared to bare glass. This is notably much higher than the value reported in this work, indicating that the developed scattering layers couple more photons to the substrate with limited parasitic absorption. As reported in **Figure 8.10b**, the scattering layer with SC=50% has the highest diffuse transmittance, implying that the SC of the TiO_2 NPs is an essential factor in reaching the appropriate light scattering regime.

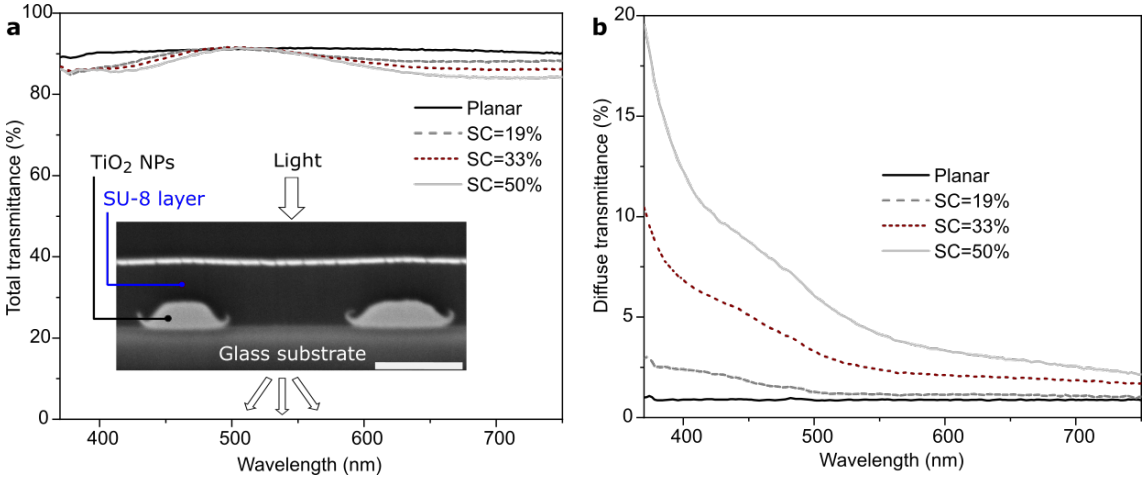

Figure 8.10. Measured (a) total and (b) diffuse transmittance with different SC of planarized TiO_2 NPs and a planar glass ("Planar") over the visible spectrum (under close to normal incidence). The inset shows a FIB-cut SEM cross-section of planarized TiO_2 NPs and depicts the measurement setup. The scale bar represents 350 nm. Adapted with permission from Ref.[142], © John Wiley & Sons.

To demonstrate the promising potential of these optical properties, the planarized TiO_2 NPs are integrated inside monochromatic, bottom-emitting OLEDs according to the layout introduced in **Figure 8.7f**.

8.2 OLED devices based on high-index scattering layers

The OLED devices incorporating the planarized TiO_2 NPs were benchmarked against devices relying on planar substrates. Owing to the planarization layer, almost no change in the electrical characteristics of the OLEDs was observed even in high voltage regions, as shown in **Figure 8.11a**. **Figure 8.11b** highlights the substantial light-extraction increase following the integration of the planarized TiO_2 NPs and reveals that the scattering effect of the TiO_2 NPs induced more light emission at lower power compared to the reference OLED. At 1000 cd/m^2, the operating voltage of both devices was 4.5 V, whereas the current efficiency is enhanced from 50 cd/A to 61 cd/A as shown in **Figure 8.11b** for configuration with SC=50%. This corresponds to a relative increase of 22% compared to a reference OLED device.

Similar behavior can be seen on the same plot for power efficiency. The OLEDs with SC=50% show an efficiency of 44 lm/W, compared to 36 lm/W, both examined at 1000 cd/m^2.

The dependence of OLED light emission on the SC of the TiO_2 NPs is also investigated. At 1000 cd/m^2, an increase of about 10% of the current efficiency and the power efficiency is obtained for the configuration with SC=33%. However, at low TiO_2 NPs SC, slight or no improvement in light efficiency was observed. For example, the configuration with SC=19% only shows a 4% improvement in current efficiency and power efficiency. This is due to the fact that at low TiO_2 NPs SC, the scattering layer shows low diffuse transmittance and hence poor optical scattering (see **Figure 8.10b**).

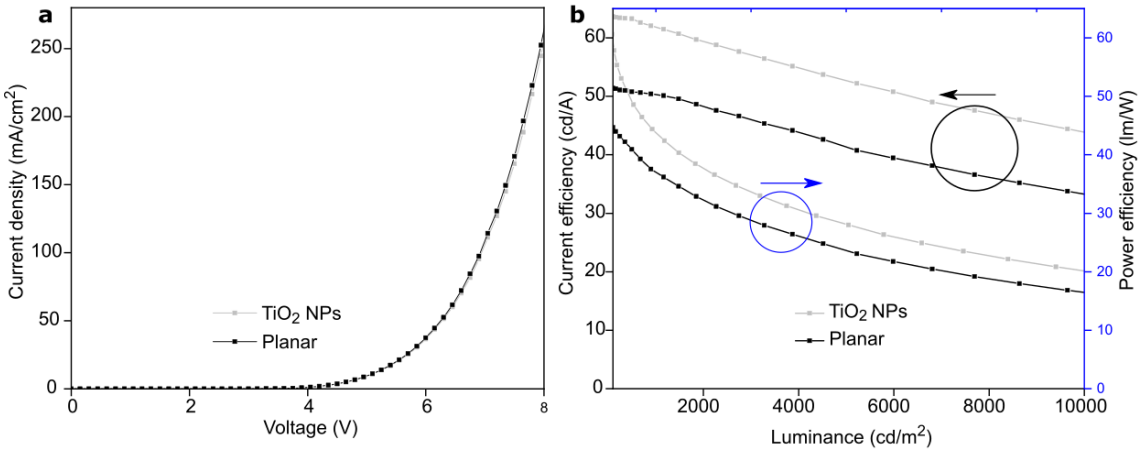

Figure 8.11. Optoelectronic characteristics of green light-emitting OLEDs without and with the compact internal light extraction layer. (a) Current density-voltage (J-V) characteristics. (b) Current and power efficiency of OLEDs with and without planarized TiO_2 NPs. The SC of TiO_2 NPs is 50%. The performance data shown is that of a representative sample; however, 8 OLEDs (each with a pixel area of 10 mm^2) on 25 mm × 25 mm substrates were tested and led to a similar enhancement. Adapted with permission from Ref.[142], © John Wiley & Sons.

The effect of the planarized TiO_2 NPs on the angular emission profile of the fabricated OLED devices is analyzed using a spectrometer pointing towards the sample, which was mounted on a rotating stage (for more details, refer to Chapter 3). **Figure 8.12a** shows the angular dependent normalized radiant intensity of the OLED devices with and without the planarized TiO_2 NPs. It can be noted that the OLED with scattering layer (SC=50%) and the reference OLED follow the angular profile of an ideal Lambertian emitter below 30°. However, the emission profile deviates from the Lambertian reference above 30° for a reference device compared to the OLED device with light scattering TiO_2 NPs. This is attributed to a weak microcavity effect in planar OLED device.[262] The emission spectra highlighted in **Figure 8.12b-c** also demonstrate that the controlled amount of optical scattering can reduce the angular spectral shift observed for planar devices. The reduced viewing angle dependence for the device with planarized TiO_2 NPs compared to the planar device supports the suitability of the developed light outcoupling layer for general lighting applications.

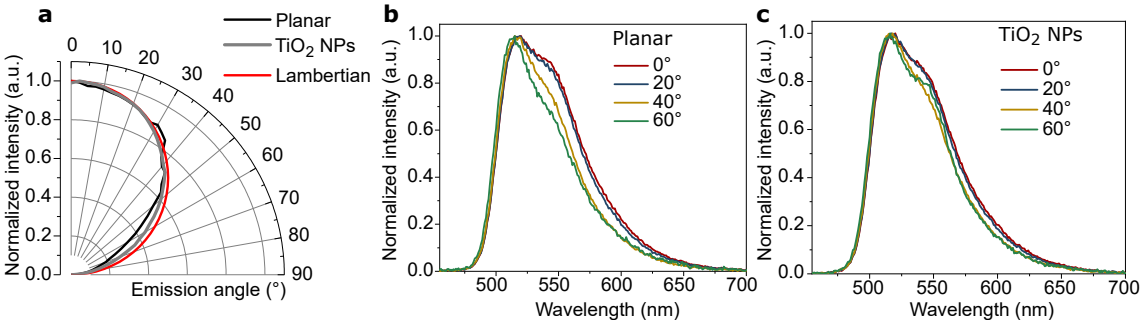

Figure 8.12. Angular emission profile of an OLED with attached macroscopic extraction hemisphere. (a) Angular distribution of normalized intensity of an OLED at a peak emission wavelength of 520 nm with and without planarized TiO_2 NPs. The redline represents Lambertian emission. Normalized spectra at 0°, 20°, 40°, and 60° emission angles of an OLED (b) without and (c) with scattering layer. Adapted with permission from Ref.[142], © John Wiley & Sons.

A continuation of this work could be dedicated to the increase in the refractive index of the planarization layer by loading the SU-8 layer with high-n nanoparticles. The high-n planarization layer can foster the leakage of trapped light modes into the light outcoupling layer, as illustrated in **Figure 8.13**. An increase of the refractive index of the planarization layer from n_{plan}=1.56 to n_{plan}=1.7 promotes the mode overlap of the dielectric waveguide mode TE with the light outcoupling layer from 17% to 26%. With this, the extraction of waveguided modes is improved. Additional work could also be dedicated to increasing the thickness of the TiO_2 NPs. Thicker light scattering NPs are known to yield better light outcoupling. TiO_2 NPs with a thickness ranging from a few micrometers to a few hundreds of nanometers can be fabricated by introducing liquid cross-linkable prepolymer in the polymer blend used for the fabrication of the nanopatterned polymeric matrix, as demonstrated in Ref.[107].

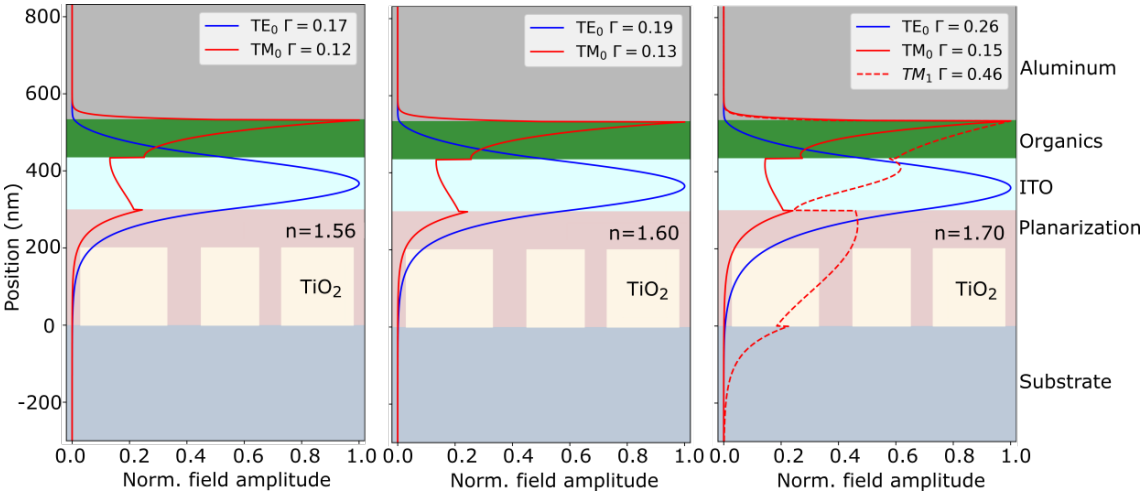

Figure 8.13. Schematic illustration of the field distribution in the light outcoupling layer and OLED thin film stack with change in the planarization layer refractive index (a) n=1.56, (b)=1.60, and (c) n=1.70. The blue and red lines represent the field distribution of the TE and TM modes, whereas Γ represents the overlap integral.

8.3 Summary and discussion

This work showed that the up-scalable polymer blend lithography (PBL) technique could be used as a versatile platform for fabricating 2D planar, disordered nanostructures for light management in OLED devices. These nanostructures can be exploited as low-and/or high-index light outcoupling structures.

First, PBL was used to fabricate low-index polystyrene (PS) nanostructures that directly serve as a light outcoupling layer at the interface between the anode and the organic layers. As a planarization layer for the light outcoupling elements, high-index materials such as TiO_2 and ZrO_2 were tested. Such layers foster the leakage of trapped waveguided modes into the low-index PS nanostructures due to their comparable refractive index with that of anode material (i.e., ITO). However, the resulting planarization layer based on TiO_2 and ZrO_2 exhibited cracks. A poor-quality planarization surface usually results in current leakage. As a result, their optical contribution to functional OLED devices is still absent in this study. This will be an interesting aspect to analyze in a follow-up study.

Next, the inverse of the first material's configuration was investigated to mitigate its limitations. Herein, PBL was used to prepare high-index light scattering nanopillars (NPs) using soft nanoimprint lithography and lift-off approaches. The latter approach allowed to fabricate reproducible samples. For the latter approach, PBL was used to fabricate a polymeric matrix containing nanoholes serving as a lift-off mask for the subsequent fabrication of TiO_2 NPs. Then, the TiO_2 NPs were planarized by a transparent epoxy (SU-8) layer, leading to a compact light extraction layer with an overall thickness of only 250 nm. To this end, the best planarized TiO_2 NPs configuration exhibits a mean total transmittance of 87% and a fraction of diffused transmitted light of 6% over the visible spectrum. As a proof-of-concept, the light outcoupling capability of this configuration was tested in a monochromatic bottom-emitting OLED, and an efficiency enhancement of up to 22% was measured with respect to a planar device.

Finally, it was shown that the introduction of planarized and controlled disordered TiO_2 NPs leads to more stable angular emission spectra that highlight the benefits of exploiting structural disorder for lighting applications. An increase in the refractive index of the planarization layer by loading the SU-8 layer with high-n nanoparticles and/or an increase in the thickness of the TiO_2 NPs is expected to yield better light outcoupling. This will also be an interesting aspect to analyze in a follow-up study.

9. Inkjet printed light outcoupling layers for OLEDs

The manufacturing cost of an OLED, aside from its light outcoupling, remains one of the significant screws left to be turned on. In the quest to lower the OLED manufacturing cost, research and development have focused on using inkjet printing (IJP) as a production method. In the future, one could therefore combine IJP of an OLED stack and of a light extraction layer for achieving low-cost and efficient devices. In this chapter, the interest in inkjet printed, phase-separated nanostructures (PSN) for improving the light extraction in OLED devices is first motivated. In section 9.1, a few selected IJP ink formulations and printing parameters that enabled the fabrication of efficient light extraction layers are reviewed. In the following section, experimental results of OLED devices with the inkjet printed light extraction layers along with benchmark devices are discussed (section 9.2). In the last section, further application possibilities arising from the IJP of light scattering layers are introduced. Parts of the results presented in this chapter have previously been published in the journal of ACS Nano.[60]

The current commercial OLED products are made out of an evaporation method. This process is problematic, as high material consumption and high machinery investment are inevitable. As a result, many panel manufacturers are paying more attention to RGB IJP technology to reduce the production cost.[263] The core technology behind inkjet printed OLED is that patterned films are fabricated without using a mask, as illustrated in **Figure 9.1**. In this approach, all of the deposited materials form the finished film. The resulting benefits include lower production costs, fewer defects, and scalability to large-size panels.[264, 265] Additionally, the maskless nature of IJP allows for freedom of design, which enables quick turn-around on customer requests, and ultimately, faster time to market.

The light outcoupling challenges of an OLED discussed in Chapter 2, and 8 remain unresolved irrespective of the device fabrication method used. Internal and external light extraction layers that can be processed using IJP are therefore required. In this direction, printable composite (volumetric) layers based on nanoparticles randomly distributed in a polymer matrix (for details, please refer to Chapter 8) attracted a

lot of attention in the last few years.[249, 250] This is because such layers promote light extraction over a broad spectral range and do not induce color distortion, which is desired, for instance, in large-area lighting applications. Besides these micrometer thick layers, more compact layouts consisting of 2D planar light scatterers (for details, please refer to Chapter 8) can be integrated into the OLED thin-film stack to allow an excellent spatial overlap of the guided modes with the light outcouplers.[91] The benefit of compact scattering layers for achieving greater design flexibility, material yield, and light outcoupling efficiency in reference to a volumetric counterparts is briefly discussed in Chapter 8.

This study shows that the up-scalable polymer blend lithography (PBL) technique is a versatile platform for fabricating such 2D planar light scatterers. Previous reports demonstrated that phase-separated light extraction layers fabricated via PBL could significantly outcouple the light confined in the OLED stack.[91, 142, 266] So far, such light extraction layers were fabricated using a spin-casting method. However, this method lacks the technology required to control the in-plane shape, the effective period, and the diameter size distribution of the PSN at pre-determined locations over the same substrate. Moreover, it does not allow incorporating the PSN into arbitrary 2D designs, as would be desired for their deployment into inkjet printed OLED devices. For the first time, this shortcoming was tackled while preserving the low-cost attractiveness and the versatility of the phase separation-based patterning approach by exploiting the unique advantages of IJP. In the design considered herein (see **Figure 9.2**), inkjet printed PSN are implemented into the active layers of the OLED stack and target waveguided and surface plasmon polariton modes. Upon optimized conditions, this study demonstrate the successful implementation of printed PSN (serving as planar light extraction layer) according to a pre-determined 2D layout in OLED devices. The proposed approach is demonstrated using monochromatic (emission peak at λ=520 nm) OLED devices and can also be applied to white OLEDs.

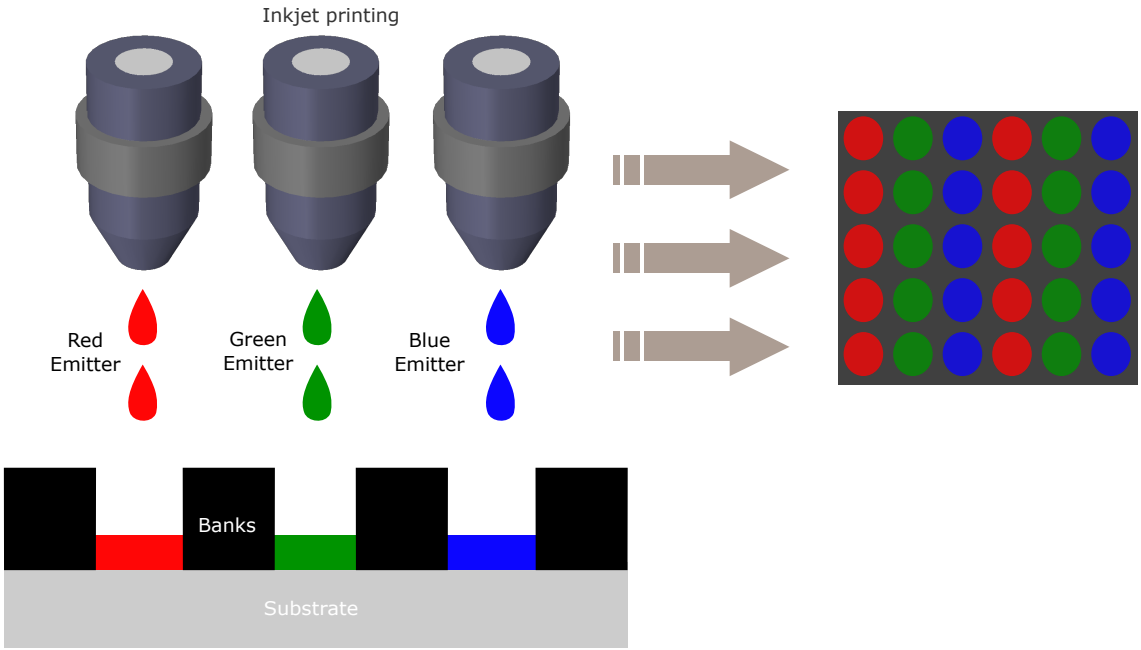

Figure 9.1. Schematic representation of an inkjet printed OLED device.

9.1 Design of inkjet printed light outcoupling layers

To fabricate inkjet-printed 2D compact light extraction layers, PBL based on a binary blend ink of poly(methyl methacrylate) (PMMA) and polystyrene (PS) is investigated. The details of PS/PMMA ink development that complies with IJP in terms of viscosity, surface tension, and vapor pressure can be found in Chapter 4. In this study, small molecular weight (MW) PS (MW=19 kg·mol^{-1}) and PMMA (MW=15 kg·mol^{-1}) polymers with a concentration of 50 kg·mol^{-1} and weight ratio of PS/PMMA=30:70 were employed to achieve light outcoupling PSN.

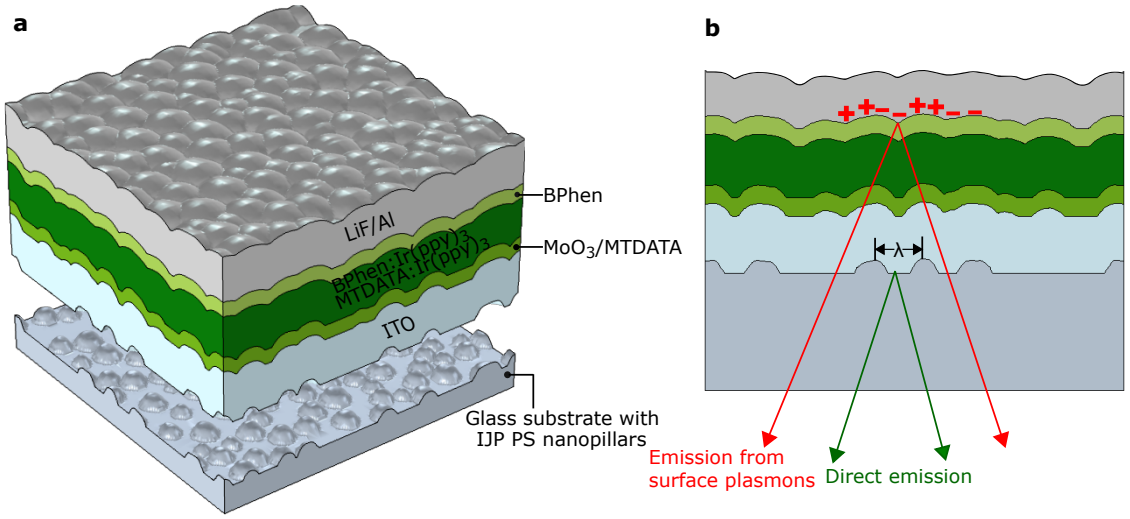

Figure 9.2. 3D representation of corrugated OLED. (a) schematic showing an OLED stack, deposited on the inkjet printed polymer nanopillar (NP) array, consists of transparent and conductive oxide layer (ITO), hole injection material (MoO_3), hole transport layer (m-MTDATA), emitter layer ($Ir(ppy)_3$), electron transport layer (BPhen)) and a cathode layer (LiF/Al). The final OLED stack consists of 5 nm MoO_3, 15 nm m-MTDATA, 20 nm m-MTDATA:$Ir(ppy)_3$, 20 nm BPhen:$Ir(ppy)_3$, 40 nm BPhen, 1 nm LiF, 100 nm Al. (b) Scattering of surface plasmons (SPs) may occur by nano-corrugated cathode/BPhen interface. Adapted with permission from Ref.[60]. © 2021 American Chemical Society.

Herein, printed PSN are incorporated between a substrate and an OLED thin-film stack without a planarization layer leading to a nano-corrugation throughout the whole device, as illustrated in **Figure 9.2**. For corrugated OLED, the height of light outcoupling nanostructures is the critical parameter to fabricate functional and reproducible devices with improved outcoupling efficiency.[254, 267] Device lifetime can also be a significant issue in corrugated OLEDs because of the possibility of non-uniform film thickness, electric field distribution and current.[254, 267, 268] This is true for large corrugation depth of light outcoupling nanostructures (mean height >100 nm).

To this end, PSN with a morphology promoting light extraction were printed with the Karlsruhe Institute of Technology (KIT) logo and half-printed glass substrates (see **Figure 9.3a-c**) using ink based on PS/PMMA (30:70) and printing resolution of 550 dpi. For this ink formulation, phase separation was assisted by a rapid thermal annealing (200 °C) process after printing. The light outcoupling PS nanopillars were achieved by the development of the phase separated PMMA matrix. For the selected

in-plane configuration, light scattering and optical transmittance were further adjusted to scatter the trapped photons efficiently and simultaneously allow a high optical transmittance. In other words, PSN that are too scattering can be detrimental to the overall performance of the OLEDs, and a trade-off between the two previously mentioned effects has to be found. To achieve this property, the highly scattering printed sample shown in **Figure 9.3b** was exposed to oxygen (O_2) plasma treatment to reduce the mean height of the PS nanopillars from 150 nm to 60 nm (see **Figure 9.3c**). **Figure 9.3d,e** shows the corresponding atomic force microscopy (AFM) topography images of the PSN. More precisely, the measured optical properties of the PS nanopillar arrays printed on a glass substrate, reported in **Figure 9.4**, are as follows: light scattering coefficient (haze) of 4.6% and total transmittance (T-total, i.e., the sum of the diffuse and direct transmittance) of 89% at the OLED peak emission wavelength (λ_{peak}=520 nm) for the O_2 treated sample (**Figure 9.3c**); and a higher haze of 18.3% as well as a lower T-total value of 82% for the untreated sample (**Figure 9.3b**). In addition to improving the haze with respect to the outcoupling efficiency, PS nanopillars with a lower aspect ratio and a smoother vertical profile, as obtained after the O_2 plasma treatment (see line profile extracted from AFM image in **Figure 9.3e**), enable a conformal deposition of the OLED thin-film stack atop the light extraction layer (see **Figure 9.5a**). Thus, the approach leads to functional and reproducible devices.

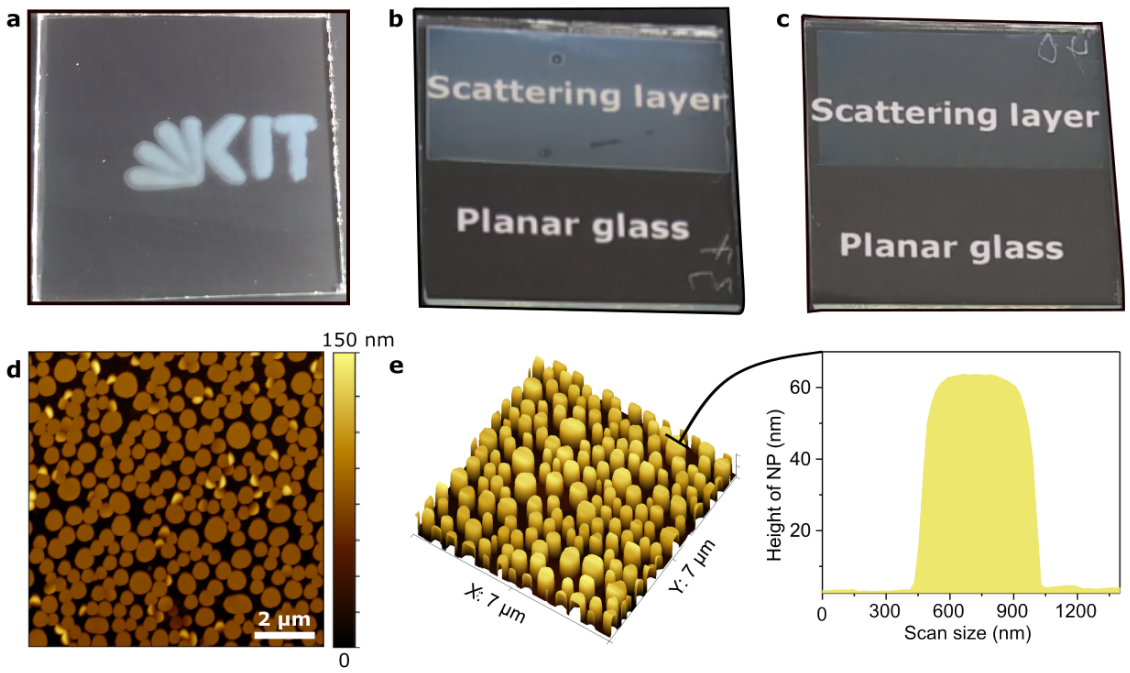

Figure 9.3. Inkjet printed internal light extraction layers. (a) Photograph of a printed logo incorporating the PSN after (O_2) plasma treatment. Photograph of a glass substrate, half-covered by the light scattering layer made of PS nanopillars, (b) before and (c) after (O_2) plasma treatment. The corresponding light outcoupling nanopillars (d) before and (e) after (O_2) plasma treatment are shown in the AFM images. The vertical profile of a single NP is measured in (e) and the inset image emphasizes a smooth transition from the base to apex. Adapted with permission from Ref.[60]. © 2021 American Chemical Society.

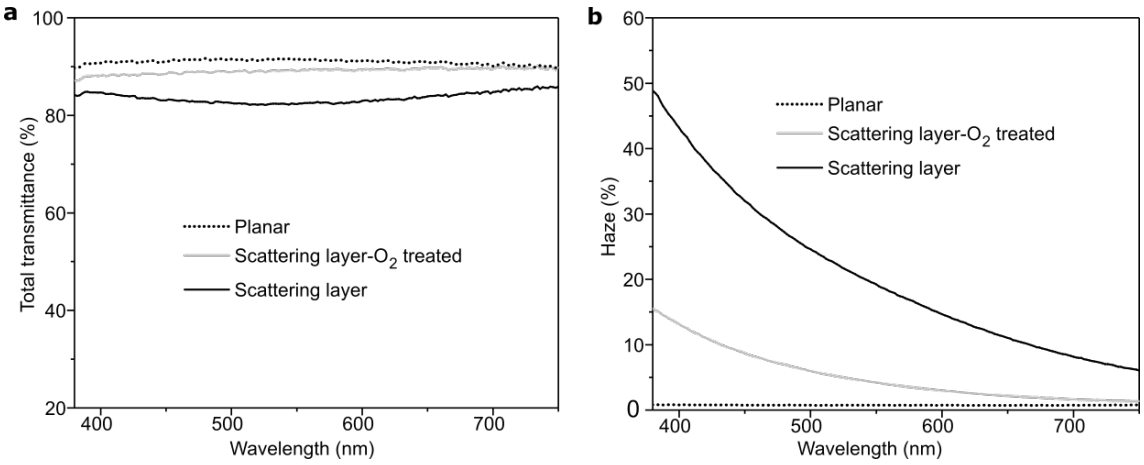

Figure 9.4. Optical properties of the standalone IJP light extraction layers. (a) Total transmittance and (b) haze of the glass substrates with the IJP scattering layer before and after (O_2) plasma treatment, compared to a pristine glass substrate. Adapted with permission from Ref.[60]. © 2021 American Chemical Society.

9.2 Corrugated OLED devices

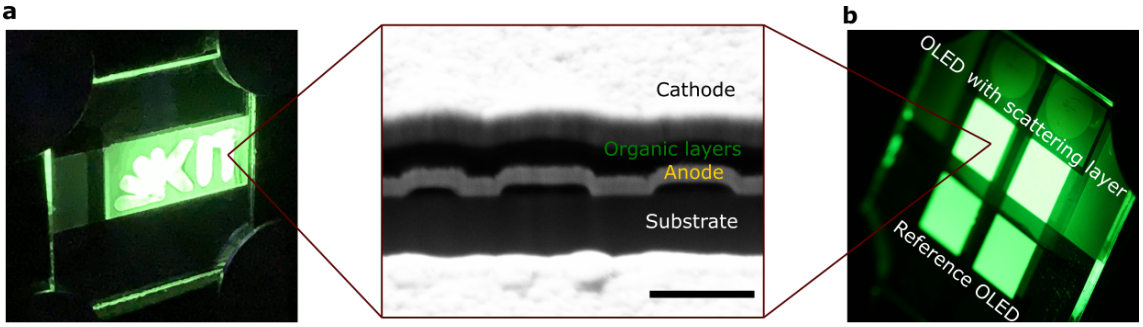

Figure 9.5. Improved light management in OLEDs processed on top of the IJP compact light extraction layer. (a) An OLED processed atop of the printed glass substrate, emitting more light from the light scattering logo (inset: corresponding SEM cross-sections of the OLED stack processed atop of the IJP compact light extraction layer. The scale bar represents 400 nm. (b) OLED processed atop of a glass substrate, half-printed with the PSN, to quantify the positive impact of the compact light extraction layer on the performance of the light-emitting devices. The size of all substrates is 25 mm × 25 mm. Adapted with permission from Ref.[60]. © 2021 American Chemical Society.

As a proof of concept, a transparent conductive oxide (ITO) was sputtered atop of the printed PSN formed over a few cm^2, followed by thermal evaporation of an OLED thin-film stack. More details regarding the stack layers fabrication and their functionality are given in Chapter 3.1 and 8. The device configuration and the associated layers' thicknesses are shown in **Figure 9.2**. The inset image in **Figure 9.5a** shows the SEM cross-section view of the OLED stack thermally evaporated on the printed PSN. **Figure 9.5a** allows to qualitatively assess the higher fraction of photons outcoupled from a light scattering layer printed so as to form the Karlsruhe Institute of Technology logo (see **Figure 9.3a**) compared to the surrounding emissive

area. Such design flexibility can be exploited for the fabrication of different LED sign boards (e.g., emergency exit lights).[269]

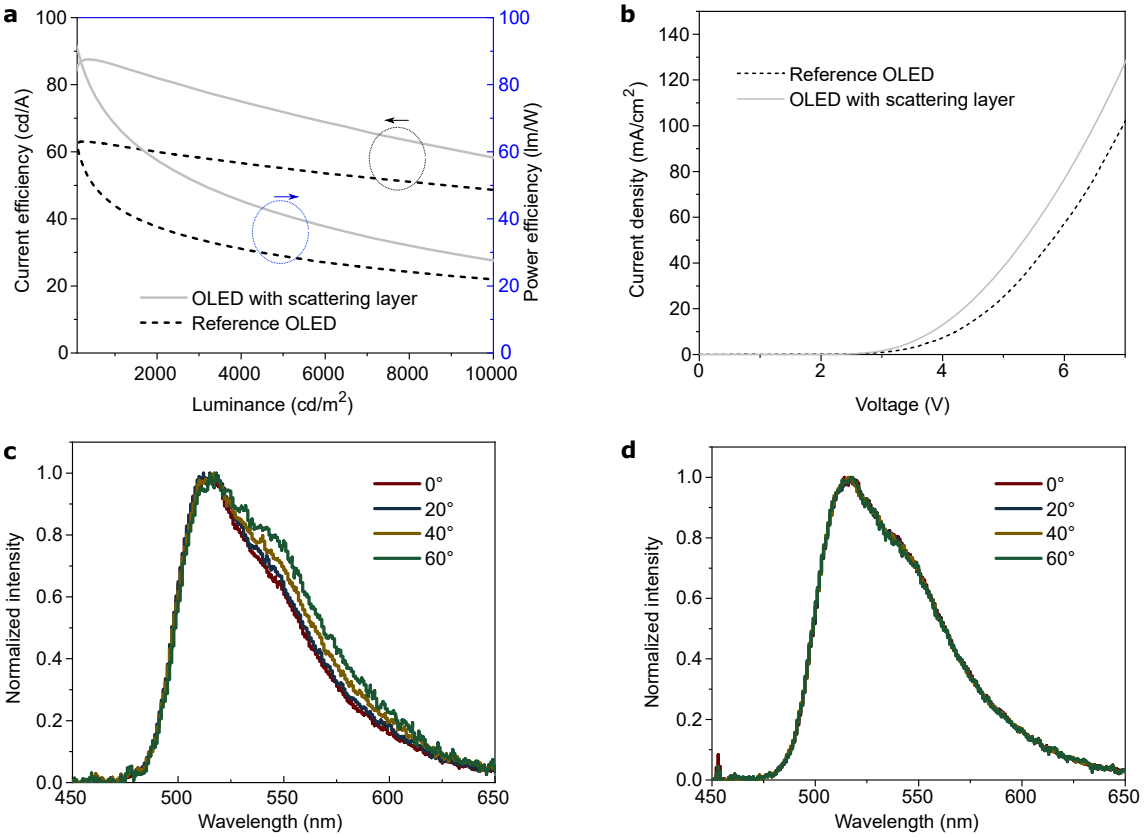

Figure 9.6. Optoelectronic characteristics of green light-emitting OLEDs without and with the IJP compact light extraction layer. (a) Current and power efficiency of OLEDs with and without IJP compact light extraction layer. (b) Current density-voltage (J-V) characteristics. (c)-(d) Goniometric measurements of the devices normalized spectra at angles between 0° and 60° for (c) reference OLED, and (d) OLED with IJP compact light extraction layer. The performance data shown is that of a representative sample; however, 8 OLEDs (each with a pixel area of 10 mm^2) on 25 mm × 25 mm substrates were tested and led to a similar enhancement. Adapted with permission from Ref.[60]. © 2021 American Chemical Society.

To quantify the optical improvement, additional OLEDs were processed by using only half-printed glass substrate (**Figure 9.3c**). These OLEDs were benchmarked against devices relying on a planar substrate. **Figure 9.6a** shows the superior light utilization of the printed PSN-based devices compared to OLED fabricated on top of the planar substrate. The power efficiencies (η_P) of the fabricated devices were 69 lm/W (OLED with scattering layer) and 44 lm/W (reference OLED), and the current efficiencies (η_L) were 86 cd/A and 62 cd/A, respectively, at a luminance of 1000 cd/m^2. This property ultimately results in power efficiency and current efficiency +57% and +39% relative to planar OLED, respectively. The influence of the structure on the outcoupling efficiency can be explained by the refractive index contrast between the printed PSN (here based on PS with n=1.6 at λ_{peak}=520 nm) and the ITO anode atop (n=2 at λ_{peak}=520 nm), which results in optical light scattering. Therefore, internal modes propagating within the organic layers and the transparent conductive oxide anode can be efficiently extracted. Moreover, the corrugated

surface profile between the organic-layer/cathode (see **Figure 9.2b** and **Figure 9.5a**) can recover some of the power dissipated to SPP modes (for details, please refer to Chapter 2).

Figure 9.6b highlights a dramatic increase of current density at the same bias voltage for OLEDs integrating the printed PSN compared to a planar reference. As revealed by the FIB-cut SEM image, this is notably attributed to the increased surface area of the ITO electrode upon introducing the printed PSN, which results in enhanced charge carrier injection. Therefore, the significant enhancement of current and power efficiency in the devices with printed PSN is caused not mainly by an increase of the outcoupling efficiency but by a change of internal quantum efficiency. In the future, one can mitigate this issue by planarizing the printed PSN before the OLED deposition (for details, please refer to Chapter 8).

In planar OLEDs, photon emission is angle-dependent (see **Figure 9.6c**) because of the confinement of the resonance mode in a microcavity.[262] As demonstrated experimentally (see **Figure 9.6d**), the printed PSN enables to maintain similar emission spectra upon a change of the viewing angle due to the controlled amount of optical scattering involved. This property leads to color distortion-free OLED devices when compared to the reference devices and thus supporting the suitability of printed PSN based light extraction layer for full-color OLED devices. In the future, one could therefore combine the IJP of the RGB pixels and of a compact light extraction layer for achieving greater design flexibility, material yield, and light outcoupling efficiency. As illustrated in **Figure 9.1**, three different emitters (Red, Green, and Blue) are required to fabricate OLED displays via IJP. Thus, it becomes more critical to print PSN with different lateral sizes over a substrate that corresponds to the emitting wavelength of the three emitters (RGB pixels) to obtain efficient OLED displays.[54, 270] For such application, the corresponding light outcoupling (inkjet printed) PSN can be achieved by adapting the printing resolution from pixel to pixel for a given ink formulation at predetermined locations over the same substrate (for more details, please refer to Chapter 4).

9.3 Summary and discussion

This study demonstrated a very elegant way towards digitally printable compact light extraction layer to improve light management in OLEDs. This technique allows to easily tune the phase separated nanostructures (PSN) morphologies, including mean diameter, density, and average inter-distance, by keeping everything and especially the ink constant. Furthermore, it allows achieving PSN with a predetermined 2D layout that exhibits the desired light scattering properties over the visible spectrum by only tailoring the printing parameters. As a proof-of-concept, the light outcoupling capability of such configuration was tested in a monochromatic bottom-emitting OLED.

The study has shown that inkjet printed (IJP) PSN significantly improve the power and current efficiency with respect to emissive pixels processed on planar substrates (η_P and η_L relative increase of +57% and +39%, respectively). Moreover, the resulting structural disorder was exploited to produce an effective light extraction layer over a broad spectral range with limited angular dependency. Further improvement in devices performance can be achieved by developing planarization layers to preserve their electrical properties and fully exploit the different printed PSN. While

this one example illustrates the potential of developed IJP PSN, its application range extends well beyond LEDs (see **Table 4.1** and **4.2** in Chapter 4), enabling the production of nanophotonic devices of different shapes, types, and designs with precision from initial prototyping to industrial manufacturing.

10. Discussion

Within the context of this thesis, I have studied the design and fabrication of phase-separated nanostructures (PSN) for photon management in thin-film optoelectronic devices, such as solar cells and OLEDs. As introduced in Chapter 1, the utilization of efficient solar cell and OLED devices cannot only produce clean energy but can also help with energy saving. In this regard, photon management is of critical importance for improving their performance. As reviewed in Chapter 2, the research field of photon management using nanostructures for solar cell and OLED devices has expanded dramatically over the last few years. A key requirement for practical applications, however, is a rapid, solution process method for fabricating the nanostructures with design flexibility and diverse feature sizes. The contribution and significance of this work to meet these requirements are discussed in the following (please refer to section 10.1). In addition, section 10.2 points out the many new possibilities opened by this work and which are still ongoing research activities.

10.1 Conclusion

Digitally printable nanophotonic structures

By combining the polymeric self-assembly method (bottom-up approach) with the inkjet printing process (top-down approach), this work demonstrated an elegant way towards digitally printable phase-separated nanophotonic structures. Phase-separated structures with sizes from a few μm down to sub-100 nm range were processed on arbitrary substrates using the developed approach—these structures were obtained within any pre-determined 2D design without requiring any template or mask. In addition, the developed approach allowed to digitally control the in-plane shape, the effective period, and the diameter size distribution of the phase-separated structures at pre-determined locations over the same substrate either by adapting the printing resolution from pixel to pixel for a given ink formulation or by working with multiple polymer inks.

Tunable and scalable nano-stamps

This work demonstrated a cost-effective route for fabricating tunable and scalable nano-stamps using a self-assembly method for nanoimprint lithography (NIL). For

NIL, OrmoStamp copies of the PS/PMMA PSN can be employed, but direct micro-/nano-structuring of OrmoStamp using a phase separation process for NIL was missing. For the first time, this work demonstrated that the self-assembly approach which is well known for the immiscible homopolymers (PMMA/PS) blend can also be used for the UV-curable polymer OrmoStamp (organic-inorganic hybrid polymer) when combined with PS. The most important issue, however, is the fact that OrmoStamp can be used subsequently as a master in NIL. This opens, for the first time, a direct route for using PSN in NIL without additional lithographic or replication steps in between. Moreover, the developed PSN-based nano-stamps can be fabricated over various rigid and flexible substrates. Hence, the nano-stamps based on PSN can be integrated seamlessly into different NIL systems regardless of the imprint contact types, such as plate-to-plate and roll-to-roll to pattern different functional materials.

Photonic contact for light trapping

It was shown that it is possible to integrate the polymeric self-assembly process into a process flow to fabricate a-Si:H based solar cells. To this end, light scattering PSN were integrated into the rear reflector of a-Si:H based solar cells to achieve broadband light trapping. Herein, a metallic layer was deposited atop the PSN whose geometrical parameters were previously adjusted to achieve a light scattering coefficient (in air) exceeding 40% in the low absorbing region of the a-Si:H active layer. The low aspect ratio and smooth profile of the PSN enabled a conformal deposition of the solar cell thin film stack atop, resulting in functional and reproducible devices. The latter exhibited a broadband absorption enhancement and a power-conversion efficiency increase of 65% relative to planar solar cells. The developed reflectors even overcome the light-harvesting properties of commercial light-scattering (Asahi-type) substrates. Optical simulations carried out on an accurate 3D model revealed that the PSN-based solar cells superior light-harvesting properties notably stem from reduced absorption losses in the reflector above λ=500 nm, compared to Asahi devices that feature sharp-edged textures. I have also numerically shown that the design is tolerant to PSN height and diameter variations. It should be noted that Hubert *et al.* (2020) extended the approach developed here for silicon-based tandem solar cells to enhance their infrared response.[179] Thus, it highlights the potential of the developed approach for other photovoltaic technologies.

"Photonized" absorber films for light-harvesting

The role of ordered versus disordered nanostructures in light trapping was elaborated using optical simulation of patterned a-Si:H absorber layers. This work demonstrated that the integrated absorption (IA) obtained by patterning the a-Si:H layer with an optimized periodic array of monodisperse holes could be overcome by introducing a controlled amount of disorder in the diameter size distribution, eventually combined with a short-range disorder of the hole position (given a fixed volume of absorbing material). This property was verified experimentally by integrating the short-range ordered PSN into a 130 nm thin a-Si:H slab standing on glass using the dry-etching method. The nanopatterned a-Si:H achieved an IA increase of $93\%_{rel}$ under normal incidence and as high as $200\%_{rel}$ at large incidence angles compared to unpatterned absorbers. The approach was further extended for perovskite materials. In contrast, perovskites are unstable materials, and thus the thermal NIL method

was implemented for nanopatterning this material. The patterned perovskite film using PSN-based nano-stamps improved the IA by 7% relative to the planar counterpart. This approach is envisioned to be integrated into roll-to-roll processable "photonized" absorbers in future. Here, the studies were partially motivated by the micro- and nanostructured scales decorating the wings of the black butterfly that harvest sunlight over a wide spectral and angular range.

Photonic contact for antireflection effect

A transparent electrode with corrugated surface, which was prepared by conformally depositing a 135 nm thick indium tin oxide (ITO) film on the PSN, was experimentally investigated to enhance the power conversion efficiency of perovskite/c-Si tandem solar cells. The design of the corrugation in order to function as antireflection nanostructure was demonstrated and elucidated in terms of impedance matching layer, smoothing the transition between the ITO and glass substrate. For dense PSN with effective period (P)=210 nm and mean height of 130 nm, the average increase of transmittance by $7\%_{rel}$ at a broad spectral window (λ=300-1200 nm) was observed compared to a planar reference. This nanostructured electrode was integrated into perovskite/c-Si tandem solar cell and thus led to an enhancement up to 1.7% (absolute) in the power conversion efficiency of the bottom c-Si solar cell. The fabrication route of investigated nanostructured ITO films can be scaled up by combining with the inkjet printed PSN. Furthermore, their application can also be extended to OLED devices.

Low- and high-index light outcoupling structures

Light outcoupling planarized high-index TiO_2 nanopillars were fabricated by combining the self-assembly and the solvent-assisted lift-off process. To this end, the best planarized TiO_2 nanopillars configuration exhibited a mean total transmittance of 87% and a fraction of diffused transmitted light of 6% over the visible spectrum. Taking the example of a bottom emitting OLED ($\lambda_{\mathbf{peak}}$=520 nm), an efficiency enhancement of 22% upon incorporating the developed light outcoupling layer was demonstrated, with ameliorated angular emission characteristics. Furthermore, the design flexibility of the inkjet-printed PSN was exploited for monochromatic OLEDs. For example, a low-index light outcoupling structure based on the PSN was printed to form the Karlsruhe Institute of Technology (KIT) logo before the deposition of the complete OLED thin-film stack atop. This approach led to a nano-corrugation throughout the whole device, and the corrugated OLED exhibited a device efficiency increase of 57%, at a luminance of 1000 cd/m^2, relative to a planar reference device. In the future, one could therefore combine the inkjet printing of the OLED stack and the compact light extraction layer for achieving a greater design flexibility, material yield and light outcoupling efficiency.

10.2 Outlook

Considering the growing interest in photonic materials obtained by additive manufacturing, I anticipate that this work will foster the widespread implementation of the printed and imprinted PSN for different nanophotonic and nanoelectronic devices well beyond PV and OLEDs (for more details, please refer to **Table 4.1** & **4.2** of Chapter 4). Besides extending the developed approaches to other technologies, I see the following opportunities:

Digitally printable nanophotonic structures at room temperature

It was found that PS/PMMA blend inks based on co-solvents lead to PSN, which is initiated by the solvent extraction at room temperature upon inkjet printing (please refer to Appendix **Figure A.1**). This finding offers the opportunity to inkjet print temperature-sensitive materials such as biopolymers. However, the printed films are inhomogeneous. The most likely explanation is non-uniform drying of the printed films caused by the limited number of used nozzles (16 in the present case). Thus, to obtain more uniform films at room temperature, it would be necessary to increase the number of nozzles to decrease the drying rate of the ink before diffusing into the film or to further optimize the printing parameters and the ink formulation.

Large area nano-stamps

Large-area nano-stamps that comply with the industrial scale roll-to-roll NIL technique can be fabricated by doctor blading the PS/OrmoStamp blend (please refer to Appendix **Figure B.1**). By further tuning the polymer blend ink formulation, the PSN-based nano-stamps may also be prepared using inkjet printing. The latter enables to realize large-area nano-stamps, but also the possibility to easily form these nano-stamps over a predefined macroscopic design without the need for additional masks and patterning steps.

High aspect-ratio nanostructures

The self-assembled OrmoStamp nanostructures can serve as an etching mask for achieving high aspect ratio nanopillar arrays through a selective dry etching process. For an average nanopillar diameter of 320 nm, a aspect ratio of approximately 6:1 was obtained by etching c-Si substrate (please refer to Appendix **Figure C.1**). The aspect ratio of the nanopillars could be further amplified by introduction of a polymer transfer layer underneath the polymer blend film.

Combining self-assembly method with photolithography

The OrmoStamp can also be used as a photoresist material for a photolithography process. Thus, it allows for incorporating ordered microstructures via photolithography into the disordered self-assembled OrmoStamp structures to generate holographic colors (please refer to Appendix **Figure D.1**). These holographic colors can potentially provide enhanced security in anti-counterfeiting applications.

Air-void optical scattering layers for OLEDs

In order to increase the outcoupling efficiency of OLEDs, an array of air void optical scattering structures has been realized on a glass substrate. The air void structure was fabricated by first depositing PSN on a substrate. A layer of TiO_2 was then coated on the PSN and finally, annealing/washing was carried out to burn out-/dissolve the PSN (please refer to Appendix **Figure E.1**). The resulting planarized air void optical scattering structure on the glass substrate led to higher broadband diffused transmittance over the visible spectrum due to the high refractive index contrast between the TiO_2 layer and the air voids. It is supposed that this approach reaches the ultimate goal of light extraction technology for practical OLED applications. It would be interesting to test the proposed approach in functional OLED devices.

Volume scattering layers for quantum dots

Preliminary results showed that the phase-separation process of the polymer blend could also be used to fabricate a volumetric scattering layer (please refer to Appendix **Figure F.1**), besides the compact layouts of 2D disordered nanostructures. Given the lack of facile fabrication methods for well-designed volumetric scattering layer for QD-based display, this one-step phase-separation process would offer a versatile and scalable fabrication route.

Appendices

A. Inkjet-printed phase-separated nanostructures at room temperature

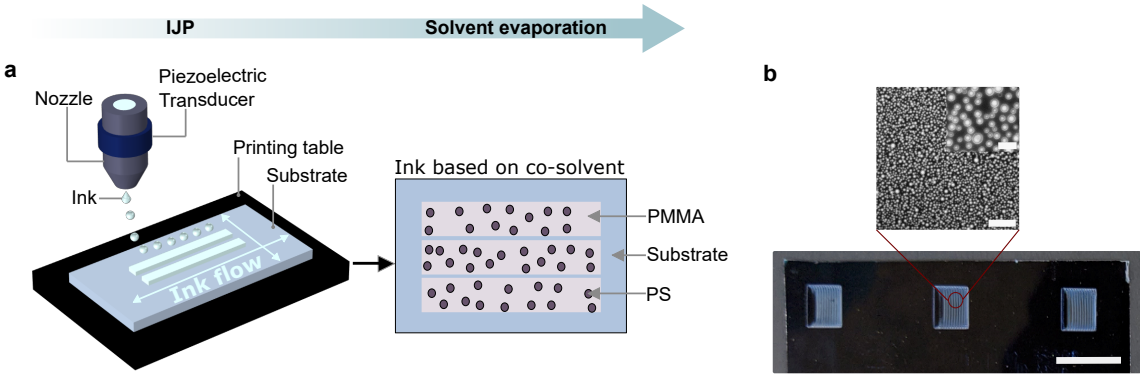

Figure A.1. Inkjet-printing (IJP) of PS/PMMA (30:70) ink with bi-directional printing direction at a substrate temperature of 25 °C. (a) Schematic illustration of the key steps involved in IJP of the PS/PMMA=30:70 ink based on cyclohexanone and Tetralin. The schematic depicts the resulting film after the solvent evaporation at room temperature. (b) Photographs of PMMA matrix (average thickness of 150 nm) after selective development of PS domains. The scale bar in the photograph of the substrate represents 1 cm. The main scale bar in the SEM image represents 5 μm and 2 μm for the inset SEM image.

B. Doctor bladed phase-separated nanostructures based nano-stamps

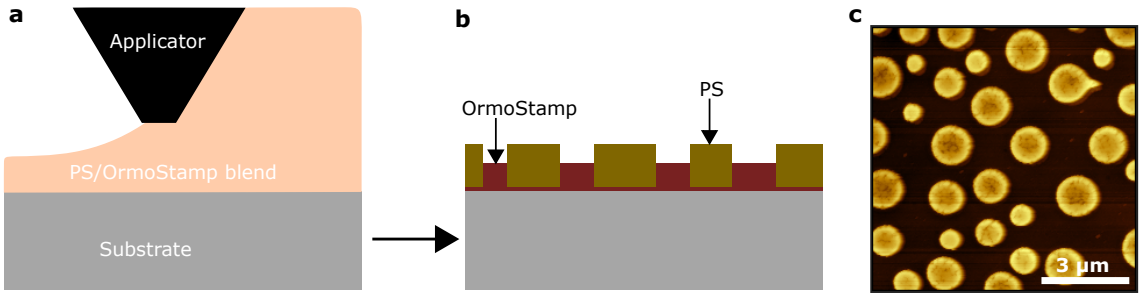

Figure B.1. Doctor blading enables large-area imprinting stamp fabrication via self-assembly method. A schematic illustration of PS/OrmoStamp blend coating using (a) doctor blading system and (b) the formation of doctor bladed phase-separated nanostructures after common solvent evaporation. (c) AFM image of the OrmoStamp nanopillars fabricated using PS/OrmoStamp=3:1 in toluene, with a concentration of 35 mg·ml^{-1} and obtained after selectively etching the PS. The applicator was positioned at 300 μm from the substrate for coating and moved with a coating speed of 50 mm/s.

C. Fabrication of high aspect-ratio structures via a self-assembly method

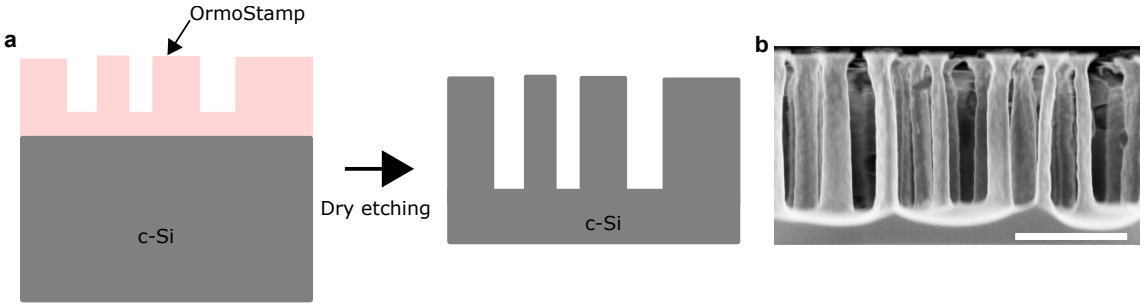

Figure C.1. Fabrication of high aspect ratio nanopillars by combining the self-assembly method with the dry-etching process. (a) Schematic of the fabrication procedure of high aspect ratio nanopillars based on the phase separation of the OrmoStamp/PS blends. (b) Cross-sectional SEM image of the nanopillars with aspect ratio as high as 6:1 formed from the phase-separated OrmoStamp nanopillars by selective etching of the c-Si substrate. The c-Si was etched using a $SF_6/O_2/Ar$-based plasma at operational pressure and power of 10 mT and 50 W, respectively. The $SF_6/O_2/Ar$ flow rate was fixed at 12/6/30 sccm. The scale bar represents 1 μm.

D. Introducing order into self-assembled disordered structures

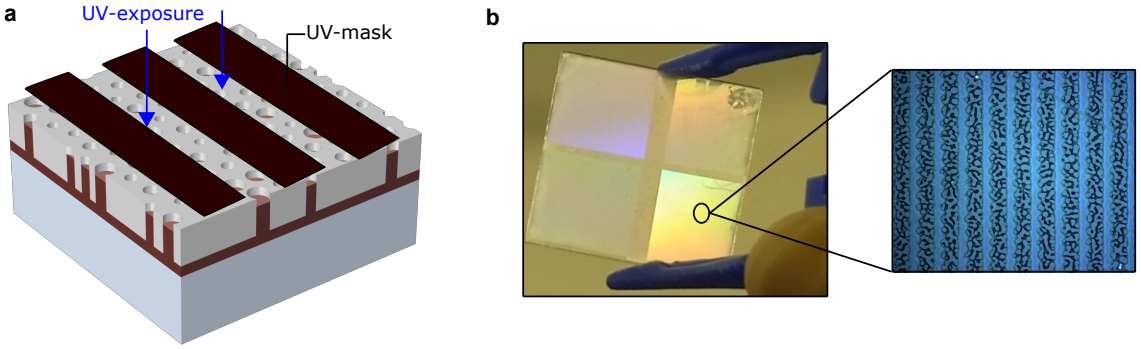

Figure D.1. Combining self-assembly method with photolithography. (a) Schematic illustration of the introduction of deterministic microstructures via photolithography into self-assembled PS/OrmoStamp nanostructures. (b) Photograph of a 25 mm × 25 mm glass substrate illuminated by a white LED from the top. The structures formed via the route shown in (a) efficiently diffract the light, revealing holographic colors. The inset optical image shows ordered and disordered microstructures with a grating width of 10 μm.

E. Air-void optical scattering structures via a self-assembly method

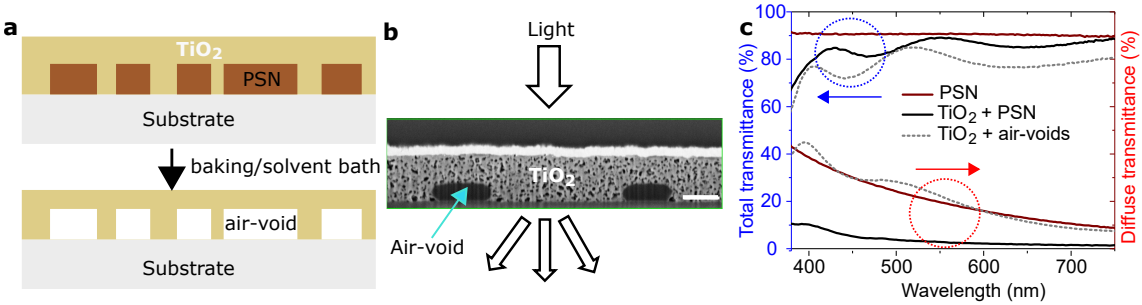

Figure E.1. Air-void optical scattering structures for high-brightness OLEDs. (a) Schematic illustration of the fabrication sequence for low-index (air-void) scattering nanopillars via polymer blend lithography. The air voids were achieved by burning or dissolving the phase-separated nanostructures (PSN) after coating them with planarizing TiO_2 nanoparticles. (b) Focused-ion-beam cut SEM cross-section image of the planarized air-void light outcoupling layer. The scale bar represents 400 nm. (c) Measured total and diffuse transmittance of (un)planarized PSN and air-voids over the visible spectrum (under close to normal incidence). The optical measurement setup is depicted in (b).

F. Volume scattering layers via a self-assembly method

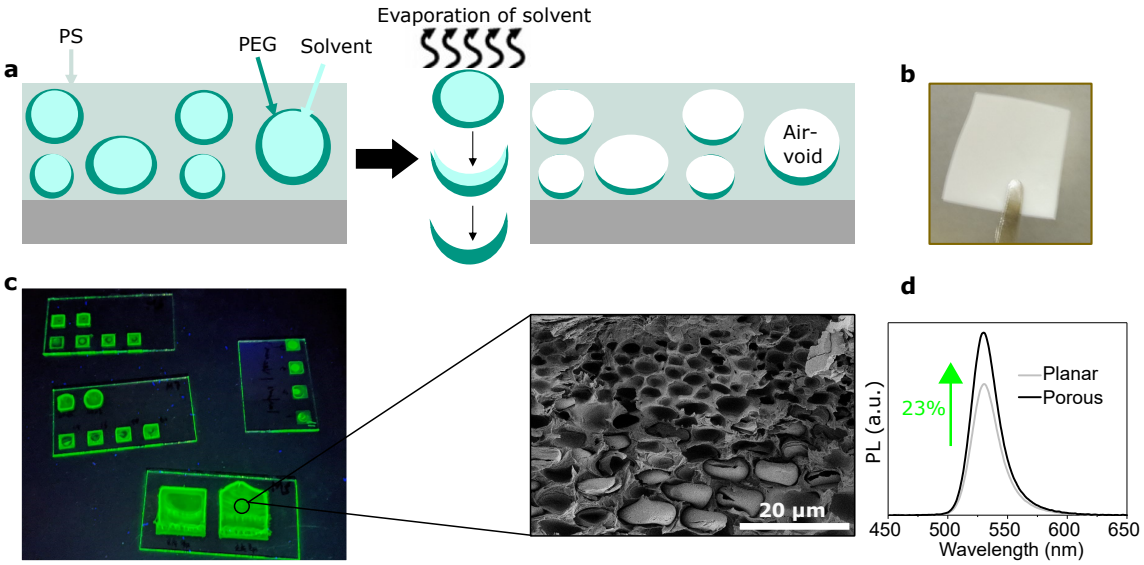

Figure F.1. Design of a hierarchical polymer blend-quantum dots composite via multiscale phase separations. (a) Schematic demonstration of the microporous structure formation of the PS/PEG mixed film during the drying process following drop-casting or inkjet printing. (b) Photograph of the dried hybrid film fabricated following the route (a). (c) Photograph of inkjet printed polymer blend-quantum dots (QD) composite samples under 366 nm UV light. The inset shows the corresponding cross-sectional SEM image of the composite sample. (d) Photoluminescence (PL) spectra of PS/QD ("Planar") and PS/PEG/QD ("Porous") films.

Bibliography

[1] Gabrielle Dreyfus and Chad Gallinat. "Rise and shine: lighting the world with 10 billion LED bulbs". In: *US Department of Energy* 7 (2015).

[2] Clay Elliott. *Energy Savings Forecast of Solid-State Lighting in General Illumination Applications*. Tech. rep. Navigant Consulting, 2019.

[3] Christophe Vieu et al. "Electron beam lithography: resolution limits and applications". In: *Applied surface science* 164.1-4 (2000), pp. 111–117.

[4] Christos Trompoukis et al. "Disordered nanostructures by hole-mask colloidal lithography for advanced light trapping in silicon solar cells". In: *Optics express* 24.2 (2016), A191–A201.

[5] Hans Fredriksson et al. "Hole–mask colloidal lithography". In: *Advanced Materials* 19.23 (2007), pp. 4297–4302.

[6] Carl V Thompson. "Solid-state dewetting of thin films". In: *Annual Review of Materials Research* 42 (2012), pp. 399–434.

[7] Hairen Tan et al. "Plasmonic light trapping in thin-film silicon solar cells with improved self-assembled silver nanoparticles". In: *Nano letters* 12.8 (2012), pp. 4070–4076.

[8] Lewis M Fraas. *Low-cost solar electric power*. Springer, 2014.

[9] Arnold B Arons and MB Peppard. "Einstein's Proposal of the Photon Concept—a Translation of the Annalen der Physik Paper of 1905". In: *American Journal of Physics* 33.5 (1965), pp. 367–374.

[10] Jara Fernández. "Development of crystalline germanium for thermophotovoltaics and high-efficiency multi-junction solar cells". PhD thesis. 2010.

[11] Menghua Zhu, Guangda Niu, and Jiang Tang. "Elemental Se: fundamentals and its optoelectronic applications". In: *Journal of Materials Chemistry C* 7.8 (2019), pp. 2199–2206.

[12] William Grylls Adams and R Evans Day. "V. The action of light on selenium". In: *Proceedings of the Royal Society of London* 25.171-178 (1877), pp. 113–117.

[13] Bruce R Wheaton. "Photoelectric effect". In: *Compendium of Quantum Physics*. Springer, 2009, pp. 472–475.

[14] Arno Smets. *The Working Principle of a Solar Cell*. TU Delft Open & Online education. 2021.

[15] Lukas Kegelmann. “Advancing charge selective contacts for efficient monolithic perovskite-silicon tandem solar cells”. PhD thesis. Universität Potsdam, 2019.

[16] Raphael Schmager. “Advanced light management concepts for perovskite photovoltaics”. PhD thesis. Karlsruher Institut für Technologie, 2020.

[17] Matthew S Branham. “Ultrathin crystalline silicon solar cells incorporating advanced light-trapping structures”. PhD thesis. Massachusetts Institute of Technology, 2015.

[18] David Eisenhauer. “Tailor-made light management textures for liquid phase crystallized silicon solar cells”. PhD thesis. Technische Universität Berlin, 2018.

[19] Min Su Kim, Ju Heon Lee, and Moon Kyu Kwak. “Surface Texturing Methods for Solar Cell Efficiency Enhancement”. In: *International Journal of Precision Engineering and Manufacturing* (2020), pp. 1–10.

[20] Olindo Isabella. “Light management in thin-film silicon solar cells”. In: (2013).

[21] Stefan Nowy. “Understanding losses in OLEDs: optical device simulation and electrical characterization using impedance spectroscopy”. In: *Inst. Phys., Univ. Augsburg* (2010).

[22] Hak-Jong Choi et al. “A review on the fabrication and applications of subwavelength anti-reflective surfaces based on biomimetics”. In: *Applied Spectroscopy Reviews* 54.9 (2019), pp. 719–735.

[23] M-Claire van Lare and Albert Polman. “Optimized scattering power spectral density of photovoltaic light-trapping patterns”. In: *Acs Photonics* 2.7 (2015), pp. 822–831.

[24] Inès Massiot. “Design and fabrication of nanostructures for light-trapping in ultra-thin solar cells”. PhD thesis. Université Paris Sud-Paris XI, 2013.

[25] Zongfu Yu, Aaswath Raman, and Shanhui Fan. “Fundamental limit of nanophotonic light trapping in solar cells”. In: *Proceedings of the National Academy of Sciences* 107.41 (2010), pp. 17491–17496.

[26] Giacomo Bergamini and Serena Silvi. “Applied Photochemistry”. In: *Lecture Notes in Chemistry* (2016).

[27] Doctor Engineer. “Laser Structuring of Organic Optoelectronic Devices”. PhD thesis. Karlsruhe Institute of Technology, 2018.

[28] Jörg Frischeisen et al. “Light extraction in organic light-emitting diodes”. PhD thesis. Universität Augsburg, 2011.

[29] Kanchan Saxena, VK Jain, and Dalip Singh Mehta. “A review on the light extraction techniques in organic electroluminescent devices”. In: *Optical Materials* 32.1 (2009), pp. 221–233.

[30] Rico Meerheim et al. “Influence of charge balance and exciton distribution on efficiency and lifetime of phosphorescent organic light-emitting devices”. In: *Journal of Applied Physics* 104.1 (2008), p. 014510.

[31] Wolfgang Brütting et al. “Device efficiency of organic light-emitting diodes: Progress by improved light outcoupling”. In: *physica status solidi (a)* 210.1 (2013), pp. 44–65.

[32] Jörg Frischeisen et al. "Strategies for light extraction from surface plasmons in organic light-emitting diodes". In: *Journal of Photonics for Energy* 1.1 (2011), p. 011004.

[33] Stephen Wedge and WL Barnes. "Surface plasmon-polariton mediated light emission through thin metal films". In: *Optics express* 12.16 (2004), pp. 3673–3685.

[34] Klaus Meerholz and David C Müller. "Outsmarting waveguide losses in thin-film light-emitting diodes". In: *Advanced Functional Materials* 11.4 (2001), pp. 251–253.

[35] Hoang-Yan Lin et al. "Optical characteristics of the OLED with microlens array film attachment". In: *Organic Light Emitting Materials and Devices XI*. Vol. 6655. International Society for Optics and Photonics. 2007, 66551H.

[36] Yilong Huang et al. "A Solution Processed Flexible Nanocomposite Substrate with Efficient Light Extraction via Periodic Wrinkles for White Organic Light-Emitting Diodes". In: *Advanced Optical Materials* 6.23 (2018), p. 1801015.

[37] Amin Salehi et al. "Recent advances in OLED optical design". In: *Advanced Functional Materials* 29.15 (2019), p. 1808803.

[38] H Kogelnik. "Theory of optical waveguides". In: *Guided-wave optoelectronics*. Springer, 1988, pp. 7–88.

[39] Peter Allen Hobson. "Photonic modes of organic light emitting structures". PhD thesis. University of Exeter, 2002.

[40] Shi-Jie Zou et al. "Recent advances in organic light-emitting diodes: toward smart lighting and displays". In: *Materials Chemistry Frontiers* 4.3 (2020), pp. 788–820.

[41] Shizuo Tokito, Tetsuo Tsutsui, and Yasunori Taga. "Microcavity organic light-emitting diodes for strongly directed pure red, green, and blue emissions". In: *Journal of applied physics* 86.5 (1999), pp. 2407–2411.

[42] Jinouk Song et al. "Organic Light-Emitting Diodes: Pushing toward the Limits and Beyond". In: *Advanced Materials* (2020), p. 1907539.

[43] Evangelos Manias and Leszek A Utracki. "Thermodynamics of polymer blends". In: *Polymer blends handbook* (2014), pp. 171–289.

[44] Cheng Huang. "Phase Separation in Thin Polymer Films: From Self Stratification to Polymer Blend Lithography". PhD thesis. Technische Universität, 2015.

[45] Michael R Bockstaller and Edwin L Thomas. "Nanostructures from phase separated polymers". In: *Dekker Encyclopedia of Nanoscience and Nanotechnology* (2008), pp. 3093–3108.

[46] Bistra Andersen. "Investigations on environmental stress cracking resistance of LDPE/EVA blends". PhD thesis. Martin-Luther-Universität Halle-Wittenberg, 2004.

[47] Vlad Smirnov et al. "Improved homogeneity of microcrystalline absorber layer in thin-film silicon tandem solar cells". In: *Materials Science and Engineering: B* 159 (2009), pp. 44–47.

[48] T Merdzhanova et al. “Single-chamber processes for a-Si: H solar cell deposition”. In: *Solar energy materials and solar cells* 98 (2012), pp. 146–153.

[49] Nicolas Sommer et al. “Role of the dopant aluminum for the growth of sputtered ZnO: Al investigated by means of a seed layer concept”. In: *Journal of applied physics* 118.3 (2015), p. 035301.

[50] Gabrielle CE Jost et al. “Reliability aspects of hydrogen-doped indium oxide”. In: *physica status solidi (a)* 213.7 (2016), pp. 1751–1759.

[51] Thomas Hofbeck and Hartmut Yersin. “The triplet state of fac-Ir (ppy) 3”. In: *Inorganic chemistry* 49.20 (2010), pp. 9290–9299.

[52] Daniel TW Toolan, Richard Hodgkinson, and Jonathan R Howse. “Stroboscopic microscopy—direct imaging of structure development and phase separation during spin-coating”. In: *Journal of Polymer Science Part B: Polymer Physics* 52.1 (2014), pp. 17–25.

[53] Graham D Martin and Ian M Hutchings. “Fundamentals of inkjet technology”. In: *Inkjet Technology for Digital Fabrication. John Wiley & Sons Ltd* (2013), pp. 21–44.

[54] Zhaoyao Zhan et al. “Inkjet-printed optoelectronics”. In: *Nanoscale* 9.3 (2017), pp. 965–993.

[55] TS Cale et al. “Introduction to Plasma Enhanced Chemical Vapor Deposition”. In: *Plasma Processing of Semiconductors*. Springer, 1997, pp. 89–108.

[56] Jian-Ming Jin. *The finite element method in electromagnetics*. John Wiley & Sons, 2015.

[57] Vivian E Ferry, Albert Polman, and Harry A Atwater. “Modeling light trapping in nanostructured solar cells”. In: *Acs Nano* 5.12 (2011), pp. 10055–10064.

[58] Ardavan Oskooi et al. “Partially disordered photonic-crystal thin films for enhanced and robust photovoltaics”. In: *Applied Physics Letters* 100.18 (2012), p. 181110.

[59] Gheorghe Stan and Richard S Gates. “Intermittent contact resonance atomic force microscopy”. In: *Nanotechnology* 25.24 (2014), p. 245702.

[60] Yidenekachew J Donie et al. “Phase-Separated Nanophotonic Structures by Inkjet Printing”. In: *ACS nano* 15.4 (2021), pp. 7305–7317.

[61] Yidenekachew J. Donie et al. “A Self-Assembly Method for Tunable and Scalable Nano-Stamps: A Versatile Approach for Imprinting Nanostructures”. In: *Advanced Materials Technologies* (2021), p. 2101008.

[62] Markus Antonietti and Stephan Förster. “Vesicles and liposomes: a self-assembly principle beyond lipids”. In: *Advanced Materials* 15.16 (2003), pp. 1323–1333.

[63] Miri Park et al. “Block copolymer lithography: periodic arrays of˜ 1011 holes in 1 square centimeter”. In: *Science* 276.5317 (1997), pp. 1401–1404.

[64] Cheng Huang et al. “Polymer blend lithography: A versatile method to fabricate nanopatterned self-assembled monolayers”. In: *Beilstein journal of nanotechnology* 3.1 (2012), pp. 620–628.

[65] Sumanta Mukherjee et al. “Beyond the “coffee ring”: re-entrant ordering in an evaporation-driven self-assembly in a colloidal suspension on a substrate”. In: *The Journal of Physical Chemistry B* 118.9 (2014), pp. 2559–2567.

[66] Chris Mack. *Fundamental principles of optical lithography: the science of microfabrication*. John Wiley & Sons, 2008.

[67] Ampere A Tseng et al. “Electron beam lithography in nanoscale fabrication: recent development”. In: *IEEE Transactions on electronics packaging manufacturing* 26.2 (2003), pp. 141–149.

[68] S Reich and Yu Cohen. “Phase separation of polymer blends in thin films”. In: *Journal of Polymer Science: Polymer Physics Edition* 19.8 (1981), pp. 1255–1267.

[69] Alamgir Karim et al. “Phase-separation-induced surface patterns in thin polymer blend films”. In: *Macromolecules* 31.3 (1998), pp. 857–862.

[70] Ricardo Ruiz et al. “Density multiplication and improved lithography by directed block copolymer assembly”. In: *Science* 321.5891 (2008), pp. 936–939.

[71] XiaoMin Yang et al. “Directed block copolymer assembly versus electron beam lithography for bit-patterned media with areal density of 1 Terabit/inch2 and beyond”. In: *Acs Nano* 3.7 (2009), pp. 1844–1858.

[72] CT Black. “Self-aligned self assembly of multi-nanowire silicon field effect transistors”. In: *Applied Physics Letters* 87.16 (2005), p. 163116.

[73] Hsinyu Tsai et al. “Two-dimensional pattern formation using graphoepitaxy of PS-b-PMMA block copolymers for advanced FinFET device and circuit fabrication”. In: *ACS nano* 8.5 (2014), pp. 5227–5232.

[74] Woon Ik Park et al. “Self-assembled incorporation of modulated block copolymer nanostructures in phase-change memory for switching power reduction”. In: *Acs Nano* 7.3 (2013), pp. 2651–2658.

[75] KW Guarini et al. “Low voltage, scalable nanocrystal FLASH memory fabricated by templated self assembly”. In: *IEEE International Electron Devices Meeting 2003*. IEEE. 2003, pp. 22–2.

[76] Honghyuk Kim et al. “Impact of InGaAs carrier collection quantum well on the performance of InAs QD active region lasers fabricated by diblock copolymer lithography and selective area epitaxy”. In: *Semiconductor Science and Technology* 34.2 (2019), p. 025012.

[77] Charles T Black et al. “High-capacity, self-assembled metal-oxide-semiconductor decoupling capacitors”. In: *IEEE Electron Device Letters* 25.9 (2004), pp. 622–624.

[78] Ju Young Kim et al. “Highly tunable refractive index visible-light metasurface from block copolymer self-assembly”. In: *Nature communications* 7.1 (2016), pp. 1–9.

[79] Radwanul Hasan Siddique et al. “Scalable and controlled self-assembly of aluminum-based random plasmonic metasurfaces”. In: *Light: Science & Applications* 6.7 (2017), e17015–e17015.

[80] Wonchul Joo, Min Soo Park, and Jin Kon Kim. "Block copolymer film with sponge-like nanoporous strucutre for antireflection coating". In: *Langmuir* 22.19 (2006), pp. 7960–7963.

[81] Stefan Walheim et al. "Nanophase-separated polymer films as high-performance antireflection coatings". In: *Science* 283.5401 (1999), pp. 520–522.

[82] Youngjong Kang et al. "Broad-wavelength-range chemically tunable block-copolymer photonic gels". In: *Nature materials* 6.12 (2007), pp. 957–960.

[83] Edwin P Chan et al. "Block copolymer photonic gel for mechanochromic sensing". In: *Advanced materials* 23.40 (2011), pp. 4702–4706.

[84] Tobias Meier and Santiago D Solares. "Rhodamine-doped nanoporous polymer films as high-performance anti-reflection coatings and optical filters". In: *Nanoscale* 8.40 (2016), pp. 17675–17685.

[85] Vinayak Narasimhan et al. "Multifunctional biophotonic nanostructures inspired by the longtail glasswing butterfly for medical devices". In: *Nature nanotechnology* 13.6 (2018), pp. 512–519.

[86] Radwanul Hasan Siddique et al. "Aluminum metasurface with hybrid multipolar plasmons for 1000-fold broadband visible fluorescence enhancement and multiplexed biosensing". In: *ACS nano* 13.12 (2019), pp. 13775–13783.

[87] Vinayak Narasimhan et al. "Enhanced broadband fluorescence detection of nucleic acids using multipolar gap-plasmons on biomimetic Au metasurfaces". In: *Nanoscale* 11.29 (2019), pp. 13750–13757.

[88] Radwanul H Siddique et al. "Bioinspired phase-separated disordered nanostructures for thin photovoltaic absorbers". In: *Science advances* 3.10 (2017), e1700232.

[89] Yidenekachew J Donie et al. "Light trapping in thin film silicon solar cells via phase separated disordered nanopillars". In: *Nanoscale* 10.14 (2018), pp. 6651–6659.

[90] Ihteaz M Hossain et al. "Nanostructured front electrodes for perovskite/c-Si tandem photovoltaics". In: *Optics Express* 28.6 (2020), pp. 8878–8897.

[91] Bo Jiao et al. "Improvement of light extraction in organic light-emitting diodes using a corrugated microcavity". In: *Optics Express* 23.4 (2015), pp. 4055–4064.

[92] Noah Strobel et al. "Semiconductor: insulator blends for speed enhancement in organic photodiodes". In: *Advanced Electronic Materials* 4.10 (2018), p. 1700345.

[93] Sang Ouk Kim et al. "Epitaxial self-assembly of block copolymers on lithographically defined nanopatterned substrates". In: *Nature* 424.6947 (2003), pp. 411–414.

[94] Joy Y Cheng et al. "Dense self-assembly on sparse chemical patterns: Rectifying and multiplying lithographic patterns using block copolymers". In: *Advanced Materials* 20.16 (2008), pp. 3155–3158.

[95] Shuaigang Xiao and XiaoMin Yang. "Graphoepitaxial cylindrical block copolymer nanodomains evaluated as bit patterned media template". In: *Journal of Vacuum Science & Technology B: Microelectronics and Nanometer Structures Processing, Measurement, and Phenomena* 25.6 (2007), pp. 1953–1957.

[96] Xiao-Chun Chen et al. "Confinement-Induced Ordering in Dewetting and Phase Separation of Polymer Blend Films". In: *Advanced Materials* 24.19 (2012), pp. 2637–2641.

[97] Chiang-Jui Chu et al. "Reversible morphology control of three-dimensional block copolymer nanostructures by the solvent-annealing-induced wetting in anodic aluminum oxide templates". In: *International Journal of Polymeric Materials and Polymeric Biomaterials* 65.13 (2016), pp. 695–701.

[98] Paschalis Alexandridis and Richard J Spontak. "Solvent-regulated ordering in block copolymers". In: *Current opinion in colloid & interface science* 4.2 (1999), pp. 130–139.

[99] Mark P Stoykovich et al. "Directed assembly of block copolymer blends into nonregular device-oriented structures". In: *Science* 308.5727 (2005), pp. 1442–1446.

[100] Mark P Stoykovich et al. "Directed self-assembly of block copolymers for nanolithography: fabrication of isolated features and essential integrated circuit geometries". In: *Acs Nano* 1.3 (2007), pp. 168–175.

[101] Karl Amundson et al. "Effect of an electric field on block copolymer microstructure". In: *Macromolecules* 24.24 (1991), pp. 6546–6548.

[102] Clemens Liedel et al. "Beyond orientation: the impact of electric fields on block copolymers". In: *Macromolecular Chemistry and Physics* 213.3 (2012), pp. 259–269.

[103] Qui Tran-Cong-Miyata et al. "Controlling the morphology of polymer blends using periodic irradiation". In: *Nature materials* 3.7 (2004), pp. 448–451.

[104] Alexander S Abyzov and Jürn WP Schmelzer. "Nucleation versus spinodal decomposition in confined binary solutions". In: *The Journal of chemical physics* 127.11 (2007), p. 114504.

[105] EP Favvas and A Ch Mitropoulos. "What is spinodal decomposition". In: *Journal of Engineering Science and Technology Review* 1 (2008), pp. 25–27.

[106] Yang Li et al. "Phase separation of silicon-containing polymer/polystyrene blends in spin-coated films". In: *Langmuir* 32.15 (2016), pp. 3670–3678.

[107] Yang Li et al. "Wafer scale fabrication of dense and high aspect ratio sub-50 nm nanopillars from phase separation of cross-linkable polysiloxane/polystyrene blend". In: *ACS applied materials & interfaces* 9.15 (2017), pp. 13685–13693.

[108] Tobias Geldhauser et al. "Influence of the relative humidity on the demixing of polymer blends on prepatterned substrates". In: *Macromolecules* 43.2 (2010), pp. 1124–1128.

[109] Liang Cui et al. "Solvent and polymer concentration effects on the surface morphology evolution of immiscible polystyrene/poly (methyl methacrylate) blends". In: *Thin Solid Films* 515.4 (2006), pp. 2038–2048.

[110] John Burke. "Solubility parameters: theory and application". In: *The American Institute for Conservation* 3 (1984).

[111] Li RunMing, Yu Wei, and Zhou ChiXing. "Phase inversion and viscoelastic properties of phase-separated polymer blends". In: *Polymer Bulletin* 59.4 (2007), pp. 545–554.

[112] LA Utracki. "On the viscosity-concentration dependence of immiscible polymer blends". In: *Journal of Rheology* 35.8 (1991), pp. 1615–1637.

[113] CJ Lawrence. "The mechanics of spin coating of polymer films". In: *The Physics of fluids* 31.10 (1988), pp. 2786–2795.

[114] D A Winesett et al. "Substrate dependence of morphology in thin film polymer blends of polystyrene and poly (methyl methacrylate)". In: *Polymer International* 49.5 (2000), pp. 458–462.

[115] Tao-Tse Huang and Wenzhuo Wu. "Inkjet-Printed Wearable Nanosystems for Self-Powered Technologies". In: *Advanced Materials Interfaces* (2020), p. 2000015.

[116] Kurt Binder et al. *Polymers in Confined Environments*. 1st ed. Vol. 138, pp 1-89. Berlin: Springer, **1999**.

[117] Xue Li, Yanchun Han, and Lijia An. "Annealing effects on the surface morphologies of thin PS/PMMA blend films with different film thickness". In: *Applied surface science* 230.1-4 (2004), pp. 115–124.

[118] Keiji Tanaka, Atsushi Takahara, and Tisato Kajiyama. "Film thickness dependence of the surface structure of immiscible polystyrene/poly (methyl methacrylate) blends". In: *Macromolecules* 29.9 (1996), pp. 3232–3239.

[119] Lin Li et al. "Surface morphology of a polymer blend examined by laser confocal fluorescence microscopy". In: *Langmuir* 10.8 (1994), pp. 2495–2497.

[120] Aleksandar Donev, Salvatore Torquato, and Frank H Stillinger. "Pair correlation function characteristics of nearly jammed disordered and ordered hard-sphere packings". In: *Physical Review E* 71.1 (2005), p. 011105.

[121] Shibing Ye et al. "Temperature-Dependent Compatibilizing Effect of Graphene Oxide as a Compatibilizer for Immiscible Polymer Blends". In: *RSC Adv.* 3.21 (2013), pp. 7987–7995.

[122] Peter W Voorhees. "The Theory of Ostwald Ripening". In: *J. Stat. Phys.* 38.1-2 (1985), pp. 231–252.

[123] Glaura Goulart Silva et al. "Domain size effects on the thermal properties of PS/PMMA blends". In: *Applied surface science* 238.1-4 (2004), pp. 64–72.

[124] Jichun You et al. "Temperature dependence of surface composition and morphology in polymer blend film". In: *Polymer* 49.20 (2008), pp. 4456–4461.

[125] Lewis M Cox et al. "Nanoimprint lithography: Emergent materials and methods of actuation". In: *Nano Today* 31 (2020), p. 100838.

[126] Stephen Y Chou, Peter R Krauss, and Preston J Renstrom. "Imprint of sub-25 nm vias and trenches in polymers". In: *Applied physics letters* 67.21 (1995), pp. 3114–3116.

[127] Jong G Ok et al. "Photo–roll lithography (PRL) for continuous and scalable patterning with application in flexible electronics". In: *Advanced materials* 25.45 (2013), pp. 6554–6561.

[128] Jong G Ok et al. "Continuous and scalable fabrication of flexible metamaterial films via roll-to-roll nanoimprint process for broadband plasmonic infrared filters". In: *Applied Physics Letters* 101.22 (2012), p. 223102.

[129] Tatsuhiko Higashiki, Tetsuro Nakasugi, and Ikuo Yoneda. "Nanoimprint lithography for semiconductor devices and future patterning innovation". In: *Alternative Lithographic Technologies III*. Vol. 7970. International Society for Optics and Photonics. 2011, p. 797003.

[130] Deying Xia, Juchao Yan, and Shifeng Hou. "Fabrication of nanofluidic biochips with nanochannels for applications in DNA analysis". In: *Small* 8.18 (2012), pp. 2787–2801.

[131] Christopher J Bettinger, Robert Langer, and Jeffrey T Borenstein. "Engineering substrate topography at the micro-and nanoscale to control cell function". In: *Angewandte Chemie International Edition* 48.30 (2009), pp. 5406–5415.

[132] Natália M Alves et al. "Controlling cell behavior through the design of polymer surfaces". In: *Small* 6.20 (2010), pp. 2208–2220.

[133] R Schmager et al. "Light coupling to quasi-guided modes in nanoimprinted perovskite solar cells". In: *Solar Energy Materials and Solar Cells* 201 (2019), p. 110080.

[134] Anne Habermehl et al. "Roll-to-Roll Hot Embossing of 1D and 2D Photonic Nanostructures". In: *Advanced Engineering Materials* 21.8 (2019), p. 1900110.

[135] Hiroshi Yoshikawa et al. "Fabrication of high-aspect-ratio pattern via high throughput roll-to-roll ultraviolet nanoimprint lithography". In: *Microelectronic engineering* 112 (2013), pp. 273–277.

[136] Se Hyun Ahn and L Jay Guo. "Large-area roll-to-roll and roll-to-plate nanoimprint lithography: a step toward high-throughput application of continuous nanoimprinting". In: *ACS nano* 3.8 (2009), pp. 2304–2310.

[137] Amalraj Peter Amalathas, Maan M Alkaisi, and J Thirumalai. "Fabrication and replication of periodic nanopyramid structures by laser interference lithography and UV nanoimprint lithography for solar cells applications". In: *Micro/Nanolithography: A Heuristic Aspect on the Enduring Technology*. IntechOpen, 2018.

[138] C-W Kuo et al. "Fabrication of large-area periodic nanopillar arrays for nanoimprint lithography using polymer colloid masks". In: *Advanced materials* 15.13 (2003), pp. 1065–1068.

[139] Benzhong Wang et al. "Formation of nanoimprinting mould through use of nanosphere lithography". In: *Journal of Crystal Growth* 288.1 (2006), pp. 200–204.

[140] U Plachetka et al. "Wafer scale patterning by soft UV-nanoimprint lithography". In: *Microelectronic Engineering* 73 (2004), pp. 167–171.

[141] M Mühlberger et al. "UV-NIL with working stamps made from Ormostamp". In: *Microelectronic Engineering* 86.4-6 (2009), pp. 691–693.

[142] Yidenekachew J Donie et al. "Planarized and Compact Light Scattering Layers Based on Disordered Titania Nanopillars for Light Extraction in Organic Light Emitting Diodes". In: *Advanced Optical Materials* (2020), p. 2001610.

[143] L Jay Guo. "Nanoimprint lithography: methods and material requirements". In: *Advanced materials* 19.4 (2007), pp. 495–513.

[144] David R Barbero et al. "High-resolution nanoimprinting with a robust and reusable polymer mold". In: *Advanced Functional Materials* 17.14 (2007), pp. 2419–2425.

[145] Xu Guo et al. "A new strategy of lithography based on phase separation of polymer blends". In: *Scientific reports* 5 (2015), p. 15947.

[146] Anna Klukowska et al. "Novel transparent hybrid polymer working stamp for UV-imprinting". In: *Microelectronic engineering* 86.4-6 (2009), pp. 697–699.

[147] Xin Tang et al. "Direct Imprinting of Quasi-3D Nanophotonic Structures into Colloidal Quantum-Dot Devices". In: *Advanced Materials* 32.9 (2020), p. 1906590.

[148] Honglei Wang et al. "Nanoimprinted perovskite nanograting photodetector with improved efficiency". In: *ACS nano* 10.12 (2016), pp. 10921–10928.

[149] Hao Jiang et al. "Molding inkjetted silver on nanostructured surfaces for high-throughput structural color printing". In: *ACS nano* 10.11 (2016), pp. 10544–10554.

[150] Chengpeng Zhang et al. "Continuous fabrication of nanostructure arrays for flexible surface enhanced Raman scattering substrate". In: *Scientific reports* 7.1 (2017), pp. 1–9.

[151] Aiman Roslizar et al. "Hot-embossed microcone-textured fluoropolymer as self-cleaning and anti-reflective photovoltaic module covers". In: *Solar Energy Materials and Solar Cells* 214 (2020), p. 110582.

[152] Aaron T Fafarman et al. "Chemically tailored dielectric-to-metal transition for the design of metamaterials from nanoimprinted colloidal nanocrystals". In: *Nano letters* 13.2 (2013), pp. 350–357.

[153] Zhengong Meng et al. "Nanoimprint Lithography-Directed Self-Assembly of Bimetallic Iron–M (M= Palladium, Platinum) Complexes for Magnetic Patterning". In: *Angewandte Chemie International Edition* (2020).

[154] Lei Zhou et al. "Light manipulation for organic optoelectronics using bio-inspired moth's eye nanostructures". In: *Scientific Reports* 4 (2014), p. 4040.

[155] Guangzhu Ding et al. "The fabrication of nanoimprinted P3HT nanograting by patterned ETFE mold at room temperature and its application for solar cell". In: *Nanoscale research letters* 11.1 (2016), pp. 1–11.

[156] Jie Zhang et al. "Low-cost fabrication of large area sub-wavelength anti-reflective structures on polymer film using a soft PUA mold". In: *Optics express* 22.2 (2014), pp. 1842–1851.

[157] Hyeong-Ho Park et al. "Photo-induced hybrid nanopatterning of titanium dioxide via direct imprint lithography". In: *Journal of Materials Chemistry* 20.10 (2010), pp. 1921–1926.

[158] Hyeong-Ho Park et al. “Facile nanopatterning of zirconium dioxide films via direct ultraviolet-assisted nanoimprint lithography”. In: *Journal of Materials Chemistry* 21.3 (2011), pp. 657–662.

[159] Jingfeng Song et al. “Fabrication of ferroelectric polymer nanostructures on flexible substrates by soft-mold reverse nanoimprint lithography”. In: *Nanotechnology* 27.1 (2015), p. 015302.

[160] Hyun-Ha Park et al. “Non-sticky polyvinylsilazane stamp with high durability for UV-nanoimprint lithography”. In: *Microelectronic engineering* 98 (2012), pp. 130–133.

[161] Marc Papenheim et al. “Flexible composite stamp for thermal nanoimprint lithography based on OrmoStamp”. In: *Journal of Vacuum Science & Technology B, Nanotechnology and Microelectronics: Materials, Processing, Measurement, and Phenomena* 33.6 (2015), 06F601.

[162] Benjamin MD O’driscoll et al. “Lateral phase separation in grafted diblock copolymer films”. In: *Macromolecules* 43.19 (2010), pp. 8177–8184.

[163] Microresist Technology. *Processing Guidelines-OrmoStamp*. Ed. by micro resist technology GmbH.

[164] Emerson Y Arashiro and Nicole R Demarquette. “Use of the pendant drop method to measure interfacial tension between molten polymers”. In: *Materials Research* 2.1 (1999), pp. 23–32.

[165] Adrián Grande. “Light scattering self-assembled nanostructures for optoelectronic devices”. Karlsruher Institut für Technologie, 2018.

[166] Manuel W Thesen et al. “Inkjetable and photo-curable resists for large-area and high-throughput roll-to-roll nanoimprint lithography”. In: *Journal of Micro/Nanolithography, MEMS, and MOEMS* 13.4 (2014), p. 043003.

[167] Jonas Skovlund Madsen et al. “In-line characterization of nanostructures produced by roll-to-roll nanoimprinting”. In: *Optics Express* 29.3 (2021), pp. 3882–3890.

[168] Robin D Nagel et al. “Large area nano-transfer printing of sub-50-nm metal nanostructures using low-cost semi-flexible hybrid templates”. In: *Nanoscale research letters* 11.1 (2016), p. 143.

[169] Songmei Wu et al. “Nanostructured surface topographies have an effect on bactericidal activity”. In: *Journal of nanobiotechnology* 16.1 (2018), p. 20.

[170] Oliver S Heavens. *Optical properties of thin solid films*. Courier Corporation, 1991.

[171] Michael G Deceglie et al. “Design of nanostructured solar cells using coupled optical and electrical modeling”. In: *Nano letters* 12.6 (2012), pp. 2894–2900.

[172] Vivian E Ferry et al. “Optimized spatial correlations for broadband light trapping nanopatterns in high efficiency ultrathin film a-Si: H solar cells”. In: *Nano letters* 11.10 (2011), pp. 4239–4245.

[173] Manuel J Mendes et al. “Colloidal plasmonic back reflectors for light trapping in solar cells”. In: *Nanoscale* 6.9 (2014), pp. 4796–4805.

[174] Amalraj Peter Amalathas and Maan M Alkaisi. “Nanostructures for light trapping in thin film solar cells”. In: *Micromachines* 10.9 (2019), p. 619.

[175] UW Paetzold et al. "Disorder improves nanophotonic light trapping in thin-film solar cells". In: *Applied physics letters* 104.13 (2014), p. 131102.

[176] R Santbergen et al. "Application of plasmonic silver island films in thin-film silicon solar cells". In: *Journal of Optics* 14.2 (2012), p. 024010.

[177] Seweryn Morawiec et al. "Broadband photocurrent enhancement in a-Si: H solar cells with plasmonic back reflectors". In: *Optics express* 22.104 (2014), A1059–A1070.

[178] Seweryn Morawiec et al. "Experimental quantification of useful and parasitic absorption of light in plasmon-enhanced thin silicon films for solar cells application". In: *Scientific reports* 6 (2016), p. 22481.

[179] Hubert Hauser et al. "Tailored disorder: a self-organized photonic contact for light trapping in silicon-based tandem solar cells". In: *Optics Express* 28.8 (2020), pp. 10909–10918.

[180] Hairen Tan et al. "Combined optical and electrical design of plasmonic back reflector for high-efficiency thin-film silicon solar cells". In: *Photovoltaic Specialists Conference (PVSC), Volume 2, 2012 IEEE 38th.* IEEE. 2012, pp. 1–6.

[181] Ulrich W Paetzold et al. "Design of nanostructured plasmonic back contacts for thin-film silicon solar cells". In: *Optics express* 19.106 (2011), A1219–A1230.

[182] Craig F Bohren and Donald R Huffman. *Absorption and scattering of light by small particles*. John Wiley & Sons, 2008.

[183] Ulrich Wilhelm Paetzold. *Light trapping with plasmonic back contacts in thin-film silicon solar cells*. Forschungszentrum Jülich, 2013.

[184] Shih-Hui Chang, Stephen K Gray, and George C Schatz. "Surface plasmon generation and light transmission by isolated nanoholes and arrays of nanoholes in thin metal films". In: *Optics express* 13.8 (2005), pp. 3150–3165.

[185] Vivian E Ferry et al. "Plasmonic nanostructure design for efficient light coupling into solar cells". In: *Nano letters* 8.12 (2008), pp. 4391–4397.

[186] Chao Zhang et al. "Influence of interface textures on light management in thin-film silicon solar cells with intermediate reflector". In: *IEEE journal of photovoltaics* 5.1 (2014), pp. 33–39.

[187] Vladislav Jovanov et al. "Influence of film formation on light-trapping properties of randomly textured silicon thin-film solar cells". In: *Applied physics express* 7.8 (2014), p. 082301.

[188] Inc. COMSOL. *COMSOL Multiphysics, Version 5.2 a*. 2016.

[189] V Jovanov et al. "Influence of interface morphologies on amorphous silicon thin film solar cells prepared on randomly textured substrates". In: *Solar Energy Materials and Solar Cells* 112 (2013), pp. 182–189.

[190] Kevin Vynck et al. "Photon management in two-dimensional disordered media". In: *arXiv preprint arXiv:1202.4601* (2012).

[191] David Nečas and Petr Klapetek. "Gwyddion: an open-source software for SPM data analysis". In: *Open Physics* 10.1 (2012), pp. 181–188.

[192] Vivian E Ferry et al. “Light trapping in ultrathin plasmonic solar cells”. In: *Optics express* 18.102 (2010), A237–A245.

[193] Dmitry Lyashenko, Aureliano Perez, and Alex Zakhidov. “High-resolution patterning of organohalide lead perovskite pixels for photodetectors using orthogonal photolithography”. In: *physica status solidi (a)* 214.1 (2017), p. 1600302.

[194] Nan Zhang et al. “Highly Reproducible Organometallic Halide Perovskite Microdevices based on Top-Down Lithography”. In: *Advanced Materials* 29.15 (2017), p. 1606205.

[195] Shuai Wang et al. “Lead Halide Perovskite Based Microdisk Lasers for On-Chip Integrated Photonic Circuits”. In: *Advanced Optical Materials* 6.6 (2018), p. 1701266.

[196] Christos Trompoukis et al. “Passivation of photonic nanostructures for crystalline silicon solar cells”. In: *Progress in Photovoltaics: Research and Applications* 23.6 (2015), pp. 734–742.

[197] Suqiong Zhou et al. “Wafer-scale integration of inverted nanopyramid arrays for advanced light trapping in crystalline silicon thin film solar cells”. In: *Nanoscale research letters* 11.1 (2016), p. 194.

[198] Jian Mao et al. “Novel direct nanopatterning approach to fabricate periodically nanostructured perovskite for optoelectronic applications”. In: *Advanced Functional Materials* 27.10 (2017), p. 1606525.

[199] Ofer Bar-On et al. “Micro lasers by scalable lithography of metal-halide perovskites”. In: *Advanced Materials Technologies* 3.12 (2018), p. 1800212.

[200] Xiaoyu Yang et al. “Patterned perovskites for optoelectronic applications”. In: *Small Methods* 2.10 (2018), p. 1800110.

[201] Laurie J Phillips et al. “Dispersion relation data for methylammonium lead triiodide perovskite deposited on a (100) silicon wafer using a two-step vapour-phase reaction process”. In: *Data in brief* 5 (2015), pp. 926–928.

[202] Guillaume Gomard et al. “Two-dimensional photonic crystal for absorption enhancement in hydrogenated amorphous silicon thin film solar cells”. In: *Journal of Applied Physics* 108.12 (2010), p. 123102.

[203] Dayu Zhou and Rana Biswas. “Photonic crystal enhanced light-trapping in thin film solar cells”. In: *Journal of Applied Physics* 103.9 (2008), p. 093102.

[204] Emiliano R Martins et al. “Deterministic quasi-random nanostructures for photon control”. In: *Nature communications* 4.1 (2013), pp. 1–7.

[205] Kezheng Li et al. “High speed e-beam writing for large area photonic nanostructures—a choice of parameters”. In: *Scientific reports* 6 (2016), p. 32945.

[206] Seweryn Morawiec et al. “Self-assembled silver nanoparticles for plasmon-enhanced solar cell back reflectors: correlation between structural and optical properties”. In: *Nanotechnology* 24.26 (2013), p. 265601.

[207] P Vukusic, JR Sambles, and CR Lawrence. “Structurally assisted blackness in butterfly scales”. In: *Proceedings of the Royal Society of London. Series B: Biological Sciences* 271.suppl_4 (2004), S237–S239.

[208] Monica Skoge et al. “Packing hyperspheres in high-dimensional Euclidean spaces”. In: *Physical Review E* 74.4 (2006), p. 041127.

[209] Stephanie L Burg and Andrew J Parnell. "Self-assembling structural colour in nature". In: *Journal of Physics: Condensed Matter* 30.41 (2018), p. 413001.

[210] Eric R Dufresne et al. "Self-assembly of amorphous biophotonic nanostructures by phase separation". In: *Soft Matter* 5.9 (2009), pp. 1792–1795.

[211] Valérie Depauw et al. "Sunlight-thin nanophotonic monocrystalline silicon solar cells". In: *Nano Futures* 1.2 (2017), p. 021001.

[212] Sergey V Makarov et al. "Multifold emission enhancement in nanoimprinted hybrid perovskite metasurfaces". In: *ACS Photonics* 4.4 (2017), pp. 728–735.

[213] Neda Pourdavoud et al. "Photonic nanostructures patterned by thermal nanoimprint directly into organo-metal halide perovskites". In: *Advanced Materials* 29.12 (2017), p. 1605003.

[214] Benjia Dou et al. "Roll-to-roll printing of perovskite solar cells". In: *ACS Energy Letters* 3.10 (2018), pp. 2558–2565.

[215] Ihteaz M Hossain et al. "Scalable processing of low-temperature TiO2 nanoparticles for high-efficiency perovskite solar cells". In: *ACS Applied Energy Materials* 2.1 (2018), pp. 47–58.

[216] Matthias Worgull. *Hot embossing: theory and technology of microreplication.* William Andrew, 2009.

[217] Yi Yang et al. "Nanoimprinted polymer solar cell". In: *ACS nano* 6.4 (2012), pp. 2877–2892.

[218] Carlos Pina-Hernandez et al. "Nanoimprinted High-Refractive Index Active Photonic Nanostructures Based on Quantum Dots for Visible Light". In: *Scientific reports* 7.1 (2017), pp. 1–8.

[219] Philipp Tockhorn et al. "Improved Quantum Efficiency by Advanced Light Management in Nanotextured Solution-Processed Perovskite Solar Cells". In: *ACS Photonics* (2020).

[220] J-Q Xi et al. "Optical thin-film materials with low refractive index for broadband elimination of Fresnel reflection". In: *Nature photonics* 1.3 (2007), pp. 176–179.

[221] D Zhang et al. "Design and fabrication of a SiOx/ITO double-layer antireflective coating for heterojunction silicon solar cells". In: *Solar Energy Materials and Solar Cells* 117 (2013), pp. 132–138.

[222] Seong Min Kang et al. "Moth-Eye TiO2 Layer for Improving Light Harvesting Efficiency in Perovskite Solar Cells". In: *Small* 12.18 (2016), pp. 2443–2449.

[223] Hemant Kumar Raut et al. "Anti-reflective coatings: A critical, in-depth review". In: *Energy & Environmental Science* 4.10 (2011), pp. 3779–3804.

[224] Natarajan Shanmugam et al. "Anti-Reflective Coating Materials: A Holistic Review from PV Perspective". In: *Energies* 13.10 (2020), p. 2631.

[225] Nivethaa R Thangavel et al. "Disordered polymer anti-reflective coating for improved perovskite photovoltaics". In: *ACS Photonics* (2020).

[226] Stuart A Boden and Darren M Bagnall. "Moth-eye antireflective structures". In: (2012).

[227] Katherine Han and Chih-Hung Chang. "Numerical modeling of sub-wavelength anti-reflective structures for solar module applications". In: *Nanomaterials* 4.1 (2014), pp. 87–128.

[228] Imran Khan et al. "Nanostructured as-deposited indium tin oxide thin films for broadband antireflection and light trapping". In: *Nanotechnology* 28.32 (2017), p. 325201.

[229] Seungmuk Ji et al. "Optimal moth eye nanostructure array on transparent glass towards broadband antireflection". In: *ACS applied materials & interfaces* 5.21 (2013), pp. 10731–10737.

[230] ZW Han et al. "Antireflective surface inspired from biology: A review". In: *Biosurface and Biotribology* 2.4 (2016), pp. 137–150.

[231] Wen-Kai Kuo et al. "Moth-eye-inspired biophotonic surfaces with antireflective and hydrophobic characteristics". In: *ACS applied materials & interfaces* 8.46 (2016), pp. 32021–32030.

[232] Lord Rayleigh. "On reflection of vibrations at the confines of two media between which the transition is gradual". In: *Proceedings of the London Mathematical Society* 1.1 (1879), pp. 51–56.

[233] Y Kanamori, M Ishimori, and K Hane. "High efficient light-emitting diodes with antireflection subwavelength gratings". In: *IEEE photonics technology letters* 14.8 (2002), pp. 1064–1066.

[234] Jung Woo Leem and Jae Su Yu. "Indium tin oxide subwavelength nanostructures with surface antireflection and superhydrophilicity for high-efficiency Si-based thin film solar cells". In: *Optics express* 20.103 (2012), A431–A440.

[235] Juha Tommila et al. "Nanostructured broadband antireflection coatings on AlInP fabricated by nanoimprint lithography". In: *Solar Energy Materials and Solar Cells* 94.10 (2010), pp. 1845–1848.

[236] Arpita Haldar, M Srinivas Reddy, and R Vijaya. "Inexpensive graded-index antireflective surfaces for silicon-based optoelectronic devices". In: *JOSA B* 33.11 (2016), pp. 2331–2338.

[237] Lesley W Chan, Daniel E Morse, and Michael J Gordon. "Moth eye-inspired anti-reflective surfaces for improved IR optical systems & visible LEDs fabricated with colloidal lithography and etching". In: *Bioinspiration & biomimetics* 13.4 (2018), p. 041001.

[238] Lalit K Verma et al. "Self-cleaning and antireflective packaging glass for solar modules". In: *Renewable Energy* 36.9 (2011), pp. 2489–2493.

[239] Jung Woo Leem, Young Min Song, and Jae Su Yu. "Broadband antireflective germanium surfaces based on subwavelength structures for photovoltaic cell applications". In: *Optics express* 19.27 (2011), pp. 26308–26317.

[240] Dan Zhao et al. "Haze-Free Highly Transparent Glass Substrates with Nanostructured Surface by Using Self-Assembled Ag Etch Masks". In: *ECS Journal of Solid State Science and Technology* 5.2 (2015), R6.

[241] Helmut Bechtel, Wolfgang Busselt, and Joachim Opitz. "Subwavelength particle layers for improved light outcoupling of OLEDs". In: *Organic Light-Emitting Materials and Devices VIII*. Vol. 5519. International Society for Optics and Photonics. 2004, pp. 194–205.

[242] Hong-Wei Chang et al. “Nano-particle based scattering layers for optical efficiency enhancement of organic light-emitting diodes and organic solar cells”. In: *Journal of Applied Physics* 113.20 (2013), p. 204502.

[243] Boris Riedel et al. “Tailored Highly Transparent Composite Hole-Injection Layer Consisting of Pedot: PSS and SiO2 Nanoparticles for Efficient Polymer Light-Emitting Diodes”. In: *Advanced Materials* 23.6 (2011), pp. 740–745.

[244] Julian Hauss et al. “Periodic Nanostructures Fabricated by Laser Interference Lithography for Guided Mode Extraction in OLEDs”. In: *Solid-State and Organic Lighting*. Optical Society of America. 2010, SOThB2.

[245] Yungui Li et al. “Tailor-made nanostructures bridging chaos and order for highly efficient white organic light-emitting diodes”. In: *Nature communications* 10.1 (2019), pp. 1–11.

[246] Rong Wang et al. “Broadband Light Out-Coupling Enhancement of Flexible Organic Light-Emitting Diodes Using Biomimetic Quasirandom Nanostructures”. In: *Advanced Optical Materials* 3.2 (2015), pp. 203–210.

[247] Won Hoe Koo, Yin Zhe, and Franky So. “Direct Fabrication of Organic Light-Emitting Diodes on Buckled Substrates for Light Extraction”. In: *Advanced Optical Materials* 1.5 (2013), pp. 404–408.

[248] Chih-Hao Chang et al. “Fourfold power efficiency improvement in organic light-emitting devices using an embedded nanocomposite scattering layer”. In: *Organic Electronics* 13.6 (2012), pp. 1073–1080.

[249] Jan B Preinfalk et al. “Large-area screen-printed internal extraction layers for organic light-emitting diodes”. In: *ACS Photonics* 4.4 (2017), pp. 928–933.

[250] Thomas Eiselt et al. “Inkjet-printed internal light extraction layers for organic light emitting diodes”. In: *Flexible and Printed Electronics* 3.1 (2018), p. 015007.

[251] Tobias Bocksrocker et al. “Efficient waveguide mode extraction in white organic light emitting diodes using ITO-anodes with integrated MgF 2-columns”. In: *Optics express* 20.6 (2012), pp. 6170–6174.

[252] Yong-Jae Lee et al. “A high-extraction-efficiency nanopatterned organic light-emitting diode”. In: *Applied Physics Letters* 82.21 (2003), pp. 3779–3781.

[253] Tobias Bocksrocker et al. “White organic light emitting diodes with enhanced internal and external outcoupling for ultra-efficient light extraction and Lambertian emission”. In: *Optics express* 20.106 (2012), A932–A940.

[254] Won Hoe Koo et al. “Light extraction from organic light-emitting diodes enhanced by spontaneously formed buckles”. In: *Nature Photonics* 4.4 (2010), p. 222.

[255] Byoungchoo Park and Hong Goo Jeon. “Spontaneous buckling in flexible organic light-emitting devices for enhanced light extraction”. In: *Optics Express* 19.105 (2011), A1117–A1125.

[256] Junhee Choi et al. “Light Extraction Enhancement in Flexible Organic Light-Emitting Diodes by a Light-Scattering Layer of Dewetted Ag Nanoparticles at Low Temperatures”. In: *ACS applied materials & interfaces* 10.38 (2018), pp. 32373–32379.

[257] Keunsoo Lee et al. “A light scattering layer for internal light extraction of organic light-emitting diodes based on silver nanowires”. In: *ACS applied materials & interfaces* 8.27 (2016), pp. 17409–17415.

[258] Christian Stamm. “Planarisierung von Streuschichten zur verbesserten Lichtauskopplung aus OLEDs”. Karlsruher Institut für Technologie, 2017.

[259] Dimitar K. Pandov. “Soft Lithography of Disordered Light Scattering Nanostructures for Solar Cells”. Karlsruher Institut für Technologie, 2018.

[260] Hongbo Lan and Yucheng Ding. *Nanoimprint lithography*. InTech Rijeka, 2010.

[261] Kayaku Microchem. “SU-8 2000 Permanent Epoxy Negative Photoresist”. In: *Data Sheet* (2015).

[262] Jin-Wook Shin et al. “Random nanostructure scattering layer for suppression of microcavity effect and light extraction in OLEDs”. In: *Optics letters* 39.12 (2014), pp. 3527–3530.

[263] Yun Li. “10.1: RGB Printed AMOLED: Challenges and Opportunities”. In: *SID Symposium Digest of Technical Papers*. Vol. 49. Wiley Online Library. 2018, pp. 95–98.

[264] Si-Tao Huo et al. “Real RGB printing AMOLED with high pixel per inch value”. In: *Journal of the Society for Information Display* 28.1 (2020), pp. 36–43.

[265] Madhusudan Singh et al. “Inkjet printing—process and its applications”. In: *Advanced materials* 22.6 (2010), pp. 673–685.

[266] Cholho Lee and Jang-Joo Kim. “Enhanced light out-coupling of OLEDs with low haze by inserting randomly dispersed nanopillar arrays formed by lateral phase separation of polymer blends”. In: *Small* 9.22 (2013), pp. 3858–3863.

[267] Masayuki Fujita et al. “Reduction of operating voltage in organic light-emitting diode by corrugated photonic crystal structure”. In: *Applied physics letters* 85.23 (2004), pp. 5769–5771.

[268] Ali Ozhan Altun et al. “Corrugated organic light emitting diodes for enhanced light extraction”. In: *Organic Electronics* 11.5 (2010), pp. 711–716.

[269] Joonseok Jung et al. “IoT Enabled Smart Emergency LED Exit Sign controller Design using Arduino”. In: *International journal of advanced smart convergence* 6.1 (2017), pp. 76–81.

[270] Sohee Jeon et al. “High-quality white OLEDs with comparable efficiencies to LEDs”. In: *Advanced Optical Materials* 6.8 (2018), p. 1701349.

Acknowledgements

I believe that the most valuable aspect of pursuing this degree has been the fantastic people I have had the privilege to learn from and work alongside. Most importantly, thank you to my advisor Prof. Dr. Uli Lemmer, for his faith in me and unwavering support throughout my study. His cheerfulness, insight, and limitless enthusiasm have kept me on track. It has been an immense privilege to develop intellectually under his tutelage. Next, I am grateful to Dr. Guillaume Gomard for providing and managing the LAMBDA project. I would not have even started this Ph.D. without the existence of this project. I am also thankful for Guillaume's patience and steadfast encouragement through the countless downs and ups that characterized this numerical and experimental effort. I particularly appreciate his investment of innumerable hours for scientific discussions and corrections of every publication. Furthermore, I would like to thank Prof. Dr.-Ing. Bernhard Schmauß for agreeing to act as the second referee.

I have been fortunate to collaborate with many institutions and groups throughout my Ph.D. In particular, many thanks to Dr. Karsten Bittkau at the Forschungszentrum Jülich GmbH for organizing all the research visits and deposition of the a-Si:H based solar cells used in this thesis. I also like to take this opportunity to acknowledge Dr. Stefan Schließke at the InnovationLab GmbH, who turned my idea of inkjet printing polymer blends during our last institute team-days break into inspiring brainstorms. Many thanks to you! My sincere gratitude additionally goes to Dr. Gerardo Hernandez-Sosa for managing this enjoyable joint project. This collaboration work partially enabled the experimental findings in Chapter 4 of this thesis. I further owe Dr. Radwanul H.Siddique (from Caltech) and Dr. Ihteaz M. Hossain a debt of gratitude for the successful joint projects, the scientific and non-scientific discussions.

I am incredibly grateful to those who provided support in my last few years, particularly Dr. Adrian Mertens, who conducted the optical-index measurements of most materials used in this thesis and several trips to InnovationLab to carry out experiments together. Fabian Schackmar was helpful in the preparation and revision of the last two publications, both experimentally and in bringing my chemistry background up to speed, for which I am very thankful. Dr. Amos Egel, Dominik Theobald, and Dr. Jan Preinfalk all contributed many ideas to OLED research. I would additionally like to thank Isabel Allegro and Dr. Raphael Schmager for their help with perovskite imprinting, Dr. Sara Moghadamzadeh for her help with titania depositions, Robert Huber and Jan Feßler for 3D printing, Christian Kayser for multiple devices instructions, and my students (Luis David Anchía Sáen, Anna Osypka, Christian Stamm, Adrian Grande, Dimitar K. Pandov, Jocelyn Van Leeuwen, Swantje Pauer, Mohamed A. Mohamed, Mark Ulanov, Yuhao Wang, Siyi Gao, Yingxuan

Yuan, and Yidan Ma). I am no less thankful to those not mentioned here—would be impossible to say all of your contributions.

I would also like to thank the Karlsruhe School of Optics and Photonics (KSOP, www.ksop.kit.edu) and the Max Planck School of Photonics (MPSP, www.photonics.maxplanckschools.org) for providing a graduate program and organizing different modules. Having platforms like KSOP and MPSP was enormous to gain insight into more applied approaches through the various modules and create contacts with other young scientists in the optics and photonics field.

Most of all, special thanks to all my friends outside of the university world for their never-ending support. Last but not least, my final and most significant thanks go to my beloved family for their constant love, never-ending support, and care throughout my many years of studies (far away from home). It's finally finished.